



HAL
open science

Mécanismes de contraste et contrôle du front d'onde en microscopie non linéaire cohérente

Nicolas Olivier

► **To cite this version:**

Nicolas Olivier. Mécanismes de contraste et contrôle du front d'onde en microscopie non linéaire cohérente. Optics [physics.optics]. Ecole Polytechnique X, 2009. English. NNT: . pastel-00006255v2

HAL Id: pastel-00006255

<https://pastel.hal.science/pastel-00006255v2>

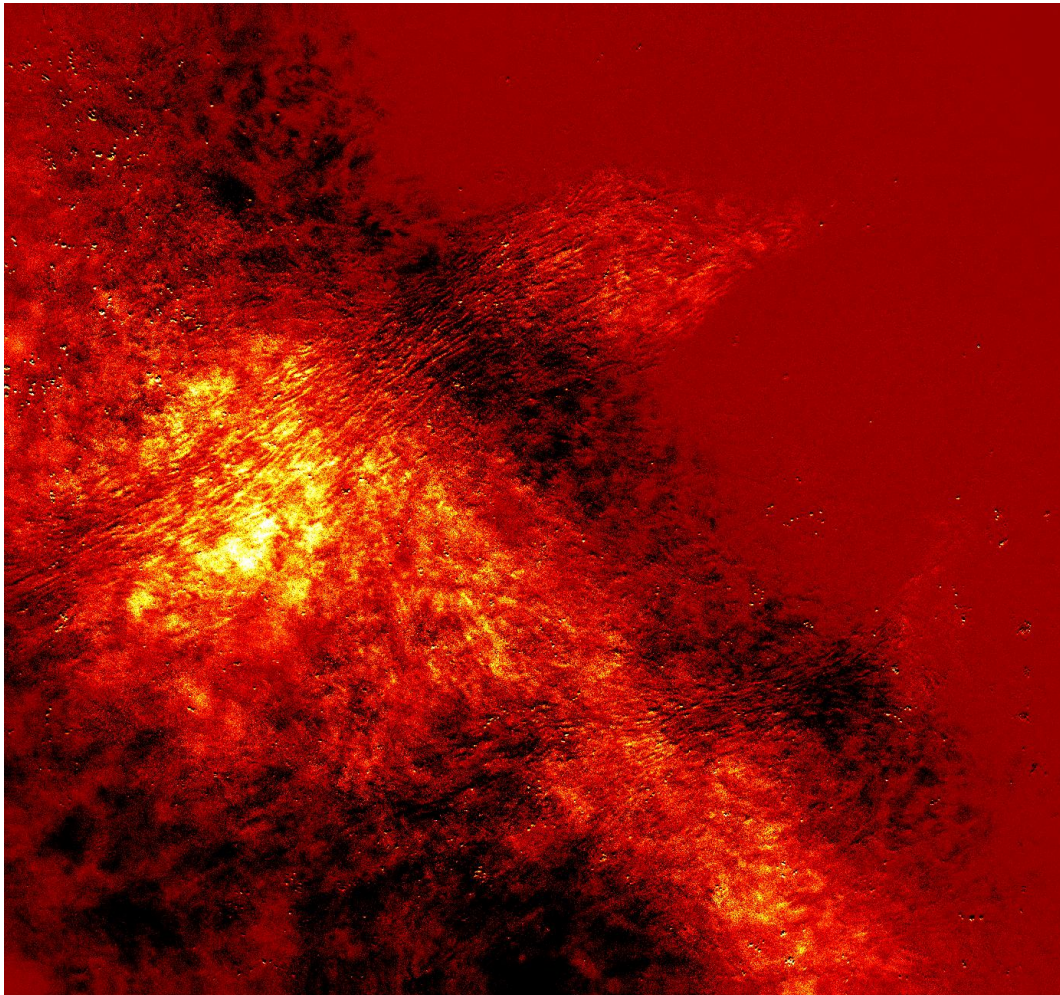
Submitted on 29 Oct 2015

HAL is a multi-disciplinary open access archive for the deposit and dissemination of scientific research documents, whether they are published or not. The documents may come from teaching and research institutions in France or abroad, or from public or private research centers.

L'archive ouverte pluridisciplinaire **HAL**, est destinée au dépôt et à la diffusion de documents scientifiques de niveau recherche, publiés ou non, émanant des établissements d'enseignement et de recherche français ou étrangers, des laboratoires publics ou privés.

Nicolas Olivier

Contrast Mechanisms & Wavefront Control in Coherent Nonlinear Microscopy





PHD THESIS

presented by :

Nicolas Olivier

On the subject of :

**Contrast Mechanisms
&
Wavefront Control
in
Coherent Nonlinear Microscopy**

LABORATORY FOR OPTICS AND BIOSCIENCES

Defended November 13th 2009

Dr. Emmanuel BEAUREPAIRE	Advisor
Pr. Laurent BOURDIEU	Reviewer
Pr. Nathalie DOSTATNI	
Dr. Valentina EMILIANI	
Pr. Jean-Louis MARTIN	
Pr. Jérôme MERTZ	Reviewer
Dr. Nadine PEYRIERAS	

Acknowledgements I

Note: Comme la plupart des gens entre les mains desquelles cette thèse va passer vont lire en premier¹ cette page pour voir si leur nom est mentionné, je vais faire un effort pour les contrarier en disséminant mes remerciements tout au long de ma thèse.²

Since this is a modern academic thesis, I decided to follow a common publication trend and to split my acknowledgements into several parts. As the first page will probably be read by most people and thus has the highest impact factor, I will thank here all the people that directly contributed to this thesis, starting with Emmanuel Beaurepaire, who introduced me to the magic world of nonlinear microscopy and gave me an fascinating³ subject to work on with both great freedom and support. I have been extremely lucky to work with you. I would also like to thank Delphine Débarre, who not only left me a microscope that worked better than most, and could use modalities none other could, but who also did all the hard part of interpreting the physical and chemical origin of the THG signal (see \approx half the references in the thesis). I know I'm already repeating myself in this first paragraph⁴, but working with both of you has been a pleasure.

Since I mentioned people who will not read this thesis in the first sentence, I would like to thank those who did read it, especially Jerome Mertz and Laurent Bourdieu who not only read it but even had to write a report on it, and, along with Nathalie Dostatni, Valentina Emiliani, Nadine Peyrieras, Jean-Louis Martin and Emmanuel Beaurepaire had to find relevant questions to ask about it. Thank you all for your time and for accepting to be part of my jury. All my thanks also go to Marie-Claire, Delphine, Emmanuel and my mother who read the thesis in its original full-of-typo form and helped me to make this (hopefully) readable version⁵. Special thanks to Alexander for making the visioconference possible.

This work is the result of several collaborations, which means I am very indebted to a lot of people, both in the lab & outside the lab:

- The zebrafish project described in chapter 5 involved many people in 4 different labs:
 - Louise Duloquin & Nadine Peyrieras at the *Institut de Neurobiologie Alfred Fessard* (INAF), Gif, France.
 - Miguel Lorengo-Oroz & Andres Santos at the *Universidad Politécnica de Madrid* (UPM), Madrid, Spain.

¹et même plus souvent uniquement

²En même temps, ils ne sont pas tellement bien cachés...

³well, I did spend 3 years working on it, so it has to be at least fascinating !

⁴I will keep on repeating myself, consider yourself warned.

⁵The acknowledgements have not been re-read, and give you an idea of how bad an uncorrected version could have been.

- Paul Bourguine & Thierry Savy at the *Centre de Recherche en Epistémologie Appliquée* (CREA), Ecole Polytechnique, Paris, France.
- Israël Veilleux, Xavier Solinas & Delphine Débarre at the *Laboratory for Optics & Biosciences* (LOB), Ecole Polytechnique, Palaiseau, France.

Thank you all, we will get this paper published soon !

- The project on the imaging of the human cornea described in chapter 5 involved quite a few people:
 - Florent Aptel, Jean-Marc Legeais and Gilles Renard, ophthalmologists at the *Laboratoire Biotechnologie et Oeil* (Université Paris V), Hôtel-Dieu Hospital, Paris France.
 - Patrick Sabatier, Banque Française des Yeux (French Eye Bank)
 - Karsten Plamann at the *Laboratory for Applied Optics* (LOA) (ENSTA-Polytechnique), Palaiseau France.
 - Ariane Deniset-Besseau & Marie-Claire Schanne-Klein at the *Laboratory for Optics & Biosciences* (LOB) (Polytechnique), Palaiseau France.

One down, one more to go !

- The project on the use of the TAG Lens in microscopy described in chapter 4:
 - Alexandre Mermillod-Blondin & Craig B. Arnold from Princeton University.
- Drosophila embryos have been used several times as a model in this thesis, and they were provided by the group of Emmanuel Farge at the Institut Curie, Paris. Thank you Emmanuel, Nicolas, Padra, Laurent and Philippe-Alexandre.
- I also wish to thank: Renaud Legouis, Erica Montani & Madelaine Åkeson for the work on C. Elegans, Agathe for the help with the bibliography, and Rajesh, Guillaume, Caroline & Manuel for showing me their work work on spectral phase shaping.

I gratefully acknowledge Xavier and Jean-Marc for all the work in electronics & mechanics they did during these 3 years, and without whom everything would have taken so much longer (if possible at all). My thanks also go to Laure & Christelle for all the paperwork they spared me and to the whole lab for both scientific and random discussions that made working in the lab such an friendly experience.

to be continued....

Contents

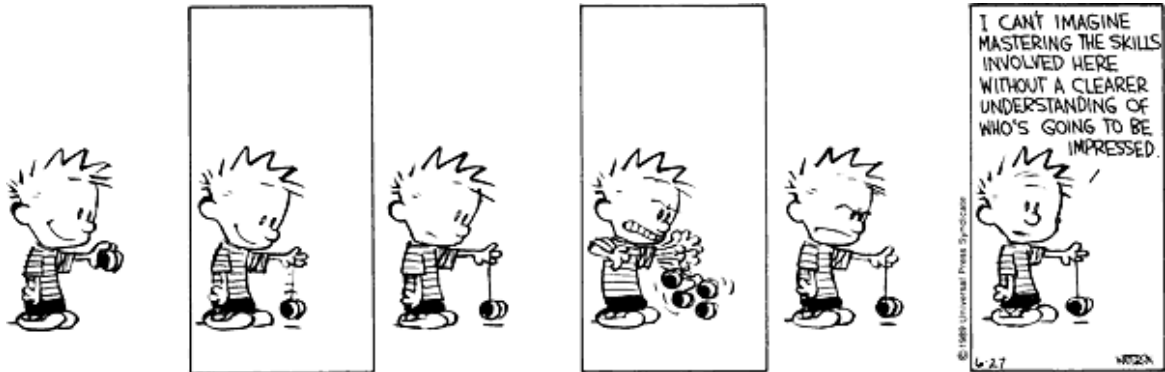
Foreword	vi
1 Multiphoton Microscopy in the Biosciences	1
1.1 Principles & Properties	1
1.1.1 Optical Sectioning	2
1.1.2 Excitation	2
1.1.3 Scanning	4
1.1.4 Resolution	5
1.1.5 Photo-bleaching	6
1.1.6 Photo-toxicity	6
1.2 Deep Tissue Imaging	6
1.2.1 Conservation of the Optical Sectioning with Depth	7
1.2.2 Absorption	7
1.2.3 Scattering	8
1.2.4 Aberrations	9
1.3 Different Types of Nonlinear Microscopies	10
1.3.1 2PEF (and 3PEF) Microscopy	10
1.3.2 SHG Microscopy	12
1.3.3 CARS Microscopy	14
1.3.4 SRS Microscopy	16
1.3.5 STED Microscopy	17
1.4 THG Microscopy	18
1.4.1 Third Harmonic Generation	18
1.4.2 THG Microscopy: First Demonstrations	18
1.4.3 Coherence: Geometrical Effects.	19
1.4.4 Identification of the Sources of Contrast	19
1.4.5 Applications in Biology	20
1.4.6 Applications In Other Domains	23
1.5 Multiple Sources of Contrast	24
1.5.1 Endogenous & Exogenous Signals	24
1.5.2 Multimodal Microscopy	25
1.6 Epidetection in Nonlinear Microscopy	26
1.6.1 Introduction	26
1.6.2 Incoherent Microscopy	26
1.6.3 THG Microscopy	28
Bibliography	33

2	Modeling Nonlinear Microscopy	49
2.1	Modeling Nonlinear Microscopy	50
2.1.1	Numerical Method	50
2.2	Modeling Incoherent Nonlinear Microscopy	51
2.2.1	Introduction	51
2.2.2	Point-Spread Function in Incoherent Multiphoton Microscopy	52
2.2.3	Deconvolution	53
2.3	Modeling Coherent Nonlinear Microscopy	54
2.3.1	Overview of the Main Model	54
2.3.2	Simplifications Implied by the Main Model	54
2.3.3	Geometry	55
2.4	Focusing of Fields Using the Angular Spectrum Representation	56
2.4.1	Assumptions	56
2.4.2	Expression of the Focal Field	57
2.4.3	Comparison Between Angular Spectrum Representation & Gaussian Paraxial Approximation	57
2.5	Modeling Nonlinear Effects	59
2.5.1	Nonlinear Polarization of the Main Nonlinear Effects	60
2.5.2	Symmetries & Tensors	60
2.6	Modeling the Propagation of the Nonlinear Polarization	61
2.6.1	Green's Function	61
2.7	Numerical Implementation	61
2.7.1	Numerical Integration of the Focal Field	61
2.7.2	Numerical Considerations: Size, Sampling	61
2.7.3	Far-Field Integration	62
2.8	Optical Confinement	62
2.8.1	Incoherent Microscopy	63
2.8.2	Influence of Scattering & Absorption	64
2.8.3	Coherent Microscopy	65
2.9	Phase Matching in Coherent Microscopy	66
2.9.1	Introduction	66
2.9.2	In Coherent Nonlinear Microscopy	68
2.9.3	3D Phase-matching - Direction of Emission	71
2.9.4	Conclusion	72
	Bibliography	74
3	Third Harmonic Generation Microscopy	79
3.1	“Bulk” THG	80
3.1.1	Description of the Model	81
3.1.2	Size Effects	82
3.1.3	Effect of Sample Anisotropy	85
3.1.4	Influence of the Numerical Aperture	89
3.2	Quasi-Phase-Matching	94
3.3	THG in Crystals & Quasi-Crystals	96
3.3.1	Introduction	96
3.3.2	Influence of the Dispersion	97
3.3.3	Dispersion Compensation Using Birefringence	97
3.3.4	Symmetries & Anti-symmetries	99
3.3.5	Tensorial Effects	100

Bibliography	106
4 Wavefront Control in Nonlinear Microscopy	111
4.1 Focus Engineering in Coherent Nonlinear Microscopy	112
4.1.1 Introduction	112
4.2 THG Microscopy with Higher Order Modes: a Numerical Study	113
4.3 THG Microscopy with Phase-Masks	128
4.3.1 2-Zone and 3-Zone Annular Phase-Masks	128
4.3.2 THG with Binary Phase-Masks	129
4.4 THG Microscopy with Bessel Beams	132
4.4.1 Bessel Beams: Definition & Properties	132
4.4.2 THG with Bessel Beams	133
4.4.3 THG Microscopy with Bessel Beams	134
4.4.4 Quasi-Phase-Matching Using Bessel Beams	137
4.5 Rapid Wavefront Modulation in 2PEF Microscopy	139
4.5.1 Introduction	139
4.5.2 Two-photon Microscopy with Simultaneous Standard & Extended Depth-of-Field Using a Tunable Acoustic Gradient-index Lens	139
4.6 Adaptive Optics	144
4.6.1 Introduction	144
4.6.2 Aberration Correction in Microscopy	144
4.6.3 Experimental Setup	145
4.6.4 Reformulation of the Optimizations Problem	145
4.6.5 Choice of the Metric	146
4.6.6 Calculation of the Aberration Basis	146
4.6.7 Dynamic Aberration Correction for Multiharmonic Microscopy	148
Bibliography	154
5 Biological Applications of Third Harmonic Generation Microscopy	163
5.1 Multimodal Multiphoton Imaging of the Human Cornea	164
5.1.1 Introduction	164
5.1.2 Nonlinear Contrasts in the Human Cornea	165
5.1.3 Multiharmonic Imaging of the Corneal Stroma	170
5.1.4 Polarization of the THG Signal	172
5.1.5 Perspectives & Conclusions	174
5.2 Zebrafish	176
5.2.1 Introduction	176
5.2.2 Reconstruction of the Zebrafish Early Development Using Multiharmonic Microscopy	178
Bibliography	188
Conclusion	192
A Nonlinear Optics	195
A.1 Nonlinear Wave Equation	195
A.1.1 Linear Isotropic Medium	196
A.1.2 Monochromatic Fields	196
A.1.3 Paraxial Approximation	197
A.1.4 Slowly Varying Amplitude Approximation	197

A.1.5	Nonlinear Wave-Equation	197
A.2	The Gaussian Beam	198
A.3	The Bessel Beam	199
A.3.1	The Bessel-Gauss Beam	199
A.4	Phase-Matching Plane Waves	200
A.4.1	Second Harmonic Generation	200
A.4.2	n^{th} Harmonic Generation	201
A.4.3	Backward Emission	201
A.4.4	Lateral Emission	202
A.5	Harmonic Generation with Focused Gaussian Beams	202
A.5.1	The J Integral	203
A.6	Harmonic Generation with Focused Bessel Beams	205
A.7	Comparison Between THG & NR-CARS	208
B	Experimental Setup	211
B.1	Description of the Setup	212
B.2	Characteristics of the Laser & OPO	213
B.2.1	Chameleon Ultra II	213
B.2.2	OPO	213
B.3	Microscope Setup with Adaptive Optics	214
B.4	Characteristics of the Deformable Mirror	215
B.5	Setup Using the TAG lens	216
B.5.1	Limitation & Perspectives	216
B.6	Characteristics of the Microscope Objectives	217
B.7	Cornea Preparation	218
	Bibliography	219

Foreword



This is the most difficult part of the thesis to write: how to make it seem like three years of work were done to answer one specific question. We can start by giving the state of the art of THG microscopy in 2006:

- Phase-matching conditions have been identified; interfaces and inclusions have been recognized as the geometries producing the most signal.
- Chemical specificity has been studied, and lipids have been described as a major source of contrast in biological samples.
- Biological applications on developing embryos and cultured cells have been demonstrated.

The easy way out would be to present it as a follow-up to Delphine Débarre's thesis, quoting from her conclusion:

Afin d'augmenter encore la qualité des données obtenues, de nombreuses améliorations techniques peuvent être envisagées, telles que la mise en forme temporelle (*pulse shaping*) ou spatiale (*PSF engineering*) des impulsions, ou encore la correction des aberrations induites par les tissus.

that can be translated to:

In order to increase the quality of the data/images, several technical improvements can be considered such as temporal pulse shaping, PSF engineering or the correction of tissue-induced aberrations.

There are therefore three main objectives in this thesis:

1. Continue the study of phase-matching conditions in coherent nonlinear microscopy.

2. Work on the aforementioned technical improvements.
3. Demonstrate new applications of THG microscopy in biology.

Outline

- Chapter 1 gives a rapid introduction to the different methods of nonlinear microscopy that are now used. A particular attention is given to THG microscopy.
- Chapter 2 describes a general method to model coherent nonlinear microscopy, and illustrates several properties using simpler analytical models.
- Chapter 3 deals with the influence of the structure of the sample on the phase-matching conditions in THG microscopy, using numerical simulations performed with the model described in chapter 2.
- Chapter 4 covers three different topics: it starts by an expansion of the third chapter for non-Gaussian excitation, and then presents two different experimental studies of wavefront control in nonlinear microscopy.
- Finally, chapter 5 presents two novel biomedical applications of nonlinear microscopy. The first one is on the multimodal nonlinear imaging of the unstained human cornea, done in collaboration with LOA⁶ (ENSTA, Palaiseau) and Hospital Hotel-Dieu (Paris). The second one is on the reconstruction of the zebrafish embryo development during the first 3 hours of development, done in collaboration with INAF⁷ (Gif), Univ. Madrid⁸ and CREA (X, Palaiseau).

⁶Laboratoire d'Optique Appliqué

⁷Institut de Neurobiologie Alfred Fessard

⁸Universidad Politécnica de Madrid

Chapter 1

Multiphoton Microscopy in the Biosciences

Contents

1.1 Principles & Properties	1
1.2 Deep Tissue Imaging	6
1.3 Different Types of Nonlinear Microscopies	10
1.4 THG Microscopy	18
1.5 Multiple Sources of Contrast	24
1.6 Epidetction in Nonlinear Microscopy	26
Bibliography	33

INTRODUCTION

Since its introduction in 1990, multiphoton¹ microscopy [1] has become a widely used tool in cell and tissue biology [2, 3]. This technique relies on the different nonlinear optical phenomena that can occur in the presence of an intense electric field [4, 5], such as the field produced by a focused femtosecond laser beam. We will briefly describe the main concepts and the properties of this type of microscopy in section 1.1, with a particular attention to the advantages it offers for deep tissue imaging in section 1.2, before detailing the different modalities that can be used in section 1.3. THG microscopy is the main focus of this thesis, and it is discussed in section 1.4, followed by a discussion on the combination of several sources of contrast in section 1.5, and finally a study of epidetction in nonlinear microscopy in section 1.6.

1.1 Principles & Properties

Nonlinear microscopy is a scanning method that relies on the nonlinear optical properties of the sample [1, 3]². Figure (1.1) gives a simple view of what a nonlinear microscope consists

¹also called nonlinear microscopy, both terms will be used indifferently in this thesis

²The equations that describe nonlinear optical phenomena can be found in Appendix A

of:

- A laser source: typically a femtosecond Ti:Sa laser.
- A scanning system: usually the beam is scanned in the sample.
- A microscope objective that focuses the laser beam into a diffraction-limited spot.
- A set of filters and detectors that are appropriate for the wavelength(s) of the nonlinear process(es) used.

A computer controls the synchronization between the scanning and the detection.



Figure 1.1: SCHEMATIC VIEW OF A MULTIPHOTON MICROSCOPE

The laser beam is focused into the sample. At the vicinity of the focal point, the intensity is high enough to allow nonlinear optical phenomena to occur. Nonlinear photons then propagate, and are detected or filtered out depending on their wavelength.

1.1.1 Optical Sectioning

Because an n^{th} order nonlinear signal is proportional to the n^{th} power of the excitation, the nonlinear signal obtained from a focused beam comes essentially from the region of highest intensity referred to as the *focal volume*. This means that the origin of the signal is intrinsically confined, as illustrated by figure (1.2), in which a solution of fluorescein is illuminated by two different lasers: a CW laser at 488nm, and a pulsed laser at 960nm. The first laser induces one-photon-excited fluorescence all along its propagation and we can clearly see the cone of excitation, whereas the pulsed laser only induces two-photon excited fluorescence where the square of the excitation intensity is highest, i.e in the vicinity of the focal plane of the objective. Thus, the origin of the nonlinear signal is confined, and the 3D distribution of nonlinear signal can be obtained by scanning the beam focus through the sample.

This intrinsic optical sectioning obviates the need for a confocal pinhole in front of the detector, contrary to the case of linear confocal microscopy where such an aperture is necessary to provide 3D resolution. Adding a pinhole in a nonlinear microscope produces only a marginal increase in resolution [6, 7], and reduces the signal collection efficiency, particularly in scattering samples.

1.1.2 Excitation

Nonlinear microscopy became a popular technique thanks to the introduction of robust commercial femtosecond laser sources, the latest generation often being turnkey computer-controlled systems. For example, typical Titanium: Sapphire (Ti:Sa) lasers provide $\approx 100fs$

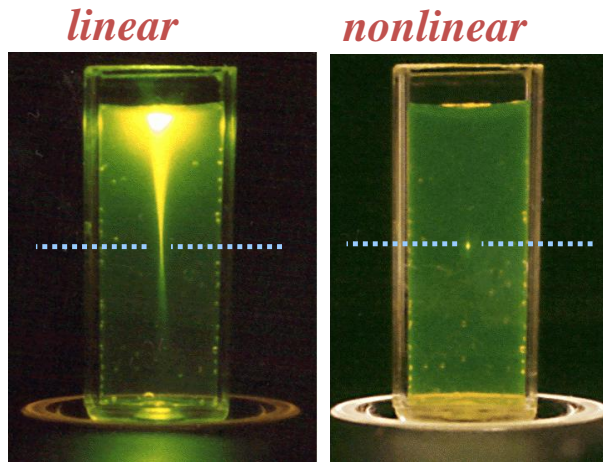


Figure 1.2: ILLUSTRATION OF OPTICAL SECTIONING IN FOCUSED NONLINEAR EXCITATION

Photographs of a solution of fluorescein after one photon excitation (left) and 2-photon excitation (right). Adapted from [3].

1st order (linear)	$S_1 = P_0$
2nd order	$S_2 \propto \frac{P_0^2}{f\tau}$
3rd order	$S_3 \propto \frac{P_0^3}{f^2\tau^2}$
Nth order	$S_n \propto \frac{P_0^n}{f^{(n-1)}\tau^{(n-1)}}$

Table 1.1: NONLINEAR SIGNAL FOR A GIVEN PULSE-DURATION AND REPETITION RATE

Linear fluorescence only depends on the average power, but the higher the nonlinear effect, the more advantageous it becomes to have short pulse-durations or low repetition rates.

pulse trains with a central wavelength tunable in the 700-980nm range, with a repetition rate of $\approx 80MHz$, and an average output power larger than 2W. These sources are well suited for two-photon excited fluorescence (2PEF) imaging of visible chromophores (eg: GFP). If we consider an n^{th} order nonlinear process, the nonlinear signal will scale as the average of the n^{th} power of the excitation [4]. If we consider a pulse duration τ and a repetition rate f for a given average power P_0 , the intensity of a single Gaussian pulse can be expressed as:

$$I(t) = \frac{P_0}{f\tau\sqrt{2\pi}} e^{-\frac{t^2}{2\tau^2}} \quad (1.1)$$

and an n^{th} order nonlinear signal S_n is then proportional to:

$$S_n \propto f \cdot \langle I(t)^n \rangle \quad (1.2)$$

The nonlinear signal for an n^{th} order nonlinear process as a function of pulse-duration and repetition rate are summed up in Table 1.1.

We see that for all the nonlinear modalities, the signal scales inversely with the pulse-duration and the repetition rate. This means that in experimental situations where the excitation is not saturated, amplified pulses such as the ones provided by regenerative amplifiers and Optical Parametric Amplifiers (OPA) can be advantageous in nonlinear microscopy, as demonstrated by Theer *et al.* [8] in the case of 2PEF microscopy. However, the low repetition rate of these sources sets upper bounds on the achievable image pixel rate. Very short lasers with pulse-durations of a few femtosecond also have an interesting potential, but require to implement dispersion compensation techniques.

As mentioned above, typical values for the repetition rate and pulse-durations are respectively 100MHz and 100fs , which means the ratio $f\tau$ is in the order of $10^8 \times 10^{-16} = 10^{-5}$: for a third order process, the difference in nonlinear signal using a CW laser or a Ti:Sa laser is 10^{-10} . Typical imaging conditions yield approximately one photon per μs , which means getting one photon using a CW laser with the same average power would take about 2 hours and 45 minutes.

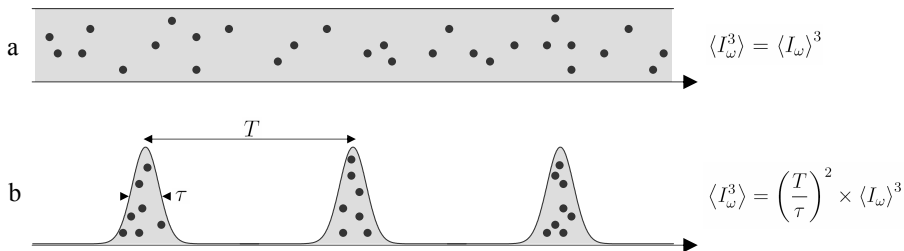


Figure 1.3: PULSED EXCITATION COMPARED WITH CONTINUOUS EXCITATION
 Comparison between the efficiency of a continuous (a) and pulsed (b) excitation for a third order nonlinear process. Adapted from [9].

The laser system used during this thesis consists of a Ti:Sa oscillator and a synchronously pumped OPO. The Ti:Sa laser is a turnkey system (Chameleon Ultra II, Coherent) that is tunable between 680nm and 1080nm and provides pulses of $\approx 100\text{fs}$. It can be used directly as an excitation source, or to pump an Optical Parametric Oscillator (OPO, APE) that provides pulses between 1050nm and $1.3\mu\text{m}$, with pulse-durations of $\approx 100\text{fs}$ (more details in Appendix B.1). This laser chain can therefore provide excitation with a center wavelength tunable in the $680\text{-}1300\text{nm}$ range, depending on the application.

1.1.3 Scanning

The spatial confinement of the nonlinear signal implies that nonlinear microscopy is intrinsically a scanning technique, which means the imaging speed is limited either by the signal level (ie: the minimum pixel acquisition time), or by the speed of the scanning method. The most common scanning technique relies on galvanometric mirrors which provide rapid beam steering (typically $100\text{-}500\ \mu\text{m}$ per ms in the sample), so the signal level is usually the limiting factor in biological samples.

Several technological developments aim at increasing the imaging speed: parallelization using multiple beams for example [10–12], means the imaging speed can be increased linearly with the number of beams. Line scanning [13, 14], which reduces the dimension of the scanning space by one, is an interesting alternative although it degrades the axial resolution and increases the

alignment complexity.

Temporal focusing is an interesting approach where the sectioning is achieved by temporal instead of spatial focusing: the spectral phase of the pulse is modulated so as to have a short pulse only at the focus of the objective, which means full field imaging is possible if the intensity is high enough, as demonstrated in the case of 2PEF microscopy by Tal *et al.* [15]. This method can be combined with line scanning techniques which allow an improved speed without compromising the resolution [16, 17], or with phase-shaping methods to increase the resolution [18, 19].

Wide field³ CARS has been demonstrated by Heinrich *et al.* [20] using a folded excitation geometry, and allows an imaging speed of a few nanoseconds which is orders of magnitude shorter than the fastest scanning techniques.

However, we note that all these parallel methods share some drawbacks: first the detection system has to be changed from a point detector (usually a photo-multiplier tube (PMT)) to a camera, or at least a multi-point detector, but more importantly they also limit the attainable imaging depth (discussed in section 1.2), as the scattering of the nonlinear photons by the sample now degrades the quality of the images. Thus, the application of these methods is somewhat restricted to thin samples, for which linear methods such as confocal microscopy are also adapted (and often cheaper).

Finally, when the signal level is not limiting, fast scanning methods can be used:

- Acousto-optic modulators [21, 22] can replace the galvanometric mirrors, as their speed is orders of magnitude higher, but they introduce several complications such as chromatic aberrations, chromatic dispersion, and important losses. These issue can be addressed [23, 24] at the price of increased experimental complexity.
- Video-rate imaging can be achieved by using a fast element for scanning along one dimension, such as a polygon scanning mirror (used in ref. [25] for coherent anti-Stokes Raman scattering microscopy) or a resonant galvanometer (used for 2PEF microscopy in ref. [26]).

1.1.4 Resolution

Resolution in multiphoton microscopy will be discussed in more details in Chapter 2. A rule of thumb, though, is that assuming a Gaussian-Gaussian spatial excitation profile the resolution for an n^{th} order nonlinear effect will depend on the wavelength divided by \sqrt{n} because the width of the n^{th} power of a Gaussian function is equal to the width of the Gaussian function divided by \sqrt{n} .

Due to the geometry of the excitation, the lateral resolution is better than the axial resolution. Approximate analytic expressions have been derived from numerical calculations in the case of an n^{th} order incoherent process assuming a Gaussian-Gaussian excitation profile as [27]:

³Wide in this case is an area of $50\mu\text{m}$ by $50\mu\text{m}$

$$\delta_{lat} = \frac{0.61\lambda}{\sin\theta\sqrt{n}} \quad (1.3)$$

$$\delta_{ax} = \frac{0.894\lambda}{(1 - \cos\theta)\sqrt{n}} \quad (1.4)$$

where 2θ is the focusing angle sustained by the objective lens (and is related to the often used Numerical Aperture (NA) by the equation $NA = n \sin(\theta)$). If we compare these resolutions with the ones achieved using confocal microscopy, we see that the resolution is not as good because of the longer wavelengths involved (typically, for an n^{th} order effect the excitation is n times the linear excitation wavelength, so the resolution is decreased by a factor \sqrt{n}). However, the spatial confinement and therefore the resolution is much better preserved when the beam is focused inside a scattering sample (which is the case of most biological tissues) in the case of 2PEF than in the case of 1PEF, as will be discussed in section 1.2.

1.1.5 Photo-bleaching

In the case of 2PEF microscopy, one advantage of the confinement of the excitation is that there is no photo-bleaching away from the focal volume. As photo-bleaching is proportional to the excitation rate, we see that in linear microscopy it is not limited to the imaged plane, and that every plane absorbs roughly the same amount of energy. The ratio of induced photo-bleaching between linear and 2PEF imaging (assuming the same axial sampling) is thus proportional to the thickness of the imaged sample divided by the axial resolution .

1.1.6 Photo-toxicity

One final advantage of nonlinear microscopy is the reduced photo-toxicity for 3D imaging. The main reason for that is that the linear absorption of biological tissues is much lower in the near-IR wavelengths (typically 700-1300nm) used for nonlinear microscopy than for the wavelengths used in linear microscopy (typically, 350 to 500nm), as illustrated in figure (1.5). This spectral region is sometimes called **transparency window** for this reason (if the wavelength is increased, the absorption of water significantly increases). Moreover, even when we consider the influence of 2-photon-excited photo-toxic effects [28–32], they are limited to the imaged plane by the same mechanism as the optical confinement, which means 3D imaging can be performed with reduced toxicity . Squirrell *et al.* [33] demonstrated the possibility to image a developing mouse embryo during hours using 2PEF microscopy without compromising its viability.

1.2 Deep Tissue Imaging

One of the main advantages of nonlinear microscopy over linear (confocal) microscopy is its ability to image deeper inside scattering tissues [8, 34–37], as illustrated by figure (1.4), where a mouse brain slice is imaged down to a depth of approximately $1mm$.

The main reason for this is that the excitation wavelength in multiphoton microscopy (typically 900nm) is longer than in linear microscopy (typically 500nm), and that two of the most limiting factors, e.g. the absorption and the scattering are wavelength dependent. This means they affect optical sectioning more severely in linear microscopy than in nonlinear microscopy,

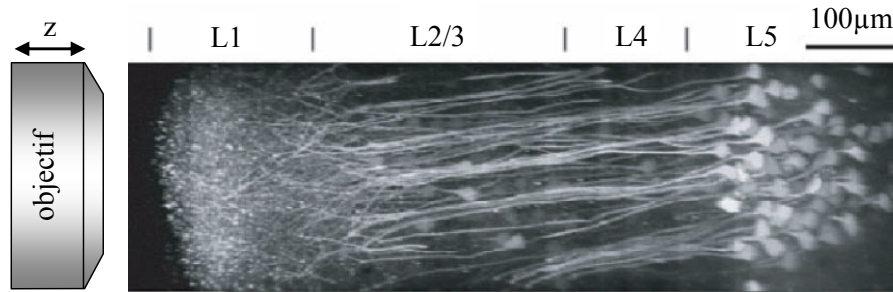


Figure 1.4: DEEP TISSUE IMAGING WITH 2PEF MICROSCOPY

2PEF microscopy image of a brain slice stained with a fluorescent dye. Adapted from [37].

as discussed below. The use of longer wavelengths in nonlinear microscopy ($\lambda > 1.2\mu m$) to achieve deeper penetration inside tissues has been recently reported [38]. Other reasons are related to the imaging mechanisms and will be discussed in the next paragraph.

1.2.1 Conservation of the Optical Sectioning with Depth

The optical sectioning in nonlinear microscopy is more robust than that of linear confocal microscopy in turbid media for two reasons:

- The confinement of the excitation due to the nonlinearity is maintained in scattering media. The scattered photons can therefore induce no fluorescence.
- In confocal microscopy, fluorescence photons originate from the whole excitation cone and from the scattered excitation photons. In order to be detected, the photons not only have to be collected, but they also have to go through a pinhole that is conjugated with the focal point of the objective. In the absence of scattering, this technique effectively filters out the out-of-focus photons, but in the presence of scattering not only can the photons created at the focal point be filtered out because they have been scattered on the way back, but out of focus photons can be detected if the scattering gives them a trajectory that seems to originate in the focal volume. The absence of out of focus fluorescence means that this does not happen in nonlinear microscopy.

1.2.2 Absorption

The absorption of a medium can be described by its absorption mean free path (noted l_a) which is defined as the average distance traveled by a photon before being absorbed. Light propagating in an absorbing medium can therefore be described by the Beer-Lambert law:

$$I(z) = I(z=0).e^{-z/l_a} \quad (1.5)$$

where $I(z)$ is the intensity after traveling a distance z inside the absorbing medium.

Absorption is an important limiting factor in linear confocal microscopy because the excitation wavelength is typically in the UV or blue part of the visible spectrum, and cells and tissue components exhibit strong absorption at these wavelengths, as illustrated by figure (1.5).

In both linear and nonlinear microscopy, the first effect of absorption is to decrease the intensity of the signal. Yet, in linear microscopy it also tends to reduce the signal-to-background

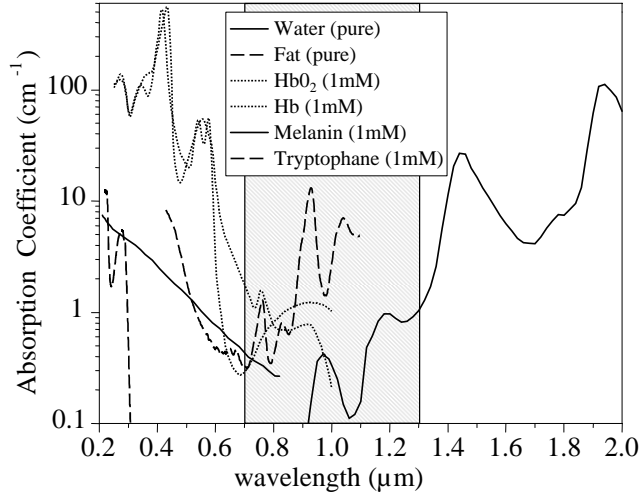


Figure 1.5: ABSORPTION SPECTRA OF THE MAIN ABSORBERS PRESENT IN BIOLOGICAL SAMPLES
Adapted from [3].

ratio. Indeed, the influence of absorption is more important on the “signal” photons propagating from the focal volume to the collection optics than on the “background” photons created in the cone of excitation.

This phenomenon is not present in nonlinear microscopy, as long as the excitation is confined to the focal volume.

1.2.3 Scattering

Like absorption, scattering is often described by a *scattering mean free path* (noted l_s), defined as the average distance traveled by a photon between two scattering events. The evolution of the intensity of the un-scattered light can thus be written as:

$$I(z) = I(z=0).e^{-z/l_s} \quad (1.6)$$

where z is the distance traveled in the scattering medium. Another parameter used to describe scattering is the *mean scattering angle*:

$$g = \langle \cos(\theta) \rangle \quad (1.7)$$

where θ is the angle between the original direction of the photon and the direction in which it is scattered.

Similarly to absorption, scattering is highly dependent on the wavelength, as illustrated by figure (1.6) which shows the scattering mean free path as a function of the wavelength for a mixture of droplets of diameters ranging from $20nm$ to $700nm$. It is also strongly sample-dependent as illustrated by table 1.2 which compares the scattering properties of the mouse brain and liver tissues.

The scattering mean free path increases with the wavelength ($l_s \propto \lambda^{2.4}$ according to reference [39]), which provides deeper excitation in nonlinear microscopy compared to linear microscopy. If multiple scattering can be neglected, the imaging depth in nonlinear microscopy is directly proportional to l_s , hence the benefit of using longer wavelengths. Scattering puts a

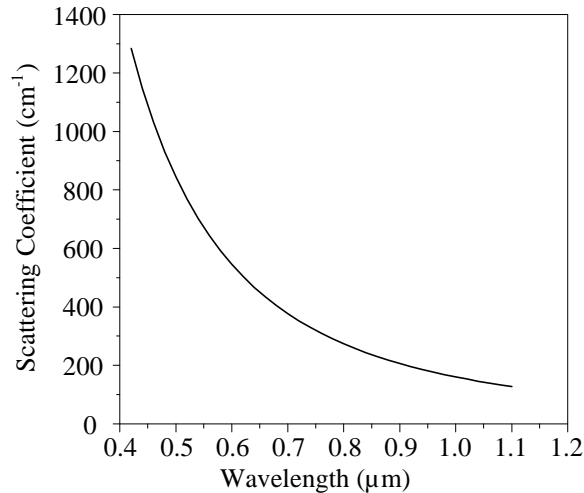


Figure 1.6: SCATTERING COEFFICIENT $\mu_s = 1/l_s$ AS A FUNCTION OF THE WAVELENGTH

for a mixture of droplets of diameters ranging from $20nm$ to $700nm$. The scattering mean free path dependence on the wavelength can be approximated by a power law. Adapted from reference [39].

	λ (nm)	l_s (μm)	g
Brain (white matter)	480	42	0.91
	850	71	0.95
	1064	91	0.95
Liver	515	35	–
	850	50	0.95
	1064	67	0.93

Table 1.2: SCATTERING PROPERTIES OF BRAIN AND LIVER TISSUES In both cases, l_s increases with the wavelength. Adapted from references [35, 40].

fundamental limit on the imaging depth, because the exponential decrease in excitation intensity eventually leads to a situation where the intensity at the surface is higher than at the focal plane [41, 42].

1.2.4 Aberrations

Another element that limits the imaging depth is the presence of optical aberrations due to refractive index-mismatches before and within the sample [43–45]. The deeper the beam is focused in the sample, the more aberrations increase the size of the focal volume, which has severe consequences on nonlinear signals. Their influence will be discussed in more details in section 4.6.

1.3 Different Types of Nonlinear Microscopies

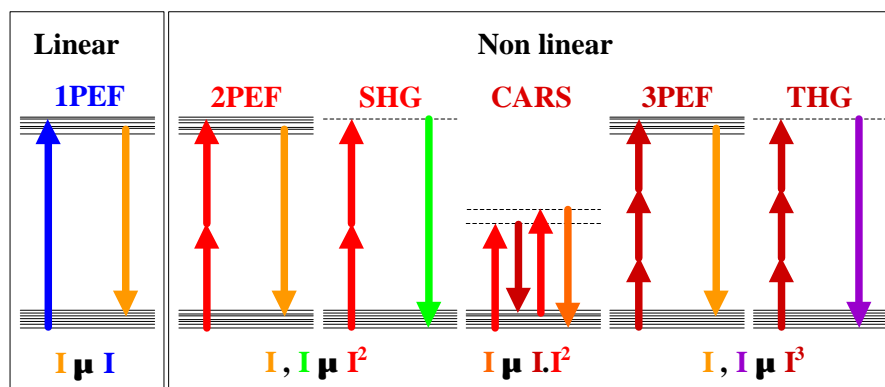


Figure 1.7: DIFFERENT TYPES OF NONLINEAR MICROSCOPIES

2PEF: 2-Photon Excited Fluorescence, 3PEF: 3-Photon Excited Fluorescence, SHG: Second Harmonic Generation, THG: Third Harmonic Generation, CARS: Coherent Anti-stokes Raman Scattering. Adapted from [9].

Although SHG and CARS microscopy were the first nonlinear imaging techniques demonstrated experimentally [46, 47], they remained mainly a curiosity for a decade, and it was not until 2PEF microscopy was also demonstrated [1] that multiphoton microscopy found applications in biology [3]. Although 2PEF is still by far the most widely used nonlinear microscopy technique in biology, the other modalities are becoming more and more relevant.

1.3.1 2PEF (and 3PEF) Microscopy

1.3.1.1 2PEF: Principles & Properties

Predicted in the first part of the XX^{th} century by Maria Göppert-Mayer [48, 49], 2-Photon-absorption was first demonstrated in 1961 in a $CaF_2 : Eu^{2+}$ crystal [50]. Two-Photon Excited Fluorescence microscopy relies on the simultaneous absorption of two photons from the exciting beam which excite a fluorescent molecule which relaxes to the ground state by emitting one fluorescence photon whose energy is equal to the sum of the energies of the absorbed photons minus the energy corresponding to the Stokes shift [27]. 2PEF is an incoherent process, and although it is a second order process (the signal scales as the squared intensity of the excitation), it depends on the imaginary part of the third-order nonlinear susceptibility $Im(\chi^{(3)})$ of the sample. For a quantum description of the two-photon excitation process, see references [51, 52] and more specifically of 2PEF microscopy, see references [4, 5, 53]. Two-Photon Excited Fluorescence microscopy usually relies on a tunable femtosecond laser source for the excitation, with pulse durations of $100 - 150 fs$ and wavelengths between $700 nm$ and $1 \mu m$.

Shorter pulses are sometimes used, but the fact that they have large spectra means they can simultaneously excite many fluorophores without specificity. Moreover, delivering sub-50fs pulses to the focus of a microscope requires to implement elaborate dispersion-compensation schemes. However, an interesting possibility offered by broadband ultrashort pulses is to combine 2PEF microscopy with coherent control methods. Indeed, by controlling the spectral phase of the excitation one can select a particular 2-photon transition (demonstrated by Meshulach *et al.* [54]). This approach allows selective excitation of different chromophores with a fast

switching ability. Implementations of this method for 2PEF imaging of living samples have been performed recently by Ogilvie *et al.* [55], and Pillai *et al.* [56].

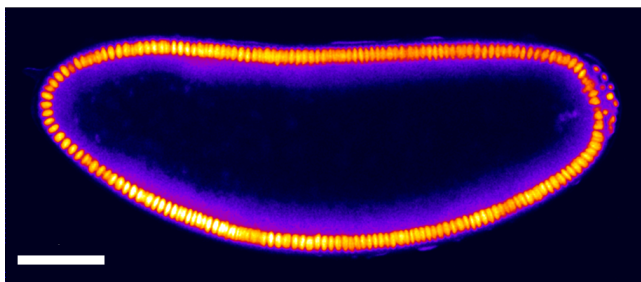


Figure 1.8: EXAMPLE OF 2PEF IMAGING IN DEVELOPMENTAL BIOLOGY
2PEF image of a nls-GFP drosophila embryo (Bloomington Stock center) at the end of the cellularization. This transgenic strain expresses eGFP in its nuclei. Scale bar = $50\mu m$. Adapted from reference [57].

Most of the fluorophores used in linear fluorescence microscopy can be used in two-photon excited fluorescence microscopy. The rule of thumb is that their 2-photon absorption spectra are shifted towards twice the linear wavelengths, and that their (one-photon) emission spectra are mostly unchanged, even though some exceptions do exist. 2PEF excitation spectra are usually broader than their 1PEF counterpart, so that multicolor imaging with several dyes is easier in 2PEF.

1.3.1.2 2PEF: Applications in Biology

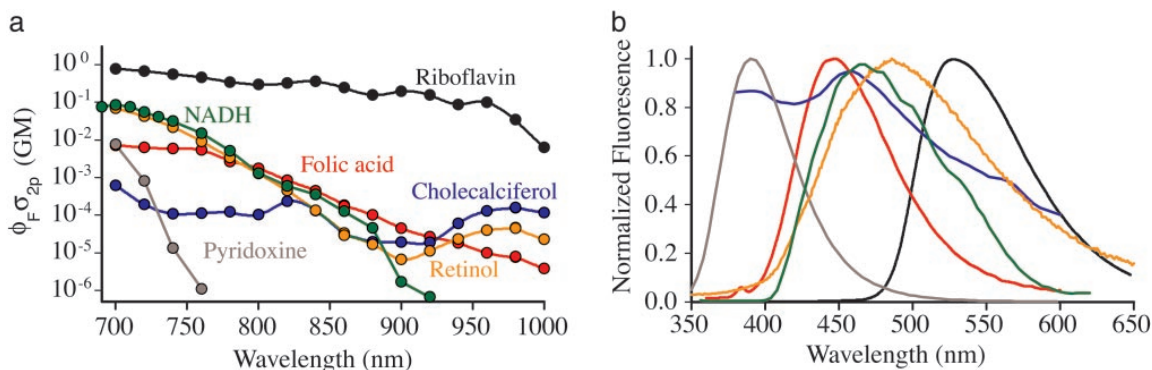


Figure 1.9: EXCITATION & EMISSION SPECTRA OF INTRINSIC FLUOROPHORES
(a) Two-photon action cross sections and (b) emission spectra of some of the major cellular fluorophores. Units: $1GM = 10^{-50}.cm^4.s$. Adapted from [58].

2PEF microscopy is by far the most widely used nonlinear imaging modality in biology. Its technological development has been propelled by the important applications it found in neuroscience [59–63], where animal models, including fluorescent transgenic constructs, are widely used, and deep tissue imaging is necessary. The transition from linear to nonlinear microscopy is easy because 2PEF can take advantage of the many fluorophores developed for morphological and functional imaging in linear fluorescence microscopy. Moreover, endogenous fluorophores can also be used as sources of signal and provide images of unstained tissues

Molecule	Process	λ_{ex} 50% max, nm*	Cross section
Tyrosine	3PE	<700	1×10^{-84}
Tryptophan	3PE	700–740	1×10^{-84}
Serotonin	3PE	700–720	4×10^{-84}
Melatonin	3PE	700–720	7×10^{-84}
5-HIAA	3PE	700–720	2×10^{-84}
5-HTOL	3PE	700–720	5×10^{-84}
Retinol	2PE	700–830	7×10^{-52}
Flavins	2PE	700–730	$1-8 \times 10^{-51}$
NADH	2PE	690–730	9×10^{-52}
Pyridoxine	2PE	690–710	8×10^{-53}
Folic acid	2PE	700–770	7×10^{-53}
Cholecalciferol	2PE	<700	6×10^{-54}
Elastin	2PE	700–740	—
NFTs	2PE	700–780	—
Lipofuscin	2PE	700–850	High ⁺
Collagen	SHG	700–740	—
Microtubules	SHG	—	—
Skel. muscle	SHG	—	—

Figure 1.10: 2P EXCITATION CROSS SECTIONS OF INTRINSIC FLUOROPHORES
2PE-action cross sections given for 700-nm excitation, in cm^4 and 3PE cross sections measured with a 720 nm excitation. Adapted from [58].

Biological applications of 2PEF microscopy cover several fields, and are reviewed in several articles [3, 36, 64]. The most relevant domain in the context of this thesis is the field of embryology [7, 33, 65, 66], where hundreds of different mutants expressing targeted fluorescent proteins are available for the most studied animal models. For example, figure (1.8) shows a transgenic drosophila embryo that expresses eGFP proteins that bind with a nuclear-targeted peptide. 2PEF microscopy has also found many applications in immunology [67–69], angiogenesis [70, 71], oncology [72, 73] and dermatology [74–76] where multiphoton endoscopes adapted to clinical use [77] are now commercially available.

3PEF microscopy [78] is not as much used, because it involves higher energies, and so photo-damage is more likely to occur. However, it is useful to reach UV bands of dyes such as serotonin that cannot be excited with 2PEF and a Titanium: Sapphire laser. 4PEF microscopy [79] is more of a curiosity, and has not found any application yet.

1.3.2 SHG Microscopy

1.3.2.1 SHG: Principles & Properties

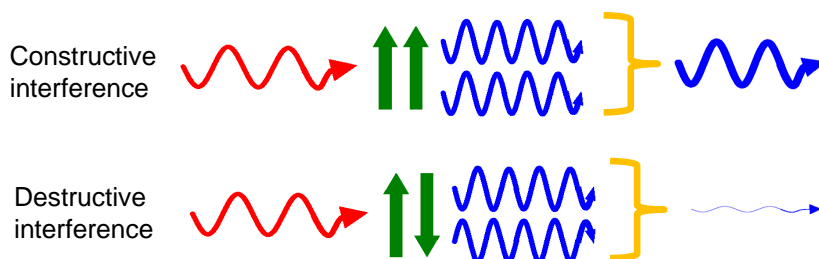


Figure 1.11: EXAMPLE OF CONSTRUCTIVE AND DESTRUCTIVE INTERFERENCE
When waves are in phase, they interfere constructively and the intensity scales as N^2 (ie: the squared number of scatterers), while when they are π out of phase the destructive interference is complete. Adapted from [80].

Second Harmonic Generation (SHG) was the first nonlinear optical phenomenon demonstrated. The demonstration was done in 1961 by Franken *et al.* [81], just after the invention of the laser [82, 83]. SHG is a degenerate 3 waves mixing process where two photons (usually from the same exciting beam) are scattered by a single molecule to produce a photon at half the wavelength. It is a coherent process, so the phase of the nonlinear photon is related to the sum of the phases of the exciting photons. Moreover, the coherent nature of SHG implies that the photons created by different molecules can interfere either constructively if they are in phase, or destructively if they are out of phase, as illustrated by figure (1.11).

SHG requires non-centrosymmetry, as the second order nonlinear susceptibility of a centrosymmetrical medium is equal to zero [4]. This means SHG is only possible in organized structures.

1.3.2.2 SHG: Biological Applications

Although SHG microscopy was one of the first nonlinear microscopy techniques demonstrated [46, 84] over 30 years ago, it remained mainly a curiosity for more than a decade until the development of efficient dyes [85, 86], and the identification of endogenous sources [58, 87–92]. A few studies focus on understanding phase matching mechanisms in organized media [85, 93, 94]. SHG is now easily combined with 2PEF microscopy, and SHG imaging is a maturing field with several applications in biology.

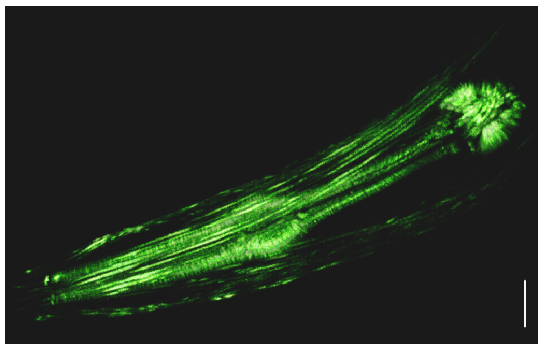


Figure 1.12: EXAMPLE OF SECOND HARMONIC GENERATION MICROSCOPY IMAGE

3D reconstruction of the SHG signal from the pharynx muscles of *C. Elegans* worm. Scale bar= $20\mu\text{m}$. Adapted from [9].

As SHG requires non-centrosymmetric macromolecular structures [95], SHG microscopy is used for imaging dense fibrillar structures such as collagen fibrils [96], for example in the skin [58, 74], in the arteries [87, 90, 97], in tendons [98] or in the cornea [99–101]. It was used by Pena, Strupler *et al.* [80, 102–104] as a scoring method of collagen accumulation in fibrotic tissues. Other harmonophores include muscle myofilaments [88, 105–108], polarized microtubule bundles in neurons [109] or the mitotic spindles of dividing cells [110].

The use of SHG producing dyes has allowed SHG imaging of membranes with high contrast [85, 86], and one promising application in neuroscience is the possibility to measure action potentials *in vivo* by using such markers [111–115].

1.3.3 CARS Microscopy

1.3.3.1 CARS: Principles & Properties

As was the case for SHG microscopy, there was a long delay between the first demonstration by Duncan [47] and the first applications which took advantage of a simplified collinear excitation geometry [116]. Coherent anti-Stokes Raman Scattering (CARS) microscopy (reviewed by Volkmer [117]), allows vibrational imaging with 3D resolution and (arguably) high sensitivity. CARS microscopy relies on a four waves mixing process described in figure (1.13) and requires two different excitation wavelengths: the Stokes field at a wavelength λ_s which is involved once, and one pump/probe field at a wavelength λ_p which is involved twice in the process. The fourth wave involved is the signal that is detected and measured. The third order nonlinear susceptibility that describes CARS signal creation can be written as [117]:

$$\chi_{CARS}^{(3)} = \chi_{NR}^{(3)} + \chi_R^{(3)}(\omega_{as}, \omega_p, -\omega_s, \omega_p) \quad (1.8)$$

where $\chi_{NR}^{(3)}$ is the non-resonant part of the $\chi^{(3)}$, and ω_s, ω_p correspond to the Stokes and pump frequencies. $\chi_R^{(3)}(\omega_{as}, \omega_p, -\omega_s, \omega_p)$ can be expressed as [117] :

$$\chi_R^{(3)}(\omega_{as}, \omega_p, -\omega_s, \omega_p) = \sum_j \frac{R_j}{\Omega_j - (\omega_p - \omega_s) - i\Gamma_j} \quad (1.9)$$

Where Ω_j , R_j and Γ_j correspond to the amplitude (R_j), and width (Γ_j) of the eigenfrequencies (Ω_j) of the Raman spectrum. $\chi_R^{(3)}(\omega_{as}, \omega_p, -\omega_s, \omega_p)$ is enhanced when the difference between pump and stokes corresponds to a vibrational resonance related to its Raman spectrum, which means CARS imaging can provide chemical specificity. However, the presence of the non-resonant $\chi^{(3)}$ means the CARS intensity can be written as:

$$I_{CARS} \propto \left| \chi_{NR}^{(3)} \right|^2 + \left| \chi_R^{(3)}(\omega_{as}, \omega_p, -\omega_s, \omega_p) \right|^2 + 2\chi_{NR}^{(3)} Re \left(\chi_R^{(3)}(\omega_{as}, \omega_p, -\omega_s, \omega_p) \right) \quad (1.10)$$

so the extraction of the Raman spectrum from the CARS signal is not easy. The most common setup consists of two different synchronized picosecond lasers, one for each wavelength, or a laser with an OPO.

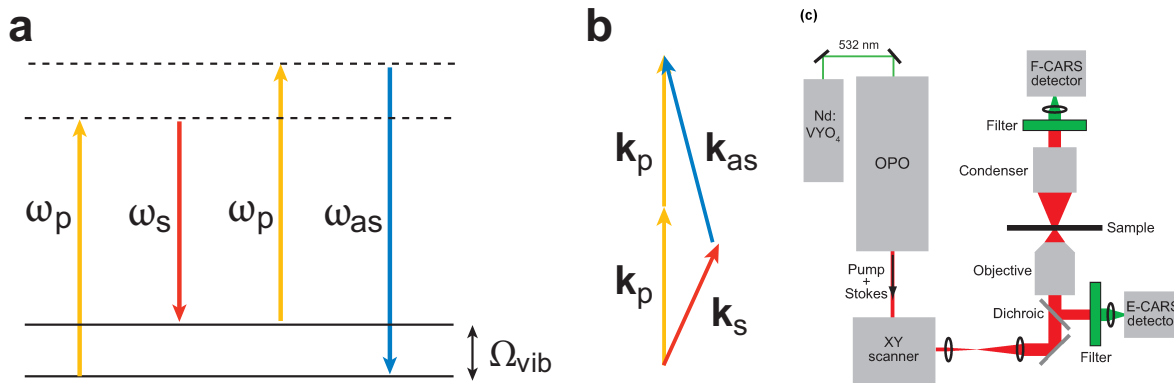


Figure 1.13: CARS MICROSCOPY

(a,b) Resonant CARS characterized by $[(\omega_p - \omega_s = \Omega_{vib})]$. (c) Typical CARS microscopy setup (adapted from reference [118]).

The main advantage of CARS microscopy is that it combines an imaging technique with a spectroscopic technique, which in theory provides an image where the chemical composition of each pixel could be known. Yet, there are a few problematic issues with CARS microscopy: first, the sensitivity is somewhat limited, as at least 10^5 to 10^6 oscillators are needed in the focal volume in order to get enough signal. Then, there is a non-resonant background in all the CARS images, because although the third order nonlinear susceptibility can be enhanced by the resonance, it is still usually different from zero out of resonance.

CARS microscopy can be implemented with two different strategies in mind:

- Recording the full spectra for each pixel, which is generally time-consuming and requires a good spectral resolution.
- Recording images of a single vibrational mode which is as fast as other nonlinear techniques, but loses the spectroscopic information.

Although the typical picosecond CARS setup is not easily compatible with other types of nonlinear imaging, there are several ways to circumvent this. One possible way is to use two chirped femtosecond pulses whose difference in frequency is constant ($\omega_p(t) - \omega_s(t) = \Omega_R$) [119]. It is even possible to use a single laser by diverting part of the beam to pump a photonic fiber to produce the Stokes beam and the rest of the laser beam is used as a pump beam [120].

One interesting alternative method is to use coherent control techniques to do single pulse CARS microscopy as demonstrated in reference [121]. These techniques modulate the spectral phase of the pulse to exploit the quantum interference between multiple paths in order to selectively populate a given vibrational level, and then probe this population using the same pulse. Additional phase shaping can even be used to reduce the non-resonant background [122].

1.3.3.2 CARS: Applications in Biology

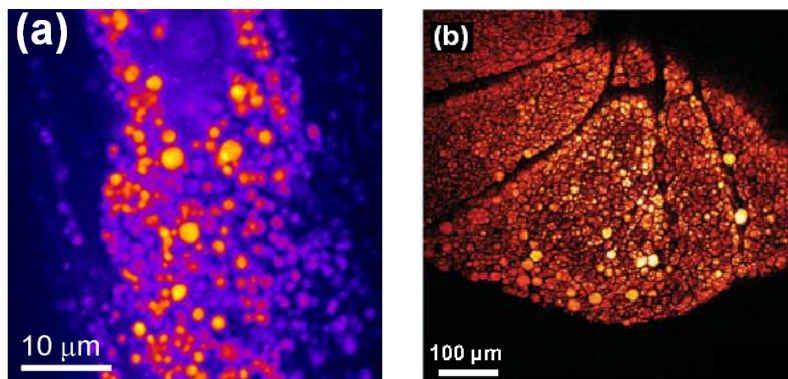


Figure 1.14: CARS MICROSCOPY IN BIOLOGY

(a) CARS microscopy image of the CH vibration stretch in *C. Elegans* (adapted from reference [123]) (b) CARS microscopy image of the CH vibration stretch in the mouse liver (adapted from reference [118]).

Currently, the most widely developed application of CARS microscopy is to image lipid structures, as lipid molecules contain many C-H bonds that exhibit a strong stretching band at 2840cm^{-1} that is attainable with most setups. Lipid droplets have been extensively studied,

for example in live fibroblast cells [124] or in the worm *C. Elegans*⁴ [123]. Lipid membranes have also been studied [125, 126]. Another good source of signal with the same vibrational properties (C-H stretch) is myelin [127], which was imaged using CARS microscopy in intact brain tissue [128]. O-H bonds in water can also be probed, and CARS microscopy has been used to examine the dynamics of water in organic environments [129]. Other applications of CARS microscopy are reviewed in reference [118].

1.3.4 SRS Microscopy

Stimulated Raman Scattering (SRS) microscopy [130–132] is a recent nonlinear microscopy technique that relies on Stimulated Raman scattering: it is a four-wave mixing process, in which a pair of spatially and temporally overlapping pump and Stokes laser pulses at frequencies ω_p and ω_s respectively interact with a nonlinear Raman-active medium characterized by its nonlinear susceptibility ($\chi_r^{(3)}$). Like in CARS microscopy, two spectrally narrow lasers are used: a pump beam at frequency ω_p , and a Stokes beam at frequency ω_s whose wavelengths are chosen so as to satisfy a resonance condition with a Raman medium characterized by the frequency Ω_{vib} :

$$\omega_p - \omega_s = \Omega_{vib} \quad (1.11)$$

When the two beams satisfy the resonance condition, Stokes and pump laser beams experience a gain and a concomitant loss, respectively, while propagating along the optical axis z . The intensities of the beams are therefore measured after propagation through the sample using lock-in amplification, and their variations can then be attributed to the interaction with the Raman medium.

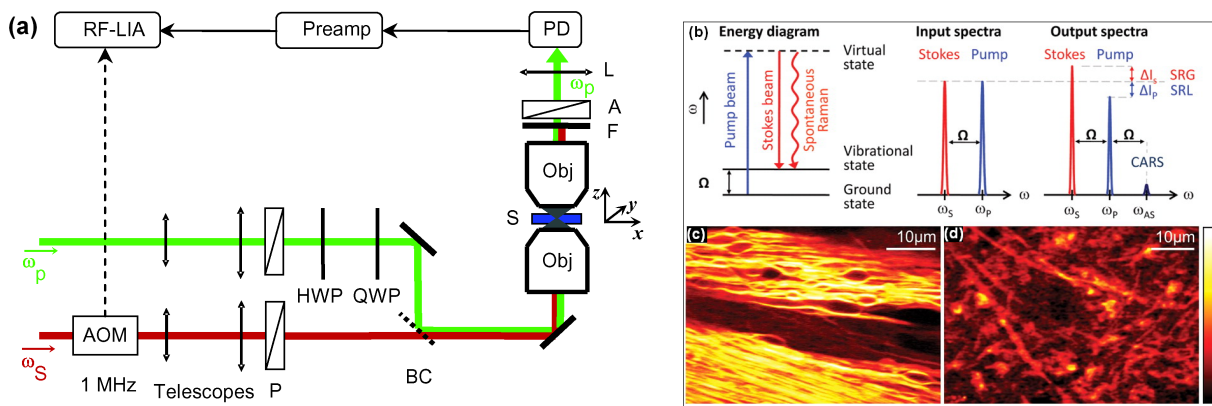


Figure 1.15: SRS MICROSCOPY

(a) Schematic of the SRS microscope. (P): polarizer; (HWP/QWP): half/quarter-wave plate; (BC): dichroic beam combiner; (Obj): objective lens; (F): filter; (A): analyzer; (L): lens; (S): sample; (AOM): acousto-optical modulator; (PD): photodiode detector; (Preamp): pre-amplifier; (RF-LIA): radio-frequency lock-in amplifier. (b) Energy-level diagram for the SRS four-wave mixing process and (c,d) SRS images of a mouse brain at the C-H stretch frequency. Adapted from [131, 132].

Despite the increased experimental complexity (lock-in detection) compared to CARS, SRS offers some advantages for vibrational imaging. In particular, the SRS signal is devoid of the

⁴*Caenorhabditis Elegans*: transparent nematode used as a model organism in developmental biology.

interference with the non-resonant contribution which complexifies the interpretation of CARS images.

1.3.5 STED Microscopy

STED⁵ microscopy [133–137] does not rely on nonlinear excitation, but on nonlinear de-excitation. It uses two beams : the first one is used for the excitation of a fluorophores and the second one for its de-excitation by stimulated emission. The two beams have different wavelengths, the excitation being around the maximum absorption of the dye, and the de-excitation being near the tail of the red part of the emission spectrum. The nonlinearity comes from the fact that stimulated emission depends nonlinearly on the field intensity. The trick used to increase the resolution is to use a hollow beam for the de-excitation, as illustrated by figure (1.16): as the intensity of this beam is increased, the size of the area excited but not de-excited by stimulated emission can be made arbitrarily small, which provides a resolution that is only limited⁶ by the signal-to-noise ratio. An extension using two de-excitation beams of different shapes means the increase in resolution can be performed isotropically [138].

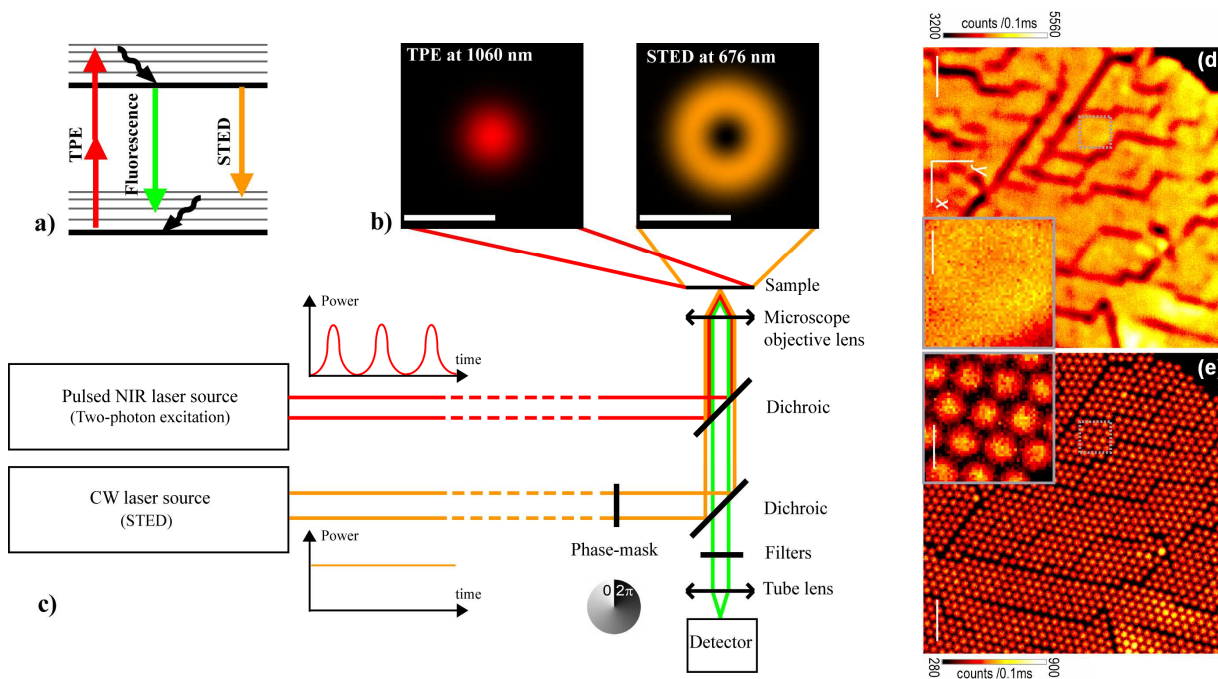


Figure 1.16: 2PSTED MICROSCOPY

Principles of the reported implementation of TPE-STED microscopy. (a) Energy diagram of the 3 processes involved. (b) Light intensity distribution of the two-photon excitation spot (left) and of the STED donut (right) in the focal plane. Scale bars represent 500nm (c) Setup. (d) & (e): Image of 200nm beads, with (d) a confocal microscope and (e) a STED microscope. Adapted from references [139, 140].

A recent demonstration used two-photon excited fluorescence [140] that may help to go deeper inside scattering tissues, although the evolution of the shape of the de-exciting beam as a function of depth stays a limiting factor.

⁵STED stands for STimulated Emission Depletion

⁶in the absence of scattering and aberrations

1.4 THG Microscopy

Since THG microscopy is one of the main focuses of this thesis, it will be described here in more details than the other techniques.

THG microscopy relies on the coherent nonlinear processes of third harmonic generation, in which three infrared photons (typically between 900nm [141] and $1.5\mu\text{m}$, our setup working usually at around $1.2\mu\text{m}$) are coherently scattered by the same molecule to produce a harmonic photon, as illustrated in figure (1.17).

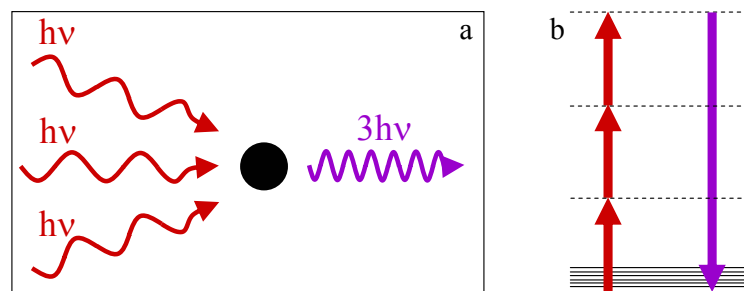


Figure 1.17: THIRD HARMONIC GENERATION

Schematic view of the THG process: (a) Quantum representation in which 3 photons of energy $h\nu$ are coherently scattered to produce a harmonic photon of energy $3h\nu$. (b) Virtual energy levels of the molecule involved in the THG process. Adapted from [9].

1.4.1 Third Harmonic Generation

The first experimental demonstrations of third harmonic generation in calcite [142, 143] gases [144, 145] and liquids [146, 147] were performed shortly after the demonstration of second harmonic generation, and an accurate theory of THG with focused Gaussian beams was proposed shortly after [144, 145]. Tsang [148, 149] later demonstrated efficient third harmonic generation at interfaces between two bulk dielectric media⁷ and opened the way to applications in microscopy.

1.4.2 THG Microscopy: First Demonstrations

THG microscopy was demonstrated by two different groups in parallel at the end of the 1990s: Barad, Eisenberg, Horowitz & Silberberg at the Weizmann institute [150, 151]; and Squier, Müller, Brakenhoff, and Wilson at UCSD [152, 153]. The authors have shown that THG can be used as a contrast mechanism and allows structural imaging of several samples (algae, neurons, yeast cells, ...) with micrometer resolution, but the contrast mechanisms were not clearly identified. They used excitation wavelengths of $1.5\mu\text{m}$ [150, 151] and $1.2\mu\text{m}$ [152, 153] that allowed detection of THG in the visible, but as they used moderate intensities ($15 - 50\text{mW}$) the acquisition of one image lasted up to several tens of seconds, which limited the potential applications in biology. The authors have shown that the THG signals mainly come from interfaces and micron-sized structures. This is in good agreement with both the experimental demonstration of THG at interfaces [148] and the theoretical analysis performed by Ward and New [145] (and extended to tight focusing conditions by Cheng and Xie [154])

⁷and Fifth Harmonic Generation at the same time, though it is not very relevant for application in biology because of the high power and longer wavelengths implied

who have shown that there is no THG from a homogeneous isotropic medium and a maximum signal from structures approximately the size of the focal volume.

1.4.3 Coherence: Geometrical Effects.

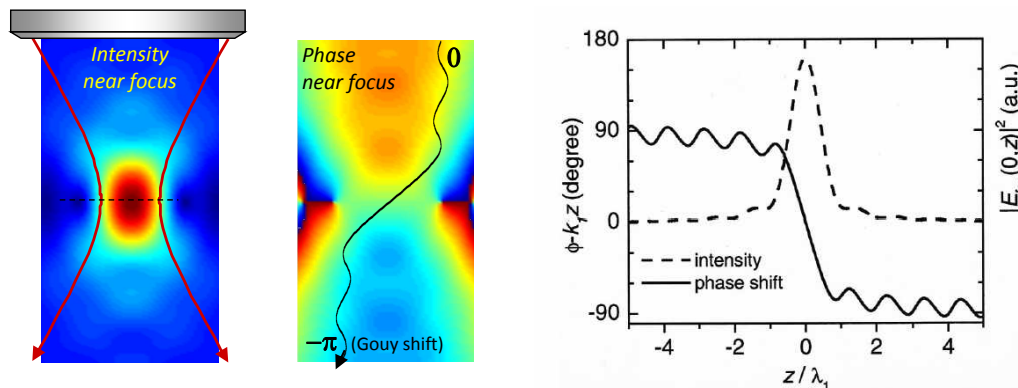


Figure 1.18: INTENSITY AND PHASE DISTRIBUTION NEAR THE FOCUS OF A HIGH NA OBJECTIVE

(Left) 2d distribution of phase and intensity in the focal volume calculated numerically using the angular spectrum representation (detailed in Chapter 2). (Right) Axial intensity and phase distribution, adapted from reference [154]. In both cases, the propagation terms of the phase have been subtracted.

The coherent nature of the signal generation process is one fundamental difference between THG and two-photon excited fluorescence, as the geometrical structure of the sample becomes an important parameter: if the sample has a "suitable" geometry, constructive interference will increase the signal, whereas a "wrong" geometry will result in destructive interference. If we consider the field distribution near the focal point illustrated in figure (1.18) we notice the presence of a progressive phase slippage called the Gouy phase-shift [155], that results in an overall π radian phase difference between a plane wave and a focused beam. The main consequence of this phase-shift is that there is no THG signal in the case of a homogeneous medium (even if it has a high $\chi^{(3)}$). In contrast a strong signal is observed in the case of an interface between two media of different optical properties. Therefore, the relevant parameter to describe THG efficiency is not $\chi^{(3)}$, but the squared difference between the $\chi^{(3)}$ of the two media.

Débarre *et al.* [156] have shown that the size of the visible structures for several geometries depends on the focusing conditions and Pilai *et al.* [157] have studied the effects of linear index-mismatch on THG at the interface between media of matching $\chi^{(3)}$. The importance of the geometrical properties of the sample will be studied in more details in chapter 3.

1.4.4 Identification of the Sources of Contrast

Some early studies [158–160] have looked at the sensitivity of THG to ion concentrations and advanced the hypothesis that THG imaging could be used to measure variations of calcium concentration. This was partly corroborated by later studies [161, 162] which showed that the nonlinear susceptibility of a solution of Calcium Chloride depended on its concentration, at least for concentration levels orders of magnitude higher than what is expected in a

biological sample. However, the measurement method used in these studies was not adapted to the high NA focusing conditions used, as shown by Pillai *et al.* [45], and the concentration sensitivity remained an open question until a more accurate measurement of the concentration dependence was realized by Débarre *et al.* [163] using a more adapted method [164]. These new measurements showed that although there is a measurable $\chi^{(3)}$ dependence on the concentration of ions or other soluble molecules, the variations are quite small, and usually undetectable at physiological concentrations. The concentration dependence values are summed up in table 1.3.

	$\frac{\partial\chi^{(3)}}{\partial C}$ ($\times 10^{-22} m^2 V^{-2} mol^{-1} L$)
NaCl	0.203 ± 0.011
KCl	0.204 ± 0.011
CaCl ₂	0.295 ± 0.015
MgCl ₂	0.306 ± 0.017
NaH ₂ PO ₄	0.188 ± 0.021
KH ₂ PO ₄	0.196 ± 0.032

Table 1.3: $\chi^{(3)}$ VARIABILITY AS A FUNCTION OF THE CONCENTRATION OF SEVERAL IONS.

Non-physiological concentrations are needed to provide a significant difference in the nonlinear susceptibilities. The excitation wavelength is $\lambda = 1064nm$. Adapted from [163].

Lipid bodies have meanwhile been identified as a strong source of contrast in biological samples by the same group [165], and the measurement of the nonlinear susceptibility of the main molecules found in biological samples has been performed using the same method as for the measurement of the concentration dependence [163]. These results have confirmed that lipids are a major source of contrast in cells and tissues, as can be seen in figure (1.19).

As shown in CARS microscopy, the nonlinear properties of a medium can be wavelength-dependent, which means resonant-enhancement of the $\chi^{(3)}$ is possible. For example, Clay *et al.* [166] identified resonant contributions from the THG signal of hemoglobin, while Bélisle *et al.* [167] took advantage of the resonance of hemozoin pigments at the harmonic wavelength to obtain sensitive detection of malaria-infected cells.

The accurate measurement of the third order nonlinear susceptibilities of common biological molecules combined with a good understanding of the contrast mechanisms have allowed a better understanding of the image generation process, and have opened the way for biological applications of THG microscopy, that are described in the next paragraph.

1.4.5 Applications in Biology

Once the contrast mechanisms were better understood, one remaining question concerning applications of THG microscopy in biology was its photo-toxicity: could a non-resonant third

$\lambda=1180\text{nm}$		$\chi^{(3)}$ ($\times 10^{-22}\text{m}^2\text{V}^{-2}$)	$ \chi^{(3)} - \chi^{(3)}_{\text{water}} ^2$
water	-	1.68 \pm 0.08	0
NaCl 1M	ions	1.79 \pm 0.09	1.2 $\times 10^{-2}$
glucose 1M	sugar	1.83 \pm 0.08	2.2 $\times 10^{-2}$
glycine 1M	amino acid	1.69 \pm 0.13	1.0 $\times 10^{-4}$
triglycine 1M	polypeptide	1.69 \pm 0.12	1.0 $\times 10^{-4}$
BSA 1mM	protein	1.75 \pm 0.13	4.9 $\times 10^{-3}$
triglycerides	lipids	2.58 \pm 0.5	0.81
oil	lipids	2.71 \pm 0.5	1.06
BK7	glass	2.79	1.2

Figure 1.19: THIRD-ORDER NONLINEAR SUSCEPTIBILITY $\chi^{(3)}$ OF SEVERAL MOLECULES COMMONLY FOUND IN BIOLOGICAL SAMPLES

Lipids have the highest non-resonant nonlinear susceptibility, and as they have the highest contrast with water, they are amongst the most visible species. The excitation wavelength is $\lambda = 1180\text{nm}$. Adapted from [163].

order process be used to image fragile biological samples ?

1.4.5.1 Photo-toxicity in THG Microscopy

THG is a non-resonant third-order nonlinear process, which means it requires high excitation intensities (average power in the order of 100mW using 80MHz 100fs excitation pulse-trains in typical imaging conditions), so the issue of the photo-toxicity of THG imaging has to be considered as these conditions using a lower wavelength would induce important photo-damage such as ionization [66]. The fact that many independent parameters are involved makes it difficult to make simple comparisons, but to summarize, the absence of energy deposition during the nonlinear interaction, and weak linear and two-photon absorption in the sample at $1.2\mu\text{m}$ make it possible to image living samples with THG microscopy. However, the damage threshold must be characterized for each application.

Débarre *et al.* [165] have shown that hepatocytes could be imaged under typical imaging conditions without compromising their survival and their enzymatic activity, and that the speed of cellularization in the drosophila embryo was not perturbed below a certain imaging rate ; while Sun *et al.* [110] have shown that zebrafish embryos could be imaged at different stages and still continue to develop normally.

1.4.5.2 Embryology

Chu *et al.* [110, 168] demonstrated the possibility of imaging developing zebrafish embryos from the cleavage stage to the larva stage using THG microscopy without damaging the embryo. They used a Chrome-forsterite laser centered at 1230nm , with a pulse-duration of $\approx 100\text{fs}$ and an average power at the sample of around 100mW . They combined THG imaging with SHG

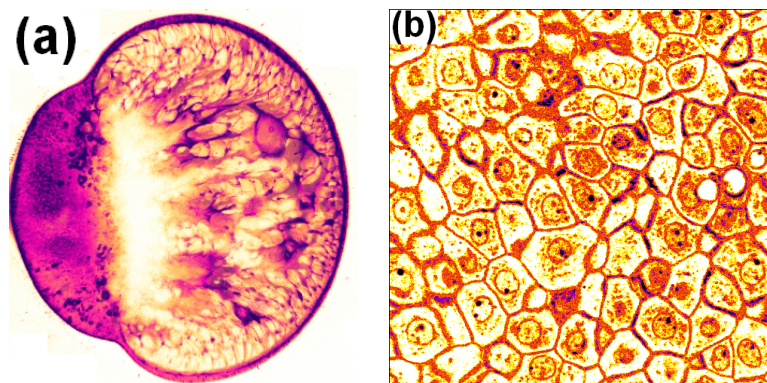


Figure 1.20: EXAMPLE OF THIRD HARMONIC GENERATION MICROSCOPY IMAGES

(a) 2D THG image of a zebrafish embryo at the one cell stage, where the yolk structure is clearly visible. (b) 2D THG image of the epithelial cells of the human cornea, where nuclear & cell membranes along with a few organelles are visible. (see chapter 5 for more details)

imaging of the microtubules of the mitotic spindles that appear during the cell division in the cleavage stage and of the myosin fibrils of muscles during the larva stage.

Débarre, Supatto *et al.* [9, 57, 66, 169] demonstrated the possibility of imaging the developing drosophila embryo using THG microscopy. The main sources of contrast in this case are the lipid droplets that are distributed in most of the embryo, and which allow structural imaging. They also demonstrated the possible combination with microablations using femtosecond lasers [170] to study the mechanosensitivity of the expression of a gene involved in early embryogenesis. They finally showed that THG images could be used to quantify morphogenetic movements using correlation-based algorithms adapted from fluid mechanics [169].

Some recent work used THG microscopy to image *C. Elegans* [171] and mouse embryos [172].

1.4.5.3 Other Applications In Biology

A number of other applications in biology have been published: after the first demonstration by Yelin *et al.* [151] of THG imaging of neuron cells, Sun *et al.* [173, 174] have reported combined THG and SHG images of the structure of the skin, without clearly identifying the sources of contrast, which they later investigated by imaging the hamster oral cavity [175] and a collection of tissue with a special attention to elastic fibers [176]. As previously mentioned, Débarre *et al.* [165] have demonstrated that lipids were an efficient source of contrast in many biological samples, and have presented in the same paper an application of THG to quantify the quantity of lipids in hepatocytes.

THG microscopy of organized structures, such as the sea urchin's spicule [177], or tooth dentin [178] has also been performed. One elegant application of THG microscopy as a sensitive tool to diagnose malaria infections by detecting hemozoin pigments [167] has been recently proposed.

1.4.5.4 THG Microscopy & Contrast Agents

Several groups have studied the possibility of using surface resonant effects that can locally enhance the electric field, and therefore the nonlinear effect, for example in nano-metallic particles [179–181], and several studies have been conducted on the size dependence of the THG signal coming from such structures [182–185]. These structures have two main advantages:

- They are highly efficient at producing harmonic signal, and so very small particles can be detected.
- Their small size allows a non-negligible part of the harmonic signal to be backward emitted.

Figure (1.21) compares the F-THG and B-THG signals from latex beads with a diameter of 330nm and gold nano-particles with a diameter of 150nm . In the F-THG image, we can see that both structures emit a comparable amount of signal, although the gold particle is twice as small, illustrating the high visibility of small metallic objects, while the B-THG image shows that the nano-particles also emit a significant amount of THG signal in the backward direction.

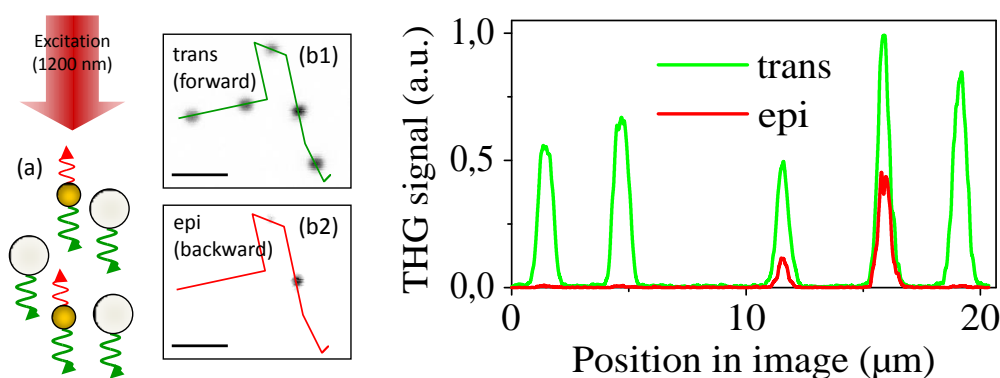


Figure 1.21: THG MICROSCOPY OF DIELECTRIC AND METALLIC PARTICLES (a) Geometry considered: the sample consists of a mixture of polystyrene beads (diameter 330nm) + gold nano-particles (diameter 150nm). (b) corresponding F-THG (b1) and B-THG (b2) images. (c) intensity profiles marked in (b1) and (b2). Published in [186].

The use of absorbing dyes at the resonant frequency as a contrast agent was also published by Yu *et al.* [187]. Quantum dots were similarly used for THG imaging at resonant frequency [188]. The main drawback of these techniques is that they involve energy deposition, which means that harmonic signal enhancement can be accompanied by heating and related photo-toxic effects.

1.4.6 Applications In Other Domains

As THG was already being used in the material sciences, the frontier between THG and THG microscopy can be quite vague. THG has found several applications in the material sciences [189, 190], and in particular for material characterization [191], for example in liquid crystals [192–194].

1.5 Multiple Sources of Contrast

In this section, we will discuss the combination of several nonlinear signals, either using a single modality or combining several modalities.

1.5.1 Endogenous & Exogenous Signals

As mentioned earlier, SHG CARS and THG microscopy often rely on endogenous contrasts (although the THG signal can be enhanced exogenously, for example with the injection of nano particles [183] or resonant dyes [187]), whereas 2PEF and 3PEF can be used for imaging both intrinsically fluorescent biological molecules (for example, NADH and Flavins) [3, 58], and artificially introduced fluorescent molecules. Both endogenous signals and exogenous signals are useful, and both have different advantages and drawbacks.

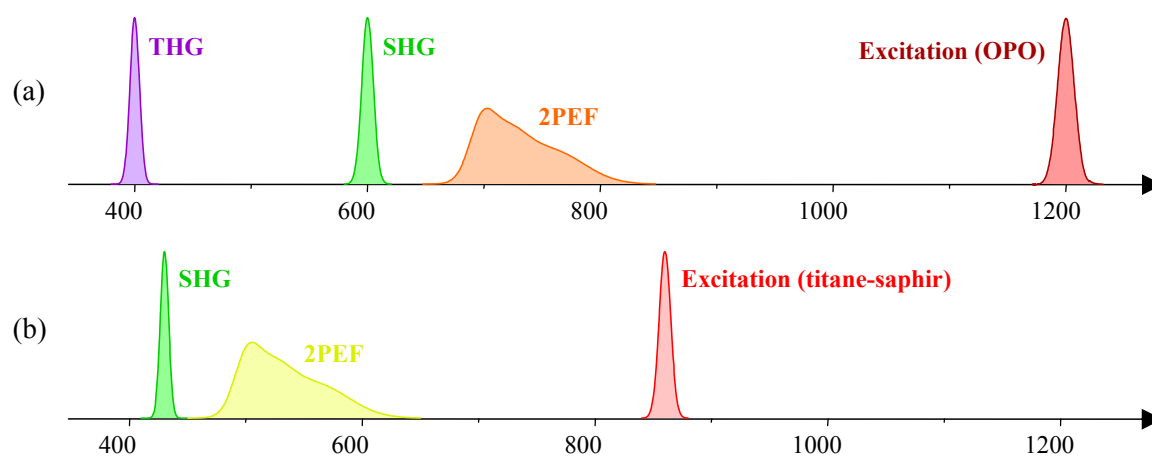


Figure 1.22: EMISSION SPECTRA OF THE MOST COMMON TYPES OF NONLINEAR MICROSCOPY

The combination of several nonlinear microscopy modalities is possible thanks to the difference in emission spectra for each process. (a) excitation centered around $\lambda = 1.2\mu\text{m}$ coming from an OPO, and (b) $\lambda = 800\text{nm}$ coming from the Ti:Sa laser. Adapted from [9].

On the one hand, exogenous signals come from dyes with well characterized emission spectra [195, 196], and large 2-photon cross sections σ_{2p} which allow rapid and efficient imaging. Moreover, dyes can be targeted to any structure of interest depending on the application. Besides, dyes that are sensitive to their chemical environment have been developed, and they can be used as functional indicators to probe physiological parameters such as pH or calcium concentration.

On the other hand, exogenous dyes have to be introduced into the specimen, which raises issues such as toxicity and biological perturbation of the sample.

The main advantage of endogenous imaging is obvious: there is no need to prepare the sample, it can be observed in a non-perturbed state. As the main sources of nonlinear contrast have been identified [3, 58, 76], endogenous sources can be used for structural imaging, sometimes with good specificity, and can even be used for spectral or fluorescence lifetime imaging [197–200].

Yet, endogenous signals are usually weaker than exogenous ones, as the dyes that have been selected or engineered to optimize their fluorescence properties are more efficient than most

biological molecules⁸.

What makes most sense is to combine both methods when needed: if the "free" endogenous signal is not good enough to study what we are interested in, it becomes necessary to use labels (or even mutants that directly express the fluorescent protein at the good location) but the endogenous signal can still be used, for example to provide structural information about the sample.

1.5.2 Multimodal Microscopy

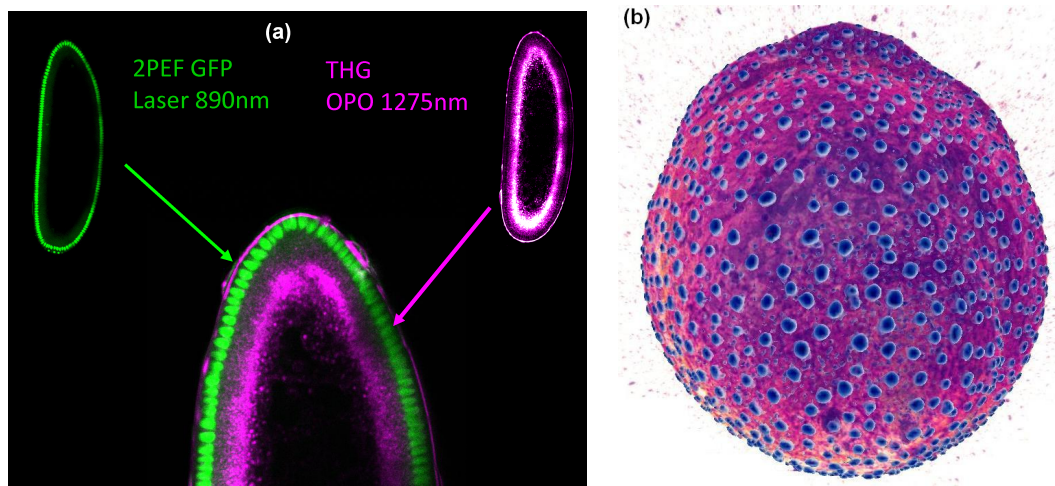


Figure 1.23: EXAMPLE OF A MULTIMODAL THG+2PEF IMAGE

(a) Simultaneous THG+2PEF imaging of a nls-GFP transgenic drosophila embryo (Bloomington Stock center) using a dual-wavelength excitation (890nm & 1275nm) 2PEF from nuclei is in green, and THG from lipids in purple. (b) 3D reconstruction of a H2B-mCherry transgenic zebrafish embryo (Collaboration N. Peyrieras) where chromatin is labeled with the red fluorescent protein mCherry (visible in dark blue), while the THG signal is visible in purple. $\lambda = 1180nm$, $NA=0.7$. (see chapter 5 for more details.)

One of the advantages of nonlinear microscopy is that several modalities can be exploited at the same time, as the emission spectra of the different nonlinear modalities often do not overlap (figure (1.22)) or sequentially using another wavelength but on the same setup. Combining different types of modalities can provide complementary information on the sample. For example, one interesting combination is THG+2PEF on a sample where the fluorescence is targeted to a specific molecule, as it allows simultaneous 3D structural imaging with an accurate localization of the molecules of interest. One example of simultaneous THG+2PEF microscopy imaging using two different wavelengths (laser at 890nm and OPO at 1280nm) is shown on figure (1.23), where the sample is a nls-GFP drosophila transgenic construct that localizes eGFP in its nuclei. Another example using a single excitation wavelength of 1.2 μm is shown for a zebrafish embryo where the chromatin is labeled with the red fluorescent protein mCherry.

It is also possible to combine more than two modalities, as illustrated by figure (1.24) where three signals are simultaneously detected using a single excitation wavelength to follow the cell

⁸although some dyes are biological molecules: GFP, for example, comes from the Jellyfish *Aequorea Victoria*

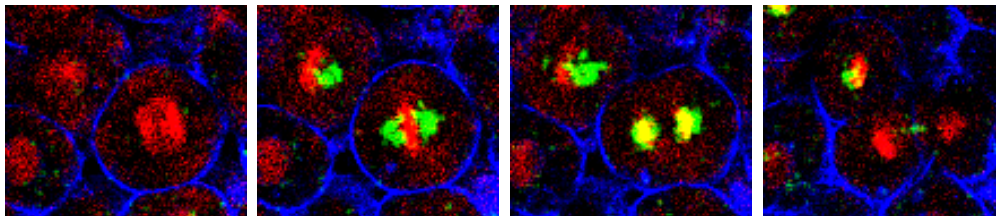


Figure 1.24: MULTIMODAL IMAGING OF A CELL DIVISION IN THE ZEBRAFISH EMBRYO

The combination of several nonlinear microscopy modalities is possible thanks to the difference in emission spectra for each process. Red: 2PEF from H2B-mCherry labeled chromatin, Green: SHG from microtubules, Blue: THG from interfaces. Transgenic Embryo provided by N. Peyrieras. $\lambda = 1.1\mu m$, NA=0.7. (see chapter 5 for more details)

division of a zebrafish embryo. The chromatin is stained with mCherry (red fluorescent protein) and is visible in red on the image, the THG signal comes from the interfaces between cells and the interstitial fluid, from the interface between the nucleus and the cytosol, and from some micron-sized organelles, and is represented in blue in the image, and finally the SHG signal comes from the polarized microtubule bundles forming the mitotic spindles, in green in the images.

1.6 Epidetection in Nonlinear Microscopy

1.6.1 Introduction

We have seen that the main application of nonlinear microscopy in the life sciences is its use as a tool to study thick samples such as intact tissue or small organisms at the micrometer scale. Yet, we have neglected an important aspect when we discussed deep tissue imaging: how can we detect the nonlinear photons in the case of thick samples when only epicollection through the focusing objective is possible ?

A handful of studies have addressed the issue of optimizing the collection of multiphoton-excited fluorescence generated inside a scattering sample such as a biological tissue [35, 201, 202], and the case of coherent microscopy has been investigated later by Debarre *et al.* [9, 186]. The situation is indeed different in the case of coherent nonlinear imaging such as SHG or THG, because unlike fluorescence, coherent nonlinear emission patterns are prescribed by the geometries of the sample and of the excitation beam. Emission is directional and often co-propagating with the excitation beam, as we will see in Chapter 2, but may subsequently be affected by incoherent scattering.

1.6.2 Incoherent Microscopy

In incoherent microscopy, the epidetected fraction depends on the depth where the imaging is performed. We will only consider the two extreme situations:

- Imaging at the surface.
- Imaging deep inside the sample (where we can describe propagation in a *diffusive regime*).

At intermediate depths, the situation can be described as a mix between these two extreme cases.

1.6.2.1 At the Surface

At the surface, two categories of epidetected photons can be defined: **ballistic photons**, that are emitted in the direction of the excitation objective, and **back-scattered photons**, that are emitted in the tissue but go through enough scattering events to be eventually back-scattered to the tissue surface. The amount of ballistic photons (P_{bal}) that can be detected relative to the total number of emitted photons can be readily calculated as the ratio between the solid angle defined by the objective and all the possible emission angles (4π since the emission is isotropic):

$$P_{bal} = \frac{2\pi(1 - \cos(\theta_{max}))}{4\pi} = \frac{1 - \cos(\theta_{max})}{2} \quad (1.12)$$

where θ_{max} is the acceptance angle of the objective.

The fraction of backscattered photons that can be detected is harder to calculate, though the rule of thumb is “the more scattering the tissue is, the more photons can be epidetected”. We first define the **reduced scattering mean free path** as :

$$l'_s = \frac{l_s}{1 - g} \quad (1.13)$$

where l_s is the scattering mean free path and g is defined in equation 1.7. l'_s corresponds to the distance it takes (on average) for a photon to lose its initial direction, as illustrated by figure (1.25).

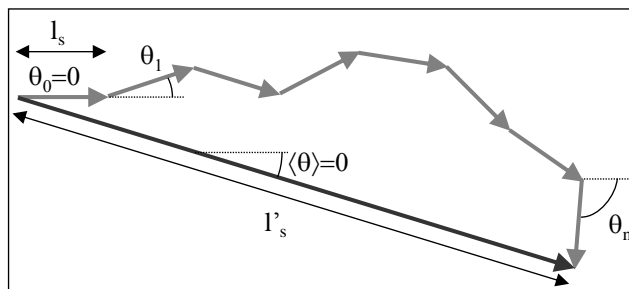


Figure 1.25: REDUCED SCATTERING MEAN FREE PATH Adapted from [9].

The photons created at the surface and emitted towards the sample seem to originate from an extended source in the sample. This is equivalent to the situation where we have an extended source located deep inside the sample that will be discussed in the next paragraph.

1.6.2.2 Deep Inside the Sample

If the imaging depth (z_0) is larger than the reduced mean free path, there are no more ballistic photons, and we can consider that there is a **diffusive regime** [203, 204] in which statistical tools of light diffusion can be used. The two most important parameters for the epidetection become the numerical aperture (described by the parameter θ_{max}) and the field of view (described by the parameter r_{max} equal to the lateral distance over which the acceptance

angle of the objective is equal to θ_{max}) of the objective, and the collection efficiency in the diffuse case can be written as [201]:

$$P_{dif} = (1 - \cos(\theta_{max})) \left[1 - \frac{z_0}{\sqrt{r_{max}^2 + z_0^2}} \right] \quad (1.14)$$

In the case of deep tissue imaging, we have $z_0 \gg r_{max}$ so we can write:

$$P = P_{dif} \approx (1 - \cos(\theta_{max})) \frac{r_{max}^2}{2z_0^2} \quad (1.15)$$

So we have a quadratic dependence of the signal on the field of view, and a quadratic decrease of the signal as a function of depth.

This expression can also be used to estimate the fraction of backscattered photons in the case of an emission at the surface as:

$$P_{dif} \approx (1 - \cos(\theta_{max})) \left[1 - \frac{l'_s}{\sqrt{r_{max}^2 + l'_s{}^2}} \right] \quad (1.16)$$

Which means that in the case of a highly scattering sample, $l'_s \ll r_{max}$, we get at the surface:

$$P = P_{bal} + P_{dif} = (1 - \cos(\theta_{max})) \quad (1.17)$$

This expression is equal to twice the value in the absence of scattering, which makes sense since an infinitely scattering medium will scatter the light isotropically from a quasi-punctual source.

1.6.3 THG Microscopy

The study of backscattering in THG microscopy (an in other forward-emitting modalities) is different from 2PEF because the emission of the harmonic signal is not isotropic but forward directed. It has been discussed in details in [9], though a few more experiments were latter performed for the article from which this paragraph is adapted [186, 205].

1.6.3.1 Influence of the Absorption

Figure (1.26) illustrates the difference between the influence of absorption in fluorescence microscopy and in THG microscopy both qualitatively and quantitatively using Monte-Carlo simulations. We have seen that in incoherent microscopy, the epidetected photons can either be ballistic photons that are not influenced by the absorption, or backscattered photons that have to travel distances larger than l'_s inside the absorbing medium, while in coherent microscopy only the backscattered contribution exists. In the case of an image recorded at the surface of an absorbing medium, the backscattered probability scales as $e^{l'_s/l_a}$ and gets vanishingly small when the absorption increases. THG imaging of an absorbing sample is thus impossible, even at the surface, and we will therefore consider non-absorbing media in the next paragraph.

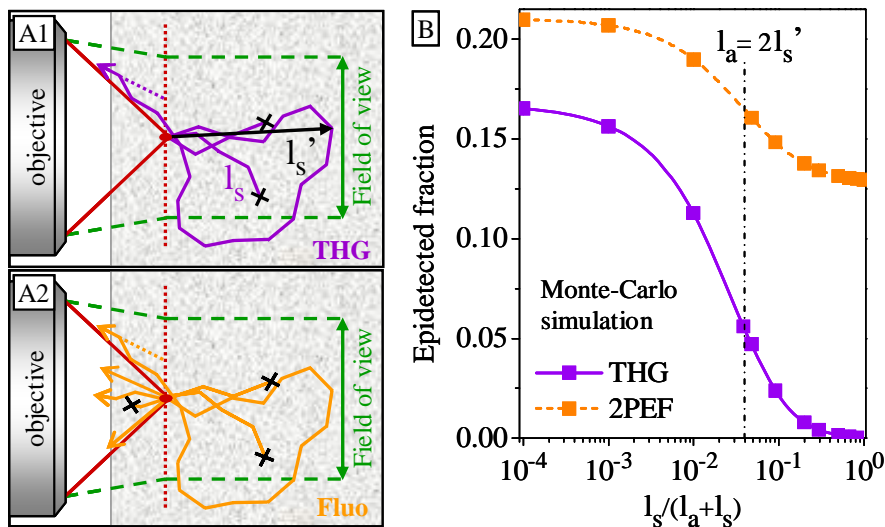


Figure 1.26: INFLUENCE OF THE ABSORPTION

Incidence of absorption and scattering on epidetection of backscattered harmonic light and multiphoton-excited fluorescence from a turbid medium. (A1) Detection of backscattered forward-emitted light (THG). (A2) Detection of light from an isotropic source (2PEF). (B) Monte Carlo simulation of the epidetected fraction of THG and 2PEF as a function of tissue albedo ($g=0.92$, $l_s=25\mu m$, $NA=0.95$, field of view= $1000\mu m$, working distance= $2mm$, sample thickness= $2500\mu m$). Published in [186].

1.6.3.2 Experimental Study of Epidetection in THG Microscopy

Figure (1.27) describes the experimental setup used to compare epidetection from a non-absorbing sample in the case of 2PEF and THG microscopy. The nonlinear photons originate from a thin ($< 10\mu m$) slab of agarose in which a low concentration of fluorescent latex beads ($330nm$, large enough to provide essentially forward emitted THG) is embedded, and the scattering sample is an agarose gel containing non fluorescent beads. The scattering gels used have constant scattering properties ($l_s(\lambda = 400) = 25\mu m$), but a variable thickness.

Figure (1.28) illustrates the results of this experiment performed with two different objectives, and the corresponding Monte Carlo simulations. They confirm several things:

1. Contrary to 2PEF microscopy, no THG epidetection is possible from a thin sample.

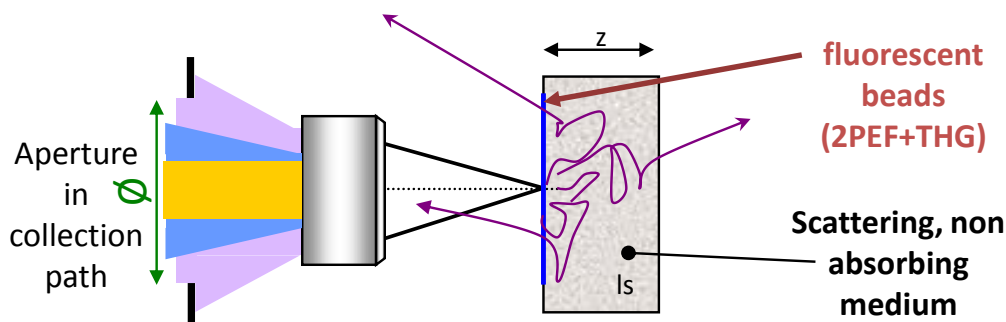


Figure 1.27: EXPERIMENTAL SETUP FOR THE STUDY OF EPIDETECTION IN NONLINEAR MICROSCOPY

THG and 2PEF photons coming from fluorescent beads are scattered by a gel of polystyrene beads. Published in [186].

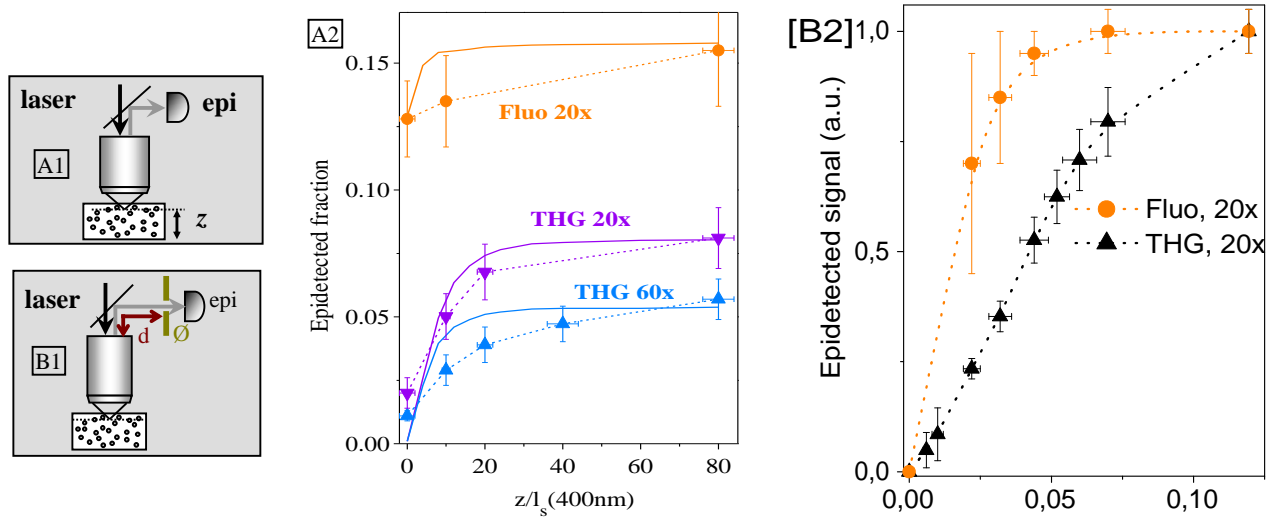


Figure 1.28: EXPERIMENTAL STUDY OF EPIDETECTION IN 2PEF & THG MICROSCOPY

Incidence of the microscope angular acceptance and field of view on epidetection of THG and 2PEF from a turbid medium. (A1 & A2) Measured epidetected fraction as a function of slab thickness (symbols and dotted lines), and corresponding Monte Carlo simulations (plain lines) for two different objectives (60x, 0.9NA and 20x, 0.95NA). Simulations assume that $l_s(400)=25\mu m$ and that the angular field of view is clipped to 0.13 rad (half-angle) by the collection optics. (B1 & B2) Measured epidetected THG and 2PEF signal at the center of the field, as a function of the angular acceptance of the collection optics. Published in [186].

- Both THG and 2PEF signals increase as the size of the scattering medium increases, but they reach a plateau (As seen in incoherent microscopy, the probability to detect a photon emitted at a depth z_0 depends on z_0^{-2} and so becomes very small when we increase the depth).
- More signal is epidetected when using a large field of view objective (both objectives have the same numerical aperture).
- The epidetected fraction is not negligible, and could (in the absence of clipping in the detection pathway) reach 20% for scattering non-absorbing samples.

The plateau and the influence of the field of view can be explained together: as the width of the scattering medium increases, more and more photons can be backscattered out of the sample. Yet, as the photons travel longer and longer distances in depth into the sample, they also travel large distances in the lateral direction, and so they get backscattered further and further away from the optical axis, which means a large field of view objective can detect more photons.

1.6.3.3 Conclusion

This study shows that THG epidetection is possible when the imaged structure is embedded in a scattering, non-absorbing tissue with thickness greater than the reduced scattering mean free path. This has been corroborated by experiments on washed lung tissue, skin tissue (non-absorbing) and liver tissues (absorbing) [186]. The data presented here indicate that this effect likely accounts for the epidetected endogenous signals reported in previous articles [165, 173–175]. Experiments and simulations indicate that more than 20% of the total

created THG signal may be detected from weakly absorbing thick tissues, provided that signal collection is optimized by using a low-magnification, high NA objective and by making sure that the microscope collection pathway does not clip scattered photons before they reach the detector. These optimization criteria also apply to CARS and SHG microscopies.

Finally, it should be noted that THG microscopy is usually performed with excitation light in the 1100-1500 nm range corresponding to a harmonic wavelength of 370-500 nm, a range where linear absorption in tissues is usually strong due to hemoglobin and other absorbers. Therefore, epidetected THG microscopy based on endogenous contrast is feasible mostly in weakly vascularized tissues such as skin, or alternatively on washed or perfused tissues.

Conclusion

Multiphoton microscopy is a very versatile tool that can be used in a large number of applications in the biosciences. Thanks to the development of affordable turn-key femtosecond sources, and the identification of the main sources of contrast in 2PEF and SHG, it is now used routinely.

Third-order methods, such as CARS and THG, have recently gained a greater attention as they can provide complementary information. However, the coherent nature of these signals mean they can be hard to interpret. The aim of the next 3 chapters is therefore to investigate the phase matching conditions that dominate the signal generation in these methods, with a special attention to THG.

Two novel biomedical applications of coherent nonlinear microscopy will be presented in the last chapter.



Bibliography

- [1] W. DENK, J.H. STRICKLER, AND W.W. WEBB. *Two-photon laser scanning fluorescence microscopy*. *Science*, 248:73–76 (1990).
- [2] K. KÖNIG. *Multiphoton microscopy in life sciences*. *J. Microsc.*, 200:83–104 (2000).
- [3] W.R. ZIPFEL, R.M. WILLIAMS, AND W.W. WEBB. *Nonlinear magic: multiphoton microscopy in the biosciences*. *Nat. Biotechnol.*, 21(11):1369–1377 (2003).
- [4] R.W. BOYD. *Nonlinear optics, 2nd edition*. Academic Press (2003).
- [5] Y. R. SHEN. *The Principles of Nonlinear Optics*. Wiley, New-York (1984).
- [6] M. GU AND C.J.R. SHEPPARD. *Comparison of three-dimensional imaging properties between two-photon and single-photon fluorescence microscopy*. *J. Microsc.*, 177:128–137 (1995).
- [7] A. PERIASAMY, P. SKOGLUND, C. NOAKS, AND R. KELLER. *An evaluation of two-photon excitation versus confocal and digital deconvolution fluorescence microscopy imaging in xenopus morphogenesis*. *Microsc. Res. Tech.*, 47:172–181 (1999).
- [8] P. THEER, M. T. HASAN, AND W. DENK. *Two-photon imaging to a depth of 1000 μm in living brains by use of a Ti:sapphire regenerative amplifier*. *Opt. Lett.*, 28(12):1022–1024 (2003).
- [9] D. DÉBARRE. *Thèse de doctorat*. Ecole Polytechnique, Palaiseau (2006).
- [10] J. BEWERSDORF, R. PICK, AND S.W. HELL. *Multifocal multiphoton microscopy*. *Opt. Lett.*, 23(9):655–657 (1998).
- [11] V. ANDRESEN, A. EGNER, AND S.W. HELL. *Time-multiplexed multifocal multiphoton microscope*. *Opt. Lett.*, 26(2):75–77 (2001).
- [12] J. E. JURELLER, H. Y. KIM, AND N. F. SCHERER. *Stochastic scanning multiphoton multifocal microscopy*. *Opt. Express*, 14(8):3406–3414 (2006).
- [13] G.J. BRAKENHOFF, J. SQUIER, T. NORRIS, A.C. BLITON, M.H. WADE, AND B. ATHEY. *Real-time two-photon confocal microscopy using a femtosecond, amplified Ti:sapphire system*. *J. Microsc.*, 181:253–259 (1996).
- [14] D. ORON AND Y. SILBERBERG. *Third-harmonic generation with cylindrical gaussian beams*. *J. Opt. Soc. Am. B*, 21(11):1964–1968 (2004).
- [15] E. TAL, D. ORON, AND Y. SILBERBERG. *Improved depth resolution in video-rate line-scanning multiphoton microscopy using temporal focusing*. *Opt. Lett.*, 30(13):1686–1688 (2005).
- [16] D. ORON AND Y. SILBERBERG. *Harmonic generation with temporally focused ultrashort pulses*. *J. Opt. Soc. Am. B*, 22(12):2660–2663 (2005).
- [17] D. ORON, E. TAL, AND Y. SILBERBERG. *Scanningless depth-resolved microscopy*. *Opt. Express*, 13(5):1468–1476 (2005).

- [18] E. PAPAGIAKOUMOU, V. DE SARS, D. ORON, AND V. EMILIANI. *Patterned two-photon illumination by spatiotemporal shaping of ultrashort pulses*. Opt. Express, 16(26):22039–22047 (2008).
- [19] E. PAPAGIAKOUMOU, V. DE SARS, V. EMILIANI, AND D. ORON. *Temporal focusing with spatially modulated excitation*. Opt. Express, 17(7):5391–5401 (2009).
- [20] C. HEINRICH, C. MEUSBURGER, S. BERNET, AND M. RITSCH-MARTE. *Cars microscopy in a wide-field geometry with nanosecond pulses*. Journal of Raman Spectroscopy, 37:675–679 (2006).
- [21] R. SALOME, Y. KREMER, S. DIEUDONNÉ, J.-F. LÉGER, O. KRICHEVSKY, C. WYART, D. CHATENAY, AND L. BOURDIEU. *Ultrafast random-access scanning in two-photon microscopy using acousto-optic deflectors*. J. Neurosci. Meth., 154(1-2):161 – 174 (2006).
- [22] W. GOBEL, B. M. KAMPA, AND F. HELMCHEN. *Imaging cellular network dynamics in three dimensions using fast 3d laser scanning*. Nat. Meth., 4(1):73 –79 (2006).
- [23] B.K. ANN NGOI, KRISHNAN VENKATAKRISHNAN, L.E.N. LIM, AND B. TAN. *Angular dispersion compensation for acousto-optic devices used for ultrashort-pulsed laser micromachining*. Opt. Express, 9(4):200–206 (2001).
- [24] Y. KREMER, J.-F. LÉGER, R. LAPOLE, N. HONNORAT, Y. CANDELA, S. DIEUDONNÉ, AND L. BOURDIEU. *A spatio-temporally compensated acousto-optic scanner for two-photon microscopy providing large field of view*. Opt. Express, 16(14):10066–10076 (2008).
- [25] C. L. EVANS, E.O. POTMA, M. PUORISHAAG, D. COTÉ, C.P. LIN, AND X.S. XIE. *Chemical imaging of tissue in vivo with video-rate coherent anti-stokes raman scattering microscopy*. Proc. Natl. Acad. Sci. USA, 102(46):16807–16812 (2005).
- [26] Q.-T. NGUYEN, N. CALLAMARAS, C. HSIEH, AND I. PARKER. *Construction of a two-photon microscope for video-rate ca^{2+} imaging*. Cell Calcium, 30(6):383 – 393 (2001).
- [27] J. MERTZ. *Molecular photodynamics involved in multi-photon excitation fluorescence microscopy*. Eur. Phys. J. D, 3:53–66 (1998).
- [28] K. KÖNIG, H. LIANG, M. W. BERNS, AND B. J. TROMBERG. *Cell damage in near-infrared multimode optical traps as a result of multiphoton absorption*. Opt. Lett., 21(14):1090–1092 (1996).
- [29] K. KÖNIG, P. T. C. SO, W. W. MANTULIN, AND E. GRATTON. *Cellular response to near-infrared femtosecond laser pulses in two-photon microscopes*. Opt. Lett., 22(2):135–136 (1997).
- [30] K. KÖNIG, T. W. BECKER, P. FISCHER, I. RIEMANN, AND K. J. HALBHUBER. *Pulse-length dependence of cellular response to intense near-infrared laser pulses in multiphoton microscopes*. Opt. Lett., 24(2):113–115 (1999).
- [31] A. HOPT AND E. NEHER. *Highly nonlinear photodamage in two-photon fluorescence microscopy*. Biophys. J., 80(4):2029–2036 (2001).

-
- [32] D. DÉBARRE AND E. BEAUREPAIRE. *Phototoxicity in third-harmonic generation microscopy*. J. Indefinitely Delayed Res., 42(13):1234–1248 (2015).
- [33] J. M. SQUIRRELL, D. L. WOKOSIN, J. G. WHITE, AND B. D. BAVISTER. *Long-term two photon fluorescence imaging of mammalian embryos without compromising viability*. Nat. Biotechnol., 17:763–767 (1999).
- [34] E. BEAUREPAIRE, M. OHEIM, AND J. MERTZ. *Ultra-deep two-photon excitation in turbid media*. Opt. Commun., 188:25–29 (2001).
- [35] M. OHEIM, E. BEAUREPAIRE, E. CHAIGNEAU, J. MERTZ, AND S. CHARPAK. *Two-photon microscopy in brain tissue: parameters influencing the imaging depth*. J. Neurosci. Meth., 111(1):29–37 (2001).
- [36] J. MERTZ. *Nonlinear microscopy: new techniques and applications*. Curr. Opin. Neurobiol., 14(5):610–616 (2004).
- [37] H. HELMCHEN AND W. DENK. *Deep tissue two-photon microscopy*. Nat. Methods, 2(12):932–940 (2005).
- [38] D. KOBAT, M. E. DURST, N. NISHIMURA, A. W. WONG, C. B. SCHAFFER, AND C. XU. *Deep tissue multiphoton microscopy using longer wavelength excitation*. Opt. Express, 17(16):13354–13364 (2009).
- [39] H.J. VAN STAVEREN, C.J.M. MOES, J. VAN MARIE, S.A. PRAHL, AND M.J.C. VAN GEMERT. *Light scattering in intralipid-10% in the wavelength range 400-1100nm*. Appl. Opt., 30(31):4507–4514 (1991).
- [40] M.H. NIEMZ. *Laser-Tissue Interactions: fundamentals and Applications*. Springer, Berlin (2004).
- [41] P. THEER AND W. DENK. *On the fundamental imaging-depth limit in two-photon microscopy*. Proc. SPIE, 5463:45–55 (2004).
- [42] P. THEER AND W. DENK. *On the fundamental imaging-depth limit in two-photon microscopy*. J. Opt. Soc. Am. A, 23(12):3139–3149 (2006).
- [43] M. SCHWERTNER, M. BOOTH, AND T. WILSON. *Characterizing specimen induced aberrations for high na adaptive optical microscopy*. Opt. Express, 12(26):6540–6552 (2004).
- [44] T.-H. TSAI, S.-P. TAI, W.-J. LEE, H.-Y. HUANG, Y.-H. LIAO, AND C.-K. SUN. *Optical signal degradation study in fixed human skin using confocal microscopy and higher-harmonic optical microscopy*. Opt. Express, 14(2):749–758 (2006).
- [45] R. S. PILLAI, G. J. BRACKENHOFF, AND M. MÜLLER. *Analysis of the influence of spherical aberration from focusing through a dielectric slab in quantitative nonlinear optical susceptibility measurements using third-harmonic generation*. Opt. Express, 14(1):260–269 (2006).
- [46] I. FREUND AND M. DEUTSCH. *Second-harmonic microscopy of biological tissue*. Opt. Lett., 11:94–96 (1986).
-

- [47] M. D. DUNCAN, J. REINTJES, AND T. J. MANUCCIA. *Scanning coherent anti-stokes raman microscope*. Opt. Lett., 7(8):350–352 (1982).
- [48] M. GÖPPERT. *Über die wahrscheinlichkeit des zusammenwirkens zweier lichtquanten in einem elementarakt*. Naturwissenschaften, 17:932–932 (1929).
- [49] M. GÖPPERT-MAYER. *Über Elementarakte mit zwei Quantensprüngen*. Annalen der Physik, 401:273–294 (1931).
- [50] W. KAISER AND C. G. GARRETT. *Two-photon excitation in $ca_f_2 : Eu^{2+}$* . Phys. Rev. Lett. , 7:229–231 (1961).
- [51] Y. R. SHEN. *Quantum statistics of nonlinear optics*. Phys. Rev., 155(3):921–931 (1967).
- [52] W. H. LOUISELL. *Quantum Statistical Properties of Radiation*. John Wiley and Sons, Inc., New York (1990).
- [53] O. NAKAMURA. *Fundamental of two-photon microscopy*. Microsc. Res. Tech., 47(3):165–171 (1999).
- [54] D. MESHULACH AND Y. SILBERBERG. *Coherent quantum control of two-photon transitions by a femtosecond laser pulse*. Nature, 396:239–242 (1998).
- [55] J. P. OGILVIE, D. DÉBARRE, X. SOLINAS, J.-L. MARTIN, E. BEAUREPAIRE, AND M. JOFFRE. *Use of coherent control for selective two-photon fluorescence microscopy in live organisms*. Opt. Express, 14(2):759–766 (2006).
- [56] R. S. PILLAI, C. BOUDOUX, G. LABROILLE, N. OLIVIER, I. VEILLEUX, E. FARGE, M. JOFFRE, AND E. BEAUREPAIRE. *Multiplexed two-photon microscopy of dynamic biological samples with shaped broadband pulses*. Opt. Express, 17(15):12741–12752 (2009).
- [57] W. SUPATTO. *Thèse de doctorat*. Université Paris VII, Paris (2005).
- [58] W.R. ZIPFEL, R.M. WILLIAMS, R. CHRISTIE, A.Y. NIKITIN, B.T. HYMAN, AND W.W. WEBB. *Live tissue intrinsic emission microscopy using multiphoton-excited native fluorescence and second-harmonic generation*. Proc. Natl. Acad. Sci. USA, 100(12):7075–7080 (2003).
- [59] S. CHARPAK, J. MERTZ, E. BEAUREPAIRE, L. MOREAUX, AND K. DELANEY. *Odor-evoked calcium signals in dendrites of rat mitral cells*. Proc. Natl. Acad. Sci. USA, 98:1230–1234 (2001).
- [60] R. YUSTE AND W. DENK. *Dendritic spines as basic functional units of neuronal integration*. Nature, 375:682–684 (1995).
- [61] Z.F. MAINEN, R. MALINOW, AND K. SVOBODA. *Synaptic calcium transients in single spines indicates that nmda receptors are not saturated*. Nature, 399:151–155 (1999).
- [62] C. STOSIEK, O. GARASCHUK, K. HOLTHOFF, AND A. KONNERTH. *In vivo two-photon calcium imaging of neuronal networks*. Proc. Natl. Acad. Sci. USA, 100:7319–7324 (2003).
- [63] M. J. LEVENE, D. A. DOMBECK, K. A. KASISCHKE, R. P. MOLLOY, AND W. W. WEBB. *In Vivo Multiphoton Microscopy of Deep Brain Tissue*. J Neurophysiol, 91(4):1908–1912 (2004).

-
- [64] K. KÖNIG. *Laser tweezers and multiphoton microscopes in life sciences*. Histochem. Cell Biol., 114:79–92 (2000).
- [65] N.D. LAWSON AND B.M. WEINSTEIN. *In vivo imaging of embryonic vascular development using transgenic zebrafish*. Dev. Biol., 248:307–318 (2002).
- [66] W. SUPATTO, D. DEBARRE, B. MOULIA, E. BROUZES, J. L. MARTIN, E. FARGE, AND E. BEAUREPAIRE. *In vivo modulation of morphogenetic movements in drosophila embryos with femtosecond laser pulses*. Proc. Natl. Acad. Sci. USA, 102(4):1047–1052 (2005).
- [67] M. D. CAHALAN, M. D. PARKER, S. H. WEI, AND M. J. MILLER. *Two-photon tissue imaging: seeing the immune system in a fresh light*. Nat. Rev. Immunol., 2:872–880 (2002).
- [68] M. J. MILLER, S. H. WEI, I. PARKER, AND M. D. CAHALAN. *Two-Photon Imaging of Lymphocyte Motility and Antigen Response in Intact Lymph Node*. Science, 296:1869–1873 (2002).
- [69] M. J. MILLER, S. H. WEI, M. D. CALAHAN, AND I. PARKER. *Autonomous t cell trafficking examined in vivo with intravital two-photon microscopy*. Proc. Natl. Acad. Sci. USA, 100:2604–2609 (2003).
- [70] E.B. BROWN, R. CAMPBELL, Y. TSUZUKI, L. XU, P. CARMELIET, D. FUKUMURA D, AND R.K. JAIN. *In vivo measurement of gene expression, angiogenesis, and physiological function in tumors using multiphoton laser scanning microscopy*. Nat. Medicine, 7(7):864–868 (2001).
- [71] D.M. McDONALD AND P.L. CHOYKE. *Imaging of angiogenesis : from microscope to clinic*. Nat. Medicine, 9:713–725 (2003).
- [72] W. WANG, J. B. WYCKOFF, V. C. FROHLICH, Y. OLEYNIKOV, S. HETTELMAIER, J. ZAVADIL, BOTTINGER E. P. CERMAK, L., R. H. SINGER, J. G. WHITE, J. E. SEGALL, AND J. S. CONDEELIS. *Single cell behavior in metastatic primary mammary tumors correlated with gene expression patterns revealed by molecular profiling*. Cancer Res., 62:6278–6288 (2002).
- [73] K. WOLF, I. MAZO, H. LEUNG, K. ENGELKE, U.H. VON ADRIAN, E.I. DERYUGINA, A.Y. STRONGIN, E.B. BRÖCKER, AND P. FRIELD. *Compensation mechanism in tumor cell migration : mesenchymal-amoeboid transition after blocking of pericellular proteolysis*. J. Cell Biol., 160:267–277 (2003).
- [74] K. KÖNIG AND I. RIEMANN. *High-resolution multiphoton tomography of human skin with subcellular spatial resolution and picosecond time resolution*. J. Biomed. Opt., 8(3):432–439 (2003).
- [75] L. H. LAIHO, S. PELET, T. M. HANCEWICZ, P. D. KAPLAN, AND P. T. C. SO. *Two-photon 3-d mapping of ex vivo human skin endogenous fluorescence species based on fluorescence emission spectra*. J. Biomed. Opt., 10(2):024016 (2005).
- [76] A.-M. PENA, M. STRUPLER, T. BOULESTEIX, AND M.-C. SCHANNE-KLEIN. *Spectroscopic analysis of keratin endogenous signal for skin multiphoton microscopy*. Opt. Express, 13(16):6268–6274 (2005).
-

- [77] K. KÖNIG, A. EHLERS, I. RIEMANN, S. SCHENKL, R. BÜCKLE, AND M. KAATZ. *Clinical two-photon microendoscopy*. *Microsc. Res. Tech.*, 70(5):398–402 (2007).
- [78] S. W. HELL, K. BAHLMANN, M. SCHRADER, A. SOINI, H. M. MALAK, I. GRZYCZYNSKI, AND J. R. LAKOWICZ. *Three-photon excitation in fluorescence microscopy*. *J. Biomed. Opt.*, 1(1):71–74 (1996).
- [79] S.-W. CHU, M.-C. CHAN, S.-P. TAI, S. KELLER, S. P. DENBAARS, AND C.-K. SUN. *Simultaneous four-photon luminescence, third-harmonic generation, and second-harmonic generation microscopy of gan*. *Opt. Lett.*, 30(18):2463–2465 (2005).
- [80] M. STRUPLER. *Thèse de doctorat*. Ecole Polytechnique, Palaiseau (2008).
- [81] P. A. FRANKEN, A. E. HILL, C. W. PETERS, AND G. WEINREICH. *Generation of optical harmonics*. *Phys. Rev. Lett.*, 7(4):118–119 (1961).
- [82] A. L. SCHAWLOW AND C. H. TOWNES. *Infrared and optical masers*. *Phys. Rev.*, 112:1940–1949 (1958).
- [83] T. H. MAIMAN. *Stimulated optical radiation in ruby*. *Nature*, 187:493–494 (1960).
- [84] R. W. HELLWARTH AND P. CHRISTENSEN. *Nonlinear optical microscope using second harmonic generation*. *Appl. Opt.*, 14:247–248 (1975).
- [85] L. MOREAUX, O. SANDRE, M. BLANCHARD-DESCE, AND J. MERTZ. *Membrane imaging by simultaneous second-harmonic generation and two-photon microscopy*. *Opt. Lett.*, 25(5):320–322 (2000).
- [86] L. MOREAUX, O. SANDRE, AND J. MERTZ. *Membrane imaging by second-harmonic generation microscopy*. *J. Opt. Soc. Am. B*, 17(10):1685–1694 (2000).
- [87] A. ZOUMI, A. YEH, AND B. J. TROMBERG. *Imaging cells and extracellular matrix in vivo by using second-harmonic generation and two-photon excited fluorescence*. *Proceedings of the National Academy of Science*, 99:11014–11019 (2002).
- [88] P. J. CAMPAGNOLA, W. MOHLER, AND A. E. MILLARD. *3-dimensional high-resolution second harmonic generation imaging of endogenous structural proteins in biological tissues*. *Biophys. J.*, 82(1):175A–175A (2002). Part 2.
- [89] P. J. CAMPAGNOLA AND L. M. LOEW. *Second-harmonic imaging microscopy for visualizing biomolecular arrays in cells, tissues and organisms*. *Nat. Biotechnol.*, 21(11):1356–1360 (2003).
- [90] A. ZOUMI, X. LU, G. KASSAB, AND B. TROMBERG. *Imaging Coronary Artery Microstructure Using Second-Harmonic and Two-Photon Fluorescence Microscopy*. *Biophysical Journal*, 87:2778–2786 (2004).
- [91] A. M. PENA, T. BOULESTEIX, T. DARTIGALONGUE, AND M.-C. SCHANNE-KLEIN. *Chiroptical effects in the second harmonic signal of collagens i and iv*. *J. Am. Chem. Soc.*, 127(29):10314–10322 (2005).
- [92] G. COX, N. MORENO, AND J. FEIJO. *Second-harmonic imaging of plant polysaccharides*. *J. Biomed. Opt.*, 10(2):02413 (2005).

-
- [93] R. LACOMB, O. NADIARNYKH, S. S. TOWNSEND, AND P. J. CAMPAGNOLA. *Phase matching considerations in second harmonic generation from tissues: Effects on emission directionality, conversion efficiency and observed morphology*. Optics Commun., 281(7):1823–1832 (2008).
- [94] S.-W. CHU, S.-P. TAI, M.-C. CHAN, C.-K. SUN, I.-C. HSIAO, C.H. LIN, Y.C. CHEN, AND B.L. LIN. *Thickness dependence of optical second harmonic generation in collagen fibrils*. Opt. Express, 15(19):12005–12010 (2007).
- [95] L. MOREAUX. *Coherent Scattering in Multi-Harmonic Light Microscopy*. Biophysical Journal, 80:1568–1574 (2001).
- [96] S. ROTH AND I. FREUND. *Second harmonic generation in collagen*. J. Chem. Phys., 70:1637 (1979).
- [97] T. BOULESTEIX, A. M. PENA, N. PAGES, G. GODEAU, M. P. SAUVIAT, E. BEAUREPAIRE, AND M.-C. SCHANNE-KLEIN. *Micrometer scale ex vivo multiphoton imaging of unstained arterial wall structure*. Cytometry A, 69A:20–26 (2006).
- [98] P. STOLLER, P. M. CELLIERS, K. M. REISER, AND A. M. RUBENCHIK. *Quantitative second-harmonic generation microscopy in collagen*. Appl. Opt. , 42:5209–5219 (2003).
- [99] A. T. YEH, N. NASSIF, A. ZOUMI, AND B.J. TROMBERG. *Selective corneal imaging using combined second-harmonic generation and two-photon excited fluorescence*. Opt. Lett., 27(23):2082–2084 (2002).
- [100] M. HAN, G. GIESE, AND J. F. BILLE. *Second harmonic generation imaging of collagen fibrils in cornea and sclera*. Opt. Express, 13(15):5791–5797 (2005).
- [101] J. G. LYUBOVITSKY, J. A. SPENCER, T. B. KRASIEVA, B. ANDERSEN, AND B. J. TROMBERG. *Imaging corneal pathology in a transgenic mouse model using nonlinear microscopy*. J. Biomed. Opt., 11(1):014013 (2006).
- [102] A.-M. PENA. *Thèse de doctorat*. Ecole Polytechnique, Palaiseau (2006).
- [103] A. M. PENA, A. FABRE, D. DÉBARRE, J. MARCHAL-SOMME, B. CRESTANI, J. L. MARTIN, E. BEAUREPAIRE, AND M.-C. SCHANNE-KLEIN. *Three-dimensional investigation and scoring of extracellular matrix remodeling during lung fibrosis using multiphoton microscopy*. Microsc. Res. Tech, 70:162–170 (2007).
- [104] M. STRUPLER, A. M. PENA, M. HERNEST, P.-L. THARAUX, J.-L. MARTIN, E. BEAUREPAIRE, AND M.-C. SCHANNE-KLEIN. *Second harmonic imaging and scoring of collagen in fibrotic tissues*. Opt. Express, 15(7):4054–4065 (2007).
- [105] T. BOULESTEIX, E. BEAUREPAIRE, M.P. SAUVIAT, AND M.C. SCHANNE-KLEIN. *Second-harmonic microscopy of unstained living cardiac myocytes : measurements of sarcomere length with 20-nm accuracy*. Opt. Lett., 269(17):2031–2033 (2004).
- [106] M. BOTH, M. VOGEL, O. FRIEDRICH, F. VON WEGNER, T. KÜNSTING, R.H.A. FINK, AND D. UTTENWEILER. *Second harmonic imaging of intrinsic signals in muscle fibers in situ*. J. Biomed. Opt., 9:882 (2004).
-

- [107] V. NUCCIOTTI, C. STRINGARI, L. SACCONI, F. VANZI, C. TESI, N. PIRODDI, C. POGGESI, C. CASTIGLIONI, A. MILANI, M. LINARI, ET AL. *Functional imaging of skeletal muscle fiber in different physiological states by second harmonic generation*. Proc. SPIE , 6630:663004 (2007).
- [108] S.V. PLOTNIKOV, A.C. MILLARD, P.J. CAMPAGNOLA, AND W.A. MOHLER. *Characterization of the myosin-based source for second-harmonic generation from muscle sarcomeres*. Biophys. J., 90(2):693–703 (2006).
- [109] D. A. DOMBECK, K. A. KASISCHKE, H. D. VISHWASRAO, M. INGELSSON, B. T. HYMAN, AND W. W. WEBB. *Uniform polarity microtubule assemblies imaged in native brain tissue by second-harmonic generation microscopy*. Proc. Natl. Acad. Sci. USA, 100(12):7081–7086 (2003).
- [110] C.-K. SUN, S.-W. CHU, S.-Y. CHEN, T.-H. TSAI, T.-M. LIU, C.-Y. LIN, AND H.-J. TSAI. *Higher harmonic generation microscopy for dev. biol.* J. Struct. Biol., 147:19–30 (2004).
- [111] L. MOREAUX, T. PONS, V. DAMBRIN, M. BLANCHARD-DESCE, AND J. MERTZ. *Electro-optic response of second-harmonic generation membrane potential sensors*. Opt. Lett., 28(8):625–627 (2003).
- [112] T. PONS, L. MOREAUX, O. MONGIN, M. BLANCHARD-DESCE, AND J. MERTZ. *Mechanisms of membrane potential sensing with second-harmonic generation microscopy*. J. Biomed. Opt., 8(3):428–431 (2003).
- [113] D. A. DOMBECK, M. BLANCHARD-DESCE, AND W. W. WEBB. *Optical Recording of Action Potentials with Second-Harmonic Generation Microscopy*. J. Neurosci., 24(4):999–1003 (2004).
- [114] A. MILLARD, L. JIN, M. WEI, J. WUSKELL, A. LEWIS, AND L. LOEW. *Sensitivity of Second Harmonic Generation from Styryl Dyes to Transmembrane Potential*. Biophysical Journal, 86:1169–1176 (2004).
- [115] L. SACCONI, DA DOMBECK, AND W. W. WEBB. *Overcoming photodamage in second-harmonic generation microscopy: Real-time optical recording of neuronal action potentials*. Proc. Natl. Acad. Sci. USA, 103(9):3124–3129 (2006).
- [116] A. ZUMBUSCH, G.R. HOLTOM, AND X.S. XIE. *Three-dimensional vibrational imaging by coherent anti-stokes raman scattering*. Phys. Rev. Lett., 82(20):4142–4145 (1999).
- [117] A. VOLKMER. *Vibrational imaging and microspectroscopies based on coherent anti-stokes raman scattering microscopy*. J. Phys. D, 38:R59–R81 (2005).
- [118] C. EVANS AND X. S. XIE. *Coherent anti-stokes raman scattering microscopy: Chemical imaging for biology and medicine*. Annual Review of Analytical Chemistry, 1(1):883–909 (2008).
- [119] T. HELLERER, A. M. K. ENEJDER, AND A. ZUMBUSCH. *Spectral focusing: High spectral resolution spectroscopy with broad-bandwidth laser pulses*. Appl. Phys. Lett. , 85:25–+ (2004).

-
- [120] T. W. KEE AND M. T. CICERONE. *Simple approach to one-laser, broadband coherent anti-stokes raman scattering microscopy*. Opt. Lett., 29(23):2701–2703 (2004).
- [121] N. DUDOVICH, D. ORON, AND Y. SILBERBERG. *Single-pulse coherently controlled nonlinear Raman spectroscopy and microscopy*. nature, 418:512–514 (2002).
- [122] D. ORON, N. DUDOVICH, AND Y. SILBERBERG. *Single-pulse phase-contrast nonlinear raman spectroscopy*. Phys. Rev. Lett., 89(27):273001 (2002).
- [123] T. HELLERER, C. AXANG, C. BRACKMANN, P. HILLERTZ, M. PILON, AND A. ENJDER. *Monitoring of lipid storage in Caenorhabditis elegans using coherent anti-Stokes Raman scattering (CARS) microscopy*. Proc. Natl. Acad. Sci. USA, 104(37):14658–14663 (2007).
- [124] X. NAN, J.-X. CHENG, AND X. S. XIE. *Vibrational imaging of lipid droplets in live fibroblast cells with coherent anti-stokes raman scattering microscopy*. J. Lipid Res., 44:2202–2208 (2003).
- [125] M. MÜLLER AND J. M. SCHINS. *Imaging the thermodynamic state of lipid membranes with multiplex cars microscopy*. The Journal of Physical Chemistry B, 106:3715–3723 (2002).
- [126] E. O. POTMA AND X. S. XIE. *Detection of single lipid bilayers with coherent anti-stokes raman scattering (cars) microscopy*. Journal of Raman Spectroscopy, 34:642–650 (2003).
- [127] H.F. WANG, Y. FU, P. ZICKMUND, R.Y. SHI, AND J.-X. CHENG. *Coherent anti-stokes raman scattering imaging of axonal myelin in live spinal tissues*. Biophys. J., 89(1):581–591 (2006).
- [128] C. EVANS, X. XU, S. KANG, X. S. XIE, S.T. C. WONG, AND G. S. YOUNG. *Chemically-selective imaging of brain structures with cars microscopy*. Opt. Express, 15(19):12076–12087 (2007).
- [129] J.-X. CHENG, S. PAUTOT, D. A. WEITZ, AND X. S. XIE. *Ordering of water molecules between phospholipid bilayers visualized by coherent anti-Stokes Raman scattering microscopy*. Proc. Natl. Acad. Sci. USA, 100(17):9826–9830 (2003).
- [130] E. PLOETZ, S. LAIMGRUBER, S. BERNER, W. ZINTH, AND P. GILCH. *Femtosecond stimulated raman microscopy*. Applied Physics B: Lasers and Optics, 87:389–393 (2007).
- [131] C. W. FREUDIGER, W. MIN, B. G. SAAR, S. LU, G. R. HOLTOM, C. HE, J. C. TSAI, J. X. KANG, AND X. S. XIE. *Label-Free Biomedical Imaging with High Sensitivity by Stimulated Raman Scattering Microscopy*. Science, 322(5909):1857–1861 (2008).
- [132] P. NANAKUMAR, A. KOVALEV, AND A. VOLKMER. *Vibrational imaging based on stimulated raman scattering microscopy*. Biophys. J., 96(3):296a–296a (2009).
- [133] S. W. HELL AND J. WICHMANN. *Breaking the diffraction resolution limit by stimulated emission: stimulated-emission-depletion fluorescence microscopy*. Opt. Lett., 19(11):780–782 (1994).
- [134] T. A. KLAR, S. JAKOBS, M. DYBA, A. EGNER, AND S. W. HELL. *Fluorescence microscopy with diffraction resolution barrier broken by stimulated emission*. Proc. Natl. Acad. Sci. USA, 97(15):8206–8210 (2000).
-

- [135] M. DYBA AND S. W. HELL. *Focal spots of size $\lambda/23$ open up far-field fluorescence microscopy at 33 nm axial resolution.* Phys. Rev. Lett., 88(16):163901 (2002).
- [136] V. WESTPHAL AND S. W. HELL. *Nanoscale resolution in the focal plane of an optical microscope.* Phys. Rev. Lett., 94(14):143903 (2005).
- [137] K. I. WILLIG, R.D JAHN, V. WESTPHAL, S. O. RIZZOLI, AND S. W. HELL. *Sted microscopy reveals that synaptotagmin remains clustered after synaptic vesicle exocytosis.* Nature, 440:935–939 (2006).
- [138] R. SCHMIDT, C. A. WURM, S. JAKOBS, J. ENGELHARDT, A. EGNER, AND S. W. HELL. *Spherical nanosized focal spot unravels the interior of cells.* Nat. Meth., 5(6):539–544 (2008).
- [139] B. HARKE, J. KELLER, C. K. ULLAL, V. WESTPHAL, A. SCHÖNLE, AND S. W. HELL. *Resolution scaling in sted microscopy.* Opt. Express, 16(6):4154–4162 (2008).
- [140] G. MONERON AND S. W. HELL. *Two-photon excitation sted microscopy.* Opt. Express, 17(17):14567–14573 (2009).
- [141] D. YELIN, D. ORON, E. KORKOTIAN, M. SEGAL, AND Y. SILBERBERG. *Third-harmonic microscopy with a titanium-sapphire laser.* Appl. Phys. B, 74(Suppl. S):S97–S101 (2002).
- [142] R. W. TERHUNE, P. D. MAKER, AND C. M. SAVAGE. *Optical harmonic generation in calcite.* Phys. Rev. Lett., 8(10):404–406 (1962).
- [143] P. D. MAKER AND R. W. TERHUNE. *Study of optical effects due to an induced polarization third order in the electric field strength.* Phys. Rev., 137(3A):A801–A818 (1965).
- [144] G. H. C. NEW AND J. F. WARD. *Optical third-harmonic generation in gases.* Phys. Rev. Lett., 19(10):556–559 (1967).
- [145] J. F. WARD AND G. H. C. NEW. *Optical third harmonic generation in gases by a focused laser beam.* Phys. Rev., 185(1):57–72 (1969).
- [146] P. P. BEY, J. F. GIULIANI, AND H. RABIN. *Generation of a phase-matched optical third harmonic by introduction of anomalous dispersion into a liquid medium.* Phys. Rev. Lett., 19(15):819–821 (1967).
- [147] F. KAJZAR AND J. MESSIER. *Third-harmonic generation in liquids.* Phys. Rev. A, 32(4):2352–2363 (1985).
- [148] T. TSANG. *Optical third-harmonic generation at interfaces.* Phys. Rev. A, 52(5):4116–4125 (1995).
- [149] T. TSANG. *Third- and fifth-harmonic generation at the interfaces of glass and liquids.* Phys. Rev. A, 54(6):5454–5457 (1996).
- [150] Y. BARAD, H. EISENBERG, M. HOROWITZ, AND Y. SILBERBERG. *Nonlinear scanning laser microscopy by third harmonic generation.* Appl. Phys. Lett., 70:922–924 (1997).
- [151] D. YELIN AND Y. SILBERBERG. *Laser scanning third-harmonic generation microscopy in biology.* Opt. Express, 5(169-175) (1999).

-
- [152] J.A. SQUIER, M. MÜLLER, G.J. BRAKENHOFF, AND K.R. WILSON. *Third harmonic generation microscopy*. Opt. Express, 3:315–324 (1998).
- [153] A.C. MILLARD, P.W. WISEMAN, D.N. FITTINGHOFF, K.R. WILSON, J.A. SQUIER, AND M. MÜLLER. *Third-harmonic generation microscopy by use of a compact, femtosecond fiber laser source*. Appl. Opt., 38(36):7393–7397 (1999).
- [154] J.-X. CHENG AND X.S. XIE. *Green’s function formulation for third harmonic generation microscopy*. J. Opt. Soc. Am. B, 19(7):1604–1610 (2002).
- [155] C. R. GOUY. *Sur une propriete nouvelle des ondes lumineuses*. Comptes rendus de l’Académie des sciences (Paris), 110:1251–1253 (1870).
- [156] D. DÉBARRE, W. SUPATTO, AND E. BEAUREPAIRE. *Structure sensitivity in third-harmonic generation microscopy*. Opt. Lett., 30(16):2134–2136 (2005).
- [157] R. S. PILLAI, G. J. BRAKENHOFF, AND M. MÜLLER. *Anomalous behavior in the third harmonic generation z response through dispersion induced shape changes and matching $\chi^{(3)}$* . Appl. Phys. Lett., 89(11):111123 (2006).
- [158] L. CANIONI, S. RIVET, L. SARGER, R. BARILLE, P. VACHER, AND P. VOISIN. *Imaging of $ca(2+)$ intracellular dynamics with a third-harmonic generation microscope*. Opt. Lett., 26(8):515–517 (2001).
- [159] R. BARILLE, L. CANIONI, S. RIVET, L. SARGER, P. VACHER, AND T. DUCRET. *Visualization of intracellular $ca2+$ dynamics with simultaneous two-photon-excited fluorescence and third-harmonic generation microscopes*. Appl. Phys. Lett., 79(24):4045–4047 (2001).
- [160] S. RIVET, L. CANIONI, L. SARGER, R. BARILLE, P. VACHER, AND T. DUCRET. *Visualization of intracellular $ca(2+)$ dynamics with simultaneous 2-photon excited fluorescence and third harmonic generation microscope*. J. Fluoresc., 12(2):197–199 (2002).
- [161] V. SCHCHESLAVSKIY, G.I. PETROV, AND V.V. YAKOVLEV. *Nonlinear optical susceptibility measurements of solutions using third-harmonic generation on the interface*. Appl. Phys. Lett., 82(22):3982–3984 (2003).
- [162] V. SCHCHESLAVSKIY, G.I. PETROV, S. SALTIEL, AND V.V. YAKOVLEV. *Quantitative characterization of aqueous solutions probed by the third-harmonic generation microscopy*. J. Struct. Biol., 147:42–49 (2004).
- [163] D. DÉBARRE AND E. BEAUREPAIRE. *Quantitative characterization of biological liquids for third-harmonic generation microscopy*. Biophys. J., 92(2):603–612 (2007).
- [164] F. KAJZAR AND J. MESSIER. *Original technique for third-harmonic-generation measurements in liquids*. Rev. Sci. Instr., 58(11):2081–2085 (1987).
- [165] D. DEBARRE, W. SUPATTO, A.-M. PENA, A. FABRE, T. TORDJMAN, L. COMBETTES, M.-C. SCHANNE-KLEIN, AND E. BEAUREPAIRE. *Imaging lipid bodies in cells and tissues using third-harmonic generation microscopy*. Nat. Methods, 3(1):47–53 (2006).
-

- [166] G.O. CLAY, A.C. MILLARD, C. B. SCHAFFER, J. AUS-DER AU, P.S. TSAI, J.A. SQUIER, AND D. KLEINFELD. *Spectroscopy of third harmonic generation: evidence for resonances in model compounds and ligated hemoglobin*. J. Opt. Soc. Am. B, 23:932–950 (2006).
- [167] J. M. BÉLISLE, S. COSTANTINO, M. L. LEIMANIS, M.-J. BELLEMARE, S. D. BOHLE, E. GEORGES, AND P. W. WISEMAN. *Sensitive detection of malaria infection by third harmonic generation imaging*. Biophys. J., 94:L26–L28 (2008).
- [168] S.-W. CHU, S.-Y. CHEN, T.-H. TSAI, T.-M. LIU, C.-Y. LIN, H.-J. TSAI, AND C.-K. SUN. *In vivo dev. biol. study using noninvasive multi-harmonic generation microscopy*. Opt. Express, 11(23):3093–3099 (2003).
- [169] D. DÉBARRE, W. SUPATTO, E. FARGE, B. MOULIA, M.-C. SCHANNE-KLEIN, AND E. BEAUREPAIRE. *Velocimetric third-harmonic generation microscopy: micrometer-scale quantification of morphogenetic movements in unstained embryos*. Opt. Lett., 29(24):2881–2883 (2004).
- [170] W. SUPATTO, D. DÉBARRE, E. FARGE, AND E. BEAUREPAIRE. *Femtosecond pulse-induced microprocessing of live drosophila embryos*. Med. Las. Appl., 20:207–216 (2005).
- [171] E. J. GUALDA, G. FILIPPIDIS, G. VOGLIS, M. MARI, C. FOTAKIS, AND N. TAVERNARAKIS. *In vivo imaging of cellular structures in caenorhabditis elegans by combined tpef, shg and thg microscopy*. J. Microsc., 229 (2008).
- [172] C.-S. HSIEH, S.-U. CHEN, Y.-W. LEE, Y.-S. YANG, AND C.-K. SUN. *Higher harmonic generation microscopy of in vitro cultured mammal oocytes and embryos*. Opt. Express, 16(15):11574–11588 (2008).
- [173] C.-K. SUN, C.-C. CHEN, S.-W. CHU, T.-H. TSAI, Y.-C. CHEN, AND B.-L. LIN. *Multiharmonic-generation biopsy of skin*. Opt. Lett., 28(24):2488–2490 (2003).
- [174] S.-P. TAI, T.-H. TSAI, W.-J. LEE, D.-B SHIEH, Y.-H LIAO, H.-Y. HUANG, K.Y.J. ZHANG, H.-L. LIU, AND C.-K; SUN. *Optical biopsy of fixed human skin with backward-collected optical harmonics signals*. Opt. Express, 13(20):8231–8242 (2005).
- [175] S.-P. TAI, W.-J. LEE, D.-B.SHIEH, P.-C. WU, H.-Y. HUANG, C.-H. YU, AND C.-K. SUN. *In vivo optical biopsy of hamster oral cavity with epi-third-harmonic generation microscopy*. Opt. Express, 14(13):6178–6187 (2006).
- [176] C.-K. SUN, C.-H. YU, S.-P. TAI, C.-T. KUNG, I.-J. WANG, H.-C. YU, H.-J. HUANG, W.-J. LEE, AND Y.-F. CHAN. *In vivo and ex vivo imaging of intra-tissue elastic fibers using third-harmonic-generation microscopy*. Opt. Express, 15(18):11167–11177 (2007).
- [177] D. ORON, E TAL, AND Y. SILBERBERG. *Depth-resolved multiphoton polarization microscopy by third-harmonic generation microscopy*. Opt. Lett., 28(23):2315–2317 (2003).
- [178] R. ELBAUM, E. TAL, A.I. PERETS, D. ORON, D. ZISKIND, Y. SILBERBERG, AND H.D. WAGNER. *Dentin micro-architecture using harmonic generation microscopy*. J. Dentistry, 35(2):150 – 155 (2007).

-
- [179] B. LAMPRECHT, J. R. KRENN, A. LEITNER, AND F. R. AUSSENEK. *Resonant and off-resonant light-driven plasmons in metal nanoparticles studied by femtosecond-resolution third-harmonic generation*. Phys. Rev. Lett. , 83:4421–4424 (1999).
- [180] R. A. GANEEV, A. I. RYASNYANSKY, S. R. KAMALOV, M. K. KODIROV, AND T. USMANOV. *Nonlinear susceptibilities, absorption coefficients and refractive indices of colloidal metals*. Journal of Physics D Applied Physics, 34:1602–1611 (2001).
- [181] S.V. FOMICHEV, S.V. POPRUZHENKO, D.F. ZARETSKY, AND W. BECKER. *Laser-induced nonlinear excitation of collective electron motion in a cluster*. J. Phys. B, 36:3817–3834 (2003).
- [182] M. LIPPITZ, M. A. VAN DIJK, AND M. ORRIT. *Third-harmonic generation from single gold nanoparticles*. Nano Lett., 5(4):799–802 (2005).
- [183] T.M. LIU, S.P. TAI, C.H. YU, Y.C. WEN, L.J. CHU, S.W. CHEN, M.R. PRASAD, K.J. LIN, AND C.K. SUN. *Measuring plasmon-resonance enhanced third-harmonic $\chi^{(3)}$ of ag nanoparticles*. Appl. Phys. Lett., 89:043122 (2006).
- [184] D. YELIN, D. ORON, S. THIBERGE, E. MOSES, AND Y. SILBERBERG. *Multiphoton plasmon-resonance microscopy*. Opt. Express, 11(12):1385–1391 (2003).
- [185] P. N. SAETA AND N. A. MILLER. *Distinguishing surface and bulk contributions to third-harmonic generation in silicon*. Appl. Phys. Lett. , 79:2704–+ (2001).
- [186] D. DÉBARRE, N. OLIVIER, AND E. BEAUREPAIRE. *Signal epidetection in third-harmonic generation microscopy of turbid media*. Opt. Express, 15(14):8913–8924 (2007).
- [187] C.-H. YU, S.-P. TAI, C.-T. KUNG, W.-J. LEE, Y.-F. CHAN, H.-L. LIU, J.-Y. LYU, AND C.-K. SUN. *Molecular third-harmonic-generation microscopy through resonance enhancement with absorbing dyes*. Opt. Lett., 33(4):387–9 (2008).
- [188] C.-F. CHANG, C.-Y. CHEN, F.-H. CHANG, S.-P. TAI, C.-Y. CHEN, C.-H. YU, Y.-B. TSENG, T.-H. TSAI, I.-S. LIU, W.-F. SU, AND C.-K. SUN. *Cell tracking and detection of molecular expression in live cells using lipid-enclosed cdse quantum dots as contrast agents for epi-third harmonic generation microscopy*. Opt. Express, 16(13):9534–9548 (2008).
- [189] R. BARILLE, L. CANIONI, L. SARGER, AND G. RIVOIRE. *Nonlinearity measurements of thin films by third-harmonic-generation microscopy*. Phys. Rev. E, 66(067602):1–4 (2002).
- [190] A. N. NAUMOV, D. A. SIDOROV-BIRYUKOV, A. B. FEDOTOV, AND A. M. ZHELTIKOV. *Third-harmonic generation in focused beams as a method of 3d microscopy of a laser-produced plasma*. Optics and Spectroscopy, 90:778–783 (2001).
- [191] J. M. SCHINS, T. SCHRAMA, J. SQUIER, G. J. BRAKENHOFF, AND M. MÜLLER. *Determination of material properties by use of third-harmonic generation microscopy*. J. Opt. Soc. Am. B, 19(7):1627–1634 (2002).
- [192] D. YELIN, Y. SILBERBERG, Y. BARAD, AND J. S. PATEL. *Depth-resolved imaging of nematic liquid crystals by third-harmonic microscopy*. Applied Physics Letters, 74(21):3107–3109 (1999).
-

- [193] D. YELIN, Y. SILBERBERG, Y. BARAD, AND J. S. PATEL. *Phase-matched third-harmonic generation in a nematic liquid crystal cell*. Phys. Rev. Lett., 82(15):3046–3049 (1999).
- [194] R. S. PILLAI, M. OH-E, H. YOKOYAMA, G. J. BRAKENHOFF, AND M. MÜLLER. *Imaging colloidal particle induced topological defects in a nematic liquid crystal using third harmonic generation microscopy*. Opt. Express, 14(26):12976–12983 (2006).
- [195] C. XU, W. ZIPFEL, J.B. SHEAR, R.M. WILLIAMS, AND W.W. WEBB. *Multiphoton fluorescence excitation: new spectral window for biological nonlinear spectroscopy*. Proc. Natl. Acad. Sci. USA, 93:10763–10768 (1996).
- [196] C. XU AND W.W. WEBB. *Measurement of two-photon excitation cross sections of molecular fluorophores with data from 690 to 1050 nm*. J. Opt. Soc. Am. B, 13(3):481–491 (1996).
- [197] A. SCHÖNLE, M. GLATZ, AND S. W. HELL. *Four-dimensional multiphoton microscopy with time-correlated single-photon counting*. Appl. Opt., 39(34):6306–6311 (2000).
- [198] J. A. PALERO, H. S. DE BRUIJN, A. VAN DER PLOEG-VAN DEN HEUVEL, H. STERENBORG, AND H. C. GERRITSEN. *In vivo nonlinear spectral imaging in mouse skin*. Opt. Express, 14(10):4395–4402 (2006).
- [199] J. A. PALERO AND H. S. ET AL. DE BRUIJN. *Spectrally Resolved Multiphoton Imaging of In Vivo and Excised Mouse Skin Tissues*. Biophys. J., 93(3):992 (2007).
- [200] D. K. BIRD, K. W. ELICEIRI, C-H. FAN, AND J. G. WHITE. *Simultaneous two-photon spectral and lifetime fluorescence microscopy*. Appl. Opt., 43(27):5173–5182 (2004).
- [201] E. BEAUREPAIRE AND J. MERTZ. *Epifluorescence collection in two-photon microscopy*. Appl. Opt., 41(25):5376–5382 (2002).
- [202] D. VUCINIC, T. M. BARTOL JR., AND T. J. SEJNOWSKI. *Hybrid reflecting objectives for functional multiphoton microscopy in turbid media*. Opt. Lett., 31(16):2447–2449 (2006).
- [203] A. ISHIMARU. *Theory and application of wave propagation and scattering in random media*. IEEE Proc., 65:1030–1061 (1977).
- [204] A. ISHIMARU. *Wave propagation and scattering in random media*. Academic Pres, Boston (1978).
- [205] N. OLIVIER, D. DÉBARRE, AND E. BEAUREPAIRE. *Contrast mechanisms and signal epidetection in thg microscopy of scattering tissues*. Proc. SPIE , 6991(1):699114 (2008).

Acknowledgements II

Je souhaite remercier ici tous les gens qui m'ont soutenu pendant ma thèse, à commencer par ceux qui ont fait le déplacement pour assister à ma soutenance en bravant les grèves de RER et qui se sont retrouvés coincés trois heures dans un amphi surchauffé à m'écouter parler. Je remercie tout d'abord ma famille: mes parents, mon frère et mon oncle d'être venu, et pour leur soutien inconditionnel toutes ces années. Merci aussi à tous ceux qui ont aidé, que ce soit pour préparer les slides, faire des répétitions (Emmanuel, Delphine, Marie-Claire), installer le pot (Ariane, Delphine, Xavier, mes parents, probablement d'autres que j'oublie...), ou pour la vidéo-diffusion de la soutenance (merci en particulier à Sacha qui aura passé presque toute sa semaine à organiser cela et à Guillaume).

Je remercie ensuite les gens qui ont eu le plus à me supporter pendant ces trois années, c'est à dire mes colloques, présents ou passés: Luciano, Julien, David, Pierre-André, Martin, Xavier, ainsi que mes co-bureaux: Alexander, Sophia, Jon, Pierre, Delphine, Ana, Alessio, Ariane, Edward. Merci de votre patience envers mon bordel, ma musique, et tous mes autres défauts qui vous ont énervés sans que je m'en rende forcément compte et bonne chance pour vos thèses/études/vrais jobs/faux jobs ! Merci aussi à tous les gens du laboratoire avec lesquels j'ai eu l'occasion de discuter.

Last but not least, un très grand MERCI ! à tous mes amis, les parisiens⁹: Agathe, Charlotte, Elo, Flo, Kathy, Amandine, Xav, Martin, Sam, Guillaume, David, Thomas les parisiens intermittents: Manu, MF, Julien, et les pas du tout parisiens: Luciano, Pascal, Mika,... Merci pour tout, j'ai passé trois très bonnes années grâce à vous.

to be continued...

⁹non Agathe & Flo, être parisien n'est pas un critère important *per se*

Chapter 2

Modeling Nonlinear Microscopy

Contents

2.1	Modeling Nonlinear Microscopy	50
2.2	Modeling Incoherent Nonlinear Microscopy	51
2.3	Modeling Coherent Nonlinear Microscopy	54
2.4	Focusing of Fields Using the Angular Spectrum Representation .	56
2.5	Modeling Nonlinear Effects	59
2.6	Modeling the Propagation of the Nonlinear Polarization	61
2.7	Numerical Implementation	61
2.8	Optical Confinement	62
2.9	Phase Matching in Coherent Microscopy	66
	Bibliography	74

Introduction

One of the objectives of this thesis was to initiate in the laboratory the study of nonlinear microscopy with focused engineered beams. The implementation of a general numerical framework to simulate nonlinear signal generation with arbitrary input field distributions (amplitude, phase, polarization) and arbitrary sample structure was therefore necessary. This Chapter describes different methods that can be used to model nonlinear microscopy. As seen in Chapter 1, nonlinear microscopy can be described as a three-step process with (1) a linear propagation (focusing) of the excitation (2) a nonlinear interaction near the focus (3) a linear propagation of the nonlinear field.

What differentiates the different nonlinear modalities is the nonlinear interaction that takes place in the focal volume. As seen in the first chapter, the nonlinear effects that can happen are either *coherent* (harmonic generation, CARS) or *incoherent* (multiphoton excited fluorescence). The modeling of incoherent multi-photon microscopy is simpler as the nonlinear photons created at the focus cannot interfere and will be described in section 2.2, while coherent

microscopy requires a different kind of modeling and will be described in sections 2.3 to 2.7.3. We will then discuss two important concepts of nonlinear microscopy: the optical confinement in section 2.8 , and the phase-matching conditions in section 2.9.

2.1 Modeling Nonlinear Microscopy

Modeling nonlinear microscopy is complex for several reasons:

- The nonlinear optical process is (unsurprisingly) described by nonlinear equations.
- We have to consider several wavelengths: the excitation wavelength (also called fundamental wavelength) that is focused into the sample, and the nonlinear wavelength that is created in the focal volume.
- The equations involve vectorial operators.

Indeed, the following (vectorial) nonlinear equation (see appendix A.1 for notations & details) has to be true for every wavelength:

$$\Delta \mathbf{E}(\omega) + \frac{n^2(\omega)\omega^2}{c^2} \mathbf{E}(\omega) = -\frac{\omega^2}{\epsilon_0 c^2} \mathbf{P}_{NL}(\omega) \quad (2.1)$$

We can choose to use a single model and stick to it, which means it must describe the propagation of fields at different wavelengths and describe the nonlinear interaction at the focus. It also means we have to use a single set of simplifications that are appropriate to describe all the parts of the microscope. Two strategies are possible with such an approach:

1. The analytical strategy, which (usually) implies a lot of simplifications. It is used in the appendix to provide analytical results from simple geometries.
2. The numerical strategy, which is more complicated to implement but can describe more complex geometries.

Alternatively, we can use different models for the description of the different parts, which increases the complexity but means we can adapt the simplifications used for each part. The method we will describe in detail in this chapter is based on such an approach.

2.1.1 Numerical Method

Numerical methods in physics are being increasingly used thanks to the availability of computers with ever increasing computing power [1, 2]. The two main numerical methods used in electrodynamics are :

- The Finite Differences Time Domain Method (FDTD) [3, 4].
- The Finite Elements Method (FEM) [5].

The FDTD method was introduced by Yee in 1966 [3], and is an application of the Finite Difference Method to Maxwell's equations in a linear isotropic non-dispersive material. It has also been applied to the nonlinear wave equations [6]. The main advantage of this method is that it is easy to use, and not very demanding computationally, at least compared with other methods. The Finite Differences Frequency Domain Method (FDFD) can also be used in cases where it is more adapted than the time-domain method. Yet the Yee algorithm relies on a regular discretization that is not adapted to all the geometries, and the dispersivity of materials is hard to take into account.

The FEM is a more powerful method that offers more freedom for the shape and properties of the materials but is much harder to implement [5, 7–9]. It also is more demanding in computing power. Other methods exist, such as the Method of Moments (MoM) [10] or the Boundary Element Method (BEM) [11] that can also be combined with the FEM [12].

The problem with numerical methods in optics is that the grid size has to be smaller than the wavelength, and so modeling 3D phenomena over large propagation distances gets very rapidly impossible. It is still possible to use these methods for modeling near field microscopy [13–15], as the propagation distances considered are much smaller. Another interesting possibility is to combine numerical methods with regular propagation methods. For example, Cheng *et al* combined the FDTD method in a small volume with Green's function propagation of the nonlinear signal in focus-engineered CARS microscopy [16, 17], and Török proposed a more general method for modeling coherent microscopy by combining vectorial focusing, FDTD in the focal volume and Green's function propagation [18].

Monte Carlo simulations [19] are adapted to the mathematical simulations of stochastic processes, for example the scattering of light [20, 21].

2.2 Modeling Incoherent Nonlinear Microscopy

2.2.1 Introduction

In incoherent nonlinear microscopy (ie: usually two-photon excited fluorescence) we can consider that the sample contains a given distribution of fluorophores, that is to say molecules that have energy transitions which allow them to reach a radiative excited state after a nonlinear excitation. The probability of having a n -photon absorption event depends on the probability of having n photons at the same place at the same time, and it is proportional to the intensity of the excitation to the power n .

Once a molecule is excited, the de-excitation timescale is in the nanosecond range, and the fluorescent photon is emitted incoherently, that is to say with a phase and direction that are not related to the phase and direction of the excitation photons. This means two neighboring molecules that are excited by the same pulse emit two photons that do not interact with each other, and so the intensity that can be detected is directly proportional to the number of molecules that are excited.

Thus, although the images nonlinearly depend on the excitation intensity, they linearly depend on the distribution of fluorophores. As the image formation process is linear, the system is completely described by its *point spread function* as we will see in the next section.

2.2.2 Point-Spread Function in Incoherent Multiphoton Microscopy

The *point spread function* (psf) of an optical system is defined as the response of the system to a Dirac delta function, or more physically as the image of an infinitely small object (one single molecule for example). We use (x, y) (resp (u, v)) as coordinates in the image (resp in the sample):

$$Image(\delta(u, v)) = PSF(x, y) \quad (2.2)$$

If the system is linear, as is the case in incoherent nonlinear microscopy, the image of a given object can then be calculated as the convolution between the object and the point spread function.

$$Image(x, y) = \iint O(u, v) PSF(x - u, y - v) du dv \quad (2.3)$$

This can also be written using convolution as:

$$Image(x, y) = (PSF \otimes Obj)(x, y) \quad (2.4)$$

What is particularly interesting in the case of 2PEF (resp. nPEF) microscopy is that when we consider that:

1. The intensity distribution is the same in every point of the sample (no spatial dependence on aberrations, scattering or absorption).
2. The collection efficiency is the same from every point of the sample.

then the point spread function of the microscope is equal to the squared (resp. n^{th} power) intensity distribution at the focus:

$$PSF(x, y) = I^n(x, y) \quad (2.5)$$

The knowledge of the intensity distribution at the focus of the microscope objective is therefore enough to characterize the system.

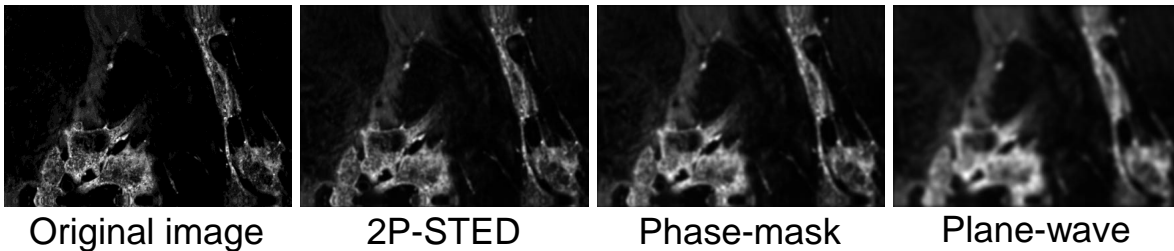


Figure 2.1: SIMULATION OF IMAGE FORMATION IN 2PEF MICROSCOPY
PSF calculations done using a 2D FTDT method. From left to right: original fluorophore distribution, image filtered using a 2PSTED psf, using a super-resolution filter psf, and using a focused plane wave psf.

Figure (2.1) illustrates the influence of a numerically calculated point-spread function on the quality of an image. The simulations were done using a 2D FTDT method based on the paraxial wave equation to calculate the intensity distribution at the focus of a virtual system. An image

was then convoluted with the squared intensity distribution to obtain a virtual microscope image. Three different conditions were computed: a focused plane wave, a super-resolution annular phase-mask [22], and a 2P-STED-like psf resulting from the subtraction of a regular psf using an excitation wavelength and a phase-mask modulated de-excitation at another wavelength.

Several other different methods can be used to calculate the field intensity at the focus of an objective, but we will only describe two: the Gaussian beam model in section 2.2.2.1 and a more general model based on the angular spectrum representation of the field [23] in section 2.2.2.2.

2.2.2.1 The Gaussian Beam

The Gaussian beam is a solution to the paraxial wave equation that can be used to describe quite accurately the output of a laser. Moreover, a Gaussian beam focused by a perfect lens also is a Gaussian beam, which makes it even more adapted to simulate optical systems.

The general expression of a Gaussian beam is given by (see appendix A.2):

$$E(x, y, z) = \frac{E_0 e^{-ikz}}{(1 + 2iz/kw_0^2)} e^{-\frac{(x^2+y^2)}{w_0^2} \frac{1}{(1+2iz/kw_0^2)}} \quad (2.6)$$

where w_0 is the beam waist. Since we usually describe our focusing conditions by using the numerical aperture of the objective, we want to express the beam parameters as a function of the NA.

Using the paraxial approximation, we can express the waist of a focused beam as a function of the focal distance of a lens f and the waist of the beam at the back aperture of the objective w_0 as:

$$w_f^2 = \frac{\lambda^2 f^2 w_0^2}{\lambda^2 f^2 + \pi^2 w_0^4} \quad (2.7)$$

and the numerical aperture can be expressed in the paraxial approximation as:

$$\frac{NA^2}{n^2} = \frac{w_0^2}{w_0^2 + f^2} \quad (2.8)$$

2.2.2.2 Non-paraxial Beams

Several methods to calculate the field of a focused non-paraxial beam exist, and in this thesis we mostly use the angular spectrum representation, that will be described in details in the next section. Using these models means that no analytical expression for the point spread function can be obtained, and that all the calculations will have to be done numerically. Yet, these methods are useful (and even necessary) as soon as the shape of the excitation is not Gaussian, as will be shown in Chapter 4.

2.2.3 Deconvolution

One of the advantages of having a linear system described by a point spread function is that *deconvolution* can be performed: as the image is the convolution between the point spread function and the sample structure, the original sample structure can be reconstructed by using

a deconvolution algorithm [24] which consists of convoluting the image by the inverse of the point spread function.

$$Image(X, Y) = (Sample(x, y) \otimes psf(u, v)) \quad (2.9)$$

$$\begin{aligned} &\Downarrow \\ Sample(x, y) &= Image(X, Y) \otimes psf^{(-1)}(u, v) \quad (2.10) \end{aligned}$$

Deconvolution algorithms are usually limited by the signal to noise ratio, which means they are not particularly well adapted to multiphoton microscopy where the photon flux is small.

2.3 Modeling Coherent Nonlinear Microscopy

In coherent microscopy, the nonlinear process is instantaneous, and the wave-vector of the harmonic photon is equal to the sum of the wave-vectors of the exciting photons. As the excitation is also coherent, there is a well defined phase relation between all the different points of the focal volume, which means they can all interfere to create either constructive or destructive interference in the far field, so the image formation is not linear and the system cannot be accurately described by a point spread function.

In this section, we will describe the model that we will use throughout this thesis to describe coherent nonlinear microscopy.

2.3.1 Overview of the Main Model

The model used in this thesis to represent a nonlinear microscope is a modification of the model proposed by Cheng *et al.* [25, 26] for coherent nonlinear microscopy, extended to take into account the vectorial aspects of the excitation. It has three different parts:

1. The excitation, calculated from initial field conditions and objective properties.
2. The sample, given by the spatial distribution of a nonlinear tensor.
3. The propagation of the nonlinear polarization to the far field.

Figure (2.2) illustrates the main model used in this thesis: the model starts at the back aperture of the focusing objective, which means we consider that everything before it is perfect. From this initial field phase and amplitude, we calculate the focal field for a given set of focusing conditions (Numerical aperture, index of refraction, ...) by using the Angular Spectrum Representation (ASR) [23, 27, 28]. The field is calculated at each point of a regular 3d grid by numerical integration. The nonlinear polarization is then calculated at each point of the grid, according to the value of the field and nonlinear susceptibility at this point. Finally, the nonlinear polarization is propagated to the far field by using the far-field Green's function.

2.3.2 Simplifications Implied by the Main Model

Two fundamental properties of our laser beams are neglected in this model:

1. The time-dependence of our field: although we use femtosecond laser pulses, we will only take into account the space-dependent terms in the equations.

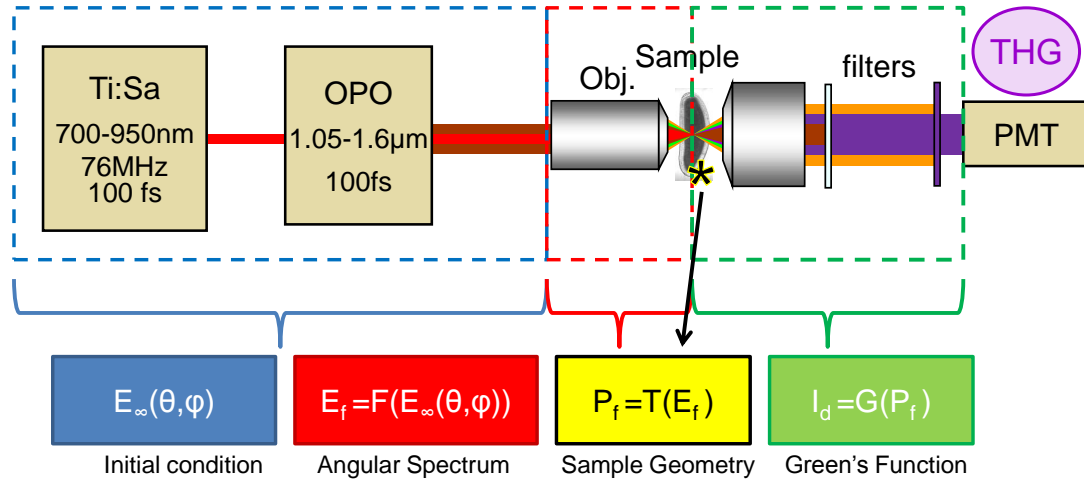


Figure 2.2: MODELING NONLINEAR MICROSCOPY

Model used throughout this thesis: The initial condition is the field distribution at the back aperture of the objective, the first part consists in calculating the focal field from this initial condition using the ASR, then the nonlinear polarization is calculated, and finally it is propagated to the far field using Green's function.

2. The spectral bandwidth of the excitation pulses: we will only consider the central frequency. This means we also neglect all the effects related to the spectral phase of the excitation.

2.3.3 Geometry

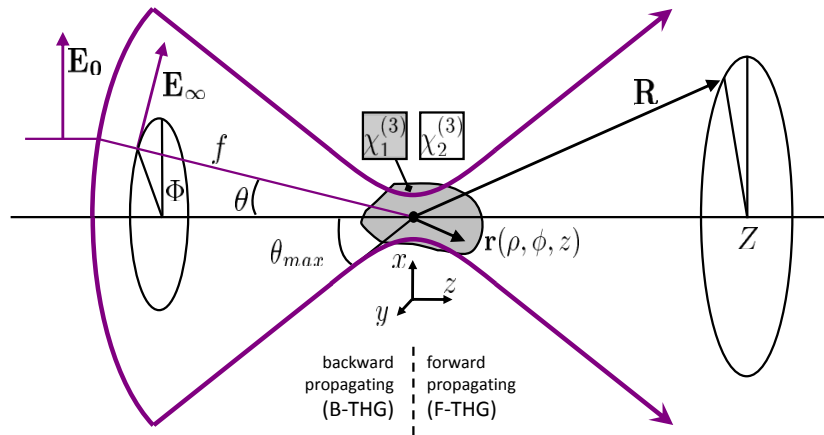


Figure 2.3: GEOMETRY USED IN CHAPTER 2 TO 4
See text for a description. Published in [29].

Figure (2.3) illustrates the geometry used in this section. The field at the back aperture of the objective is expressed as $E_0(\theta, \phi)$ using cylindrical coordinates, while the focal field is written $E_f(\mathbf{r})$ in spherical coordinates centered at the focal point, but is sometimes expanded

in Cartesian coordinates as $E_f(x, y, z)$. Finally, the far-field nonlinear field is written $E_{ff}(\mathbf{R})$ (resp. $E_{ff}(X, Y, Z)$) in spherical (resp. Cartesian) coordinates.

The objective is characterized by its numerical aperture (NA), that can be expressed as:

$$NA = n \cdot \sin(\theta_{max}) \quad (2.11)$$

where θ_{max} is the half-angle of the maximum cone of light that can exit the objective lens (defined in figure (2.3)).

The sample is described by two media of nonlinear susceptibilities $\chi^{(n)}$ and $\chi_0^{(n)} = 0$, and by a single couple of linear indices at the fundamental and nonlinear frequencies: (n_{exc}, n_{nl}) .

2.4 Focusing of Fields Using the Angular Spectrum Representation

In this theoretical treatment, we follow the theory established by Richards and Wolf [27, 28], and expanded by Novotny [23]. In the angular spectrum representation, the field is the sum of plane waves with variable amplitudes and propagation directions, so that in order to compute the propagation of the beam, we propagate all the plane waves and then sum them up coherently. Assuming a homogeneous isotropic linear medium, we have:

$$E(x, y, z) = \iint_{-\infty}^{\infty} \hat{E}(k_x, k_y, 0) e^{i[k_x x + k_y y - k_z z]} dk_x dk_y \quad (2.12)$$

where:

$$k_z^2 = k^2 - k_x^2 - k_y^2 \quad (2.13)$$

$$k = \frac{\omega}{n \cdot c} \quad (2.14)$$

2.4.1 Assumptions

We accept the following hypotheses:

1. the incoming beam is polarized along the x direction, which means: $\mathbf{E}_{inc} = E_{inc} \mathbf{n}_x$. Then, the exciting field propagates only in homogeneous isotropic media, and there are no index-mismatches, which means :

$$\chi^{(1)}(z) = \chi^{(1)} \quad (2.15)$$

2. we consider an objective with perfect anti-reflection coating, Numerical Aperture NA^1 , and cone angle θ_m given by:

$$\theta_m = \arcsin(NA/n) \quad (2.16)$$

¹We will usually consider in this chapter high values of the numerical aperture (typically $NA=1.4$) because the vectorial effects are more important in this case.

2.4.2 Expression of the Focal Field

In the geometry illustrated by figure (2.3), the expression of the incoming field E_∞ just after the objective can be written as:

$$\mathbf{E}_\infty(\theta, \phi) = \frac{E_{inc}\sqrt{\cos(\theta)}}{2} \begin{bmatrix} 1 + \cos(\theta) \cos(2\phi)(1 - \cos(\theta)) \\ \sin(2\phi)(\cos(\theta) - 1) \\ -2 \cos(\phi) \sin(\theta) \end{bmatrix} \quad (2.17)$$

This field can be propagated using equation (2.12):

$$\mathbf{E}(\rho, \phi, z) = \frac{ikfe^{-ikf}}{2\pi} \int_0^{\theta_m} \int_0^{2\pi} e^{-ikz\cos(\theta)} e^{-ik\rho\sin(\theta)\cos(\phi-\Phi)} \sin(\theta) \mathbf{E}_\infty(\theta, \phi) d\Phi d\theta \quad (2.18)$$

$$= \frac{ikfe^{-ikf}}{4\pi} \int_0^{\theta_m} \int_0^{2\pi} E_{inc}\sqrt{\cos\theta} e^{-ikz\cos\theta} e^{-ik\rho\sin\theta\cos(\phi-\Phi)} \sin\theta \times \begin{bmatrix} 1 + \cos\theta - \cos(2\phi)(1 - \cos\theta) \\ \sin(2\phi)(\cos\theta - 1) \\ -2\cos\phi\sin\theta \end{bmatrix} d\Phi d\theta \quad (2.19)$$

$$= \frac{ikfe^{-ikf}}{4\pi} \int_0^{\theta_m} E_{inc}\sqrt{\cos\theta} e^{-ikz\cos\theta} \sin\theta \begin{bmatrix} A_x \\ A_y \\ A_z \end{bmatrix} d\theta \quad (2.20)$$

with

$$\begin{bmatrix} A_x \\ A_y \\ A_z \end{bmatrix} = \begin{bmatrix} \int_0^{2\pi} e^{-ik\rho\sin\theta\cos(\phi-\Phi)} [1 + \cos\theta - \cos(2\phi)(1 - \cos\theta)] d\Phi \\ \int_0^{2\pi} e^{-ik\rho\sin\theta\cos(\phi-\Phi)} \sin(2\phi)(\cos\theta - 1) d\Phi \\ -2 \int_0^{2\pi} e^{-ik\rho\sin\theta\cos(\phi-\Phi)} \cos\phi\sin\theta d\Phi \end{bmatrix} \quad (2.21)$$

$$= \begin{bmatrix} 2\pi(1 + \cos\theta)J_0(k\rho\sin\theta) - \int_0^{2\pi} e^{-ik\rho\sin\theta\cos(\phi-\Phi)} \cos(2\phi)(1 - \cos\theta) d\Phi \\ \int_0^{2\pi} e^{-ik\rho\sin\theta\cos(\phi-\Phi)} \sin(2\phi)(\cos\theta - 1) d\Phi \\ -2 \int_0^{2\pi} e^{-ik\rho\sin\theta\cos(\phi-\Phi)} \cos\phi\sin\theta d\Phi \end{bmatrix}$$

If we expand $\mathbf{E}_0(\theta, \Phi)$ as a polynomial expansion of $\cos(\Phi)$ and $\sin(\Phi)$ functions, this 2D integral can be reduced to a 1D integral involving Bessel functions J_n . We can then use the following abbreviations to express the focal fields of a number of modes (Gaussian, but also Laguerre-Gaussian and Hermite-Gaussian, as we will see in chapter 4).

$$I_{lmn}^{\alpha\beta}(\rho, z) = \int_\alpha^\beta f_w(\theta) (\cos\theta)^{1/2} \sin^m\theta \cos^n\theta J_l(k\rho\sin\theta) e^{ikz\cos\theta} d\theta \quad (2.22)$$

where $f_w(\theta) = \exp(-(\sin(\theta)/(f_0 \sin\theta_{max}))^2)$ is a filling factor that takes into account the ratio (f_0) between the beam size (related to w_0) and the back aperture of the objective ($f \sin\theta_{max}$).

2.4.3 Comparison Between Angular Spectrum Representation & Gaussian Paraxial Approximation

We remind the expression for a focused Gaussian beam derived in appendix A.2:

$$E(x, y, z) = E_0 \frac{w_0}{w(z)} e^{-\frac{(x^2+y^2)}{w(z)^2}} e^{i(kz - \eta(z) + k(x^2+y^2)/(2R(z)))} \quad (2.23)$$

where:

$$w(z) = w_0 \sqrt{1 + \frac{z^2}{b^2}} \quad (2.24)$$

In this section, we will compare the field predicted by the paraxial approximation and by the angular spectrum representation in the case of a linearly polarized beam with a Gaussian intensity distribution and a flat phase at the back aperture of the objective.

2.4.3.1 Vectorial Aspects

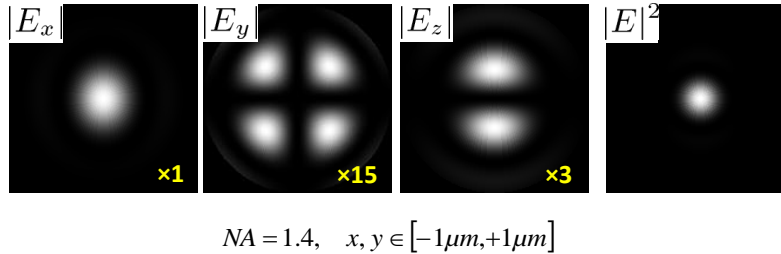


Figure 2.4: VECTORIAL ASPECTS USING THE ASR

Electric field distribution of a focused linearly polarized Gaussian beam. Conditions: $NA=1.4$, $n=1.5$. Published in [29].

The first fundamental difference between the two models is that the angular spectrum representation takes into account the vectorial nature of the electric field: even if we consider a perfectly linear polarization at the back aperture of the objective, the polarization at the focus can be completely different. For example, the different components of the electric field at the focus of a high NA objective with a Gaussian intensity distribution at the back aperture are shown in figure (2.4), and we can see that the intensity of the axially polarized component of the excitation is only three times smaller than the x -polarized component.

However, in the case of a Gaussian beam, the vectorial effects are limited, especially if we consider the n^{th} power of the electric field as the axially polarized and laterally polarized components of the field do not spatially overlap, but for other polarizations and other field distributions at the back aperture, the effect can be more drastic. For example, the focusing of donut shaped Laguerre-Gaussian (LG01) beams can either yield to a donut intensity at the focus when it is linearly polarized, or a single peaked intensity distribution when it is radially polarized as illustrated in figure (2.5), discussed in more detail in chapter 4.

2.4.3.2 Differences in E_x

Even if we only consider the linear part of the focal field, there are still some differences between the angular spectrum representation and the Gaussian beam. Figure (2.6) illustrates the cubed intensity and phase distribution for both models, as well as the difference between models. We find a better agreement for the intensity than for the phase.

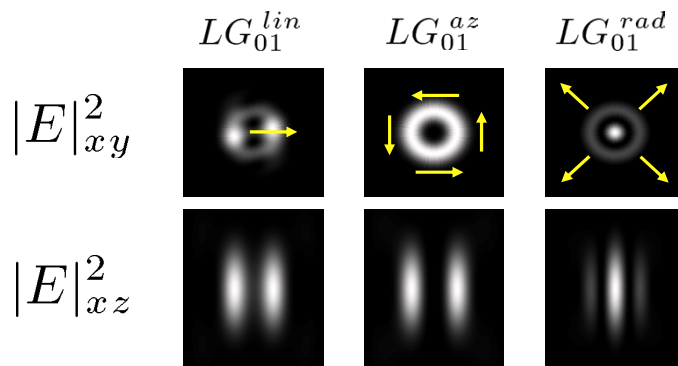


Figure 2.5: INFLUENCE OF THE INCOMING POLARIZATION xy and xz components of the focal fields resulting from the focusing of radially, azimuthally and linearly polarized Laguerre-Gaussian LG_{01} beams. The yellow arrows denote the direction of the polarization in the focal plane. Conditions: $NA=1.4$, $n=1.5$. Published in [29].

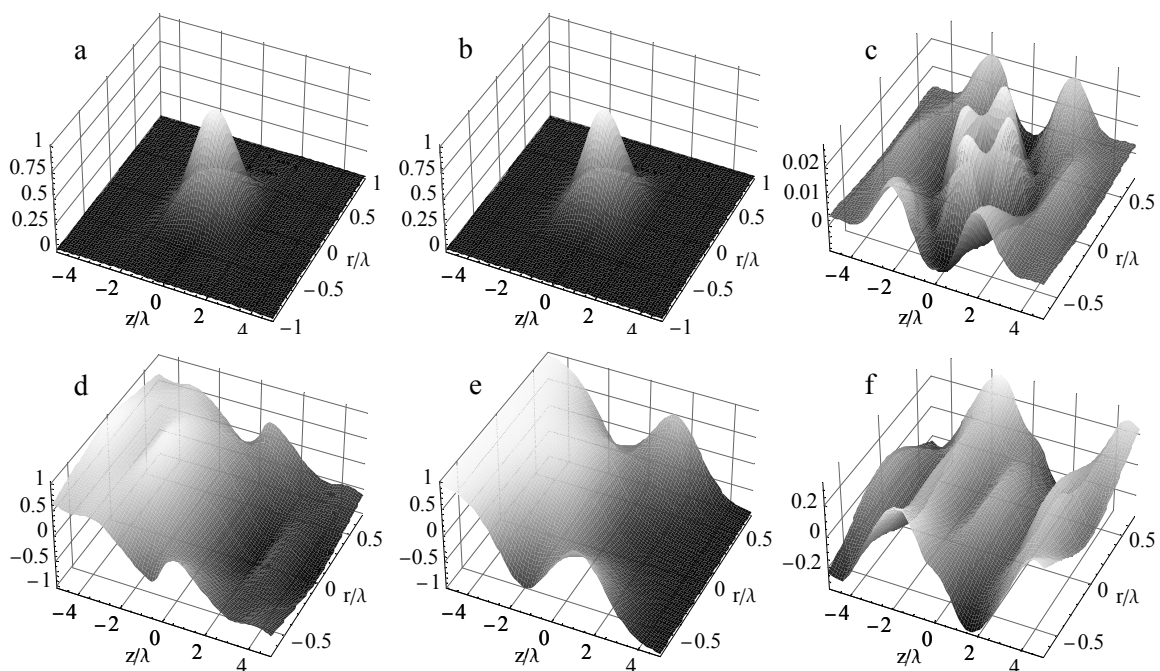


Figure 2.6: DIFFERENCES BETWEEN GAUSSIAN PARAXIAL & ASR Cubed intensity difference of a focused Gaussian beam with (a) a paraxial model (b) a non-paraxial model (c) difference, and phase distribution using (d) a paraxial model (e) a non-paraxial model (f) the difference. Conditions: $NA=1.4$, $n=1.5$. Adapted from [30].

2.5 Modeling Nonlinear Effects

The nonlinear interactions that occur at the focus of a coherent nonlinear microscope are described by the nonlinear wave-equation (described in more details in appendix A.1) :

$$(\nabla + k^2)\mathbf{E}(n\omega) = -\frac{\omega^2}{\epsilon_0 c^2}\mathbf{P}_{NL}(n\omega) \quad (2.25)$$

where $\mathbf{P}_{NL}(\omega)$ is the induced nonlinear polarization that depends on:

1. The sample structure described by a nonlinear tensor $\chi^{(n)}$, whose properties are discussed in section 2.5.2.
2. The excitation field: for an n^{th} order nonlinear effect, the nonlinear polarization is proportional to $E_f^n(\omega)$.

2.5.1 Nonlinear Polarization of the Main Nonlinear Effects

The nonlinear polarization for the process of second harmonic generation can be written as:

$$P_i^{(SHG)}(2\omega) = \sum_{j,k} \chi_{ijk}^{(2)} \cdot E_j(\omega) \cdot E_k(\omega) \quad (2.26)$$

for third harmonic generation:

$$P_i^{(THG)}(3\omega) = \sum_{j,k,l} \chi_{ijkl}^{(3)} \cdot E_j(\omega) E_k(\omega) E_l(\omega) \quad (2.27)$$

for n^{th} harmonic generation:

$$P_i^{(NHG)}(n\omega) = \sum_{j_1, \dots, j_n} \chi_{ij_1 \dots j_n}^{(n)} \cdot E_{j_1}(\omega) \dots E_{j_n}(\omega) \quad (2.28)$$

and for CARS (with two different excitation wavelengths: λ_p and λ_s) :

$$P_i^{(CARS)}(2\omega_p - \omega_s) = \sum_{j,k,l} \chi_{ijkl}^{(3)} \cdot E_j(\omega_p) E_k^*(\omega_s) E_l(\omega_p) \quad (2.29)$$

The vectorial aspects of second and third harmonic generation have been studied, for example in reference [31].

2.5.2 Symmetries & Tensors

The $\chi^{(n)}$ tensors are $n + 1$ order tensors called hyperpolarizability tensors. If a medium possesses symmetry properties related to its organization, then its tensor also has some properties. For example, if we consider a homogeneous medium, we have strict symmetry conditions [32–34]:

- The tensor $\chi^{(2)}(2\omega, \omega, \omega)$ describing second harmonic generation is a third order tensor that can be non-zero only in non-centrosymmetric media.
- The tensor $\chi^{(3)}(3\omega, \omega, \omega, \omega)$ describing third harmonic generation is a fourth order tensor that does not require non-centrosymmetry, and is discussed in more details in chapter 3

When we consider degenerate processes like SHG or THG, we get some extra symmetry conditions. If we consider for example the third order hyperpolarizability of an isotropic homogeneous medium, $\chi^{(3)}(\omega_1 + \omega_2 + \omega_3, \omega_1, \omega_2, \omega_3)$ has three independent elements, while if we consider a THG process $\chi^{(3)}(3\omega, \omega, \omega, \omega)$, there is only one independent tensor element, and all the other non-zero elements are proportional to it.

2.6 Modeling the Propagation of the Nonlinear Polarization

2.6.1 Green's Function

In order to calculate the far field interference pattern created by the nonlinear polarization, we use the far field Green's function, defined as the electric field radiated by a single dipole, and sum up all the contributions of the sources located in the focal volume.

The harmonic field originating from all positions \mathbf{r} in the focal region and propagated to a position \mathbf{R} in the collection optics aperture can be expressed as [23, 25]:

$$E_{FF}(\mathbf{R}) = \int_V \mathbf{P}^{(nl)}(\mathbf{r}) \mathbf{G}_{FF}(\mathbf{R} - \mathbf{r}) dV \quad (2.30)$$

where V spans the excitation volume and \mathbf{G}_{FF} is the far field Green's function:

$$\mathbf{G}_{FF} = \frac{\exp(ikR)}{4\pi R} [\mathbf{I} - \mathbf{R}\mathbf{R}/R^2] \quad (2.31)$$

where \mathbf{R} is the coordinate of a point in the far field (see figure (2.3)) and \mathbf{I} is the third-order identity tensor.

2.7 Numerical Implementation

This section provides some details about the practical numerical implementation of the numerical simulations.

2.7.1 Numerical Integration of the Focal Field

We have seen in section 2.4 that the focal field can be expressed as a sum of $I_{lmn}^{\alpha\beta}(\rho, z)$ integrals. The problem is that these integrals have no analytical solutions, and have to be calculated numerically. We used Matlab quadrature algorithms [35] to evaluate these integrals.

$$I_{lmn}^{\alpha\beta}(\rho, z) = \int_{\alpha}^{\beta} f_w(\theta) (\cos\theta)^{1/2} \sin^m\theta \cos^n\theta J_l(k\rho\sin\theta) e^{ikz\cos\theta} d\theta \quad (2.32)$$

2.7.2 Numerical Considerations: Size, Sampling

The question of the size of both the total dimensions and the step size of the grid in our numerical simulations is non-trivial.

2.7.2.1 Size of the Focal Volume

As a benchmark for the simulations, we often used THG from an isotropic medium since it reaches zero for a homogeneous sample. However, the method is valid for any kind of nonlinear effect if we replace "reaching zero" by reaching a given plateau.

The choice of the size of the focal volume used for our simulations is then quite straightforward, as any domain large enough to yield *zero* signal² works. Practically, we used a domain

²we never get zero signal, but we can get it arbitrarily close to zero

as small as possible that satisfied this condition, which meant it depended on the geometry considered: B-THG domains could be made very small, while F-THG domains are usually larger. In the case of non-Gaussian excitation, (as in Chapter 4) or in the case of negative dispersion (described in section 3.3) the question becomes trickier, as the THG signal can be non zero even on homogeneous media. In this case, the focal volume is calculated by increasing the dimensions of the domain until the calculated nonlinear signal reaches a plateau.

2.7.2.2 Size of the Grid Steps

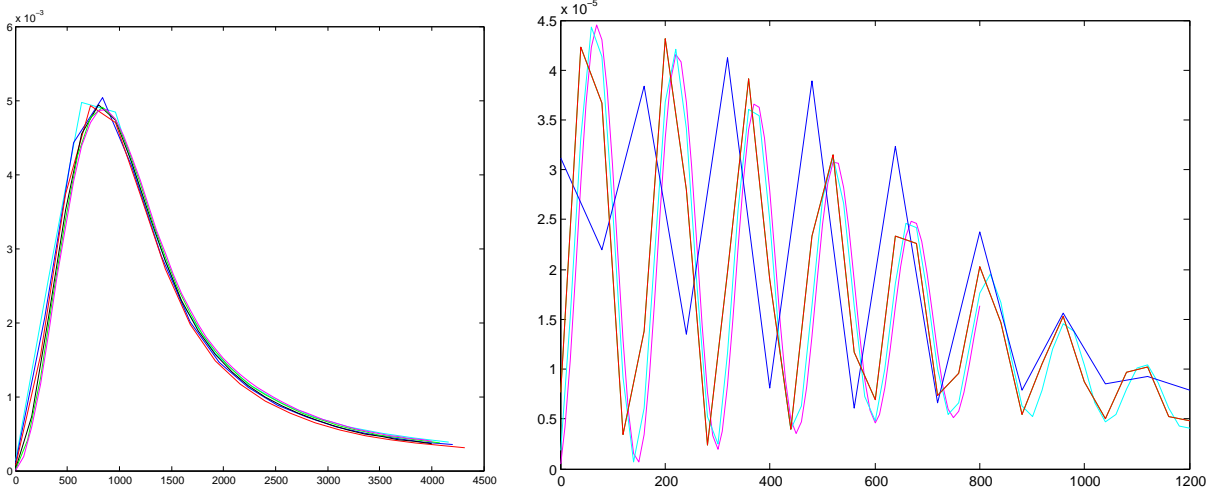


Figure 2.7: INFLUENCE OF THE SAMPLING CONDITIONS IN OUR SIMULATIONS (Left) F-THG signal as a function of the width (in nm) of a centered slab: Magenta: $d\rho=20nm$, Green $d\rho=30nm$; Black: $d\rho=40nm$; Red $d\rho=60nm$; Blue: $d\rho=50nm$; Cyan $d\rho=60nm$; (Right) B-THG from a centered slab: Magenta: $d\rho=5nm$, Cyan $d\rho=10nm$; Orange: $d\rho=20nm$; Blue $d\rho=40nm$; Conditions: $NA=1.3$, $n_\omega = n_{3\omega} = 1.5$.

Figure (2.7) illustrates two different simulations using different sampling sizes. The grid sizes that can be used depend a lot on the geometry of the sample: in the case of F-THG, it can be relatively large (even with $d\rho = 80nm = \lambda/5$, we get the same qualitative result). Contrariwise, in the case of B-THG, as soon as the sampling used step is not small as compared to the coherence length, the numerical result starts to deviate significantly from the correct result.

2.7.3 Far-Field Integration

The far field harmonic radiation is calculated on another regular grid, and the signal in each point is the sum of all the propagated contributions from the sample grid points. The numerical propagation involves a multiplication by a propagation phase factor and a division by a distance factor. The number of points in the far field also depends on the geometry considered, and typically goes from ≈ 400 to ≈ 6000 .

2.8 Optical Confinement

One of the most interesting properties of nonlinear microscopy is that the origin of the signal is confined to the focal volume. This is only true under certain conditions, though, as the signal

does not only depend on the excitation field, but also on the sample structure. One of the ways to understand optical confinement is then to consider a homogeneous isotropic sample, and to calculate the origin of the signal.

2.8.1 Incoherent Microscopy

The easiest case to consider is the case of incoherent microscopy, because only the intensity distribution of the excitation has to be considered. In order to simplify our calculations, we will consider that our sample has a homogeneous distribution of fluorophores.

2.8.1.1 Axial Confinement

We first determine the confinement obtained along the direction of propagation (z direction) by calculating the amount of signal created in the volume defined by a width parameter a along the z axis, and infinite in the x and y directions, that can be expressed for an n^{th} order process as :

$$S_n(a)/S_n^\infty = \frac{\int_{-a}^a \int_{-\infty}^{\infty} \int_{-\infty}^{\infty} I^n(x, y, z) dx dy dz}{\int_{-\infty}^{\infty} \int_{-\infty}^{\infty} \int_{-\infty}^{\infty} I^n(x, y, z) dx dy dz} \quad (2.33)$$

using the expression of the intensity distribution of a Gaussian beam given in appendix A.2, this integral can be evaluated as:

$$\begin{aligned} S_n(a) &= \int_{-a}^a \int_{-\infty}^{\infty} \int_{-\infty}^{\infty} \left(I_0 \frac{w_0^2}{w(z)^2} e^{-\frac{2(x^2+y^2)}{w(z)^2}} \right)^n dy dy dz \\ &= I_0^n \int_{-a}^a \left(\frac{w_0^2}{w(z)^2} \right)^n \cdot \left(\frac{\pi w(z)}{\sqrt{2n}} \right) dz \\ &= \frac{\pi w_0^{2n} I_0^n}{\sqrt{2n}} \int_{-a}^a \frac{1}{(w(z))^{2n-1}} dz \end{aligned} \quad (2.34)$$

we remind that $w(z) = w_0 \sqrt{1 + z^2/b^2}$, where b is the Rayleigh range of the beam, and we get:

$$S_n(a) = \frac{\pi w_0^{2n} I_0^n}{\sqrt{2n}} \int_{-a}^a \frac{1}{(1 + z^2/b^2)^{n-1/2}} dz \quad (2.35)$$

For a second order effect this integral is equal to:

$$S_2(a) = \frac{a}{\sqrt{1 + a^2/b^2}} \quad (2.36)$$

and for a third order effect:

$$S_3(a) = \frac{2a^3 + 3ab^2}{3b^2(1 + a^2/b^2)^{3/2}} \quad (2.37)$$

We can see from equation (2.36 and 2.37) that when a goes to infinity, the total signal scales as b^n . However this is because we have not normalized the intensity.

We can then define an arbitrary threshold, for example 95% or 99% and consider that the nonlinear signal creation is confined to this area. Figure 2.8 illustrates the value of $S(a)/S(\infty)$ for second order and third order effects.

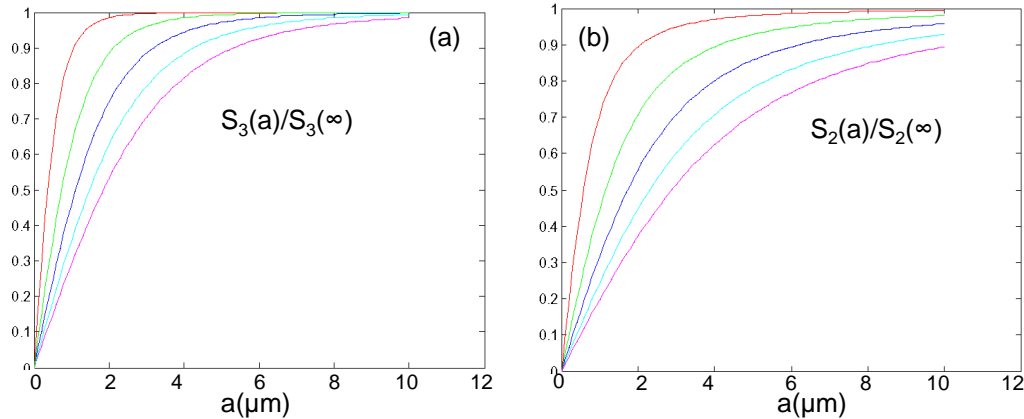


Figure 2.8: AXIAL CONFINEMENT

(a) $S_3(a)/S_3(\infty)$, and (b) $S_2(a)/S_2(\infty)$ for $b = 1\mu\text{m}$ (red), $2\mu\text{m}$ (green), $3\mu\text{m}$ (blue), $4\mu\text{m}$ (cyan), and $5\mu\text{m}$ (magenta).

We could estimate the confinement in the xy plane by doing the same calculation, but integrating x and y over a finite domain. We also have to remember that this confinement is true only for an isotropic sample: if we consider really abnormal samples, we can get a significant amount of signal created outside the previously-defined **focal volume**. For example, a (very pathological) example is when the distribution of fluorophores is equal to the inverse of the squared intensity: in this case the signal can originate from any plane, as the probability to emit one nonlinear photon is the same everywhere in the sample.

2.8.2 Influence of Scattering & Absorption

We have seen in the first chapter that absorption and scattering are the most limiting factors in microscopy. Multiphoton microscopy improves the imaging depth as compared to linear microscopy, in part because it uses longer excitation wavelengths that reduce the influence of scattering and absorption, but they remain a limiting factor, as we will see in this paragraph.

2.8.2.1 Scattering & Absorption

The effects of scattering and absorption on the attainable imaging depth are complex, as outlined in section 1.6. However, if we only consider the confinement due to the excitation intensity distribution, we can use a simple model for both scattering and absorption where the intensity decreases exponentially. This model assumes that scattered excitation light does not generate any 2PEF, so it should be considered as a first order approximation. If we consider that the scattering/absorbing medium starts at $z = z_0$, the intensity can be expressed as:

$$\left(\frac{I_0 w_0^2}{w(z)^2} e^{-\frac{2(x^2+y^2)}{w(z)^2}} \right) e^{(z_0-z)/l_a} \quad (2.38)$$

so if we follow the same strategy as previously, we can define confinement efficiency as a function of depth:

$$\begin{aligned} S_n(a, b, z_0) &= \int_{-a}^a \int_{-\infty}^{\infty} \int_{-\infty}^{\infty} \left(\frac{w_0^2}{w(z)^2} e^{-\frac{2(x^2+y^2)}{w(z)^2}} e^{(z_0-z)/l_a} \right)^n .dy .dz \\ &= S_0 \int_{-a}^a \frac{e^{n(z_0-z)/l_a}}{(1+z^2/b^2)^{n-1/2}} dz \end{aligned} \quad (2.39)$$

However, the exponential decrease has introduced an asymmetry in the intensity distribution, which means it is easier to represent the influence of scattering and absorption by plotting the origin of the nonlinear signal instead of its integral. In figure (2.9), we consider that the beam is focused $100\mu m$ into the sample, and the value of l_a increases until the confinement is lost.

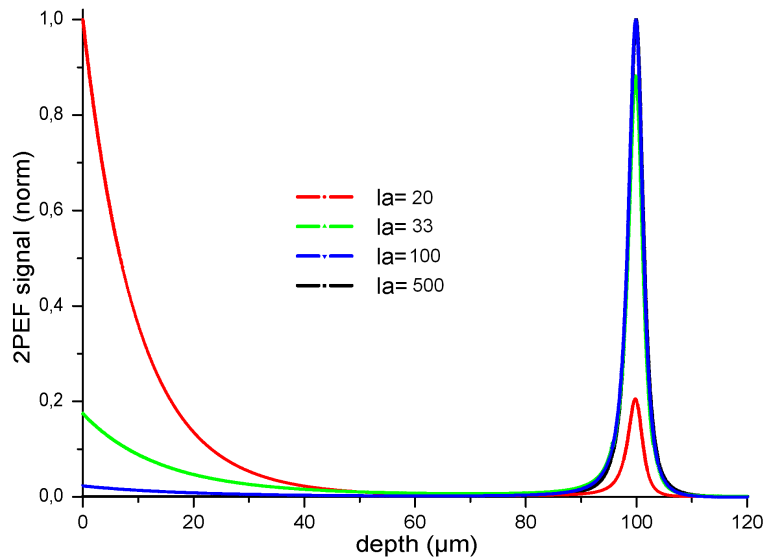


Figure 2.9: INFLUENCE OF SCATTERING & ABSORPTION

Origin of the 2PEF signal for a Gaussian beam focused $100\mu m$ into a scattering sample.

The imaging limit may be defined as the situation where shot noise from the near-surface region is larger than the “useful” signal originating from the near-focus region.

2.8.3 Coherent Microscopy

In the case of coherent microscopy, two different effects affect the optical confinement:

- Intensity effects, similarly to what is observed in incoherent microscopy.
- Phase effects, from which we either have a coherent increase or decrease of the signal.

Moreover, the coherent nature of the signal implies that the intensity of a phase-matched process increases as the squared number of emitters, instead of linearly in incoherent microscopy. This means the simple model described in section 2.8.1 is not valid anymore.

There are two main phase effects: the first one is the index-mismatch between the exciting field and the harmonic field. Indeed, the optical index is wavelength dependent and is generally (ie: neglecting resonances) increasing over the visible and near infra-red range typically used for nonlinear microscopy. The second effect is the Gouy phase-shift [36]: in the focal region, the phase of a focused beam experiences a progressive π radian phase-shift, as illustrated in figure (2.10).

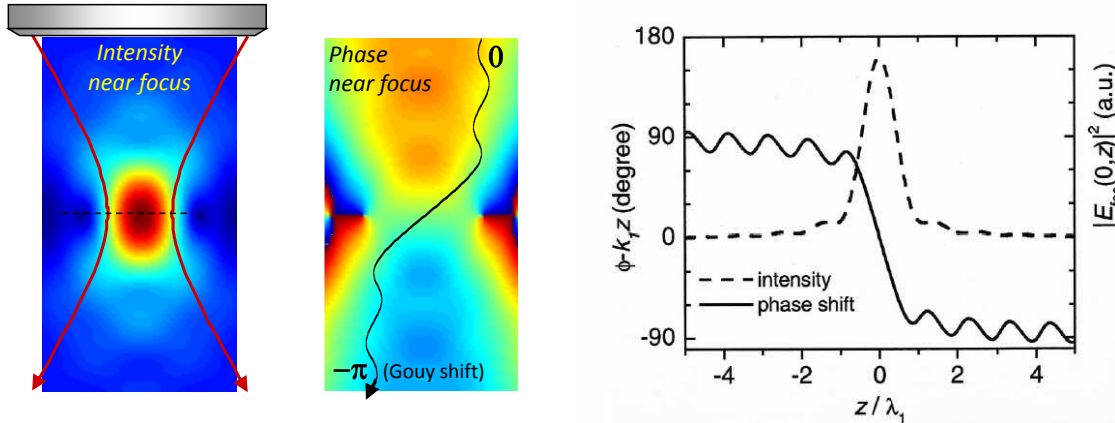


Figure 2.10: INTENSITY AND PHASE DISTRIBUTION NEAR THE FOCUS OF A HIGH NA OBJECTIVE

(Left) 2D distribution of phase and intensity in the focal volume calculated numerically using the angular spectrum representation. (Right) Axial intensity and phase distribution, adapted from reference [25]. In both cases, the propagation terms of the phase have been neglected.

The interplay between the intensity and phase effects will be discussed in the next section.

2.9 Phase Matching in Coherent Microscopy

2.9.1 Introduction

The concepts of phase-matching come from nonlinear optics, where weak focusing conditions are commonly used, and the interaction distances are usually large as compared to the optical wavelength. An easy way to understand it is to consider the interaction between 1D plane-waves. In the case of second harmonic generation, the excitation - that can be written as $E(z, t) = E_0 e^{i(k_\omega z - \omega t)}$ - induces a second order nonlinear polarization that can be written as $P^{(2)}(z, t) \propto \chi^{(2)} E(z, t)^2$. If we want the second harmonic field - that can be written as $E_{2\omega}(z, t) = E_1 e^{i(k_{2\omega} z - 2\omega t)}$ - and the nonlinear polarization to interfere constructively then they must have the same phase, that is to say $k_{2\omega} = 2k_\omega$. This condition is called the **phase-matching condition**.

The case of second harmonic generation is described in appendix A.4, and we recall the equation describing the interaction as:

$$\frac{dA_2}{dz} = C_2 e^{i(\Delta k z)} \quad (2.40)$$

Where $A_2(z)$ is the amplitude of the harmonic field, $\Delta k = k_{2\omega} - 2k_\omega$ and C_2 is proportional to A_1^2 . This equation can easily be integrated, and yields:

$$A_2(z = L) = C_2 \frac{\sin(\Delta k L/2)}{\Delta k} \quad (2.41)$$

If we consider perfect phase-matching conditions, the amplitude of the SH field increases linearly with the interaction distance, but if $\Delta k \neq 0$ then the harmonic field amplitude reaches a maximum for an interaction distance $L = \frac{\pi}{\Delta k}$ and then oscillates.

This model implies the following assumptions:

1. The first one is the ***non-depleted pump approximation***, which means that we consider that the amplitude of the fundamental wavelength is not modified by the interaction with the nonlinear field. Since nonlinear microscopy relies on very inefficient effects, this is a valid assumption.
2. The second one is the ***plane-wave approximation***, which means we consider that the amplitude of the fundamental beam is constant and does not depend on the position. This assumption is obviously ***not*** valid in the case of nonlinear microscopy where we have tightly focused beams.

In the next section, we will therefore consider the case of Gaussian beams.

2.9.1.1 Phase-matching Gaussian Beams

The previous model considers that the excitation does not depend on z , which is not adapted to nonlinear microscopy. A better model would be to consider Gaussian beams instead of plane waves, and this model is described in [34]. Two main aspects are taken into account here:

1. The ***global*** effect of index-mismatch, whose influence was studied in the previous case.
2. The ***local*** effect of intensity variations and Gouy phase-shift.

We consider that both fundamental and harmonic fields can be described as Gaussian beams:

$$E_n(r, z) = \frac{A_n(z)}{1 + 2iz/b_n} e^{-r^2/w_n^2(1+2iz/b_n)} \quad (2.42)$$

with:

$$b_n = k_{n\omega} w_n^2 \quad (2.43)$$

The integration assuming an non-depleted pump ($A_1(z) = A_1$) is performed in appendix A.5, and we find:

$$A(z, \Delta k, b_1) = A_0 \int_{z_0}^z \frac{e^{i\Delta k \zeta} d\zeta}{(1 + 2i\zeta/b_1)^{(n-1)}} \quad (2.44)$$

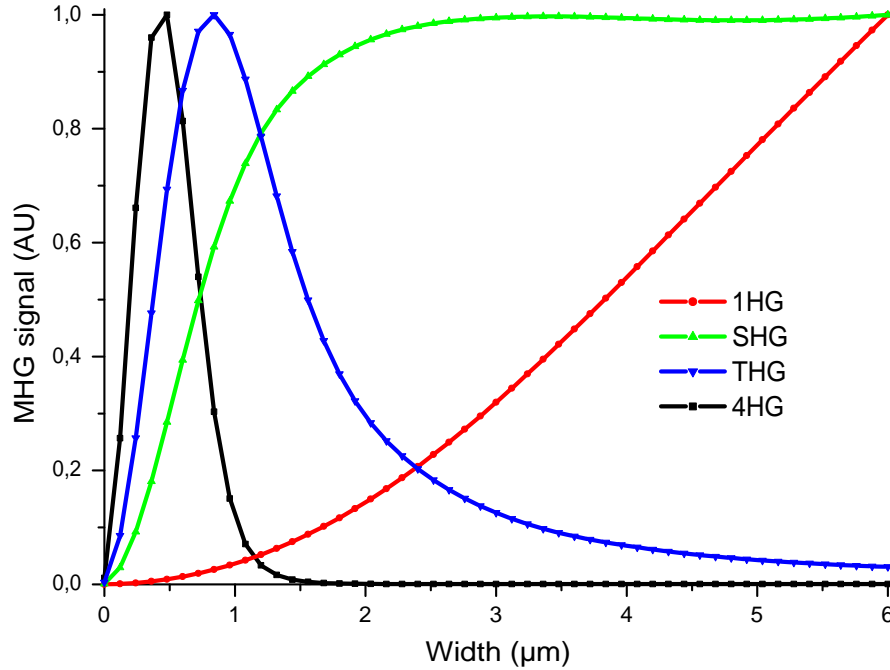


Figure 2.11: PHASE-MATCHING FOR THE FIRST COHERENT NONLINEAR EFFECTS

Multi Harmonic Generation signal as a function of the axial size of a z -oriented slab, for the first four coherent nonlinear effects. Conditions: $\lambda = 1.2\mu m$, $NA=1.4$, $n_{exc} = n_{nl} = 1.5$.

The properties of this integral are studied in appendix A.5.1. Although second harmonic generation is not properly described by this model (for example this model predicts that we obtain no SHG signal from a non-dispersive medium while more accurate studies have shown that it is not the case [37]), several results can be obtained with this model, the most important one being that no THG signal is obtained from an isotropic normally dispersive (or even non-dispersive) homogeneous medium.

2.9.2 In Coherent Nonlinear Microscopy

In coherent nonlinear microscopy, phase-matching fundamentally becomes a 3D phenomenon that can be re-formulated as: given a 3D phase and intensity distribution, in which direction are the interferences constructive, and in which direction are they destructive? Our numerical model described previously is perfectly adapted to answer this question.

Figure 2.11 illustrates the amount of forward emitted signal for the four first coherent effects ('1HG', SHG, THG and 4HG), considering perfect index-matching and an isotropic medium³. In all these cases, the harmonic field is quite accurately described by a Gaussian beam.

- The linear scattering effect is - as expected - not confined, and as there is no index-mismatch, it increases with the width of the slab.
- The SHG signal reaches a plateau when the size of the domain gets bigger than the size corresponding to the optical confinement.

³The is physically impossible in the case of SHG and 4HG, but mathematically way more convenient

- The THG and 4HG signals have similar behaviors: the harmonic signal reaches a maximum for a domain smaller than the optical confinement, and decreases down to zero due to destructive interference. If we go on and consider 5HG or MHG, we get the same kind of response.

The cause of the destructive interferences that kill the harmonic signal in the case of THG and 4HG is the Gouy phase-shift, described in figure (2.10).

2.9.2.1 Influence of the Gouy Phase-shift

In order to illustrate the influence of the Gouy phase-shift, we consider third harmonic generation with a hypothetical (physically impossible) excitation field distribution for which the amount of phase-shift can be adjusted independently of the intensity.

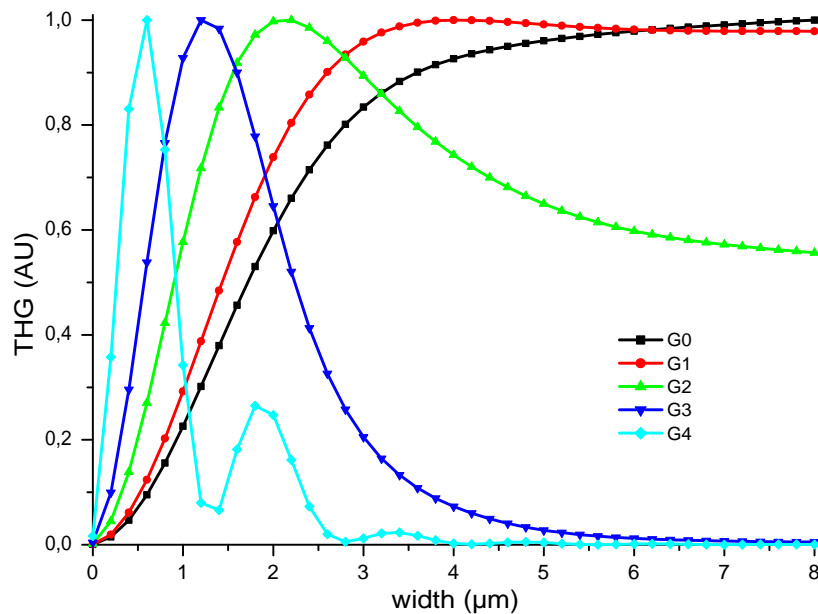


Figure 2.12: INFLUENCE OF THE GOUY PHASE-SHIFT IN THG
 THG signal as a function of the width of the slab with different amounts of Gouy phase-shift. Conditions: $\lambda = 1.2\mu m$, $NA=1.4$, $n_\omega = n_{3\omega} = 1.5$.

Figure (2.12) illustrates the influence of the Gouy phase-shift in the case of third harmonic generation. The number of times the Gouy phase-shift is involved in the nonlinear process is controlled by calculating a different nonlinear polarization for each process:

$$P_{3\omega}^{(3)} = |E_\omega|^3 * \left(\frac{E_\omega}{|E_\omega|} \right)^n \quad (2.45)$$

The blue curve corresponds to the normal situation, in which case the Gouy phase-shift is involved three times.

- In the green curve ($n = 2$) we decrease the number of times that the Gouy phase-shift is involved so the destructive interference is not as strong: the maximum signal is reached for a larger width, and the signal decreases until it reaches a non-zero plateau.

- In the red and black curves ($n = 1$ and $n = 2$) the signal increases and reaches a maximum that once again corresponds to the optical confinement due to the $|E_\omega|^3$ term in the equation.
- In the cyan curve, ($n = 4$), the phase matching conditions are worse than in the usual case, so the maximum is reached sooner, and we can see the harmonic signal oscillate before it reaches zero.

2.9.2.2 Influence of the Index-mismatch

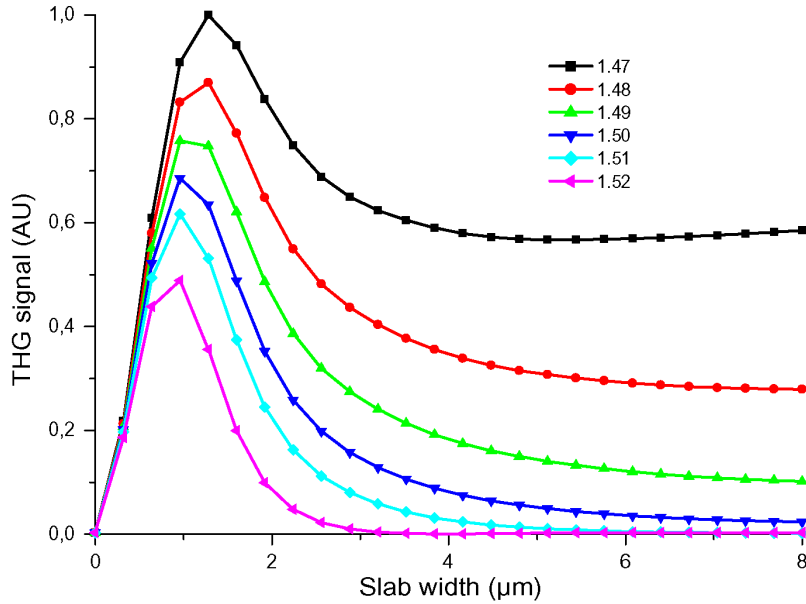


Figure 2.13: INFLUENCE OF THE INDEX-MISMATCH IN THG

THG signal as a function of the width of the slab with different index-mismatches.

Conditions: $\lambda = 1.2\mu\text{m}$, $\text{NA}=1.4$, $n_{3\omega} = 1.5$, $1.47 \leq n_\omega \leq 1.53$.

Figure (3.22) illustrates the influence of the index-mismatch in the case of third harmonic generation. The blue curve corresponds to the zero-dispersion case, in which $n_\omega = n_{3\omega}$, and we have the usual coherent increase followed by the onset of destructive interferences and a signal that goes to zero. If we consider a normally dispersive material ($n_\omega > n_{3\omega}$), as in the green and cyan curves, the phase-mismatch is increased, so the coherence length is decreased. Therefore, the signal reaches a smaller maximum and goes down to zero more rapidly. On the other hand, if we consider an abnormally dispersive medium ($n_\omega < n_{3\omega}$, black and red curves) then the phase-mismatch is decreased and the coherence length is increased. Moreover, in this case destructive interference is not complete, and the signal reaches a plateau once the width of the slab is larger than the focal volume.

We have discussed the influence of several factors that can influence coherent nonlinear processes. However, we have only considered the integrated harmonic signal emitted in the forward direction, and not the shape and direction of the harmonic fields. This aspect will be described in the next section.

2.9.3 3D Phase-matching - Direction of Emission

2.9.3.1 Axial/Lateral Phase-Matching

Since we always consider exciting beams that propagate along the optical (z) axis, we can treat separately phase-matching conditions in the transverse and axial directions. In the plane wave model, we even completely neglect the transverse dimensions, and in the paraxial hypothesis, we make different hypotheses for the axial and transverse dimensions. The reason for this is that the phase propagation term mostly depends on the position along the optical axis. Even in the case of high NA focusing, for which the intensity distribution can be almost isotropic along the axial and lateral directions, the phase variations (due to both the propagation and the Gouy phase-shift) are still mainly along the optical axis, as illustrated in figure (2.10).

This means we can simplify our discussion on phase matching by considering that only the amplitude depends on both axial and lateral coordinates, and that the phase is the same along the x and y directions [38]:

$$E_{ff}(x, y, z) = A(x, y, z)e^{i\phi(z)} \quad (2.46)$$

The main consequence of this assumption is that out-of-axis emission becomes impossible to phase-match in a bulk isotropic medium. However, our goal is not to have perfect phase-matching conditions, but to identify the structures that provide a non-zero signal through any kind of quasi-phase-matching. In the case of a heterogeneity in the lateral direction, quasi-phase matching is possible and provides out-of-axis harmonic emission, as we will see in the next section.

2.9.3.2 Multi Harmonic Generation From Axial Interfaces

A well studied example [25, 30, 38, 39] is the case of harmonic generation from an interface along the optical axis. The phase matching conditions for Multi Harmonic Generation (MHG) can be written as:

$$\Delta k = |n(\mathbf{k}_\omega + \mathbf{k}_g) - \mathbf{k}_{n\omega}| \quad (2.47)$$

where k_g describes the Gouy phase shift. If we consider the case of an interface along the xz plane, we have: $(\mathbf{k}_\omega + \mathbf{k}_g) = (k_\omega + k_g)\mathbf{e}_z$, and $\mathbf{k}_{n\omega} = k_{n\omega} \cos(\theta)\mathbf{e}_z + k_{n\omega} \sin(\theta)\mathbf{e}_x$, and the phase-matching conditions become:

$$\begin{aligned} \Delta k_z(\theta) &= n(k_\omega + k_g) - k_{n\omega} \cos(\theta) \\ \Delta k_x(\theta) &= k_{n\omega} \sin(\theta) \end{aligned} \quad (2.48)$$

If we consider an emission at an angle ($\theta \neq 0$), we can have $\Delta k_z(\theta_0) = 0$ but $\Delta k_x(\theta)$ increases very rapidly. However, since we consider an interface in this direction, this phase-matching condition is not completely restrictive (this is similar to the forward emission on an interface perpendicular to the propagation direction), which means the emission at the angle θ_0 is possible. θ_0 can be calculated by solving equation (2.48):

$$\cos(\theta) = \frac{n(k_\omega + k_g)}{k_{n\omega}} \quad (2.49)$$

This is true for a heterogeneity in any direction: in this case the direction without the heterogeneity requires full phase-matching that can sometimes be obtained by degrading the phase-matching conditions in the other direction.

2.9.4 Conclusion

Discussing coherent nonlinear microscopy *in general* is not easy, since the different modalities can have such different properties. Moreover, the concepts of resolution, and point-spread function do not work well, and the methods used in nonlinear optics usually rely on long interaction distances and are not always adapted. Therefore, we think that the identification of the geometries that generate signal efficiently when excited by a particular focal field distribution is relevant, and this is what we are going to do in chapters 3 and 4 in the case of third harmonic generation.

Conclusion

There are several ways to model multiphoton microscopy, depending on which effect is considered to dominate. We have described a general method that is easy to implement and that takes into account the full vectorial nature of the phase and intensity distribution of the exciting and harmonic fields. The method relies on the optical confinement of nonlinear signals which imply that the nonlinear signal originates from a finite domain of the sample dubbed the *focal volume*. In this focal volume, the signal creation is dominated by quasi-phase-matching effects that are specific to each geometry.

This method will be used to simulate third harmonic generation microscopy in different geometries in the next chapters, with chapter 3 dealing with the well-described case of third harmonic generation with Gaussian beams, and chapter 4 dealing with different aspects of focus engineering and wavefront control in nonlinear microscopy. The vectorial aspects of the simulations will be particularly significant in this chapter 4.



Bibliography

- [1] C. SANDRIN. *Thèse de doctorat*. Université Paris XI, Paris (2010: Bon courage et bonne chance !).
- [2] E. GAGNAIRE-RENOU. *Thèse de doctorat*. Université de Toulon, Toulon (2009).
- [3] K. YEE. *Numerical solution of initial boundary value problems involving maxwell's equations in isotropic media*. IEEE Transactions on Antennas and Propagation, 14:302–307 (1966).
- [4] A. TAFLOVE AND S. C. HAGNESS. *Computational Electrodynamics: The Finite Difference Time-domain Method*. Taylor & Francis, Boston (2005).
- [5] J.-M. JIN. *The Finite Element Method in Electromagnetics*. Wiley (1993).
- [6] R. M. JOSEPH AND A. TAFLOVE. *Fdtd maxwell's equations models for nonlinear electrodynamics and optics*. IEEE Transactions on Antennas and Propagation, 45:364–374 (1997).
- [7] S. NOSAL. *Thèse de doctorat*. Ecole Centrale, Paris (2009).
- [8] X. DAVOINE. *Thèse de doctorat*. Université Versaille Saint-Quentin, Versaille (2009).
- [9] D. K. DOYEN. *Thèse de doctorat*. Université Paris Est, Paris (2010).
- [10] R. F. HARRINGTON. *Field Computation by Moment Methods*. Wiley-IEEE Press (1993).
- [11] S. KAGAMI AND I. FUKAI. *Application of boundary-element method to electromagnetic field problems*. IEEE Transactions on Microwave Theory Techniques, 32:455–461 (1984).
- [12] S. J. SALON. *The hybrid finite-element boundary element method in electromagnetism*. IEEE Transactions on magnetics, 21(5):1829–1834 (1985).
- [13] M. GOLOSOVSKY, E. MANIV, D. DAVIDOV, AND A. FRENKEL. *Near-field of a scanning aperture microwave probe: a 3-d finite element analysis*. Instrumentation and Measurement, IEEE Transactions on, 51(5):1090–1096 (2002).
- [14] J-B. MASSON, M-P. SAUVIAT, J-L. MARTIN, AND G. GALLOT. *Ionic contrast terahertz near-field imaging of axonal water fluxes*. Proc. Natl. Acad. Sci. USA, 103(13):4808–4812 (2006).
- [15] J-B. MASSON AND G. GALLOT. *True near field versus contrast near field imaging*. Opt. Express, 14(24):11566–11574 (2006).
- [16] L. CHENG AND D. Y. KIM. *Differential imaging in coherent anti-stokes raman scattering microscopy with laguerre- gaussian excitation beams*. Opt. Express, 15(16):10123–10134 (2007).
- [17] L. CHENG, S. VEETIL, AND D. Y. KIM. *Differential imaging in coherent anti-stokes raman scattering microscopy ii: a filter-assisted laguerre-gaussian beam detection scheme*. Opt. Express, 15(19):12050–12059 (2007).
- [18] P. TÖRÖK, P. R. T. MUNRO, AND EM. E. KRIEZIS. *High numerical aperture vectorial imaging in coherent optical microscopes*. Opt. Express, 16(2):507–523 (2008).

-
- [19] N. METROPOLIS AND S. ULAM. *The monte carlo method*. Journal of the American Statistical Association, 247 (1949).
- [20] S. A. PRAHL, M. KEIJZER, S. L. JACQUES, AND A. J. WELCH. *A monte carlo model of light propagation in tissue*. In *SPIE Proceedings of Dosimetry of Laser Radiation in Medicine and Biology*, pages 102–111. Press (1989).
- [21] D. DÉBARRE, N. OLIVIER, AND E. BEAUREPAIRE. *Signal epidetection in third-harmonic generation microscopy of turbid media*. Opt. Express, 15(14):8913–8924 (2007).
- [22] I. J. COX, C. J. R. SHEPPARD, AND T. WILSON. *Reappraisal of arrays of concentric annuli as superresolving filters*. J. Opt. Soc. Am., 72(9):1287–1291 (1982).
- [23] L. NOVOTNY AND B. HECHT. *Principles of Nano-Optics*. Cambridge Univ Press (2006).
- [24] J. G. McNALLY, T. KARPOVA, J. COOPER, AND J. A. CONCHELLO. *Three-dimensional imaging by deconvolution microscopy*. Methods, 19(3):373 – 385 (1999).
- [25] J.-X. CHENG AND X.S. XIE. *Green’s function formulation for third harmonic generation microscopy*. J. Opt. Soc. Am. B, 19(7):1604–1610 (2002).
- [26] J.-X. CHENG, A. VOLKMER, AND X.S. XIE. *Theoretical and experimental characterization of coherent anti-stokes raman scattering microscopy*. J. Opt. Soc. Am. B, 19(6):1363–1375 (2002).
- [27] E. WOLF. *Electromagnetic diffraction in optical systems. i. an integral representation of the image field*. Proc. Royal Soc. A, 253:349–357 (1959).
- [28] B. RICHARDS AND E. WOLF. *Electromagnetic diffraction in optical systems ii. structure of the image field in an aplanetic system*. Proc. Royal Soc. A, 253:358–379 (1959).
- [29] N. OLIVIER AND E. BEAUREPAIRE. *Third-harmonic generation microscopy with focus-engineered beams: a numerical study*. Opt. Express, 16(19):14703–14715 (2008).
- [30] D. DÉBARRE. *Thèse de doctorat*. Ecole Polytechnique, Palaiseau (2006).
- [31] S. CARRASCO, B. E. A. SALEH, M. C. TEICH, AND J. T. FOURKAS. *Second- and third-harmonic generation with vector gaussian beams*. J. Opt. Soc. Am. B, 23(10):2134–2141 (2006).
- [32] P. N. BUTCHER. *Nonlinear optical phenomena*. Ohio State University (1965).
- [33] R. HELLWARTH. *Third-order optical susceptibilities of liquids and solids*. Progress in Quantum Electronics, 5:1–68 (1979).
- [34] R.W. BOYD. *Nonlinear optics, 2nd edition*. Academic Press (2003).
- [35] W. GANDER AND W. GAUTSCHI. *Adaptive quadrature-revisited*. Bit Num. Math., 40:84–101(18) (2000).
- [36] C. R. GOUY. *Sur une propriete nouvelle des ondes lumineuses*. Comptes rendus de l’Académie des sciences (Paris), 110:1251–1253 (1870).
- [37] D. A. KLEINMAN, A. ASHKIN, AND G. D. BOYD. *Second-harmonic generation of light by focused laser beams*. Phys. Rev., 145(1):338–379 (1966).
-

- [38] L. MOREAUX, O. SANDRE, M. BLANCHARD-DESCE, AND J. MERTZ. *Membrane imaging by simultaneous second-harmonic generation and two-photon microscopy*. *Opt. Lett.*, 25(5):320–322 (2000).
- [39] L. MOREAUX, O. SANDRE, AND J. MERTZ. *Membrane imaging by second-harmonic generation microscopy*. *J. Opt. Soc. Am. B*, 17(10):1685–1694 (2000).

Acknowledgements III

Football is important. Maybe no as important as, say, Drosophila or Nonlinear Optics, but important nonetheless. I therefore wish to thank everyone in the lab who played or cheered for the Lab's football team, some of which were unlucky enough to be photographed in the process (all apologies).



Figure 2.14: LOB Football teams 2008-2009 “Because the thing about football - the important thing about football - is that it is not just about football.” (Terry Pratchett)

I also wish to thank all the players of the Loreal football team who let me play in their team for two years, especially Thomas for bringing me there.

to be continued....

Chapter 3

Third Harmonic Generation Microscopy

Contents

3.1	“Bulk” THG	80
3.1.1	Description of the Model	81
3.1.2	Size Effects	82
3.1.3	Effect of Sample Anisotropy	85
3.1.4	Influence of the Numerical Aperture	89
3.2	Quasi-Phase-Matching	94
3.3	THG in Crystals & Quasi-Crystals	96
3.3.1	Introduction	96
3.3.2	Influence of the Dispersion	97
3.3.3	Dispersion Compensation Using Birefringence	97
3.3.4	Symmetries & Anti-symmetries	99
3.3.5	Tensorial Effects	100
	Bibliography	106

INTRODUCTION

This chapter deals with contrast mechanisms in third harmonic generation microscopy with focused non-paraxial Gaussian excitation using the numerical model described in chapter 2. Our aim is to identify the structures that are visible in a THG image, with a special attention on what we will call the *geometrical effect*: the size and shape of our sample. In a first part (section 3.1), we will expand on the work of Cheng *et al.* [1] and Débarre *et al.* [2, 3] on the phase-matching conditions for THG in isotropic homogeneous samples for geometries corresponding to what we could find in a typical biological specimen, before considering THG from organized structures in sections 3.2 and 3.3.

3.1 “Bulk” THG

In this section, we will only consider simple geometries that consist of two isotropic homogeneous media which have the same linear index of refraction but two different third order nonlinear susceptibilities. Some of the results shown in this part have already been demonstrated by Cheng *et al.* [1] and Débarre *et al.* [2, 3] using a scalar model, but they are presented again in order to provide a continuity. They also validate the vectorial model that will be used in more complex geometries later in section 3.3 and in chapter 4.

We will consider three different geometries, and study the influence of size and orientation parameters:

1. Interfaces, that we see in biological samples each time we have structures larger than the focal volume.
2. Spheres, that can represent small organelles or lipid droplets.
3. Cuboids, that are often described as slabs when the extension in one or two dimensions is larger than the focal volume. They can be used to model domains that are not thick enough to be modeled as interfaces.

Figure (3.1) gives an example of a THG image from a zebrafish embryo where the signal comes from all three types of structures. We observe a THG signal from the interfaces between nuclei and cytoplasm, circled in blue. We also see small organelles that can be modeled as spheres, and are circled in red. Finally, the strong signal that seems to come from the cellular membranes (in yellow) is due to the presence of an intercellular medium that is optically different from the cytoplasm, and corresponds to a slab geometry.

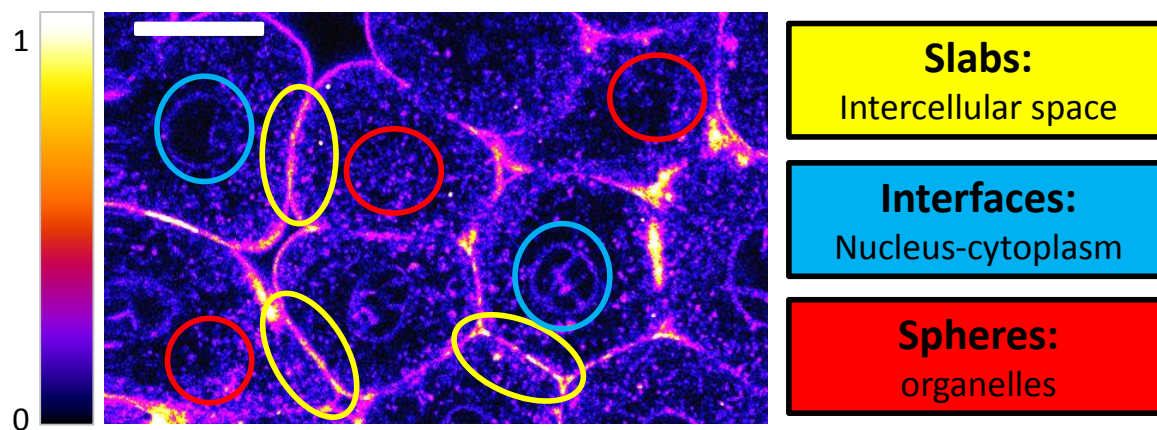


Figure 3.1: IDENTIFICATION OF THE STRUCTURES YIELDING THG SIGNAL IN THE BLASTODERM OF THE ZEBRAFISH EMBRYO.

Scale bar= 10μ m. Zebrafish embryo provided by N.Peyrieras. (More details in chapter 5.)

Moreover, as it has been shown that the relative contrast between such structures could be modified by changing the focusing conditions [2], we will study the influence of the numerical aperture of the excitation on these three geometries in section 3.1.4.

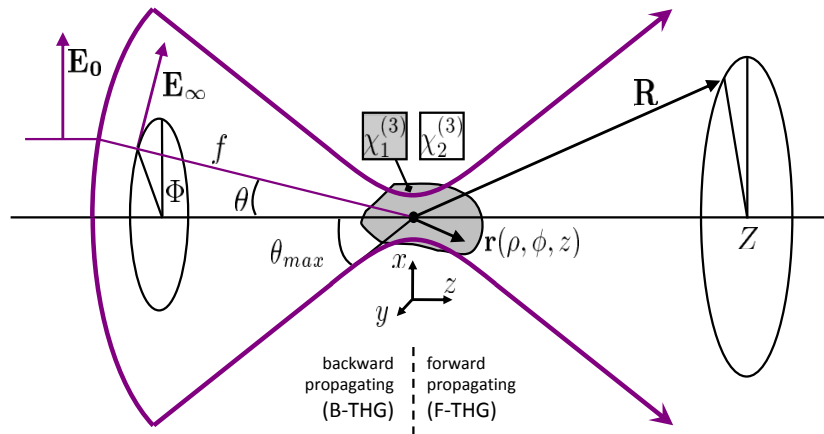


Figure 3.2: GEOMETRY CONSIDERED THROUGHOUT CHAPTER 3
 For a complete description of the geometry, see chapter 2.

3.1.1 Description of the Model

As seen in Chapter 2, the field created by a Gaussian beam focused by a high N.A. objective can be expressed as:

$$\mathbf{E}(\rho, \phi, z) = E_1 \begin{bmatrix} I_{010}(\rho, z) + I_{011}(\rho, z) + (I_{210}(\rho, z) - I_{211}(\rho, z)) \cos(2\phi) \\ (I_{210}(\rho, z) - I_{211}(\rho, z)) \sin(2\phi) \\ -2iI_{120}(\rho, z) \cos(\phi) \end{bmatrix} \quad (3.1)$$

where I_{jkl} is defined in equation (2.22) and (ρ, ϕ, z) are defined in figure (3.2). We then consider that our focal volume is made of two isotropic homogeneous media that have the same linear optical properties described by the tensor $\chi_{ij}^{(1)} = n_\omega \delta_{ij}$, but with different third order nonlinear susceptibilities. As the medium is homogeneous and isotropic, the two tensors can be written as [4]:

$$\chi_{ijkl}^{(3)} = \chi_0 \cdot (\delta_{ij} \cdot \delta_{kl} + \delta_{ik} \cdot \delta_{jl} + \delta_{il} \cdot \delta_{jk}) \quad (3.2)$$

with a different constant χ_0 for the two media. The induced third order polarization is equal to:

$$P_i^{(3\omega)} = \sum_{jkl} \chi_{ijkl}^{(3)} E_j(\omega) E_k(\omega) E_l(\omega) \quad (3.3)$$

so if we take the expression of the tensor given in equation (3.2), we can write:

$$\mathbf{P}^{(3\omega)} = 3\chi_0 \begin{bmatrix} E_x(E_x^2 + E_y^2 + E_z^2) \\ E_y(E_x^2 + E_y^2 + E_z^2) \\ E_z(E_x^2 + E_y^2 + E_z^2) \end{bmatrix} \quad (3.4)$$

The nonlinear polarization from each point in the focal region \mathbf{r} can then be propagated to the far field by using the far field Green's functions [5]:

$$\mathbf{G}_{FF}(\mathbf{R}) = \frac{\exp(ikR)}{4\pi R} [\mathbf{I} - \mathbf{R}\mathbf{R}/R^2] \quad (3.5)$$

where \mathbf{R} is the coordinate of a point in the far field and \mathbf{I} is the third-order identity tensor. The amplitude of the third harmonic field in the far field results from the coherent summation of the contributions from all points in the focal volume [1]:

$$\mathbf{E}_{FF}(\mathbf{R}) = \int_V \mathbf{G}_{FF}(\mathbf{R} - \mathbf{r}) \mathbf{P}^{(3\omega)}(\mathbf{r}) dV \quad (3.6)$$

where V spans the *excitation volume* and \mathbf{G}_{FF} is the far field Green's function. To perform an exact calculation, the integration volume V should be considered infinite, but for numerical calculations we consider instead a finite excitation volume. This volume is calculated for each focusing condition by increasing the size of the volume until the new contributions are negligible. Total THG power emitted in the forward (F-THG) or backward (B-THG) directions can be estimated by integrating $|E_{FF}(\mathbf{R})|^2$ over the front aperture of an epi-collecting or trans-collecting objective (see Figure (3.2)).

3.1.2 Size Effects

The dependence of the THG signal on sample size has already been investigated theoretically by Cheng *et al* [1] using the same method (but neglecting the vectorial aspects of the excitation), but we found it clearer to discuss these phenomena before elaborating further.

We consider two different geometries in this paragraph: the case of a slab of infinite dimensions in the x and y directions, and of width d_z along the z axis, centered at the focal point, and the case of a sphere of diameter d also centered at the focus. Figure (3.3) illustrates the two geometries.

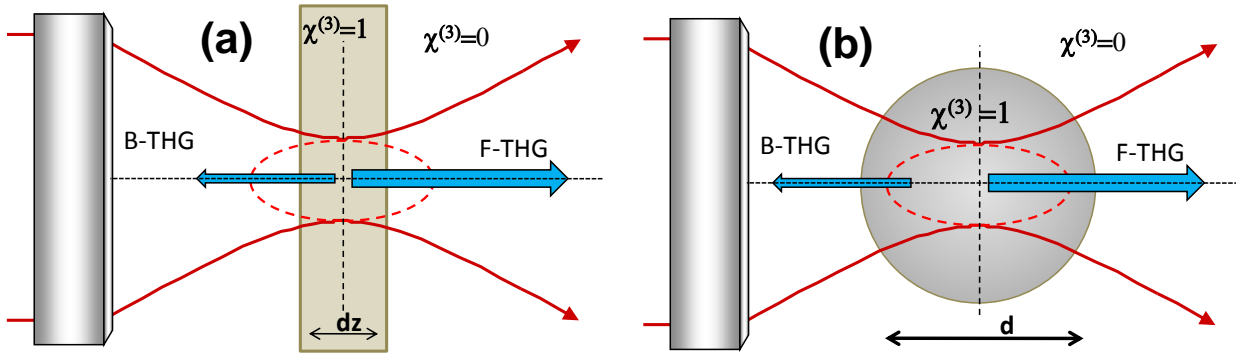


Figure 3.3: GEOMETRIES CONSIDERED IN THIS PARAGRAPH

The excitation beam is focused in the middle of (a) an xy -oriented slab of width d_z and (b) a sphere of diameter d centered at the focal point.

3.1.2.1 Slabs

Because there is no far-field THG signal from an isotropic normally dispersive homogeneous medium [6], and because the propagation of the harmonic field is a linear process, it is equivalent to consider a first medium with a nonlinear susceptibility $\chi_1^{(3)}$ embedded in a second medium with a nonlinear susceptibility $\chi_2^{(3)}$, and to consider a first medium with a nonlinear susceptibility $\chi_1^{(3)} - \chi_2^{(3)}$ embedded in a second medium with $\chi_0^{(3)} = 0$. Accordingly, the geometry that we will consider here is a slab of infinite dimensions in the x and y directions and of width d_z along the z axis, centered at the focal point and with a nonlinear susceptibility $\chi^{(3)} = 1$

sandwiched between two domains of a medium with the same index of refraction, but a null nonlinear susceptibility, as illustrated by figure (3.3.a).

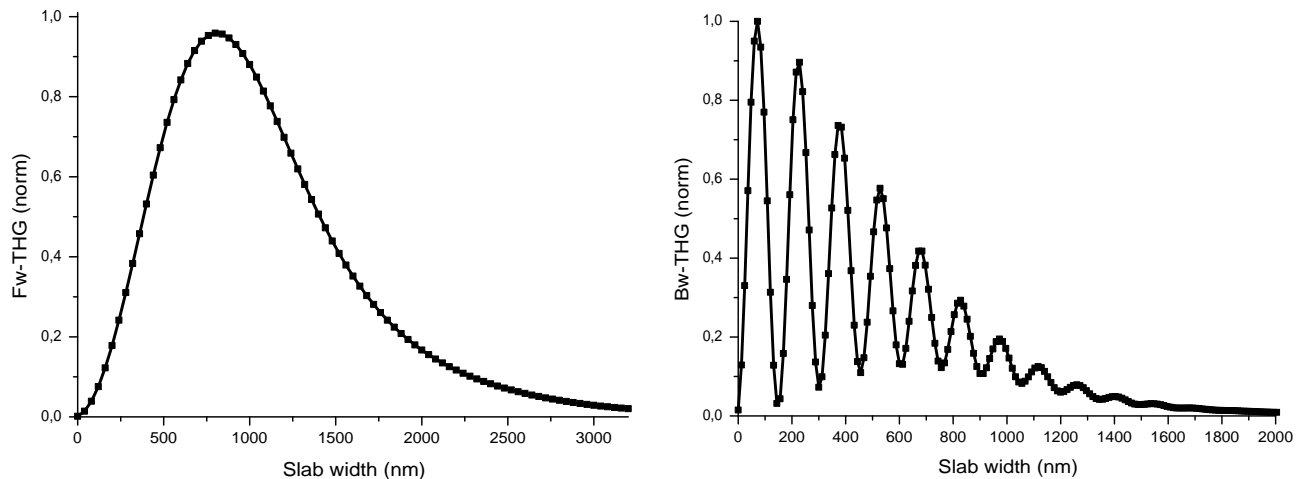


Figure 3.4: THG SIGNAL AS A FUNCTION OF THE SIZE OF A xy ORIENTED SLAB CENTERED AT THE FOCAL POINT
 (Left) F-THG as a function of the width of the slab (Right) B-THG as a function of the width of the slab. The geometry is illustrated in figure (3.3). Conditions: $\lambda = 1.2\mu m$
 $NA = 1.4$, $n_\omega = n_{3\omega} = 1.5$.

Figure (3.4) illustrates the dependence of both F-THG and B-THG signals on the slab width. As the width increases from zero, both F-THG and B-THG signals exhibit a coherent increase characterized by a quadratic intensity dependence on the number of emitters (in this geometry, it corresponds to a quadratic dependence with the width of the slab). Yet, as the size of the slab further increases, destructive interferences start to appear in the backward direction and the signal decreases. This is due to the very important phase-mismatch in that direction. The coherence length of B-THG can be approximated as:

$$l_{bw} = \frac{\pi}{3k_\omega + k_{3\omega}} \approx \frac{\pi}{6 \cdot k_\omega} \approx \frac{\lambda}{12n_\omega} \quad (3.7)$$

If we take the same parameters as in the simulation, we find $l_{bw} \approx 70nm$, which is consistent with the maximum signal value observed. The B-THG then follows damped oscillations with a period corresponding to twice the coherence length.

Another way to explain these damped oscillations is to see them as the combination of an oscillatory behavior due to the phase-mismatch plus a decrease related to the variations of the cubed intensity along the optical axis, which holds as long as the phase matching conditions are the same everywhere.

The F-THG signal has a simpler size dependence: it increases until destructive interferences that are due to the Gouy phase-shift (and, when present, index-mismatch between the fundamental and the harmonic field) make it decrease till it reaches zero for a slab that is large enough to be considered as a homogeneous medium compared to the size of the excitation volume. The forward coherence length can be written as:

$$l_{fw} = \frac{\pi}{\Delta k} = \frac{\pi}{3(k_\omega + k_g) - k_{3\omega}} \quad (3.8)$$

where k_g is the linear phase variation induced by the Gouy phase-shift. The forward coherence length was estimated in reference [1] as: $l_{fw} \approx 0.7\lambda$ in the conditions we used, this value being close to the observed maximum signal.

There are no visible oscillations on the F-THG signal because the excitation intensity at twice the coherence length is negligible as compared with what it was at the focal point. Yet, if we change the phase-matching conditions, for example by considering a large index-mismatch, then oscillations start to appear also in the forward direction.

3.1.2.2 Spheres

The geometry we will consider here is that of a sphere with a nonlinear susceptibility $\chi^{(3)} = 1$ centered at the focus and surrounded by a medium with the same linear index of refraction, but a nonlinear susceptibility equal to zero, as illustrated by figure (3.3.b).

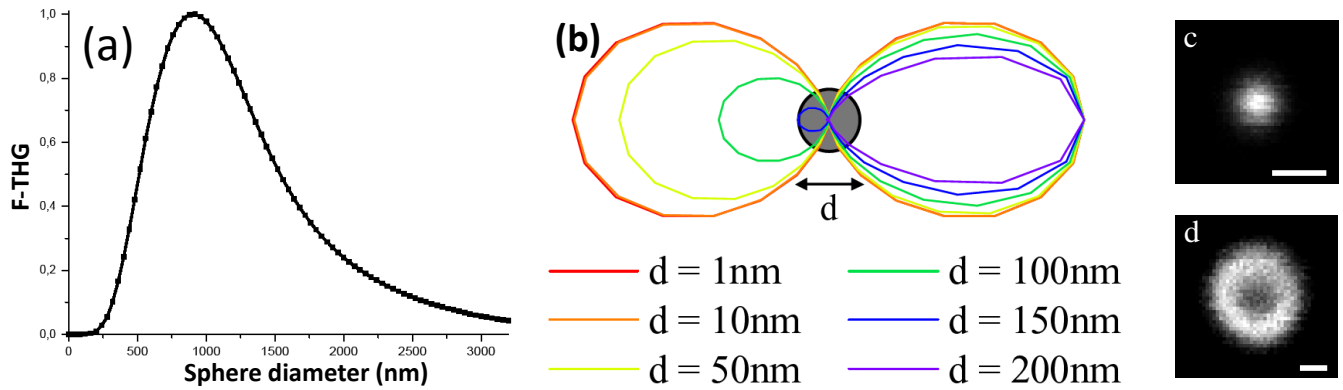


Figure 3.5: THG SIGNAL AS A FUNCTION OF THE SIZE OF A CENTERED SPHERE
 The geometry is illustrated in figure (3.3) (a) The excitation is focused in the center of a sphere of size d . Conditions: $NA = 1.2$, $n_\omega = n_{3\omega} = 1.33$, $\lambda = 1.2\mu m$ (b) The emission patterns are represented for several sphere sizes. Adapted from [7]. (c)&(d) THG images of 600nm and $3\mu m$ diameter beads. The larger bead appears hollow. Scale bar= $3\mu m$, $NA = 0.8$, $\lambda = 1.2\mu m$. Adapted from [3].

The signal dependence of THG on the size of the sphere is illustrated in figures (3.5.a and 3.6). It is very similar to what was obtained from slabs, except that the maximum forward THG signal is obtained for a diameter slightly larger than the width of the slab in the forward direction, and that the backward THG signal initially shows oscillations of increasing amplitude which are afterwards damped.

These similarities come from the fact that axial phase matching dominates the phase matching conditions, which means that the most important parameter is the extension along the z -axis. The differences between slabs and spheres can be explained by considering the number of emitters in the focal volume. In the backward direction in particular, the number of emitters depends on the diameter cubed, so there are 8 times more emitters in the second oscillation than in the first compared with only twice as many in the case of a slab, which more than compensates for the differences in intensity¹.

¹at least at the beginning.

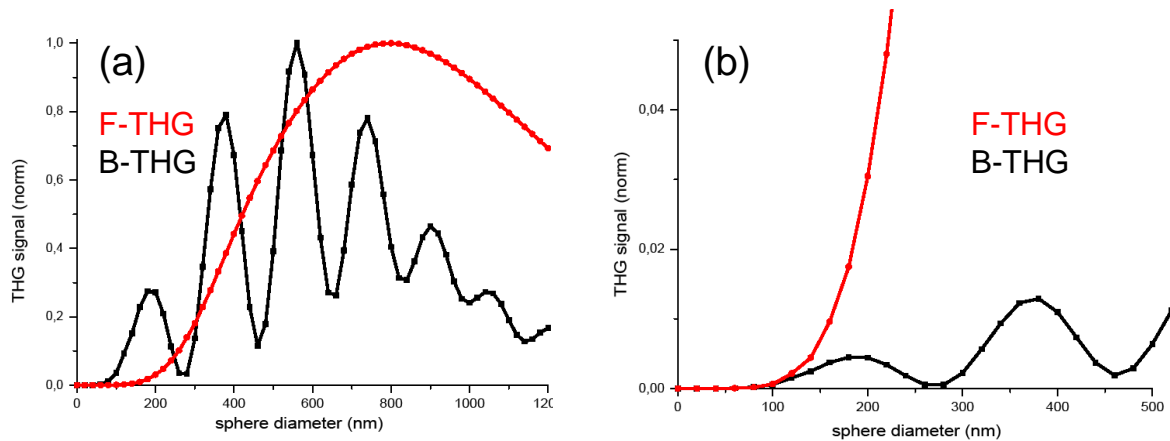


Figure 3.6: F-THG AND B-THG FROM A CENTERED SPHERE:

(a) F-THG & B-THG each normalized to 1. ($\max \text{F-THG} \approx 50 \times \max \text{B-THG}$) (b) F-THG & B-THG on the same scale. Conditions: $NA = 1.2$, $n_\omega = n_{3\omega} = 1.33$, $\lambda = 1.2 \mu\text{m}$.

It is the same effect that causes the shift in the forward direction: the increase in the number of emitters located where the interferences are constructive (that is to say where z is small and ρ is large) compensates for a while the increase in the number of emitters which cause destructive interferences (that are located where ρ is small and z is large).

Figure (3.5.c&d) illustrates the fact that the signal reaches zero for a sphere larger than the focal volume by comparing THG images from two beads of different sizes: a 600nm -diameter one that has a maximum signal at the center and a $3\mu\text{m}$ -diameter one that appears hollow on the image.

Concerning the emission patterns illustrated in figure (3.5.b), we see that for very small objects the emission has two wide lobes, one in the forward and one in backward direction. However, as the size increases the phase-matching conditions get more and more limiting and the emission becomes more and more narrowly forward directed, since the phase-mismatch is less important in this direction.

3.1.3 Effect of Sample Anisotropy

3.1.3.1 Rectangular Cuboid

In this paragraph, we consider the geometry of a rectangular cuboid of length d_z and width both equal to d_ρ oriented along the optical axis and centered at the focal point, as illustrated by figure (3.7). The THG signal as a function of the length and width of the cuboid is illustrated in figure (3.8). The maximum THG signal comes from structures that are either a few hundred nanometers ($\approx 300\text{nm}$) wide in the lateral dimension, or roughly three times as large ($800 - 900\text{nm}$) in the axial direction.

It is interesting to note here that the emission diagrams are completely different in the case of an inhomogeneity along the optical (z) axis or perpendicular to this axis, as illustrated by figure (3.8.c): in the case of heterogeneity along the optical axis (c2), the far field emission is Gaussian with a low divergence, while in the case of an elongated geometry with a symmetry along the z axis, the emission is ring shaped and more divergent (c1). This is due to the

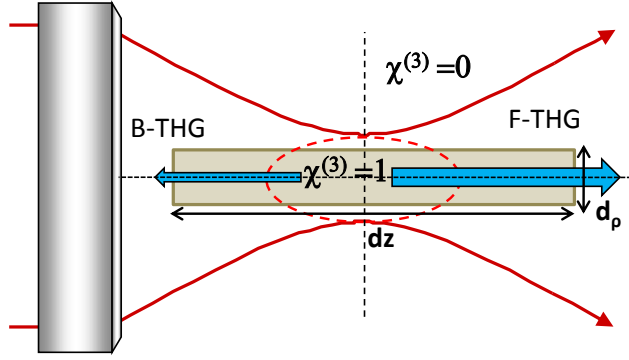


Figure 3.7: ANISOTROPY IN THG MICROSCOPY: geometry considered in this section.

fact that the phase-matching conditions are intrinsically vectorial, and that the presence of an heterogeneity along one direction means that conditions in this direction are modified.

The vectorial phase matching condition can be written as:

$$|3(\mathbf{k}_\omega + \mathbf{k}_g) - \mathbf{k}_{3\omega}| = 0 \quad (3.9)$$

If we consider an emission with an angle θ relative to the optical axis, and neglect the index-mismatch, we have in projection along the z axis:

$$|3(k_\omega + k_g) - \cos(\theta)k_{3\omega}| = 0 \quad (3.10)$$

which means we have:

$$\cos(\theta) = 1 + \frac{3k_g}{k_{3\omega}} \quad (3.11)$$

In the conditions of the simulation² ($n_\omega = n_{3\omega} = 1.33$, $NA = 1.2$) this equation yields $\theta \approx 34^\circ$, which is close to the maximum value of the emission pattern.

3.1.3.2 Slabs with Different Orientations

The geometry considered here is fairly similar to the one described in the previous paragraph, except that instead of having $d_x = d_y$, we now consider that the extension along the y axis is infinite and only consider the influence of d_x and d_z . This geometry has two limiting cases that are illustrated in figure (3.9) and correspond to x and z -oriented slabs.

Figure (3.10) illustrates the F-THG signal as a function of the lateral and axial extensions of the slabs. What we observe is similar to the case of the cuboid, except that the emission diagrams differ significantly, with an emission along two lobes in the case of a slab along the z axis instead of along a ring for the cuboid. Indeed, since we now have an heterogeneity only along one direction, the phase-matching conditions have to be satisfied in the other lateral direction. The emission angle is calculated by solving exactly the same equation.

Moreover, a very important difference exists between the amount of third harmonic signal produced by laterally oriented slabs and axially oriented slabs: for “small” slabs (a few hundreds of nanometers) an axially oriented slab will yield way more signal than a laterally oriented one.

² k_g is estimated directly from $E(0, z)$

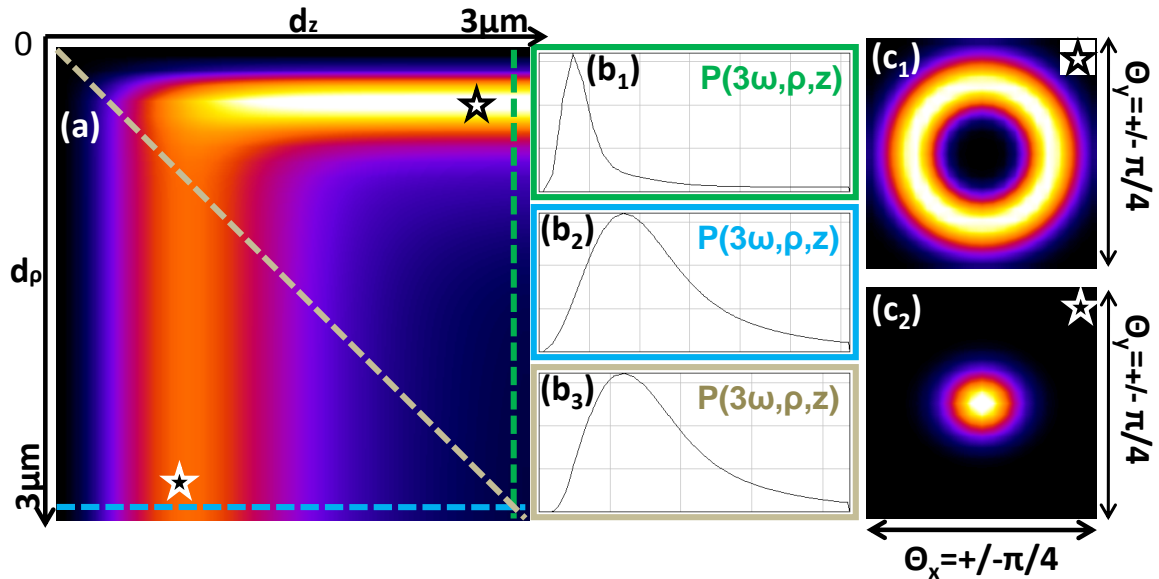


Figure 3.8: ANISOTROPY IN THG MICROSCOPY:

(a) THG signal as a function of the length and widths of a cuboid oriented along the optical axis and centered at the focal point. (b) Intensity profiles taken along the 3 different directions marked in (a) with dotted lines. (c) Emission diagrams in the two limiting cases $d_\rho \gg dz$ and $dz \gg d_\rho$ (when both d_ρ and d_z are large, there is no THG). Conditions: $NA = 1.2$, $n = 1.33$, $\lambda = 1.2\mu\text{m}$.

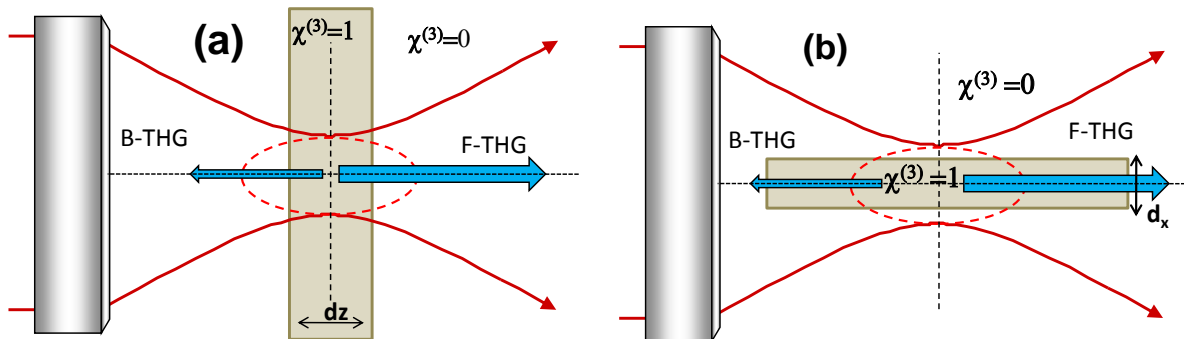


Figure 3.9: GEOMETRY CONSIDERED IN SECTION 3.1.3.2

The laser beam is focused in the middle of a slab. (a): xy -oriented slab, and (b) xz -oriented slab.

Since we have small structures, this signal is not dominated by the phase-matching conditions (though the angle of emission is) but by the intensity distribution of the field that is much higher along the optical axis.

An illustration of this type of anisotropy in THG images is shown on figure (3.11.b), where the yolk of the zebrafish embryo is shown either in the xy image (figure 3.11.a.1) or in the xz re-projection (figure 3.11.a.2). The yolk is made of large globules filled with proteins and lipids called yolk granule that are separated by an aqueous medium, so we expect THG signal to originate from these aqueous slabs that all have approximately the same thickness but different orientations. While in the first xy image a beehive structure is visible, in the xz re-projection only the vertical signal corresponding to vertically extended structures subsists, and the signal corresponding to the horizontally extended structures disappears. The ratio between vertical

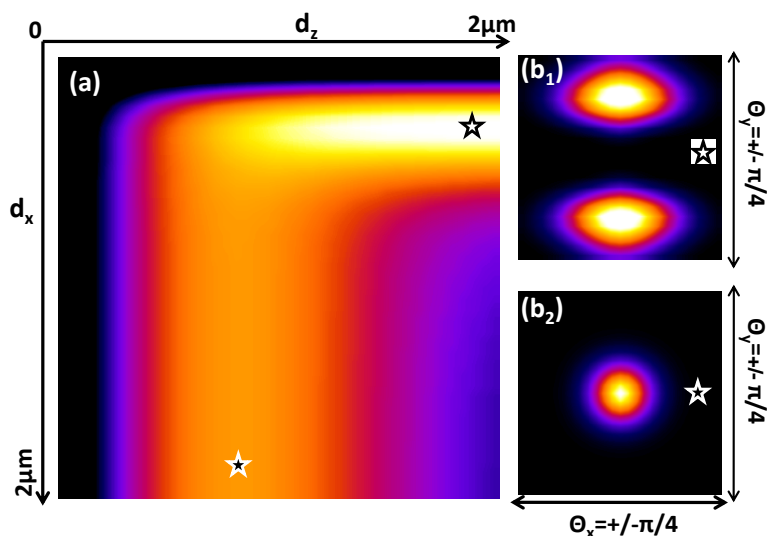


Figure 3.10: ANISOTROPY: SLABS WITH DIFFERENT ORIENTATIONS

(a) THG signal as a function of the axial and lateral extension of slabs centered at the focal point. (b) Emission diagrams in the two limiting cases $d_x \gg d_z$ (b1) and $d_z \gg d_x$ (b2). Conditions: $NA = 1.2$, $n_\omega = n_{3\omega} = 1.33$, $\lambda = 1.2\mu\text{m}$.

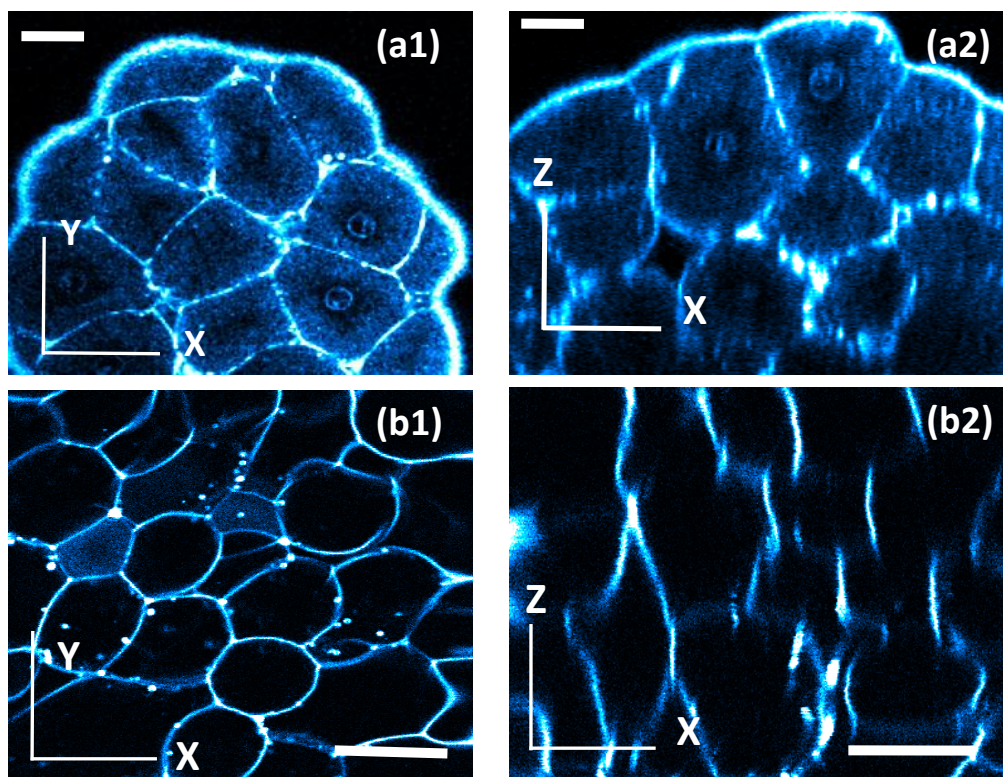


Figure 3.11: ANISOTROPY IN THG MICROSCOPY: EXAMPLE OF THE ZEBRAFISH

(a1): xy THG image of the cells of the zebrafish embryo. (a2): xz reprojection. (b1): xy THG Image of the yolk of the zebrafish embryo and (b2): xz reprojection. Conditions: $NA = 0.7$, $\lambda = 1.2\mu\text{m}$, scale bar $25\mu\text{m}$.

and horizontal slabs measured in the images is $r = 10$, which is consistent with structures approximately 300nm large. In the case of larger slabs, however, the signal obtained from both orientation is comparable, as illustrated if figure (3.11.a) where the boundary between

cells are visible in both the xy image (a1) and the xz -reprojection (a2) with the same imaging conditions.

3.1.3.3 Interfaces

The third geometry we consider is an interface between a medium with a nonlinear susceptibility $\chi^{(3)}$ and another medium with the same linear index of refraction, but with a nonlinear susceptibility equal to zero. Figure (3.12.d) illustrates the different geometries used in this paragraph: we consider interfaces along all three axis, and calculate the THG signal as a function of the angle with the third axis.

In the case of an interface along the optical axis (figure (3.12.a)), we find, consistently with the results obtained by Cheng *et al* [1] in the case of spheres, that there is a weak though not negligible orientation dependence ($\approx 20\%$). This is related to the anisotropy in the focusing of a linearly polarized beam (the factor $\cos(2\phi)$ in equation 3.1). Similarly to the case of axially oriented slabs, the emission is along two lobes that are perpendicular to the interface, for the same phase-matching reasons.

If we now consider the case of an interface along the xz or yz axis (figure (3.12b & c)), we find a lower contrast than Cheng *et al* [1], which can be explained by the difference in numerical aperture and linear dispersion considered. The emission diagrams evolve from a single peaked emission in the case of an interface perpendicular to the optical axis, to the aforementioned symmetric double peaked emission in the case of an interface parallel to the optical axis, with intermediate positions showing an asymmetric double peaked emission.

We confirmed this orientation dependence experimentally by imaging one of the top corners of a glass coverslip (figure (3.13.a)). In this geometry, we have access to the signal from three glass/water interfaces that are each perpendicular to one of the axes. While the signal obtained from the vertical interfaces and the horizontal one can hardly be compared because of the presence of aberrations caused by the focusing on an interface, the aberrations in the case of the two vertical interfaces are comparable, so we have measured the intensity of the THG at each interface as a function of the polarization of the excitation beam. The results of this experiment are illustrated in figure (3.13.b), and both the period and the amplitude of the oscillations are consistent with the theoretical prediction plotted on the same graph.

3.1.4 Influence of the Numerical Aperture

The influence of the focusing condition on the THG signal of isotropic structures has already been studied by Débarre *et al.* [2, 3], so we will just illustrate that dependence in the case of spheres and slabs, and move on to the dependence of the anisotropy between structures of the same size but different orientations with the focusing conditions.

3.1.4.1 Beads

We consider one last time the THG signal as a function of the size of a centered sphere. In a nutshell, the more we defocus, the bigger the structures we can see: as illustrated by figure (3.14), the signal increases more slowly when the NA used is smaller because the intensity of the focused beam is not as large, but as the coherence length is larger, there is a gain up to

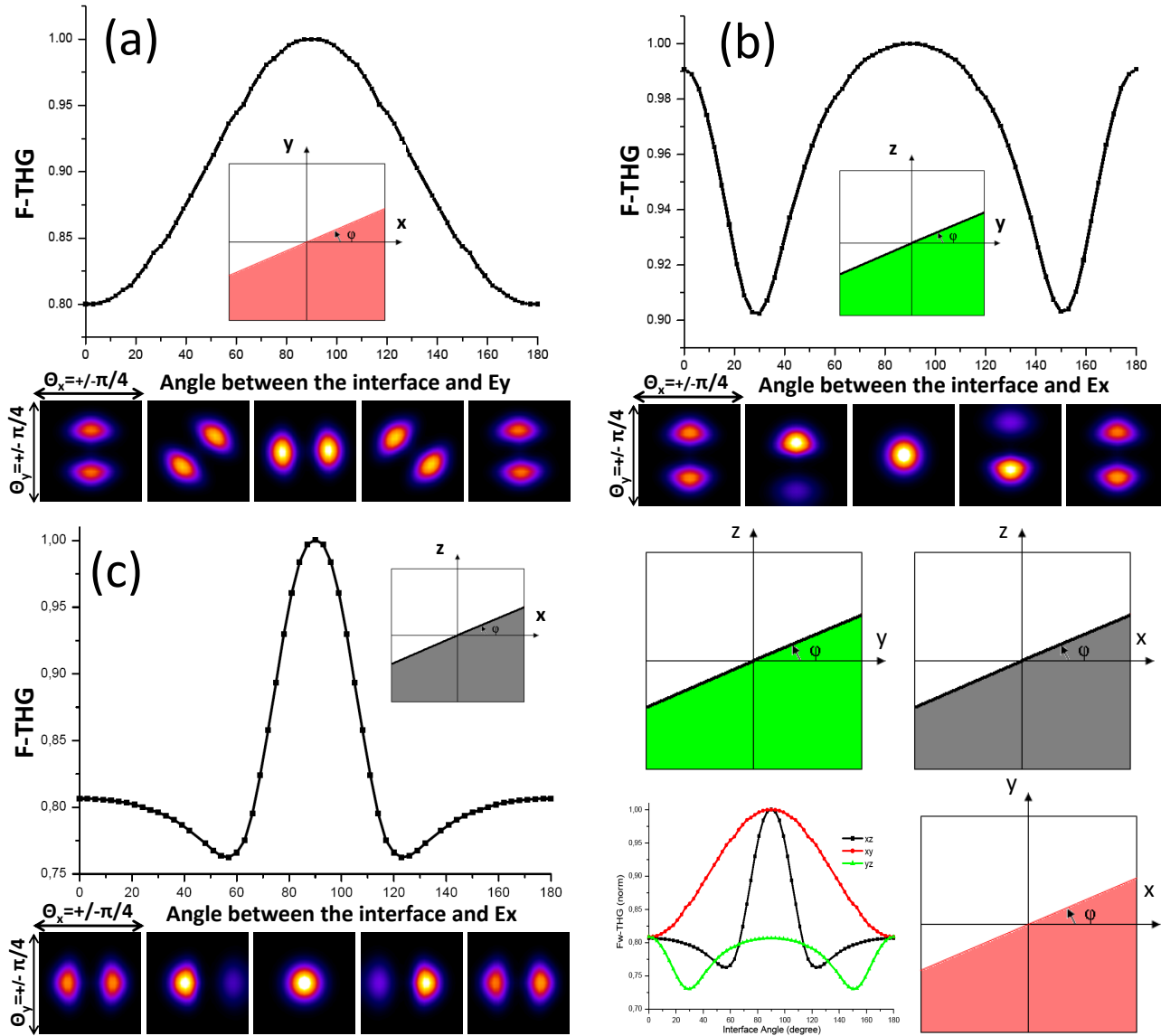


Figure 3.12: THG AS A FUNCTION OF THE INTERFACE ORIENTATION

(a): THG signal obtained from an interface between two semi-infinite domains divided along the z axis as a function of the angle θ relative to the x axis. Underneath the curve are the far-field harmonic field distribution for various interface angles. (b) and (c): Same geometry except with the x (resp y) axis and an angle relative to the y (resp x) axis. (d): Geometries considered, and comparison between the different orientations on the same scale.

a larger diameter threshold.

Figure (3.14) also illustrates the difference in the images obtained with two different focusing conditions on a zebrafish embryo. In this particular example, what is remarkable is that although the resolution is increased by using a higher numerical aperture, the contrast is reduced as all the structures give more or less the same amount of signal. In the lower resolution image, we see the interface between cells much more clearly than the rest, which allows these structures to be detected by automated segmentation algorithms as we will see in chapter 5.

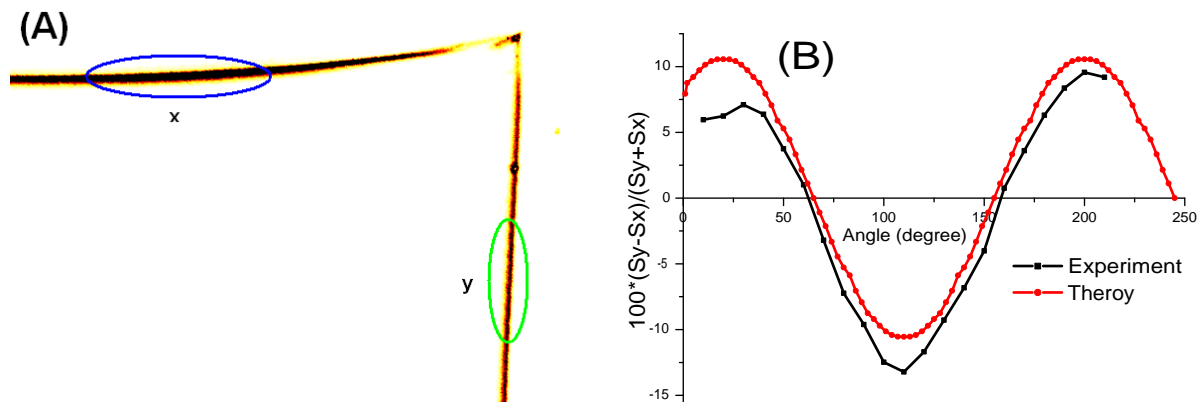


Figure 3.13: THG AS A FUNCTION OF THE POLARIZATION DIRECTION.

(A) THG image of a coverslip, where both xz and yz glass/water interfaces are visible. (B) Ratio between the signal obtained from the xz -oriented interface and the signal from the yz -oriented interface as a function of the direction of the excitation polarization.

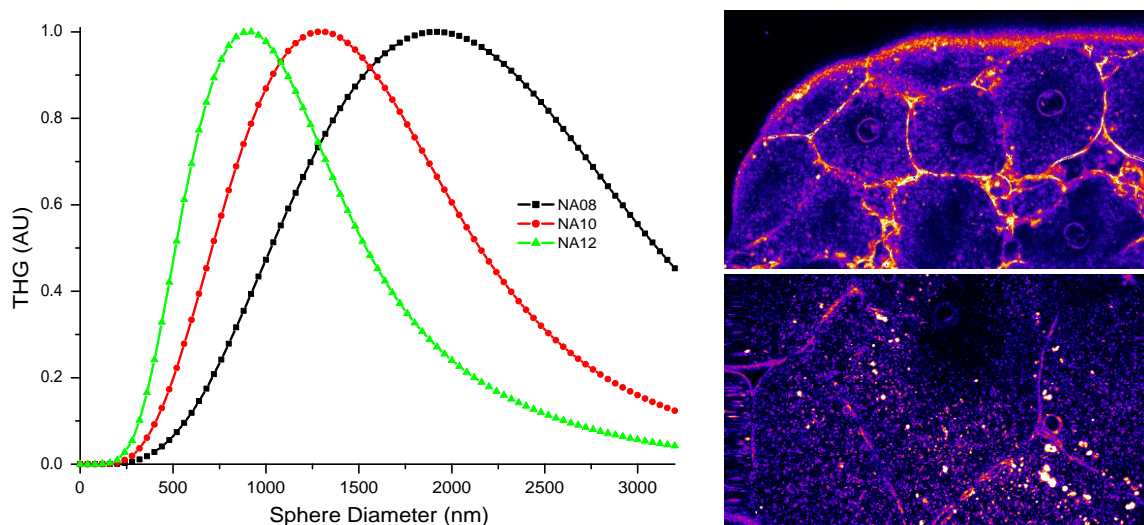


Figure 3.14: THG SIGNAL FROM A CENTERED SPHERE AS A FUNCTION OF THE NUMERICAL APERTURE

(Left) Ratio between the signal obtained from a centered sphere, with three different focusing conditions. (Right) THG images of a zebrafish embryo at the cleavage stage. (Top) $NA = 0.7$ (Bottom) $NA = 1.2$. Zebrafish Embryo provided by N. Peyrieras. (more details in chapter 5.)

3.1.4.2 Slabs

If we consider the same geometry as in section 3.1.2.1, but change the numerical aperture, we see a completely different behavior between forward THG and backward THG, as illustrated by figure (3.15). Indeed, we can see that in the case of backward emission, the size dependence curves are almost the same for all the focusing conditions (when the curves are normalized with regard to the maximum signal). This is due to the fact that the phase-matching conditions are heavily dominated by the direction phase-mismatch between a forward propagating beam (the excitation) and a backward propagating one (the harmonic field), which can be easily

calculated, assuming that the index-mismatch is negligible (ie: $n_\omega \approx n_{3\omega}$) as:

$$l = \frac{\pi}{3k_\omega + k_{3\omega}} \approx \frac{\pi}{6 \cdot k_\omega} \approx \frac{\lambda}{12n_\omega} \quad (3.12)$$

for the parameters used in the simulation ($\lambda = 1.2\mu\text{m}, n_\omega = 1.5$) we find $l = 67\text{nm}$, which is in good agreement with the simulation where the maximum value is reached for a width of $\approx 70 - 75\text{nm}$. If we wanted to be more accurate, we should take into account the Gouy phase-shift, which can be approximated accurately as a linear phase-shift whose slope depends on the numerical aperture.

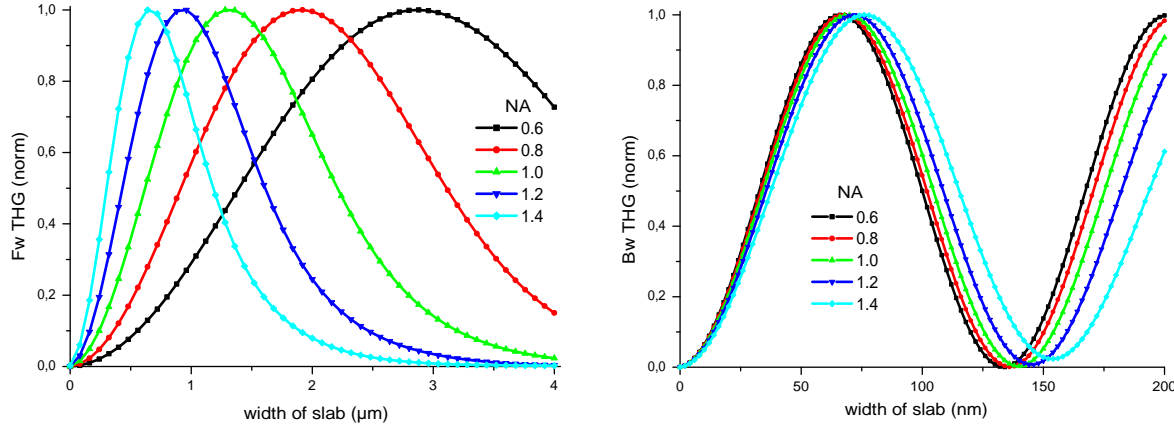


Figure 3.15: INFLUENCE OF THE NUMERICAL APERTURE IN THG MICROSCOPY:

(Left) F-THG signal as a function of the width of a centered slab for four different NAs, and (Right) B-THG signal as a function of the width of a centered slab for four different NAs

In the case of forward emission, the size dependence is heavily influenced by the value of the numerical aperture, with a maximum signal shifted from a size of less than $1\mu\text{m}$ at a numerical aperture of 1.2, to more than $2\mu\text{m}$ at a numerical aperture of 0.8. The reason for this is that the phase-mismatch in this direction is strongly dominated by the presence of the Gouy phase-shift:

$$l_{fw} = \frac{\pi}{\Delta k} = \frac{\pi}{3(k_\omega + k_g) - k_{3\omega}} \approx \frac{\pi}{3k_g} \quad (3.13)$$

If we consider a paraxial Gaussian excitation, the phase-shift can be written as $\arctan(z/b)$, which means if we consider that it is linear between $z = -b$ and $z = +b$, we have a phase-shift of:

$$k_g \approx \frac{\pi}{4b} \quad (3.14)$$

and the coherence length can now be approximated as:

$$l_{fw} \approx \frac{4b}{3} \quad (3.15)$$

If we use the geometrical relation between the numerical aperture and the waist at the focus defined in equation (2.8), we have:

$$b \propto \frac{1}{NA^2} \quad (3.16)$$

so finally, we have:

$$l_{fw} \propto \frac{1}{NA^2} \quad (3.17)$$

This result is consistent with the coherence lengths calculated in figure (3.15): for example the ratio between the size of the structures that yield a maximum signal for the numerical apertures of 0.8 and 1.2 is equal to $\approx 2/0.9 \approx 2.2$, while the ratio between the squared numerical apertures is equal to 2.25.

3.1.4.3 Anisotropy Due to the Orientation

We have seen that the axial phase matching is the dominant factor of THG signal creation, and that the lateral and axial extensions of an object do not play the same role for the visibility of an object, which means the THG signal is orientation dependent. The purpose of this paragraph is to characterize how the focusing conditions modify this anisotropy through the study of slabs with different orientations.

3.1.4.4 Slabs

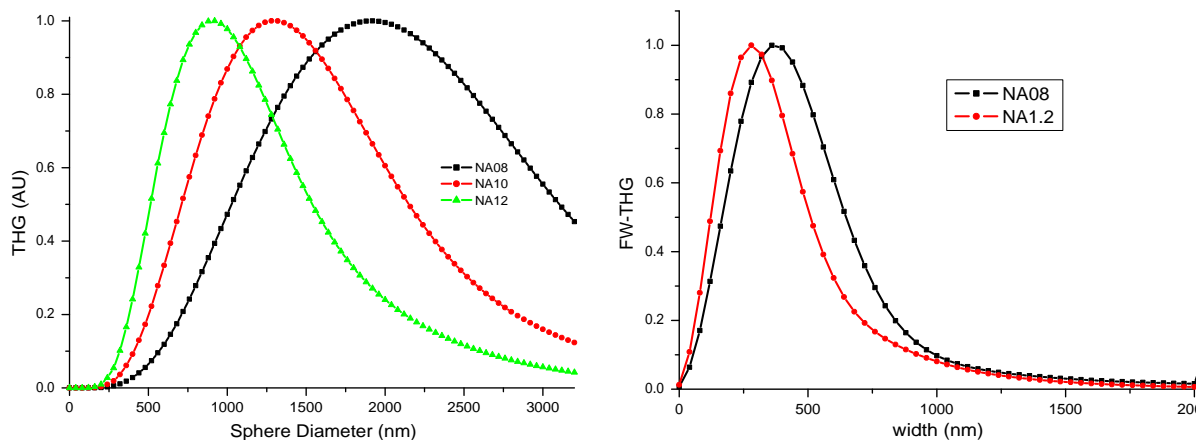


Figure 3.16: INFLUENCE OF THE NUMERICAL APERTURE IN THG MICROSCOPY:

(Left) F-THG signal as a function of the width of a centered xy oriented slab, and
(Right) F-THG signal as a function of the width of a centered xz oriented slab.

The geometry we consider here is the same as in section 3.1.3.2: a centered slab with a non-linear susceptibility $\chi^{(3)}$ oriented either along the x , y or z axes as illustrated by figure (3.16). We calculated the THG signal as a function of both the orientation and the size of the slabs, and the results are presented in figure (3.16).

As expected, the THG signal as a function of the width of an xy -oriented slab varies pretty much like in the case of a centered sphere (see section 3.1.4.1), for mostly the same reason (Gouy phase-shift). In the case of an xz oriented slab, though, the focusing conditions are not as important and the size dependence is only slightly shifted toward larger structures. This means that the ratio between the signal for structures of a given size as a function of their orientation relative to the optical axis changes with the focusing conditions: the tighter the focusing conditions, the more isotropic the signal gets, as illustrated by figure (3.17) which

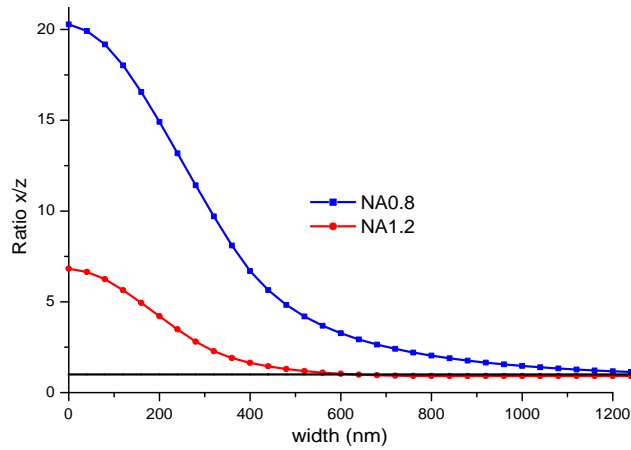


Figure 3.17: ANISOTROPY FACTOR FOR 2 DIFFERENT NUMERICAL APERTURE Ratio between the signal obtained from an xz -oriented slab and an xy -oriented one, for two different focusing conditions.

compares the anisotropy ratio for numerical apertures of 0.8 and 1.2.

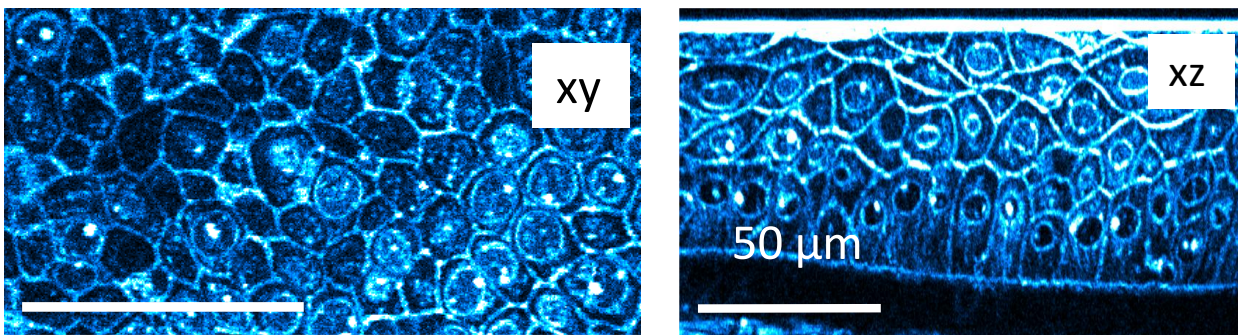


Figure 3.18: EXAMPLE OF ISOTROPIC THG IMAGING (Left) xy THG Image of the epithelium of the human cornea and (Right) xz reprojection. Conditions: $NA = 1.2$, $\lambda = 1.2\mu m$. (More details in chapter 5.)

The anisotropy factor is very important for small structures (This can be seen on figure (3.17) in the case of a numerical aperture of 0.7), but when we reach a given size the signal becomes isotropic, and this threshold is reached for much smaller sizes for $NA=1.2$ ($\approx 500nm$) than for $NA=0.8$ ($\approx 1.2\mu m$). When we are below that threshold, structures are equally visible in both orientations (although we can still see the resolution difference), as illustrated by figure (3.18) in the case of the epithelium of the cornea, while when we are above this threshold, the xz reprojection only shows the axially oriented structures, as illustrated by the zebrafish yolk also in figure (3.11).

3.2 Quasi-Phase-Matching

The THG signal depends on the interplay between the field structure and the sample structure. **Quasi-phase-matching** (QPM) is an idea developed in nonlinear optics (NLO) where the conversion efficiency is an important parameter, and stems from the consideration that

it is sometimes easier to change the structure of the sample (nonlinear crystal in NLO) than to change the structure of the excitation (usually focused Gaussian beams). It is usually implemented in a non-centrosymmetric medium by having a periodic arrangement of alternative perpendicular orientations, with a period corresponding to the coherence length of the nonlinear process. That way, the interferences are always constructive and the signal always increases.

Quasi phase matching has been demonstrated for simple nonlinear processes [8–10] as well as for more complex processes such as THG by cascaded SHG/SFG³ [11].

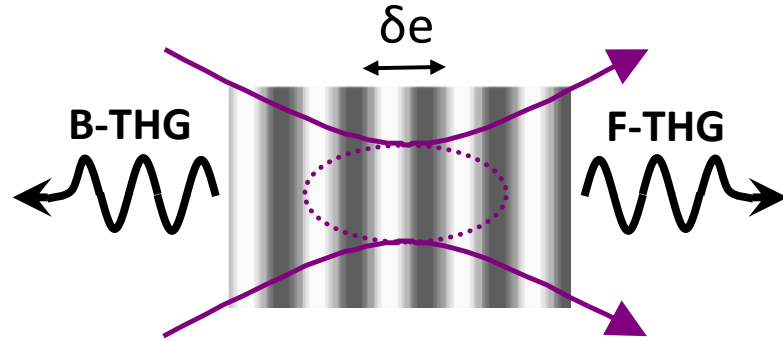


Figure 3.19: QUASI-PHASE MATCHING GEOMETRY
The medium exhibits a sinusoidal variation of its $\chi^{(3)}$ along the optical axis.

In our case, we will not consider the usual arrangement, as it implies variations of the linear indices (and usually of birefringence), but we will consider instead the periodic oscillation of the nonlinear properties of the medium. Figure (3.19) illustrates our quasi phase matching geometry: it consists of a medium that exhibits a sinusoidal variation of $\chi^{(3)}$ from 0 to 1 with a period δe , while keeping a constant linear index.

$$\chi^{(3)}(z) = \frac{1}{2} \left(1 + \sin\left(\frac{2\pi z}{\delta e}\right) \right) \quad (3.18)$$

The F-THG and B-THG from a focused Gaussian beam on this geometry as a function of the period δe are shown in figure (3.20). The THG intensity is normalized by the F-THG signal obtained from an interface perpendicular to the optical axis, so that all geometries have the same number of emitters in the focal volume. This allows a direct comparison of the THG signal that is only due to the quasi-phase-matching conditions. In both cases, we notice a large enhancement of the harmonic signal for a particular resonance frequency. The backward QPM period is much smaller, and much narrower than the F-THG QPM period. This is due to the much larger phase-mismatch in that direction, as previously discussed. The theoretical value for the resonance QPM period can be expressed as :

$$\delta e = 2.l_c \quad (3.19)$$

It can be noted that the B-THG resonant period corresponds closely to the theoretical value ($l_{bw} \approx 70nm$, as seen in section 3.1.2.1, and the maximum B-THG is obtained for $\delta e \approx 150nm$), as the phase and intensity distribution can be approximated as constant at this scale. Moreover, the backward resonance is a useful tool, since it can be used to characterize the organization of

³SFG=Sum-Frequency Generation.

a material much below the resolution limit.

Unfortunately, the coherence length is so dominated by the phase-mismatch induced by the wave-vector directions that it is hard to change this resonance frequency by changing the focusing conditions unless we use focus engineering techniques to greatly modify the shape of field in the focal volume, as we will see in chapter 4.

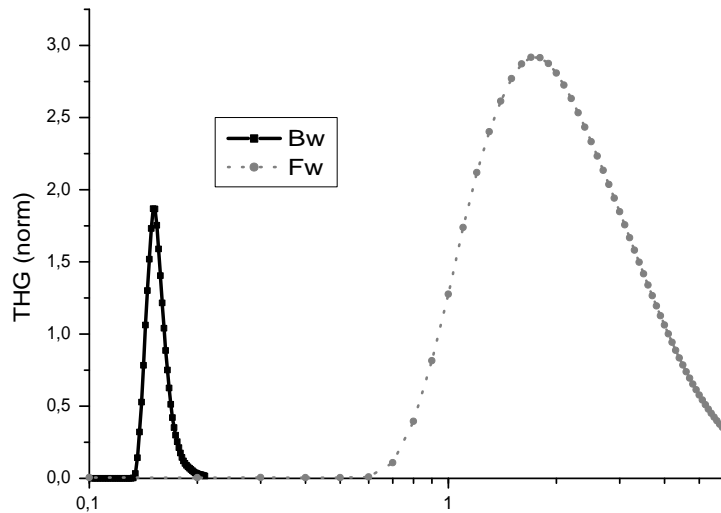


Figure 3.20: QUASI-PHASE MATCHED THG

F-THG and B-THG as a function of the axial period δe of the sample (expressed in μm) as described in figure (3.19). Conditions: $\lambda = 1.2\mu m$, $NA=1.2$, $n=1.5$. Adapted from

The F-THG QPM period yields an increase in intensity by a factor 3 compared to the interface, and there is a very broad range of periods that can provide a significant amount of THG. However, since the intensity and phase distribution of the excitation vary a lot on the scale of these periods, the gain in harmonic signal is not as large as what we have in the backward direction.

3.3 THG in Crystals & Quasi-Crystals

3.3.1 Introduction

In this last section, we consider structures (crystals, or more often in biological samples quasi-crystals) that present different forms of anisotropy. This anisotropy can have different forms:

1. It can be a linear anisotropy, in which case the linear index of refraction depends on the polarization of the field.
2. It can be a nonlinear anisotropy, in which case the nonlinear index of refraction (which is already polarization-dependent but possesses a large number of symmetries) loses some of its symmetries and so the induced nonlinear polarization becomes more sensitive to the polarization of the excitation.

However, most materials combine both types of anisotropy. For example, figure (3.21) illustrates THG microscopy with circularly polarized excitation of the zebrafish otolith, which is made of calcite (Oron *et al.* [12] have already demonstrated THG imaging of calcite when using circularly polarized excitation, and presented an application to the specific imaging of the sea urchin spicule, using the absence of signal from isotropic media).

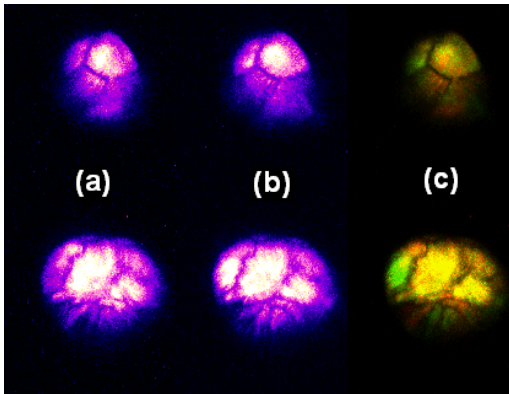


Figure 3.21: THG IMAGE OF THE ZEBRAFISH OTOLITHS

The excitation is circularly polarized, and the detection is polarization-resolved. (a) x -polarized harmonic signal (b) y -polarized harmonic signal (c) ratio P_x/P_y .

In order to understand these images, we will dissociate the different types of anisotropy. Therefore, we will discuss in a first section the effect of birefringence, before considering the effects of $\chi^{(3)}$ anisotropies in section 3.3.5.

3.3.2 Influence of the Dispersion

Figure (3.22) illustrates the influence of linear dispersion in the case of slabs oriented along the z -axis. We notice that for all the dispersions considered we have a bell-shaped THG response, with a coherent increase followed by the apparition of destructive interferences that decrease the signal. Yet, in the case of negative dispersion, the dispersion partly compensates the effect of the Gouy phase-shift, and the destructive interference is not complete.

We also notice that for THG to occur in a homogeneous medium, it needs to have a large negative dispersion. Moreover, if we look closely at the case where we have a very large positive dispersion, we see the apparition of damped oscillations similar to those observed in the backward direction. This means complete destructive interference happens before the confinement due to the variation in the intensity occurs.

However, negative dispersion in an isotropic non-absorbing medium is not possible, so the presence of an organized structure is necessary for phase-matching THG, as we will see in the next section.

3.3.3 Dispersion Compensation Using Birefringence

Birefringent media have the property that their indices of refraction depends on the polarization of the light. When the material has a single axis of symmetry, the birefringence can

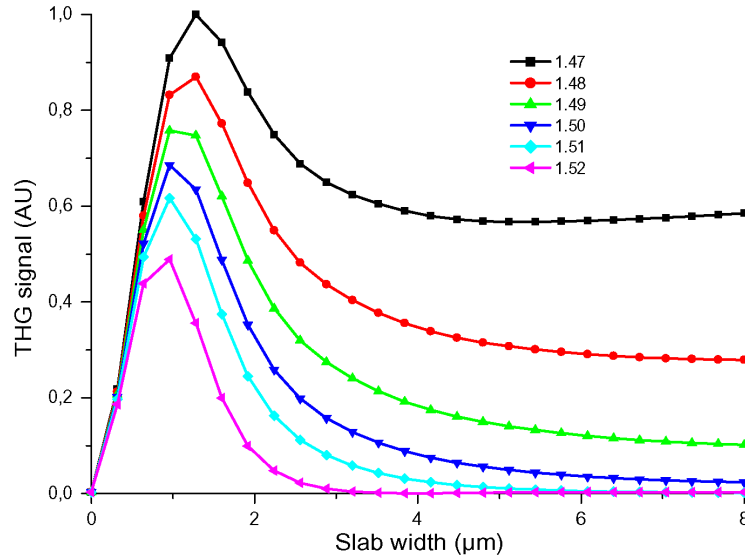


Figure 3.22: INFLUENCE OF DISPERSION ON THG SIGNAL FROM SLABS
 F-THG as a function of the amount of dispersion in the sample. Conditions: $n_{3\omega} = 1.5$, $1.47 < n_{\omega} < 1.53$, $NA = 1.2$.

be formalized by assigning two different refractive indices to the material for different polarizations: one along the ordinary axis (perpendicular to the axis of symmetry) and another along the extraordinary axis (parallel to the axis of symmetry).

Third harmonic generation in highly birefringent structures such as calcite crystals (calcium carbonate ($CaCO_3$)) or liquid crystals [13] has been described by Oron *et al.* [12, 14]. Calcite is one of the most birefringent structures we can find in biological samples, and has been used in nonlinear optics for a long time for this reason. At a wavelength of 590 nm calcite has ordinary and extraordinary refractive indices of 1.658 and 1.486 respectively.

Since we have tensor elements that create a nonlinear field polarized perpendicularly to the excitation, we can have an excitation that propagates along the ordinary axis, while the harmonic field propagates along the extraordinary axis, thus producing an effective negative dispersion for the harmonic generation process.

Numerical simulations of THG in a slab of calcite-like medium considering an incoming beam polarized along the ordinary axis are illustrated in figure (3.23). We neglect the wavelength dependence of the medium (zero dispersion), so the linear indices are $n_o = 1.66$ and $n_e = 1.49$. In a first simulation (red curve), we consider only the tensor elements that produce an harmonic field along the ordinary axis. The size response in this case is the typical single peaked curve that reaches its maximum for a size approximately equal to the coherence length, and then decreases until it reaches zero. If we now take into account the tensor elements that induce a nonlinear polarization along the extraordinary axis however (black curve) the negative dispersion compensates the Gouy phase-shift and the THG signal increases until it reaches a plateau.

We have seen how quasi-phase-matching can be obtained with birefringence. We will now move on to the properties of the $\chi^{(3)}$ tensor of anisotropic media.

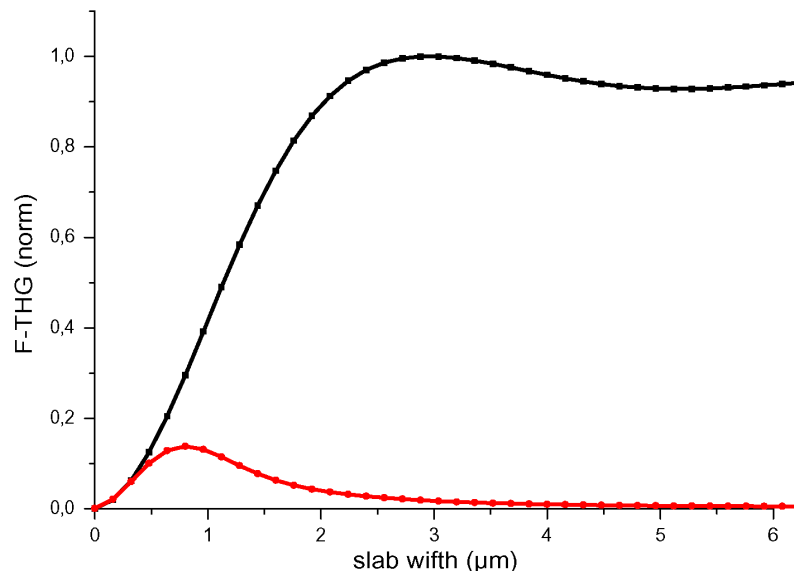


Figure 3.23: THG IN CALCITE

Comparison between THG from a calcite-like medium considering either only tensor elements in the ordinary-ordinary axis (red) or also taking into account the ordinary-extraordinary elements (black) Conditions: $NA = 1.2$, $n_o = 1.66$, $n_e = 1.49$.

3.3.4 Symmetries & Anti-symmetries

In a medium characterized by its third-order nonlinear tensor $\chi_{ijkl}^{(3)}(\mathbf{r})$, we remind that the excitation field induces a polarization density described by:

$$P_i^{(3\omega)} = \sum_{j,k,l} \chi_{ijkl}^{(3)} E_j E_k E_l \quad (3.20)$$

For an homogeneous isotropic medium, we can then express the nonlinear polarization induced by the exciting field \mathbf{E} in Cartesian coordinates as:

$$\mathbf{P}^{(3\omega)} = 3\chi_0 \begin{bmatrix} E_x(E_x^2 + E_y^2 + E_z^2) \\ E_y(E_x^2 + E_y^2 + E_z^2) \\ E_z(E_x^2 + E_y^2 + E_z^2) \end{bmatrix} \quad (3.21)$$

Several things can be noticed from this equation:

1. Although THG is a third order process, P_y and P_z depend both linearly and nonlinearly on E_y & E_z . This means we have to be very careful before deciding to neglect the vectorial components of the exciting field. Of particular importance is the spatial overlap between the different polarizations. For example if we consider a Gaussian beam, as illustrated by figure (3.24), the E_y and E_z components of the electric field have their maxima away from the optical axis, and so their overlap with E_x is small. This is one of the reasons why the paraxial scalar approximation works well for THG microscopy.
2. If we consider a circular polarization in the paraxial approximation, we have $E_x = iE_y$ so $P_x = P_y = 0$. This is the reason why no THG is obtained with circularly polarized light on isotropic samples, even at interfaces. Even if we take into account the vectorial component of the excitation, the focal field can be expressed as:

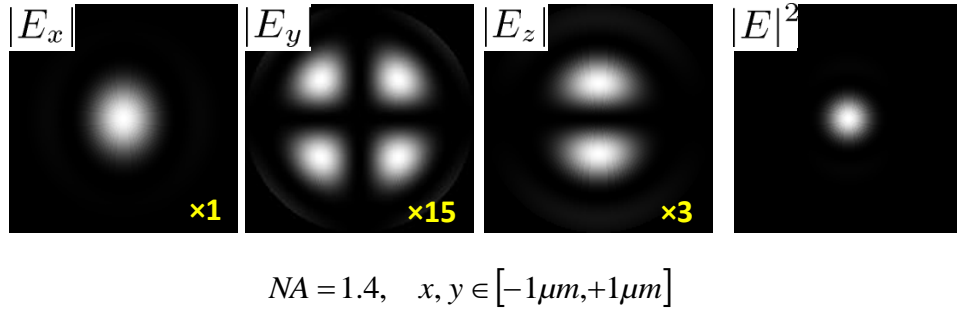


Figure 3.24: VECTORIAL ASPECTS OF THE FOCUSED GAUSSIAN BEAM
 Electric field at the focus of a Gaussian beam. Conditions: $NA=1.4$, $n=1.5$

$$\mathbf{E}(\rho, \phi, z) = E_1 \begin{bmatrix} I_{010} + I_{011} + (I_{210} - I_{211}) \cos(2\phi) + i(I_{210} - I_{211}) \sin(2\phi) \\ (I_{210} - I_{211}) \sin(2\phi) + i(I_{010} + I_{011} - (I_{210} - I_{211}) \cos(2\phi)) \\ 2iI_{120}(\sin \phi - \cos \phi) \end{bmatrix} \quad (3.22)$$

and the amount of THG signal expected from a circularly polarized beam focused on the an interface between two isotropic media is still negligible compared to what we expect from a linearly polarized beam.

The absence of signal using circularly polarized light comes from the tensor symmetries, which means that if we have a piecewise organized medium with different symmetries, we may still get some signal as we will see in the next section.

3.3.5 Tensorial Effects

In this section, we neglect refractive index dispersion and linear birefringence (*i.e.*: $n_\omega = n_{3\omega}$ everywhere). The nonlinear tensor, however, is not that of a homogeneous isotropic sample anymore.

3.3.5.1 Tensors & Nonlinear Polarizations

The form of the third order nonlinear susceptibility for various symmetries has been studied by Butcher [15], expanded by Hellwarth [16], and can be found in a number of references, including [4].

The form of the isotropic tensor has been given in equation (3.2). There are several symmetries we could consider, but the one we have chosen is that of a crystal with one main axis along the x -axis with a $C_{\infty v}$ symmetry, because it corresponds to the structure of the stroma of the cornea, that will be described in chapter 5. we have three independent tensor elements:

$$\begin{aligned} \chi_{\parallel} &= \chi_{xxxx} \\ \chi_{xxyy} &= \chi_{xyyx} = \chi_{xyxy} = \chi_{xxzz} = \chi_{xzzx} = \chi_{zzxx} \\ \chi_{yyzz} &= \chi_{yzyy} = \chi_{yzyz} = \chi_{zzyy} = \chi_{zyzy} = \chi_{zyyz} \\ &= \chi_{yyxx} = \chi_{yxyx} = \chi_{yxxz} = \chi_{zzxx} = \chi_{zxxz} = \chi_{zzzz} \\ \chi_{zzzz} &= \chi_{yyyy} = 3\chi_{yyzz} \end{aligned} \quad (3.23)$$

If we assume $\chi_{\parallel} = \chi_{xxxx}, \chi_{cr} = 3\chi_{xxyy}, \chi_{\perp} = 3\chi_{yyzz}$, we can then write the nonlinear polarization as:

$$\mathbf{P}^{(3\omega)} = \begin{bmatrix} E_x(\chi_{\parallel} \cdot E_x^2 + \chi_{cr} \cdot E_y^2 + \chi_{cr} \cdot E_z^2) \\ E_y(\chi_{cr} \cdot E_x^2 + \chi_{\perp} \cdot E_y^2 + \chi_{\perp} \cdot E_z^2) \\ E_z(\chi_{cr} \cdot E_x^2 + \chi_{\perp} \cdot E_y^2 + \chi_{\perp} \cdot E_z^2) \end{bmatrix} \quad (3.24)$$

We neglect the z component of the excitation⁴ to have more simple expressions, (although the numerical calculations are still performed using the complete vectorial model) and we now have:

$$\mathbf{P}^{(3\omega)} = \begin{bmatrix} E_x(\chi_{\parallel} E_x^2 + \chi_{cr} E_y^2) \\ E_y(\chi_{cr} E_x^2 + \chi_{\perp} E_y^2) \\ 0 \end{bmatrix} \quad (3.25)$$

The degenerate situation in which $\chi_{cr} = \chi_{\parallel} = \chi_{\perp}$, corresponds to the isotropic medium. We consider an elliptically polarized Gaussian beam, created by introducing a quarter wave-plate with an angle α relative to the x -axis. The field distribution at the focal plane can be written as:

$$E_x = \cos(\alpha) E_G \quad (3.26)$$

$$E_y = i \sin(\alpha) E_G \quad (3.27)$$

where E_G is defined as:

$$E_G = E_x(\rho, \phi, z) = I_{010} + I_{011} + (I_{210} - I_{211}) \cos(2\phi) \quad (3.28)$$

where I_{jkl} is defined in equation (2.22). If we take this expression and insert it into the nonlinear polarization, we find:

$$\mathbf{P}^{(3\omega)} = \begin{bmatrix} \cos(\alpha) E_G^3 (\chi_{\parallel} \cos(\alpha)^2 - \chi_{cr} \sin(\alpha)^2) \\ i \sin(\alpha) E_G^3 (\chi_{cr} \cos(\alpha)^2 + \chi_{\perp} \sin(\alpha)^2) \\ 0 \end{bmatrix} \quad (3.29)$$

We will consider two different geometries in the next sections: an interface between an anisotropic medium and air, and an interface between two media with perpendicular anisotropy.

3.3.5.2 Interface Between an Anisotropic Medium and Air

We denote $C_0(z)$ the THG signal obtained when the focus is z -scanned across the interface between an isotropic medium ($\chi^{(3)} = \chi_0$) and air ($\chi^{(3)} = 0$), where z the distance between the interface and the focal plane. This case has been investigated previously [1, 18, 19] and is illustrated in figure (3.25).

- **Linear Polarization**

We consider the case of an interface between air and the uni-axial crystal, in the case of a linearly polarized Gaussian excitation and an angle θ between the incident polarization and the axis of the crystal.

⁴this approximation is generally valid in practical situations, see references [1, 17]

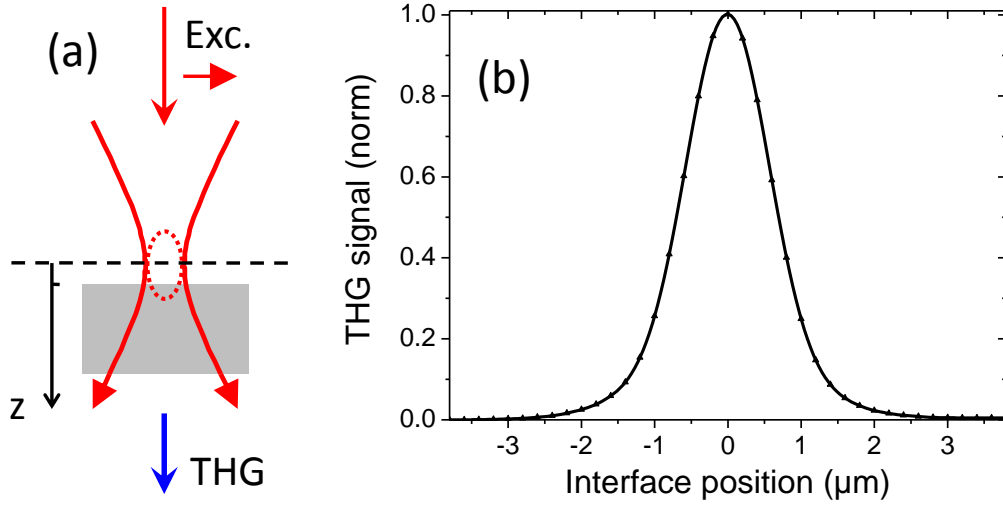


Figure 3.25: THG ON AN INTERFACE WITH LINEARLY POLARIZED LIGHT (a) Geometry considered, and (b) $C_0(z)$: numerical calculation of the THG signal obtained when the excitation beam is z -scanned across a xy interface between an isotropic medium and air. $NA = 1.2$, $\lambda = 1.18 \mu m$.

The nonlinear polarization in the anisotropic medium can be expressed as:

$$\mathbf{P}^{(3\omega)} = G_0^3 \begin{bmatrix} \cos(\theta)(\chi_{\parallel} \cdot \cos(\theta)^2 + \chi_{cr} \cdot \sin(\theta)^2) \\ \sin(\theta)(\chi_{cr} \cdot \cos(\theta)^2 + \chi_{\perp} \sin(\theta)^2) \\ 0 \end{bmatrix} \quad (3.30)$$

and the THG signal scales as:

$$I_{THG} \propto C_0(z) [\cos(\theta)^2(\chi_{\parallel} \cdot \cos(\theta)^2 + \chi_{cr} \cdot \sin(\theta)^2)^2 + \sin(\theta)^2(\chi_{cr} \cdot \cos(\theta)^2 + \chi_{\perp} \cdot \sin(\theta)^2)^2]$$

This means that the anisotropy in the tensor alone does not allow quasi-phase-matching: we still have no signal in a homogeneous anisotropic sample, and the signal from an interface is proportional to the signal expected from the interface between two isotropic media.

• Circular Polarization

In the case of a circularly polarized excitation, the nonlinear polarization in the anisotropic medium can then be written as:

$$\mathbf{P}^{(3\omega)} = \frac{1}{2\sqrt{2}} G_0^3 \begin{bmatrix} (\chi_{\parallel} - \chi_{cr}) \\ i \cdot (\chi_{cr} - \chi_{\perp}) \\ 0 \end{bmatrix} \quad (3.31)$$

and the THG signal scales as $C_0(z)((\chi_{\parallel} - \chi_{cr})^2 + (\chi_{cr} - \chi_{\perp})^2)$. Figure (3.26) illustrates the THG signal as a function of the value of χ_{\parallel} and χ_{cr} (assuming $\chi_{\perp} = 1$). The degenerate situation $\chi_{\parallel} = \chi_{cr} = \chi_{\perp}$ yields, as expected, no THG signal.

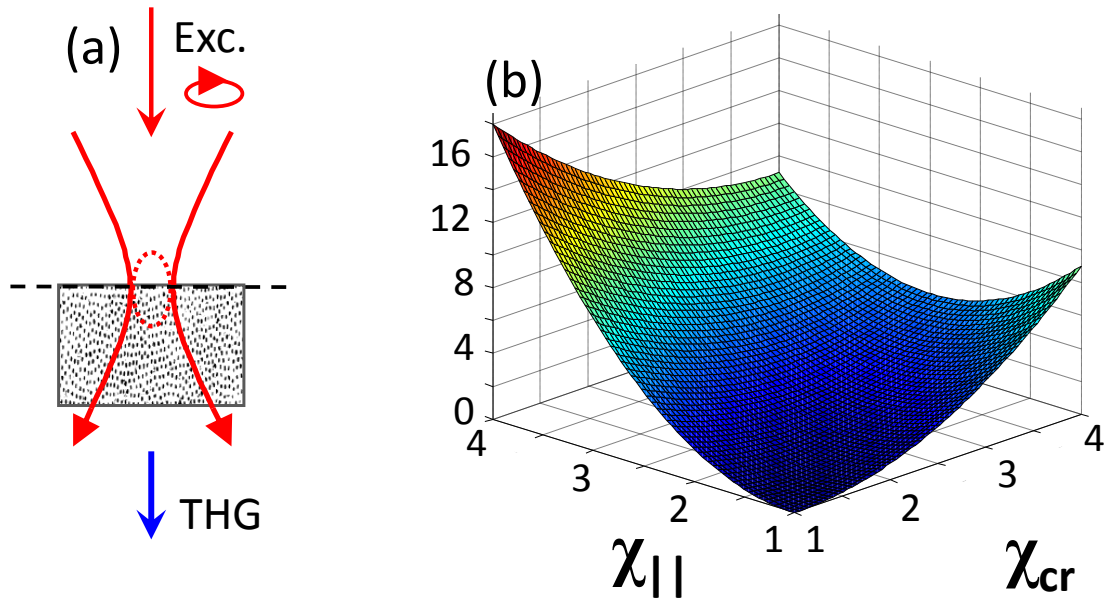


Figure 3.26: INFLUENCE OF THE TENSOR ELEMENTS

(a) Geometry considered and (b) THG signal obtained with circular incident polarization at the interface between an anisotropic medium and air, as a function of the parameters χ_{\parallel} and χ_{cr} with $\chi_{\perp} = 1$ (see text). No signal is obtained in the case of an isotropic medium ($\chi_{\parallel} = \chi_{cr} = \chi_{\perp} = 1$).

3.3.5.3 Interface Between Two Semi-infinite Slabs with Different Orientations

We now consider the case of circularly polarized light only. We assume that the first slab is oriented along the x axis and the second one along the y axis, so the nonlinear polarization $\mathbf{P}_+^{(3\omega)}$ and $\mathbf{P}_-^{(3\omega)}$ created in the successive media can be expressed as:

$$\mathbf{P}_+^{(3\omega)} = \frac{G_0^3}{2\sqrt{2}} \begin{bmatrix} (\chi_{\parallel} - \chi_{cr}) \\ i(\chi_{cr} - \chi_{\perp}) \\ 0 \end{bmatrix} \quad (3.32)$$

$$\mathbf{P}_-^{(3\omega)} = \frac{G_0^3}{2\sqrt{2}} \begin{bmatrix} (\chi_{\perp} - \chi_{cr}) \\ i(\chi_{cr} - \chi_{\parallel}) \\ 0 \end{bmatrix} \quad (3.33)$$

Since no THG is obtained from a homogeneous medium, we have an equivalent system by adding $(\chi_{cr} - \chi_{\perp})G_0^3$ (resp. $i(\chi_{\perp} - \chi_{cr})G_0^3$) to the x (resp. y) polarization terms in both layers; and we obtain:

$$\mathbf{P}_+^{(3\omega)} = \frac{G_0^3}{2\sqrt{2}} \begin{bmatrix} (\chi_{\parallel} - \chi_{\perp}) \\ 0 \\ 0 \end{bmatrix} \quad (3.34)$$

$$\mathbf{P}_-^{(3\omega)} = \frac{G_0^3}{2\sqrt{2}} \begin{bmatrix} 0 \\ i(\chi_{\perp} - \chi_{\parallel}) \\ 0 \end{bmatrix} \quad (3.35)$$

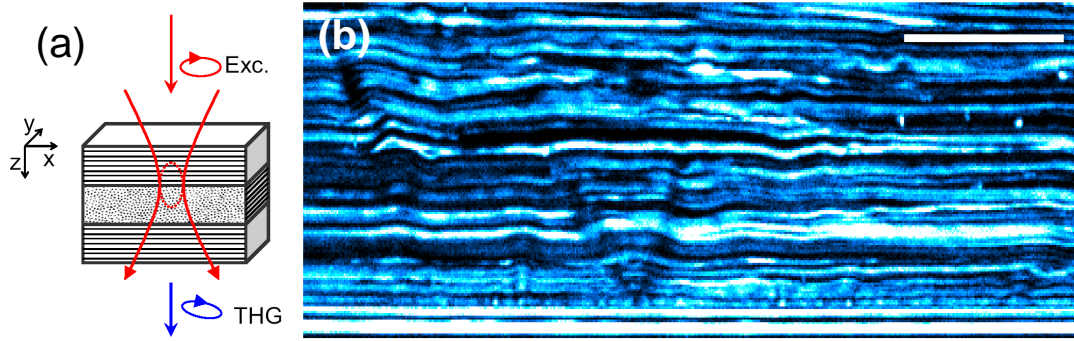


Figure 3.27: CIRCULARLY POLARIZED THG IMAGE OF THE CORNEAL STROMA
 (a) Structure of the model cornea (b) $x - z$ -reprojection of a stack of THG images of the corneal stroma Conditions: $NA=1.2$ $\lambda = 1.18$ scale bar = $20 \mu\text{m}$.

These expressions show that the case of the interface between orthogonal lamellae is similar to the case of an interface between air and an anisotropic medium, yielding a signal proportional to $C_0(z) \cdot (\chi_{\parallel} - \chi_{\perp})^2$ and circularly polarized⁵. The absence of χ_{cr} in this expression is not surprising, as it is a term that couples the x and y polarization components and has a similar influence on both axes.

An example of such a medium is the cornea in which alternate lamellae of collagen exhibit a preferential direction with orthogonal directions relative to their neighbors. Figure (3.27) shows a xz -reprojection of the THG signal obtained from the stroma of the cornea, and the interfaces between the different lamellae are clearly visible. The origin of the harmonic signals in the cornea are discussed in more details in section 5.1.3 of chapter 5.

⁵This assumes that the x polarized and y polarized nonlinear fields from the two slabs do not interfere

Conclusion

We have reviewed in this section the main contrast mechanisms of third harmonic generation microscopy. On isotropic media, the large phase-mismatch induced by the Gouy phase-shift means that there is no signal from a homogeneous medium, and that only structures from which destructive interference is incomplete are visible. Moreover, the shape and size of the structures that can be seen depend on the focusing conditions, and this aspect will be expanded in the next chapter.

We have considered several types of organized structures, and identified their quasi-phase-matching conditions: some allow THG from homogeneous media using birefringence, while some allow THG from circularly polarized light because of their nonlinear anisotropy.

We will now move on to non-Gaussian excitation in chapter 4.



Bibliography

- [1] J.-X. CHENG AND X.S. XIE. *Green's function formulation for third harmonic generation microscopy*. J. Opt. Soc. Am. B, 19(7):1604–1610 (2002).
- [2] D. DÉBARRE, W. SUPATTO, AND E. BEAUREPAIRE. *Structure sensitivity in third-harmonic generation microscopy*. Opt. Lett., 30(16):2134–2136 (2005).
- [3] D. DÉBARRE. *Thèse de doctorat*. Ecole Polytechnique, Palaiseau (2006).
- [4] R.W. BOYD. *Nonlinear optics, 2nd edition*. Academic Press (2003).
- [5] L. NOVOTNY AND B. HECHT. *Principles of Nano-Optics*. Cambridge Univ Press (2006).
- [6] J. F. WARD AND G. H. C. NEW. *Optical third harmonic generation in gases by a focused laser beam*. Phys. Rev., 185(1):57–72 (1969).
- [7] D. DÉBARRE, N. OLIVIER, AND E. BEAUREPAIRE. *Signal epidetection in third-harmonic generation microscopy of turbid media*. Opt. Express, 15(14):8913–8924 (2007).
- [8] E. J. LIM, M. M. FEJER, AND R. L. BYER. *Second-harmonic generation of green light in periodically poled planar lithium niobate waveguide*. Electronics Letters, 25(3):174–175 (1989).
- [9] M.M. FEJER, G.A. MAGEL, D.H. JUNDT, AND R.L. BYER. *Quasi-phase-matched second harmonic generation: tuning and tolerances*. Quantum Electronics, IEEE Journal of, 28(11):2631–2654 (1992).
- [10] L. E. MYERS, R. C. ECKARDT, M. M. FEJER, R. L. BYER, W. R. BOSENBERG, AND J. W. PIERCE. *Quasi-phase-matched optical parametric oscillators in bulk periodically poled linbo3*. J. Opt. Soc. Am. B, 12(11):2102–2116 (1995).
- [11] S. ZHU, Y-Y. ZHU, AND N-B. MING. *Quasi-Phase-Matched Third-Harmonic Generation in a Quasi-Periodic Optical Superlattice*. Science, 278(5339):843–846 (1997).
- [12] D. ORON, E TAL, AND Y. SILBERBERG. *Depth-resolved multiphoton polarization microscopy by third-harmonic generation microscopy*. Opt. Lett., 28(23):2315–2317 (2003).
- [13] D. YELIN, Y. SILBERBERG, Y. BARAD, AND J. S. PATEL. *Phase-matched third-harmonic generation in a nematic liquid crystal cell*. Phys. Rev. Lett., 82(15):3046–3049 (1999).
- [14] D. ORON, D. YELIN, E. TAL, S. RAZ, R. FACHIMA, AND Y. SILBERBERG. *Depth-resolved structural imaging by third-harmonic generation microscopy*. J. Struct. Biol., 147:3–11 (2004).
- [15] P. N. BUTCHER. *Nonlinear optical phenomena*. Ohio State University (1965).
- [16] R. HELLWARTH. *Third-order optical susceptibilities of liquids and solids*. Progress in Quantum Electronics, 5:1–68 (1979).
- [17] N. OLIVIER AND E. BEAUREPAIRE. *Third-harmonic generation microscopy with focus-engineered beams: a numerical study*. Opt. Express, 16(19):14703–14715 (2008).

- [18] T. TSANG. *Third- and fifth-harmonic generation at the interfaces of glass and liquids.* Phys. Rev. A, 54(6):5454–5457 (1996).
- [19] Y. BARAD, H. EISENBERG, M. HOROWITZ, AND Y. SILBERBERG. *Nonlinear scanning laser microscopy by third harmonic generation.* Appl. Phys. Lett., 70:922–924 (1997).

Acknowledgements IV

The room in which the nonlinear microscope dwells is a dark and dreary place: no (visible) light is allowed because of the sensitive photon-counting detectors, the laser requires air conditioning colder than in an American shopping mall and implies the presence of noisy fans, and one is surrounded by the gloom created by the ghosts of dead drosophila & zebrafish embryos. Fortunately, there are two ways to remain sane in this environment: company (see previous Acknowledgements) & music.

I therefore wish to express my gratitude to the following musicians & bands (in no particular order):

Opeth, Leonard Cohen, Enslaved, Bob Dylan, Johnny Cash, The Ocean, Wolves in the Throne Room, Celeste, Cult of Luna, Breach, Candlemass, The Beatles, Katatonia, Watain, Vital remains, Kyuss, Samothrace, Simon & Garfunkel, Shining, Sigur Ros, Cobalt, In Flames, Queen of the Stone Age, Pink Floyd, Mogwai, Metallica, Slayer, Mouth of the Architect, Pelican, Red Sparrows, Arcade Fire, Gerard Manset, Gogira, Mono, Neil Young, Agalloch, System of a Down, Taint, Capricorns, My Dying Bride, Nachtmystium, Dimmu Borgir, Cradle of Filth, Baroness, Burst, Krallice, Amen Ra, Mastodon, Primordial, Amon Amarth, Septic Flesh, Vader, Kylesa, Year of no Light, Dirge, Nirvana, 5ive, Iron Maiden, Pearl Jam, Alice in Chains, Renaud, Neurosis, Isis, Led Zeppelin, Warning, Moonsorrow, Bruce Springsteen, Deathspell Omega, Fall of Efrafa, Mano Solo, Rancid, Behemoth, Giant Squid . . .

Consequently, the following pages are meant to be read while listening to the appropriate music (usually a song, sometimes an album), that will be described in footnotes and will be preceded by a ■⁶

to be continued....

⁶■ Sigur Ros, Takk (2005) works for all the Acknowledgements

Chapter 4

Wavefront Control in Nonlinear Microscopy

Contents

4.1	Focus Engineering in Coherent Nonlinear Microscopy	112
4.2	THG Microscopy with Higher Order Modes: a Numerical Study	113
4.3	THG Microscopy with Phase-Masks	128
4.4	THG Microscopy with Bessel Beams	132
4.5	Rapid Wavefront Modulation in 2PEF Microscopy	139
4.6	Adaptive Optics	144
	Bibliography	154

INTRODUCTION

The aim of this chapter is to discuss different methods of wavefront control (we will consider only spatial shaping¹) and their applications in nonlinear microscopy, with a special attention to THG microscopy. We will start in section 4.1 by introducing the concepts of focus engineering, then we will discuss third harmonic generation with focus engineered beams in sections 4.2 to 4.4.2, before moving on to an application in incoherent microscopy using an acousto-optic modulator in section 4.5, and finally presenting an application of aberration correction in nonlinear microscopy in section 4.6.

This chapter is structured around 3 articles that are reproduced integrally. They are each preceded by an introduction that remind the general context, and in one case completed by further calculations.

¹Spectral phase-shaping also exists and has already been mentioned, but we will not discuss it in this chapter

4.1 Focus Engineering in Coherent Nonlinear Microscopy

4.1.1 Introduction

The concept of focus engineering is an extension of Fourier Optics [1] applied to the high NA focusing conditions used in microscopy. It takes advantage of the relation that exists between two planes in the paraxial hypothesis:

$$E_u(x, y, z) = \iint E_u(k_x, k_y) e^{j(k_x x + k_y y)} e^{\pm jz(k - \frac{k_x^2 + k_y^2}{2k})} dk_x dk_y \quad (4.1)$$

If we consider a converging lens, then the field in the focal plane is equal to the Fourier transform of the field in the back focal plane (or Fourier plane) of the lens. The basic idea behind focus engineering is: how much can we control the field distribution near the focus by modulating the phase and the polarization of the excitation before focusing it, and what can we do with it? The tailoring of arbitrary fields [2–4] is in itself an important subject, and there are several applications of focus engineering in microscopy, some of the most important ones being super-resolution [5–10], extended depth of field [11–15], trapping and cooling [16, 17], or STED microscopy [18–22].

In incoherent nonlinear microscopy, focus engineering was used to increase the lateral resolution [23], to provide isotropic 3D resolution [24], or to provide multi-spot excitation [25–27]. It has also been used to produce arbitrary focal spot shapes for nonlinear uncaging [4].

The case of coherent nonlinear microscopy is more complicated, as both phase and intensity distribution near the focus are important: the nonlinear signal depends on the interplay between the excitation distribution and the sample structure, thus by controlling the shape² of the excitation we can select the type of structures that will provide highest signal. Two possible types of applications of focus engineering can be envisioned³:

1. It could be used to specifically detect sample structures that are compatible with the structure of the excitation.
2. It could be used to characterize unknown structures by taking several images with different shapes.

There have been a few contributions to this field:

- In SHG microscopy, Yew *et al.* [28, 29] investigated the theoretical aspects of SHG using a radially polarized excitation that increases the axial component of the focal field and Yoshiki *et al.* [30] demonstrated this method experimentally by imaging collagen fibers oriented along the optical axis.
- In CARS microscopy, Krishnamachari *et al.* [31] have investigated numerically CARS microscopy using one or two focus engineered beams, and several experimental confirmations have later been provided [32–34]. The use of a radially polarized excitation to image axially oriented molecules has been investigated recently [35], and an interesting approach using a spatial filtering of the detection has also been proposed [36].

²The intensity distribution of engineered beam has received much more attention than the phase distribution, so one of our objective was to investigate such phase effects.

³This is similar to CARS microscopy where complete spectral imaging or single frequency imaging can be performed

- In THG microscopy, the influence of the numerical aperture has been studied by Débarre *et al.* [37], while Oron *et al.* [38] investigated the use of cylindrical Gaussian beams. A numerical study on THG using radially polarized Gauss-Bessel beams [39] has been published, and very recently, Masihzadeh *et al.* [40, 41] has investigated the possibilities offered by polarization control in THG, both for polarimetric measurements and for increasing the resolution.

4.2 THG Microscopy with Higher Order Modes: a Numerical Study

We have seen in the previous chapter that the signal in coherent microscopy depends on the interplay between the sample structure and the exciting field structure. As the sample structure is what we are interested in, and the exciting field is a parameter we can control, how much information about the sample can we get from using different excitations shapes? For example, we have seen that dependence of the THG signal on sample size means that by using different numerical apertures we could get information about the size of the imaged structure.

This section consists of an article in which we investigated the influence of several higher order Hermite-Gaussian and Laguerre-Gaussian modes on THG from different simple geometries.



Figure 4.1: CTRL+C/V

Nicolas Olivier and Emmanuel Beaurepaire
Third-harmonic generation microscopy with focus-engineered beams:
a numerical study
OPTICS EXPRESS / vol. 16 issue 19 p. 1470 / (2008)

Third-harmonic generation microscopy with focus-engineered beams: a numerical study

Nicolas Olivier and Emmanuel Beaurepaire

*Laboratoire d'optique et biosciences, Ecole Polytechnique, CNRS, F-91128 Palaiseau,
France, and INSERM U696, Palaiseau, France*

nicolas.olivier@polytechnique.edu, emmanuel.beaurepaire@polytechnique.edu

Abstract: We use a vector field model to analyze third-harmonic generation (THG) from model geometries (interfaces, slabs, periodic structures) illuminated by Hermite-Gaussian (HG) and Laguerre-Gaussian (LG) beams focused by a high NA lens. Calculations show that phase matching conditions are significantly affected by the tailoring of the field distribution near focus. In the case of an interface parallel to the optical axis illuminated by an odd HG mode, the emission patterns and signal level reflect the relative orientation of the interface and the focal field structure. In the case of slabs and periodic structures, the emission patterns reflect the interplay between focal field distribution (amplitude and phase) and sample structure. Forward-to-backward emission ratios using different beam shapes provide sub-wavelength information about sample spatial frequencies.

© 2008 Optical Society of America

OCIS codes: (180.6900) Three-dimensional microscopy; (190.4160) Multiharmonic generation; (170.3880) Medical and biomedical imaging.

References and links

1. E. Yew and C. Sheppard, "Second harmonic generation microscopy with tightly focused linearly and radially polarized beams," *Opt. Commun.* **275**, 453-457 (2007).
2. K. Yoshiki, R. Kanamaru, M. Hashimoto, N. Hashimoto, and T. Araki, "Second-harmonic-generation microscope using eight-segment polarization-mode converter to observe three-dimensional molecular orientation," *Opt. Lett.* **32**, 1680-1682 (2007).
3. V. V. Krishnamachari and E. O. Potma, "Focus-engineered coherent anti-Stokes Raman scattering microscopy: a numerical investigation," *J. Opt. Soc. Am. A* **24**, 1138-1147 (2007).
4. V. V. Krishnamachari and E. O. Potma, "Imaging chemical interfaces perpendicular to the optical axis with focus-engineered coherent anti-Stokes Raman scattering microscopy," *Chem. Phys.* **341**, 81-88 (2007).
5. Y. Barad, H. Eisenberg, M. Horowitz, and Y. Silberberg, "Nonlinear scanning laser microscopy by third harmonic generation," *Appl. Phys. Lett.* **70**, 922-924 (1997).
6. M. Müller, J. Squier, K. R. Wilson, and G. J. Brakenhoff, "3D-microscopy of transparent objects using third-harmonic generation," *J. Microsc.* **191**, 266-274 (1998).
7. D. Débarre and E. Beaurepaire, "Quantitative characterization of biological liquids for third-harmonic generation microscopy," *Biophys. J.* **92**, 603-612 (2007).
8. D. Yelin, and Y. Silberberg, "Laser scanning third-harmonic generation microscopy in biology," *Opt. Express* **5** (1999).
9. D. Oron, D. Yelin, E. Tal, S. Raz, R. Fachima, and Y. Silberberg, "Depth-resolved structural imaging by third-harmonic generation microscopy," *J. Struct. Biol.* **147**, 3-11 (2004).
10. D. Débarre, W. Supatto, E. Farge, B. Moullia, M.-C. Schanne-Klein, and E. Beaurepaire, "Velocimetric third-harmonic generation microscopy: micrometer-scale quantification of morphogenetic movements in unstained embryos," *Opt. Lett.* **29**, 2881-2883 (2004).
11. C.-K. Sun, S.-W. Chu, S.-Y. Chen, T.-H. Tsai, T.-M. Liu, C.-Y. Lin, and H.-J. Tsai, "Higher harmonic generation microscopy for developmental biology," *J. Struct. Biol.* **147**, 19-30 (2004).

12. W. Supatto, D. Débarre, B. Mouliat, E. Brouzés, J.-L. Martin, E. Farge, and E. Beaurepaire, "In vivo modulation of morphogenetic movements in Drosophila embryos with femtosecond laser pulses," *Proc. Nat. Acad. Sci. USA* **102**, 1047-1052 (2005).
13. D. Débarre, W. Supatto, A.-M. Pena, A. Fabre, T. Tordjmann, L. Combettes, M.-C. Schanne-Klein, and E. Beaurepaire, "Imaging lipid bodies in cells and tissues using third-harmonic generation microscopy," *Nat. Methods* **3**, 47-53 (2006).
14. D. Débarre, W. Supatto, and E. Beaurepaire, "Structure sensitivity in third-harmonic generation microscopy," *Opt. Lett.* **30**, 2134-2136 (2005).
15. J.-X. Cheng and X. S. Xie, "Green's function formulation for third harmonic generation microscopy," *J. Opt. Soc. Am. B* **19**, 1604-1610 (2002).
16. B. Richards and E. Wolf, "Electromagnetic diffraction in optical systems II. Structure of the image field in an aplanetic system.," *Proc. Royal Soc. A* **253**, 358-379 (1959).
17. L. Novotny and B. Hecht, *Principles of nano-optics* (Cambridge Univ Press, 2006).
18. Boyd, R. W. *Nonlinear optics*, 2nd edition, (Academic Press 2003).
19. H. Kogelnik, and T. Li, "Laser beams and resonators," *Appl. Opt.* **5**, 1550 (1966).
20. K. Youngworth and T. Brown, "Focusing of high numerical aperture cylindrical-vector beams," *Opt. Express* **7**, 77-87 (2000).
21. D. Débarre, N. Olivier, and E. Beaurepaire, "Signal epidetection in third-harmonic generation microscopy of turbid media," *Opt. Express* **15**, 8913-8924 (2007).
22. E. Y. S. Yew, and C. J. R. Sheppard, "Fractional Gouy phase," *Opt. Lett.* **33**, 1363-1365 (2008).
23. J. Mertz, and L. Moreaux, "Second-harmonic generation by focused excitation of inhomogeneously distributed scatterers," *Opt. Commun.* **196**, 325-330 (2001).
24. C. J. R. Sheppard, "High-aperture beams," *J. Opt. Soc. Am. A* **18**, 1579-1587 (2001).
25. S. Quabis, R. Dorn, M. Eberler, O. Glöckl, and G. Leuchs, "Focusing light to a tighter spot," *Opt. Commun.* **179**, 1-7 (2000).
26. S. Carrasco, B. E. A. Saleh, M. C. Teich, and J. T. Fourkas, "Second- and third-harmonic generation with vector Gaussian beams," *J. Opt. Soc. Am. B* **23**, 2134-2141 (2006).
27. S. S. Sherif, M. R. Foreman, and P. Török, "Eigenfunction expansion of the electric fields in the focal region of a high numerical aperture focusing system," *Opt. Express* **16**, 3397-3407 (2008).
28. M. R. Foreman, S. S. Sherif, P. R. T. Munro, and P. Török, "Inversion of the Debye-Wolf diffraction integral using an eigenfunction representation of the electric fields in the focal region," *Opt. Express* **16**, 4901-4917 (2008).

1. Introduction

Coherent nonlinear microscopies based on parametric processes such as coherent anti-Stokes Raman scattering (CARS), second-harmonic generation (SHG) or third-harmonic generation (THG) are receiving considerable attention. All these imaging modalities are compatible with two-photon excited fluorescence microscopy and provide different information on biological and non biological media with micrometer 3D resolution. A remarkable property of coherent nonlinear imaging techniques is that they are very sensitive to both the sub-micrometer sample structure and to the focal field structure. Indeed, the far field signal results from the coherent superposition in the detection plane of waves emitted at different locations near focus, and interference phenomena define the visibility of a particular distribution of scatterers.

Engineering the focal field structure is therefore a logical step in coherent nonlinear imaging. Intensity, phase and polarization may be modified by controlling the wavefront at the pupil of the objective, resulting in a modulation of phase-matching conditions and far-field emission patterns. This concept has been explored recently for SHG microscopy, where focused beams with strong axial components were used to enhance signal from fibers parallel to the optical axis [1, 2], and in CARS microscopy where focus engineering was used to highlight interfaces [3, 4].

In this article, we study the use of engineered beams in THG microscopy. THG microscopy relies on the third-order nonlinear susceptibility $\chi^{(3)}$ of the sample to provide contrast [5, 6, 7], and has proved effective for imaging biological samples [8, 9, 10, 11, 12, 13]. The imaging properties of THG microscopy strongly depend on the field distribution near focus. The most salient characteristic of THG microscopy with Gaussian beams is that no signal is obtained from a homogeneous normally dispersive sample [5]. Signal is obtained around $\chi^{(3)}$ inhomogeneous

genities, with an efficiency depending on the relative sizes of the inhomogeneity and of the focal volume [14]. Since most materials have a non-negligible $\chi^{(3)}$, THG signal creation for a particular sample geometry is essentially determined by interference effects. Focus engineered THG microscopy is therefore expected to give access to sub-wavelength structural information about the sample. We here present a numerical study of vectorial and phase-matching aspects of THG by tightly focused Gaussian, Hermite-Gaussian (*HG*), and Laguerre-Gaussian (*LG*) beams incident on slabs, interfaces, and axially periodic samples. These calculations provide insight on the interplay between field and sample structure in THG microscopy with focused complex beams, and should more generally prove useful for designing coherent nonlinear microscopy (SHG, THG, CARS) experiments with engineered beams. Our strategy for simulations follows the framework described in [15], but integrates a complete vector field model to account for vectorial effects with arbitrary excitation beam profiles.

2. Theory and numerical implementation

A general method for analyzing signal generation in nonlinear microscopy can be described as follows (see Figure 1 for notations). First, the focal field distribution is calculated using a Debye-Wolf diffraction integral [16]. Then the induced nonlinear polarization in the focal volume is calculated for a given sample geometry. Finally, the resulting nonlinear field is propagated using Green's functions into the far field [15], where signal level and radiation patterns are analyzed. This theoretical description is summarized below.

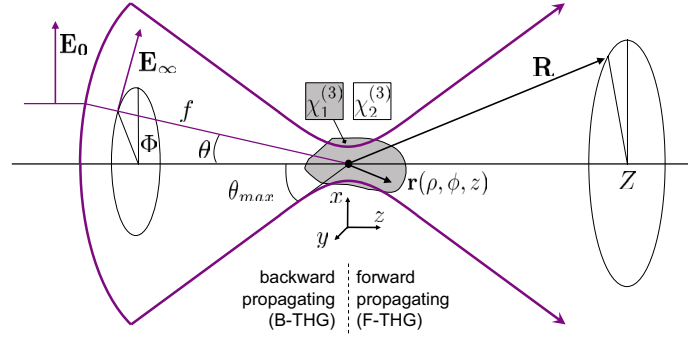


Fig. 1. Geometry and notations (see text)

2.1. Excitation field near focus

The field distribution near the focus of a high numerical aperture (NA) and anti-reflexion-coated objective lens given an arbitrary field at the back pupil can be calculated using the angular spectrum representation method [16, 17]:

$$\mathbf{E}(\rho, \phi, z) = \frac{ik_{\omega}f e^{-ik_{\omega}f}}{2\pi} \int_0^{\theta_m} \int_0^{2\pi} e^{-ik_{\omega}z \cos(\theta)} e^{-ik_{\rho} \sin(\theta) \cos(\Phi - \phi)} \sin(\theta) \mathbf{E}_{\infty}(\theta, \Phi) d\Phi d\theta \quad (1)$$

with:

$$\mathbf{E}_{\infty}(\theta, \Phi) = (\cos \theta)^{1/2} \left[\mathbf{E}_0(\theta, \Phi) \cdot \begin{pmatrix} -\sin \Phi \\ \cos \Phi \\ 0 \end{pmatrix} \right] \begin{pmatrix} -\sin \Phi \\ \cos \Phi \\ 0 \end{pmatrix}$$

$$+ (\cos \theta)^{1/2} \left[\mathbf{E}_0(\theta, \Phi) \cdot \begin{pmatrix} \cos \Phi \\ \sin \Phi \\ 0 \end{pmatrix} \right] \begin{pmatrix} \cos \Phi \cos \theta \\ \sin \Phi \cos \theta \\ -\sin \theta \end{pmatrix} \quad (2)$$

where $\mathbf{E}_0(\theta, \Phi)$ describes the field phase and intensity distribution at the back aperture of the objective, $k = k_\omega = 2\pi\omega/n_\omega$ is the wavenumber, f is the focal length of the objective, n_ω is the refractive index at frequency ω , (ρ, θ, z) are cylindrical coordinates near focus, and $\theta_{max} = \sin^{-1}(NA/n)$ is the maximum focusing angle of the objective.

If we expand $\mathbf{E}_0(\theta, \Phi)$ as a polynomial expansion of $\cos(\Phi)$ and $\sin(\Phi)$ functions, this 2D integral can be reduced to a 1D integral involving Bessel functions J_n . We can then use the following abbreviations to express the focal fields of the various beam modes considered in this study:

$$I_{lmn}^{\alpha\beta}(\rho, z) = \int_\alpha^\beta f_w(\theta) (\cos \theta)^{1/2} \sin^m \theta \cos^n \theta J_l(k\rho \sin \theta) e^{ikz \cos \theta} d\theta \quad (3)$$

where $f_w(\theta) = \exp(-(\sin(\theta)/(f_0 \sin \theta_{max}))^2)$ is a filling factor that takes into account the ratio (f_0) between the beam size (related to w_0) and the back aperture of the objective ($f \sin \theta_{max}$).

We introduce the following shorthand notations:

$$I_{lmn} = I_{lmn}^{0\theta_{max}} ; E_1 = \frac{ikf}{2} E_0 e^{-ikf} ; E_2 = \frac{ikf^2}{2w_0} E_0 e^{-ikf} \quad (4)$$

Expressions for focused Hermite-Gaussian and Laguerre-Gaussian modes can then be derived as [17]:

Focused x - polarized HG_{00} (Gaussian) mode:

$$\mathbf{E}(\rho, \phi, z) = E_1 \begin{bmatrix} I_{010} + I_{011} + (I_{210} - I_{211}) \cos(2\phi) \\ (I_{210} - I_{211}) \sin(2\phi) \\ -2iI_{120} \cos \phi \end{bmatrix} \quad (5)$$

Focused x - polarized HG_{10} mode:

$$\mathbf{E}(\rho, \phi, z) = E_2 \begin{bmatrix} i(I_{120} + 3I_{121}) \cos \phi + i(I_{320} - I_{321}) \cos(3\phi) \\ -i(I_{120} - I_{121}) \sin \phi + i(I_{320} - I_{321}) \sin(3\phi) \\ -2iI_{030} + 2I_{230} \cos(2\phi) \end{bmatrix} \quad (6)$$

Focused x - polarized HG_{01} mode:

$$\mathbf{E}(\rho, \phi, z) = E_2 \begin{bmatrix} i(3I_{120} + I_{121}) \sin \phi + i(I_{320} - I_{321}) \sin(3\phi) \\ -i(2I_{120} - 2I_{121}) \cos \phi - i(I_{320} - I_{321}) \cos(3\phi) \\ 2I_{230} \sin(2\phi) \end{bmatrix} \quad (7)$$

Focused x - polarized HG_{20} mode:

$$\mathbf{E}(\rho, \phi, z) = E_2 \begin{bmatrix} 3I_{031} - 2(I_{010} + I_{011}) - 2\cos(2\phi)[2I_{231} + I_{210} - I_{211}] + \cos(4\phi)I_{140} \\ 2\sin(2\phi)[I_{230} - I_{231} + I_{211} - I_{210}] + 2\sin(4\phi)[I_{431} - I_{430}] \\ \cos(\phi)[4I_{120} - 3I_{140}] + 2i\cos(3\phi)I_{340} \end{bmatrix} \quad (8)$$

Focused linearly polarized LG_{01}^{lin} ('donut') mode:

$$LG_{01}^{lin} = HG_{10} + iHG_{01} \quad (9)$$

Focused azimuthally polarized LG_{01}^{az} mode:

$$\mathbf{E}(\rho, \phi, z) = E_2 \begin{bmatrix} 4iI_{120}\sin\phi \\ -4iI_{120}\cos\phi \\ 0 \end{bmatrix} \quad (10)$$

Focused radially polarized LG_{01}^{rad} mode:

$$\mathbf{E}(\rho, \phi, z) = E_2 \begin{bmatrix} 4iI_{121}\cos\phi \\ 4iI_{121}\sin\phi \\ -4I_{030} \end{bmatrix} \quad (11)$$

For future reference in this article, we summarize the calculated field distributions near focus for these various cases in Figure 2. Phase distributions are presented without the propagation term $\exp(-ik_0z)$ in order to highlight the differences between the modes.

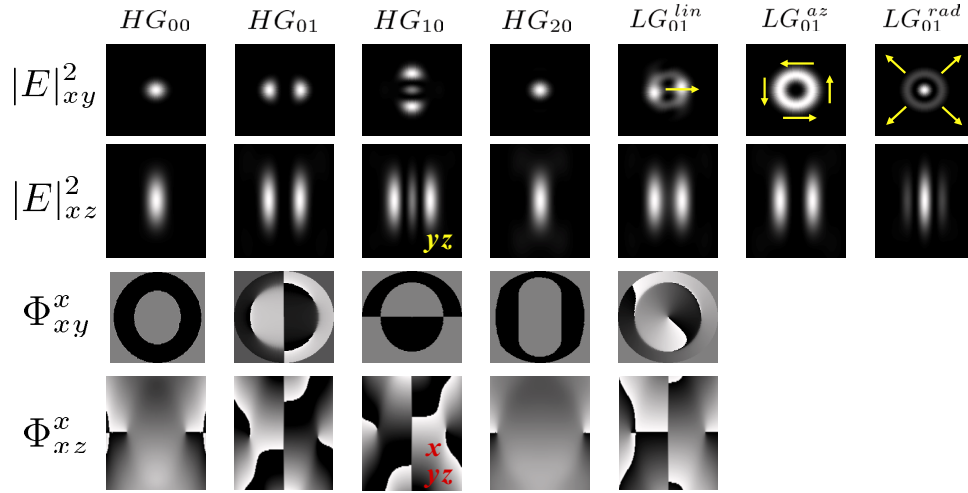


Fig. 2. Distributions in the xy and xz planes of the focal field intensity and of the phase of the x -polarized component when relevant, for the modes described by Eqs.(5-11). Arrows indicate the direction of polarization in the xy plane for focused LG_{01} beams. Intensity plots are normalized to their maximum values. Phase color table ranges from white ($-\pi$ rad) to black (π rad). $NA = 1.4$, $x, y \in [-1, 1]\mu m$, $z \in [-2, 2]\mu m$.

2.2. Calculation of the induced third-order non-linear polarization

In a medium characterized by its third-order nonlinear tensor $\chi_{ijkl}^{(3)}(\mathbf{r})$, the excitation field induces a polarization density described by:

$$P_i^{(3\omega)} = \sum_{j,k,l} \chi_{ijkl}^{(3)} E_j E_k E_l \quad (12)$$

The $\chi^{(3)}$ tensor of a homogeneous isotropic medium can be expressed as [18]:

$$\chi_{ijkl}^{(3)} = \chi_0 (\delta_{ij}\delta_{kl} + \delta_{ik}\delta_{jl} + \delta_{il}\delta_{jk}) \quad (13)$$

We can then express the nonlinear polarization induced by the exciting field E in cartesian coordinates as:

$$\mathbf{P}^{(3\omega)} = \chi_0 \begin{bmatrix} E_x(3E_x^2 + E_y^2 + E_z^2) \\ E_y(E_x^2 + 3E_y^2 + E_z^2) \\ E_z(E_x^2 + E_y^2 + 3E_z^2) \end{bmatrix} \quad (14)$$

2.3. Propagation of the harmonic field

Finally, the harmonic field originating from all positions \mathbf{r} in the focal region and propagated to a position \mathbf{R} in the collection optics aperture can be expressed as [17, 15]:

$$E_{FF}(\mathbf{R}) = \int_V \mathbf{P}^{(3\omega)}(\mathbf{r}) \mathbf{G}_{FF}(\mathbf{R} - \mathbf{r}) dV \quad (15)$$

where V spans the excitation volume and \mathbf{G}_{FF} is the far field Green's function:

$$\mathbf{G}_{FF} = \frac{\exp(ikR)}{4\pi R} [\mathbf{I} - \mathbf{R}\mathbf{R}/R^2] \quad (16)$$

where \mathbf{R} is the coordinate of a point in the far field (see Fig. 1) and \mathbf{I} is the third-order identity tensor.

Emission diagrams can be analyzed from these equations by calculating the squared harmonic field $|E_{FF}(\mathbf{R})|^2$ at different positions \mathbf{R} . Alternatively, total THG power emitted in the forward (F-THG) or backward (B-THG) directions can be estimated by integrating $|E_{FF}(\mathbf{R})|^2$ over the front aperture of an epicollecting or trans-collecting objective.

To simplify the analysis of the results, we assume no linear index mismatch and we neglect temporal aspects such as group velocity mismatch for ultrashort pulses. However we assume that the samples consist of normally dispersive media (which is usually the case in biological THG imaging), since dispersion plays a significant role in THG contrast formation: for example, negative dispersion in homogeneous gas samples can result in bulk emission [18].

2.4. Numerical implementation

Calculations are performed using Matlab. We typically discretize the focal volume over a $200 \times 140 \times 140 \times (\lambda/40)$ grid, and evaluate the excitation field using quadrature algorithms. Unless otherwise stated, we use the following parameters: $\lambda = 1.2\mu\text{m}$, $NA = 1.4$ or 1.2 , $f_0 = 2$, $n_\omega = 1.5$, $n_{3\omega} = 1.52$. We note that incorporating positive dispersion in the model is numerically advantageous because smaller focal volumes can be considered, and calculations are generally less noise-sensitive than in the limit case of zero-dispersion. For a given sample/focal field combination, we calculate the projection of the forward- and backward- emission patterns on planes perpendicular to the optical axis located at $Z = \pm 10\text{cm}$. We choose to present projected far-field patterns rather than angular emission diagrams because they appeared to be more readable in the case of complex emission profiles. For the interface and slab sample geometries, we assume that the focal volume encompasses two homogeneous isotropic media with third-order nonlinear susceptibilities $\chi_1^{(3)} = 1$ and $\chi_2^{(3)} = 0$. This choice is motivated by the fact that, for excitation geometries where bulk THG emission is canceled by destructive interference, THG from an interface scales as $|\chi_1^{(3)} - \chi_2^{(3)}|^2$. For periodic samples, we assume a sine-like variation $\chi^{(3)} = 1 + \sin(2\pi z/\delta e)/2$ along the optical axis. We then iterate for each beam shape and for various sample positions the calculation of emission patterns, F-THG and B-THG powers. Normalization is done by considering the same total intensity in the focal volume for every mode.

3. Results

3.1. Vectorial aspect of THG microscopy with tightly focused beams

Although studies of THG by focused Gaussian beams generally neglect vectorial aspects, a general analysis of THG microscopy requires *a priori* a vector field model because high NA focusing does not preserve linear polarization. Furthermore it is seen from Eq.14 that the induced

nonlinear polarization $\mathbf{P}^{(3\omega)}$ can *linearly* depend on a particular field component. For example if E_z is strong at a particular location near focus and spatially overlaps with E_x , a cross-term proportional to $E_z E_x^2$ will significantly contribute to $\mathbf{P}_x^{(3\omega)}$. Conversely if E_z does not overlap with E_x , only the E_x^3 term will contribute to the THG signal. In particular, in the case of a tightly focused Gaussian beam with initial linear polarization the axial component near focus is important (see Fig. 3): $Max(E_z) \approx Max(E_x)/3$ for $NA = 1.4$. However in this case there is little overlap between E_x and E_z , so that E_z contributes little to THG. Thus, a scalar approximation will usually work well for THG from simple interfaces excited by a focused linearly polarized Gaussian beam. However it will typically not be accurate for higher-order beam shapes or other input polarization patterns. Recalling that the phase distribution (including the Gouy shift) is generally different for the various field components [17, 19], cross-terms may define different coherence lengths within the focal volume and affect the imaging properties. Furthermore, focused radially polarized beams typically exhibit strong axial components (see e.g. LG_{01}^{rad} mode in Fig. 3) [20, 1, 2] which give them original imaging properties.

We also point out that a well-described vectorial aspect of THG microscopy is the absence of THG signal when a HG_{00} beam with circular polarization is focused on an interface between isotropic media [9].

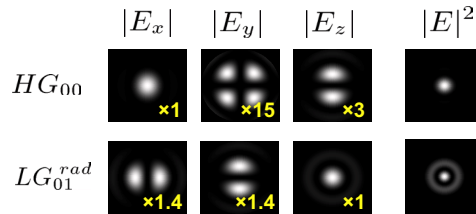


Fig. 3. Distribution of the different field polarization components and total intensity in the transverse focal plane for focused HG_{00} and LG_{01}^{rad} beams. $x, y \in [-1, 1] \mu m$.

3.2. THG imaging of XY interfaces with HG and LG beams

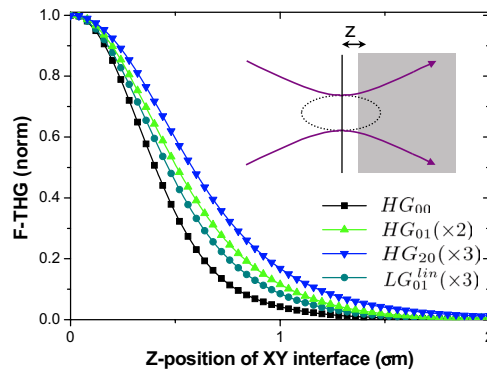


Fig. 4. F-THG during an axial scan through a xy interface with HG and LG beams. Curves are normalized by the factors indicated in the inset.

We begin our study of THG microscopy with non-standard beams by considering the simplest sample geometry, namely an interface between two media with different nonlinear susceptibil-

ities $\chi_1^{(3)}$ and $\chi_2^{(3)}$. A well-known fact in the case of a XY-interface (i.e. perpendicular to the optical axis) excited by a tightly focused HG_{00} beam is that a z-scan produces a symmetric Gaussian (or Lorentzian if the objective aperture is overfilled) curve peaking when the interface is at the focus. Our simulations predict similar behaviors for THG emission with all the higher-order HG and LG modes considered in this study (see Fig. 4 for characteristic examples), whether or not they possess cylindrical symmetry. The main difference lies in the widths of the z-scan responses, which are related to the axial extents of the corresponding excitation field distributions. The single-peaked nature of the z-scans reflects the fact that the modes considered here exhibit a single axial maximum. We note that emission is essentially forward-directed, as in the case of Gaussian excitation [21]. However different modes produce different emission patterns. For example, on-axis harmonic emission is prevented with focused HG_{01} modes due to the laterally antisymmetric nature of the focal phase distribution, as predicted for CARS emission from bulk media [3].

We also point out that the HG_{00} case is qualitatively well-described by the paraxial approximation (not shown) even at high NA (in contrast with [15] where an inappropriate value of the confocal parameter was used). Paraxial approximation provides meaningful results for non-linear processes involving Gaussian beams and simple geometries because over the region of highest intensity where most signal creation occurs, both the intensity and the Gouy phase shift (which varies almost linearly with z) are accurately approximated. Of course, the situation can be quite different with complex field distributions.

3.3. THG imaging of XZ/YZ interfaces with focused HG beams

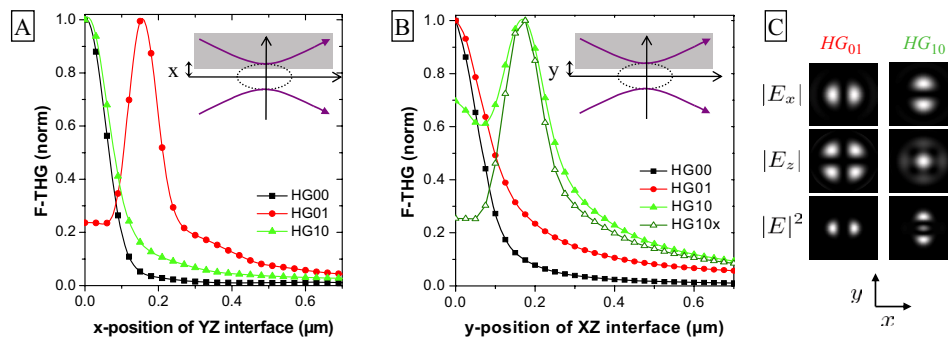


Fig. 5. F-THG during lateral scans through interfaces parallel to the optical axis. (a) x -scan through a YZ interface. (b) y -scan through a XZ interface. The HG_{10x} curve (empty green triangles) is the behavior predicted when the z component of HG_{10} is omitted. (c) Excitation field and intensity distribution in the focal plane for focused HG_{01} and HG_{10} beams.

More interesting is the case of an interface parallel to the optical axis excited by an asymmetric field distribution such as a focused HG_{01} or HG_{10} beam. When a YZ interface is x -scanned across a focused HG_{01} beam (Fig. 5(a)), the F-THG response exhibits a double peak reflecting the field distribution in the focal plane (see Fig. 5(c)), contrasting with the case of a focused HG_{00} or HG_{10} . Even more striking is the case of a XZ interface being y -scanned across a focused HG_{10} beam (Fig. 5(b)). In this case the THG response exhibits a triple peak. The central peak results from the presence of a significant axially polarized component in the strongly focused x -polarized HG_{10} field (I_{030} term in Eq. 6 which is not present in the HG_{01} case, see also Fig. 5(c)). This vectorial interpretation is corroborated by the double-peaked shape of the THG y -scan obtained when the axial component is omitted in the simulation (Fig. 5(b)).

Since this situation is equivalent to that of a single half-space with susceptibility $|\chi_1^{(3)} - \chi_2^{(3)}|$, maximum emission is obtained when one of the two main excitation peaks is incident on the interface.

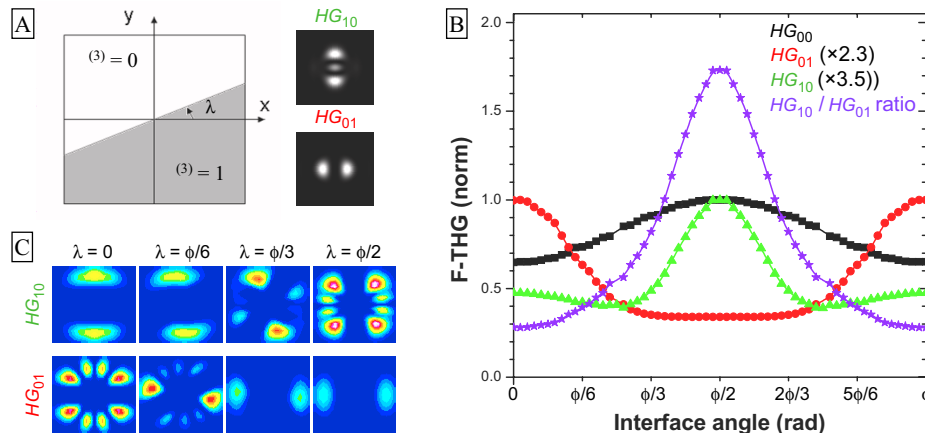


Fig. 6. Sensitivity to the orientation of an interface parallel to the optical axis using asymmetric excitation (HG_{01} and HG_{10}). (a) Geometry of the sample and distribution of the excitation intensity in the focal plane. (b) Normalized F-THG signal as a function of interface angle ϕ for HG_{00} (black squares), HG_{01} (red discs) and HG_{10} (green triangles). Normalization factors are indicated in the inset. The HG_{10}/HG_{01} signal ratio (purple stars) probes the interface orientation within the focal volume with good contrast. (c) Projected far-field emission patterns as a function of interface angle for HG_{01} and HG_{10} excitation. (Media1): TH emission patterns for HG_{00} , HG_{01} , and HG_{10} excitation, as a function of interface orientation. Patterns are evaluated at $z=+10\text{cm}$ over a $15 \times 15\text{cm}$ area transverse to the optical axis, which corresponds to a detection NA of approximately 0.5.

We now seek to take advantage of the laterally asymmetric nature of odd HG beams to probe sample orientation. We analyze the THG response obtained from HG_{01} and HG_{10} beams focused on an interface parallel to the optical axis as a function of the angle ϕ that it makes relative to the X axis (see Fig. 6(a)). As anticipated from the shape of the focal fields, THG emission is strongly modulated ($>50\%$) as a function of the interface angle. This is because the geometry is roughly equivalent to that of a single-peaked excitation where the distance between the focal spot and the interface is proportional to the sine (or cosine) of the interface angle. Therefore, anti-correlated behaviors are predicted with HG_{01} and HG_{10} beams (Fig. 6(b)), and a combination of measurements with two such beam shapes provides sub- μm information about sample orientation. The corresponding far-field emission patterns exhibit even more subtle variations (Fig. 6(c)). When the two main peaks of the focal field lie on both sides of the interface (i.e. $\phi = 0$ with HG_{10} excitation or $\phi = 90$ with HG_{01} excitation), F-THG emission occurs along two off-axis lobes. These emission patterns are reminiscent of the case of Gaussian excitation of a XY interface [15], where the Gouy shift prevents on-axis phase matching and deflects the emission. However when both excitation peaks are incident on the interface (i.e. $\phi \approx 90$ with HG_{01} or $\phi \approx 0$ with HG_{10}), the emission originates from two sources and interferences structure it into a non-trivial 8-lobes pattern. The relative intensities of these lobes are tightly related to the sample orientation (Fig. 6). See (Media1).

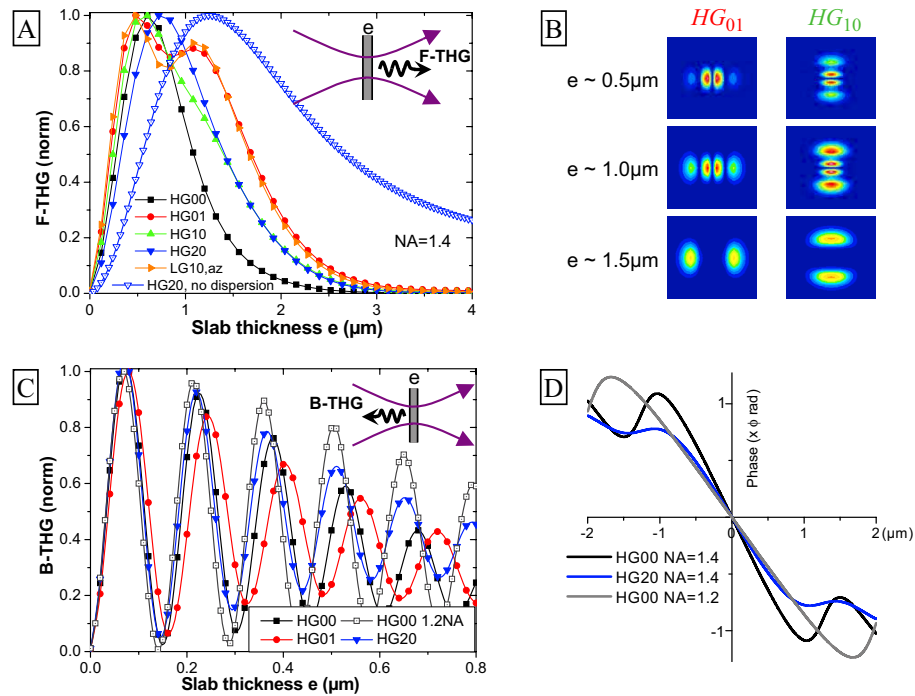


Fig. 7. F-THG and B-THG from slabs of varying thicknesses using different beam shapes. (a) F-THG as a function of slab thickness indicates the forward coherence length associated with a particular field profile. The inset depicts the corresponding geometry. HG_{20} excitation (blue triangles) results in larger forward coherence length than HG_{00} (black squares). HG_{01} excitation (red disc) produce a double-peaked response as a function of thickness, corresponding to distinct emission patterns. The double peak behavior is blurred for HG_{10} excitation (see text). The HG_{20} case without dispersion is also presented for comparison (empty triangles). For all the modes considered here, the peak TH signal intensity is between 1.5 and 2 times higher than that obtained from a semi-infinite slab. (b) Far-field emission patterns using HG_{01} and HG_{10} excitation, for different slab thicknesses. (c) B-THG as a function of slab thickness, according to the geometry depicted in the inset. Oscillation period indicates the backward coherence length. (d) On-axis phase distribution (without propagation term) for HG_{00} and HG_{20} modes with different NAs.

3.4. Focus-engineered THG from slabs

Coherent nonlinear microscopies are particularly sensitive to the axial phase distribution in the regions of highest intensity. In THG microscopy with HG_{00} excitation, the Gouy shift defines a signal coherent construction length of $\approx 0.7\lambda$ for forward emission (F-THG) [15] and the wave vector mismatch Δk defines a construction length of $\pi/\Delta k \approx \lambda/12n_\omega$ for backward emission (B-THG) [21]. The coherence length for forward emission has a major influence on imaging properties, since it acts as a spatial bandpass filter that highlights objects of a given size in F-THG images [14]. Elaborating on this idea, we point out that when focusing non-Gaussian beams such as higher-order HG and LG modes, focal field components exhibit altered phase distributions [19, 22] (see e.g. Fig. 7(d)).

We therefore simulate F-THG and B-THG from slabs of varying thicknesses to gain insight into the axial coherence lengths associated with non-Gaussian beams. Fig. 7 shows that forward- and backward- coherence lengths can indeed be modulated when using alternate modes. A particularly clear illustration comes when comparing HG_{00} and HG_{20} excitations. Focused HG_{20} resembles HG_{00} because it exhibits a single peak along the optical axis, albeit with a slower phase variation and a broader intensity distribution than focused HG_{00} . Accordingly, the axial coherence length is increased for F-THG and reduced for B-THG. Reduced B-THG coherence length manifests itself through the reduced oscillation period as a function of slab thickness (Fig. 7(c)). We point out that moving from HG_{00} to HG_{20} excitation here produces an effect comparable to changing the excitation NA from 1.4 to ≈ 1.2 (see Fig. 7(d)) and comes at the cost of reduced signal level by a factor ≈ 2 . Fig. 7(a) also illustrates the consequence of including/excluding dispersion, for the HG_{20} case (filled and empty blue triangles). For all the cases studied here, we essentially find that dispersion reduces TH efficiency for large objects without affecting the relative behaviors obtained with different beam shapes.

However beam shaping offers more degrees of freedom than merely changing the NA. This is exemplified by the dependence on slab thickness of F-THG with e.g. HG_{01} excitation. The thickness response is double-peaked, and can be seen as resulting from two different coherence lengths with the two components exhibiting distinct emission patterns (see Fig. 7(b)). This behavior is related to the dominating I_{120} terms in Eq. 7, and is not obtained with HG_{10} excitation because the z -polarized I_{030} term (Eq. 6) produces an additional contribution that blurs the double-peak behavior. Even more dramatic effects can be obtained when imaging complex samples, as will be discussed in the next section.

3.5. Focus-engineered THG from axially periodic structures

THG emission from dielectric media excited with Gaussian beams is mostly forward-directed [21] and vanishes in a homogeneous medium. The forward-directed nature of the emission stems from the fact that the large wave vector mismatch in the backward direction Δk limits signal creation to a small region ($\approx 65nm$ for $\lambda = 1200nm$ and $n_\omega = 1.5$) around an heterogeneity (see fig 7). However the situation can be quite different in the case of a structured sample: if the sample exhibits appropriate axial periodicity, the density distribution of emitters can provide an additional momentum that puts the emitted waves in phase in a particular direction [21, 23]. Efficient THG emission may be obtained either in the forward or backward direction, depending on sample structure. Under HG_{00} excitation focused at 1.4 NA, an axial sine-like $\chi^{(3)}$ modulation with spatial period $\delta e \approx 2\pi/\Delta k \approx \lambda/6n_\omega = 135nm$ is expected to produce efficient B-THG emission, and a similar distribution with $\delta e \approx 2\mu m$ is expected to produce efficient F-THG emission [21].

This idea can be pushed further with focal field engineering: alternative field distributions can modify these spatial resonances. Figure 8 presents the dependence of B-THG and F-THG on sample spatial period, for the set of beam modes considered in this study. Resonances are

observed for both F-THG and B-THG for all excitation modes, with pronounced differences depending on the focal field profile. We note that although the precise axial localization of the sample can modulate the THG power by up to 40%, it does not significantly change the resonances (not shown). Not surprisingly, the characteristic sample lengths that enhance F-THG emission using HG modes are reminiscent of the coherence lengths that can be estimated by F-THG from slabs (Fig. 8). The backward emission behaviors are more complex, particularly for polarization-shaped LG_{01} beams. Together, these calculations show that the measurement of F-THG and B-THG with a properly chosen set of beam shapes can provide information on sample characteristic lengths in the ranges $130 - 250\text{nm}$ and $0.7 - 7\mu\text{m}$. We point out that the angular emission patterns are also closely related to the sample spatial frequencies (Fig. 8). Finally we note that these ideas are transposable to other coherent processes such as SHG and CARS. For example, efficient backward emission with HG_{00} excitation should be possible from a structure exhibiting a spatial frequency of $\delta e \approx \lambda/4n_\omega$ for SHG and $\delta e \approx \lambda_{as}/2n_{as}$ (where as refer to the anti-Stokes frequency) for CARS. Excitation with alternative field distributions is expected to shift these spatial resonances.

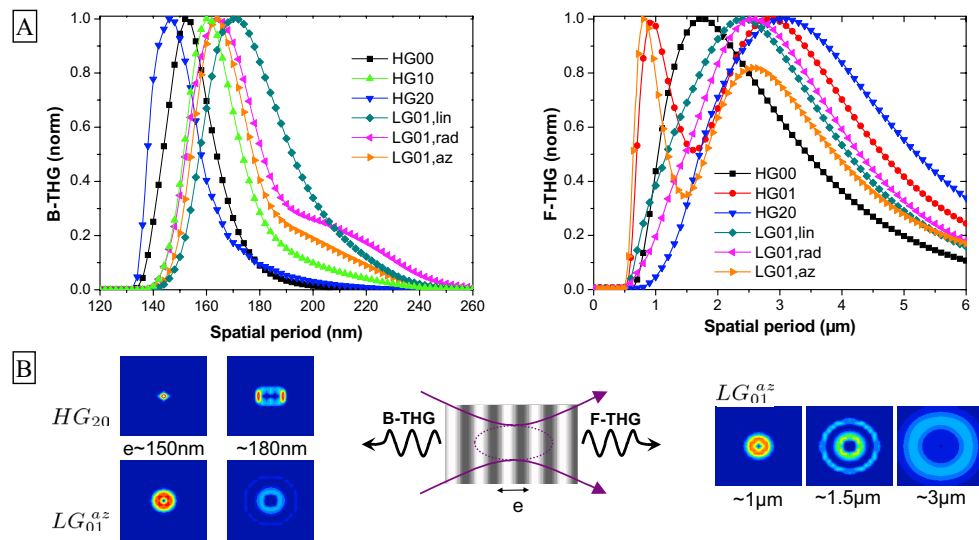


Fig. 8. F-THG and B-THG signal obtained from an axially periodic sample using different focal field distributions. (a) B-THG and F-THG as a function of sample period, for various HG and polarization-shaped LG_{01} beams. Different field shapes result in different spatial resonances. THG measurements with a properly chosen set of beam shapes provide information on sample characteristic lengths at different scales. Normalization factors for B-THG (resp F-THG) curves with respect to F-THG from a semi-infinite slab with a gaussian excitation: $HG_{00} \times 1.5(\times 2)$; $HG_{01} \times 1(\times 1)$; $HG_{10} \times 0.4(\times 0.3)$; $HG_{20} \times 0.3(\times 0.3)$; $LG_{01}^{lin} \times 0.3(\times 0.4)$; $LG_{01}^{rad} \times 0.1(\times 0.1)$; $LG_{01}^{az} \times 0.5(\times 0.6)$. (b) Characteristic examples of emission patterns in the forward and backward direction, as a function of sample periodicity.

4. Conclusion

Focal field engineering for coherent nonlinear microscopy is a rich and promising subject. The general idea is that measurable emission patterns reflect the interplay between the (unknown) sample structure and a known field distribution. The vectorial and phase properties of tightly

focused higher-order beams are an active area of research [24, 25, 22], and so are the vectorial aspects of nonlinear microscopy [2, 26]. Studying focus-engineered THG is informative because third-harmonic generation can be obtained from simple (isotropic) sample geometries and is highly sensitive to the focal phase distribution. Therefore it is a convenient means to study the impact of focus engineering on phase-matching conditions. Moreover, THG microscopy is usually a non-spectroscopic, structure-sensitive [14] imaging technique that provides morphological information about unstained samples. The results presented here show the potential of focus-engineered THG microscopy to provide sub-resolution information about complex samples: angles and characteristic lengths in the $130 - 250nm$ range are reflected in the emission patterns and can be probed using simple ratiometric measurements. A perspective is to design pupil functions producing a targeted field distribution [27, 28], axial field engineering (bottle beams [3], etc) being of particular relevance. Finally we note that the ideas explored in this article are generally transposable to other imaging modalities such as CARS and SHG. For example, CARS emission from an axial interface excited with a laterally asymmetric field distributions should exhibit a behavior similar that shown in Fig. 6(b). Also, focus engineering can be used to alter the spatial resonances resulting in efficient SHG and CARS emission in a particular direction, as in Fig. 8. It is anticipated that additional studies will explore the potential of focal field engineering for coherent nonlinear microscopy.

Acknowledgments

We thank Marie-Claire Schanne-Klein, François Hache and Paul Abbyad for comments on the manuscript, and Daniel Côté for seminal discussions. This work was supported by the Délégation Générale pour l'Armement (DGA) and by the Agence Nationale de la Recherche (ANR).

4.3 THG Microscopy with Phase-Masks

This section presents calculations that supplement the previous paper. The article considered beam shapes that could be easily calculated using the angular spectrum representation; we now consider radial phase-masks located in the back focal plane of the objective which allow easy calculations based on the Gaussian beam model(as discussed in chapter 2).

4.3.1 2-Zone and 3-Zone Annular Phase-Masks

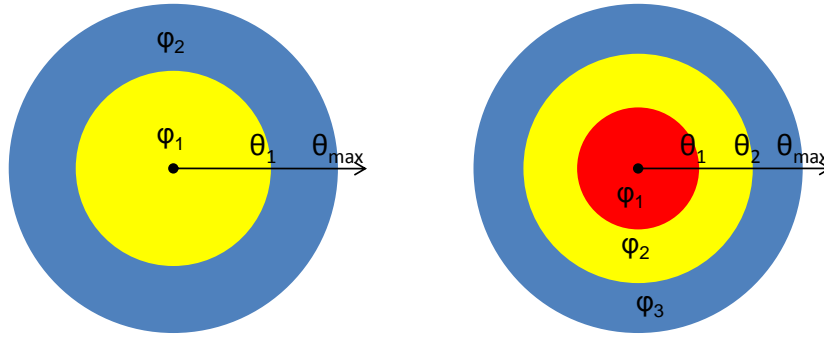


Figure 4.2: GEOMETRY OF THE TWO ZONE AND THREE-ZONE PHASE-MASKS
There is a π radian phase difference between the different zones.

We first studied the case of binary phase-masks. These phase-masks are made of two or three concentric zones that either add a π radian phase-shift, or no phase-shift at all, and their geometries are illustrated in figure (4.2). Their effect on the focal field, and especially the axial modulation of the intensity that they provide have been extensively studied [42]. The main advantage of using this type of phase-mask is that it only depend on 1 or 2 parameters, which allows a relatively easy analysis.

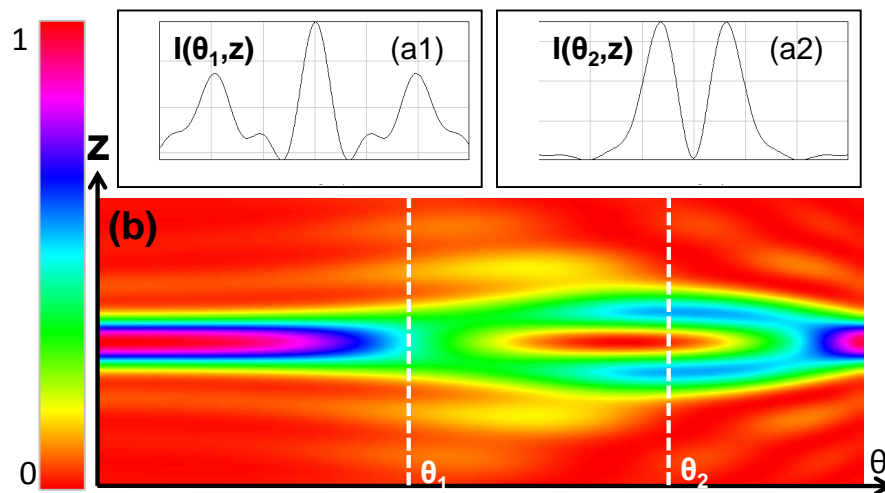


Figure 4.3: TWO ZONE PHASE-MASKS

(b) Intensity along the z -axis as a function of the θ parameter of the 2-zone binary phase mask. (a1) & (a2): Intensity distribution for a given value of the angle θ marked in (b). Conditions: $NA=1.4$, $n=1.5$, $\lambda = 1.2\mu m$, $0 < \theta < \sin^{-1}(NA/n)$, $-5\lambda < z < +5\lambda$.

Figure (4.3) illustrates the axial intensity distribution at the focus of a Gaussian beam phase-modulated by a two-zone binary phase-mask. The minimum ($\theta = 0$) and maximum ($\theta = \theta_{max}$) values of the θ parameter correspond to a uniform phase-mask, and in this case we obtain an intensity distribution corresponding to the regular focused Gaussian beam. The most interesting situation is when the intensity at the focus is equal to zero. This corresponds to the case of the so called *optical bottle beam* that has been described by Arlt *et al.* [16], and used for several applications including trapping, laser cooling or STED microscopy.

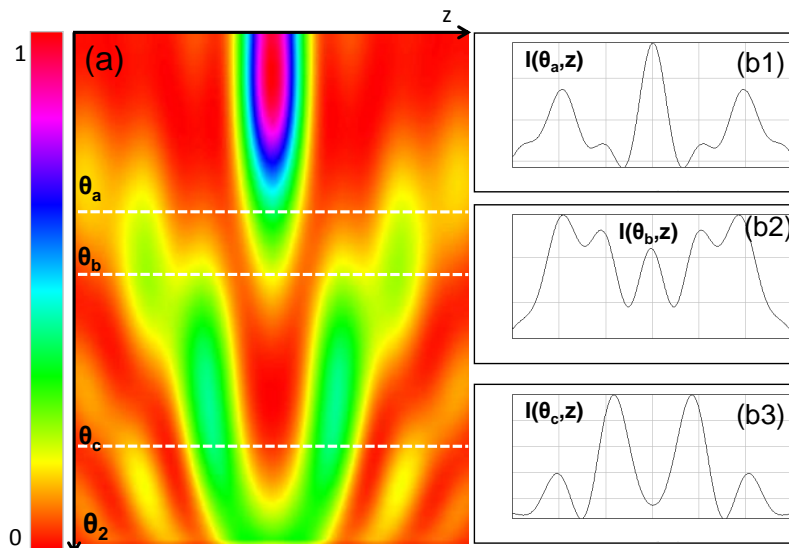


Figure 4.4: THREE ZONE PHASE-MASKS

Axial intensity distribution as a function of z and of the θ_2 parameter of the 3-zone phase mask. Conditions: $NA=1.4$, $n=1.5$, $\lambda = 1.2\mu m$, $n \sin(\theta_1) = 0.6$ $0 < \theta_2 < \sin^{-1}(NA/n)$, $-5\lambda < z < +5\lambda$.

Figure (4.4) illustrates the axial intensity distribution at the focus of a Gaussian beam phase-modulated by a three-zone binary phase-mask as a function of the angle defining the second ring (θ_2), for a given value of the first ring ($n \sin(\theta_1) = 0.6$). We can notice that there is a larger spread in the axial intensity distributions, and that we can not only get a double-peaked excitation like in the case of a two-zone filter, but also 3-peaked or even 5-peaked distributions.

We have used these phase-masks to simulate THG from various geometries, and the results obtained will be presented in the next section.

4.3.2 THG with Binary Phase-Masks

Our idea when studying this type of phase-masks was to see how far we could modify the forward and backward coherence lengths by introducing a modulation in our phase and intensity distribution, but the problem is far more complicated than we thought. Indeed, the axial intensity profiles illustrated in figures (4.3 and 4.4) are somehow misleading since the lateral intensity distribution are far from being Gaussian: we get lateral intensity profiles that are a succession of rings and single peaks, and the phase distribution also changes shape significantly in both axial and transverse directions. The consequence of that is that although we can shift significantly the phase-matching conditions and thus the size and shape of the structures that yield a maximum THG signal (as we will see in section 4.3.2.1), we have a very limited *control* over it.

4.3.2.1 Size Dependence - Coherence Length

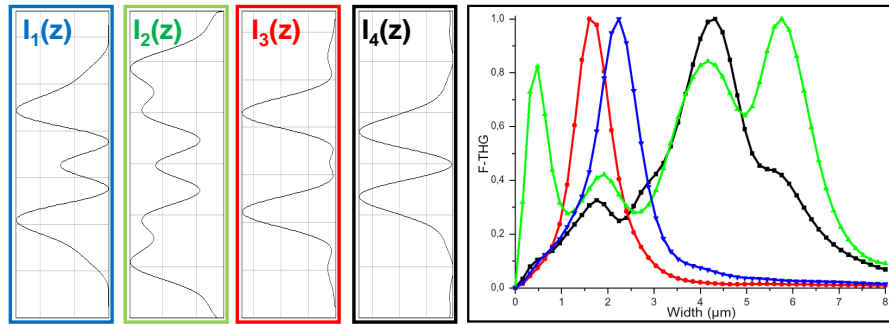


Figure 4.5: THG COHERENCE LENGTH USING PHASE-MASKS

(Left) Axial Intensity distribution and (Right) F-THG signal as a function of the width of a z -oriented slab for 4 different phase masks.

The THG signal from a centered xy -oriented slab using a phase-mask-modulated excitation is given in figure (4.5) for four different phase-masks. While these simulations confirm that we can shift these curves away from what a Gaussian excitation would yield (see figure (3.4 for reference), their interpretation remains complex, since the intensity and phase distribution are modified in all three dimensions. For example, the size dependence curves given by the blue and red excitations that have relatively similar axial intensity distributions are significantly different.

Although we could give a rough estimate of the effective coherence length by looking at the signal dependence on the width of the slab (at least when we have a mostly single-peaked profile), it would still only be an averaged estimate as the phase-matching conditions are also dependent on the position of the slab within the focal volume, and so it this strategy would be practical only for large structures.

4.3.2.2 Quasi-Phase-Matching in Periodic Structures

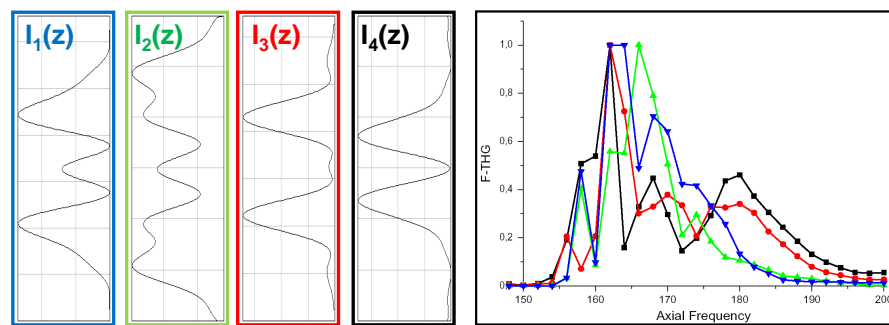


Figure 4.6: QPM B-THG USING PHASE-MASKS

(Left) Axial Intensity distribution and (Right) B-THG signal as a function of the axial period for 4 different phase masks.

Since we can easily have an excitation with several axial peaks instead of one main peak, we thought initially that we could significantly change the quasi-phase-matching conditions and thus enlarge the range of axial frequencies that could provide B-THG signal. However, this is not that easy, as we can see in figure (4.6): the backward phase-matching conditions are still dominated by the \mathbf{k} vector direction mismatch, and the frequency of the axial modulations

provided by the phase-mask are too long to compensate it efficiently.

In the forward direction, we have mostly the same problem as in the case of slabs: since quasi-phase-matching relies on the correction of a constant phase-mismatch, it is difficult to control with field distributions that are too irregular. Moreover, when a given frequency does yield a significant increase in THG signal, changing the initial sample spatial phase can alter the signal, meaning it is yet again a complex approach.

In the next section, we will discuss a simpler modulation scheme that relies on an amplitude-mask and yields a Bessel beam.

4.4 THG Microscopy with Bessel Beams

4.4.1 Bessel Beams: Definition & Properties

Before the Bessel beam was defined, the use of an annular aperture in the back focal plane of a lens had been investigated [11], and such beams had been shown to increase the depth of field [12, 43]. However, in the literature Bessel beams are distinct from the annular aperture beams, and we can mostly divide the field into two parts: the field of Bessel beams whose main interest lies in the non-diffractive property of Bessel beams, and the field of aperture filters which is more concerned about the focal intensity distribution⁴.

Bessel beams were first defined as such by Durnin *et al.* [45–47] who introduced them as a theoretical solution of the wave equation that is non-diffracting [48]. They can also be defined as the field created by an infinitely small annular aperture placed in the back focal plane of a focusing lens, which can be written as :

$$\mathbf{E}(\rho, \phi, z) = \frac{ikf e^{-ikf}}{2\pi} \int_0^{\theta_m} \int_0^{2\pi} e^{-ikz \cos(\theta)} e^{-ik\rho \sin(\theta) \cos(\phi-\theta)} \sin(\theta) \mathbf{E}_0 \delta(\theta_0) d\phi d\theta \quad (4.2)$$

$$= B_0(\theta_0) e^{-ikz \cos(\theta_0)} \int_0^{2\pi} e^{-ik\rho \sin(\theta) \cos(\phi-\theta)} d\phi \quad (4.3)$$

$$= B_0(\theta_0) e^{-ikz \cos(\theta_0)} J_0(k\rho \sin(\theta_0)) \quad (4.4)$$

where J_0 is the 0th order Bessel function.

We can see directly from this equation the non-diffractive property of Bessel beams, as their intensity distribution does not depend on the value of the z (axial) coordinate. Figure (4.8) illustrates the phase and intensity distribution of a perfect Bessel beam, as defined in equation 4.4.

There are several ways to produce Bessel beams experimentally [49]:

- An amplitude-mask placed at the back focal plane of a lens was the first method used [45, 46], and is the closest to the definition given in equation 4.4
- Conical axicon lenses [50–52] have been used to produce Bessel-like beams.
- Phase-masks [53, 54] relying on the fact that the Fourier transform of a Bessel function is a ring are more efficient than amplitude-masks.

When using the amplitude-mask described in figure (4.7), the field at the focus considering a Gaussian intensity profile just before the mask can be written as:

$$\mathbf{E}(\rho, \phi, z) = E_1 \begin{bmatrix} I_{010}^{\theta_0^-, \theta_0^+} + I_{011}^{\theta_0^-, \theta_0^+} + (I_{210}^{\theta_0^-, \theta_0^+} - I_{211}^{\theta_0^-, \theta_0^+}) \cos(2\phi) \\ (I_{210}^{\theta_0^-, \theta_0^+} - I_{211}^{\theta_0^-, \theta_0^+}) \sin(2\phi) \\ -2i I_{120}^{\theta_0^-, \theta_0^+} \cos \phi \end{bmatrix} \quad (4.5)$$

where $I_{jkl}^{\alpha\beta}$ is defined in equation (2.22), $\theta_0^+ = \theta_0 + \Delta\theta$ and $\theta_0^- = \theta_0 - \Delta\theta$, which is the same expression as for a Gaussian beam, except θ is integrated only over a small interval.

⁴see for example the erratum of reference [44] for a comment on that subject

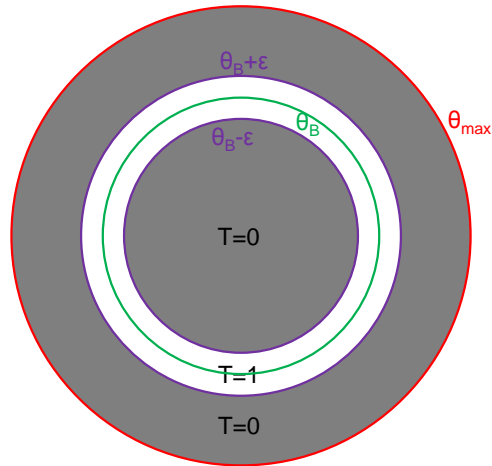


Figure 4.7: AMPLITUDE-MASK USED TO SIMULATE BESSEL BEAMS

The amplitude-mask is an annular aperture described by its numerical aperture θ and the width of the aperture $\Delta\theta$.

Figure (4.8) illustrates the phase and cubed intensity distribution of a Bessel Beam both in the perfect case described in equation (4.4) and with numerical simulations done using an amplitude-mask described by equation (4.5). Several important observations can be made from this field distribution:

- The perfect Bessel beam is a valid approximation in the focal volume.
- The absence of Gouy phase-shift: instead of an abrupt π phase-shift, we have a constant phase-shift over the focal volume.
- The cubed intensity distributions show a lateral intensity distribution that follows a Bessel-function profile. However, in our numerical simulations the axial intensity distribution is not constant like in a perfect Bessel beam, though it is much longer than what we would get from a focused Gaussian beam with the same lateral FWHM.

4.4.2 THG with Bessel Beams

Glushlow *et al.* [55] experimentally demonstrated what they called *self-phase matching* in third-harmonic generation in gases using ring beams obtained using an annular aperture. Tewari *et al.* [56, 57], showed that these beams corresponded to what had been described by Durnin *et al.* [45, 46] as Bessel beams, and derived a paraxial scalar theory of third harmonic generation using Bessel beams in homogeneous media. Peet *et al.* [58, 59], and Caron in the case of the more realistic Bessel-Gauss beam [60, 61] later expanded this theory. Second harmonic generation using Bessel beams has also been investigated [44, 62, 63].

The idea behind self-phase matching is that when we consider a phase-matched process it is usually highly dependent on the sample properties (in particular on its refractive indices). However, in the case of harmonic generation with Bessel beams, the process is much more robust. The paraxial theory developed in references [56, 57] explains this phenomenon by considering a Bessel-Bessel interaction and studying the constraints given by the phase-matching conditions.

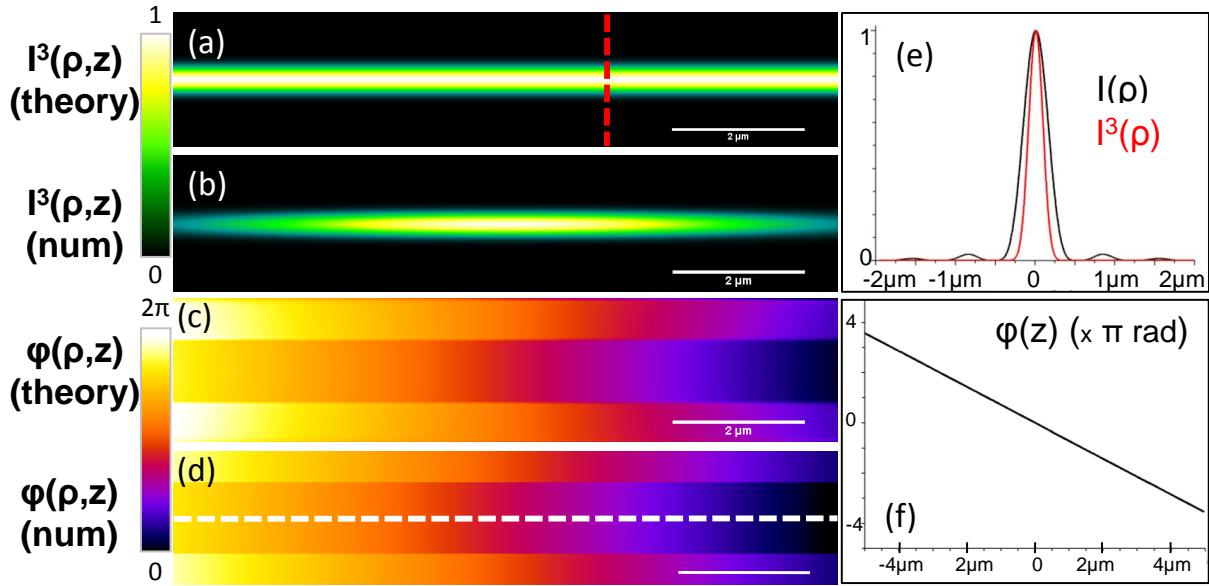


Figure 4.8: INTENSITY AND PHASE DISTRIBUTION OF THE PERFECT AND AMPLITUDE-MASK GENERATED BESSEL BEAM

Cubed intensity (I^3) (resp phase) of the perfect Bessel beam (a) (resp (c)) described by equation 4.4 and of the amplitude-mask generated Bessel beam described by equation 4.5 (b) (resp (d)).

We will discuss THG with focused Bessel beams in the next section. In particular we will investigate whether *self-phase matching* is possible in regular dispersive media under tight-focusing conditions.

4.4.3 THG Microscopy with Bessel Beams

We remind the phase matching conditions for third harmonic generation:

$$\Delta k = |3(\mathbf{k}_\omega) - \mathbf{k}_{3\omega}| \quad (4.6)$$

We consider a Bessel beam characterized by an excitation angle α as an excitation, so we can write $\mathbf{k}_\omega = k_\omega \cos(\alpha) \mathbf{e}_z$. We can now consider two different hypotheses for the harmonic field:

1. It can be a plane wave emitted at an angle ϕ from the optical axis.
2. It can be a Bessel beam described by an angle β ⁵.

4.4.3.1 Bessel - Plane Wave Interaction

We consider an emission with an angle ϕ relative to the optical axis. The projection of equation 4.6 on the z axis yields:

⁵Described in more details in the appendix A.6

$$\Delta k = |3(k_\omega \cos(\theta_0)) - k_{3\omega} \cos(\phi)| \quad (4.7)$$

$$\begin{aligned} &\Downarrow \\ \cos(\phi) &= \frac{3(k_\omega \cos(\theta_0))}{k_{3\omega}} \end{aligned} \quad (4.8)$$

When there is positive dispersion, $\phi > \alpha$, no dispersion $\phi = \alpha$ and negative dispersion $\phi < \alpha$.

The projection of the phase matching conditions perpendicularly to the optical axis yields $\Delta k_\rho = k_{3\omega} \sin(\phi)$. However, if we consider the nonlinear wave equation, the two directions cannot be de-coupled, and we have a 2D differential equation. This is why we will consider a Bessel-Bessel interaction in the next section.

4.4.3.2 Bessel-Bessel Interaction

The axial phase-matching conditions can be written as:

$$3k_\omega \cos(\alpha) = k_{3\omega} \cos(\beta) \quad (4.9)$$

The relation between α and β is the same as between α and ϕ : when there is so positive dispersion, $\beta > \alpha$, no dispersion $\beta = \alpha$ and negative dispersion $\beta < \alpha$.

The consequence of this phase-matching condition is illustrated in figure (4.9), where the far field THG intensity is calculated for two cases:

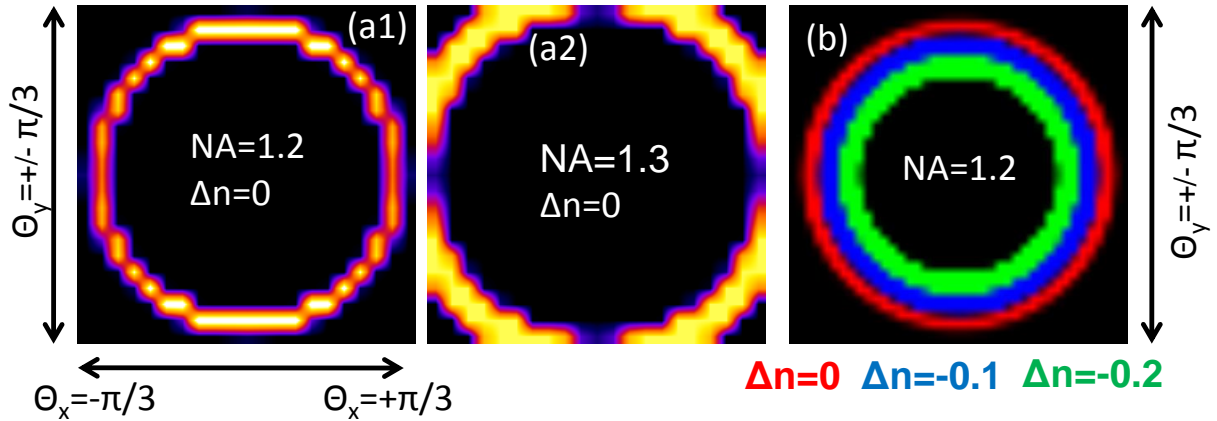


Figure 4.9: THG WITH BESSEL BEAMS: FAR-FIELD EMISSIONS

(a) & (b): $I(3\omega, x, y)$ for $z = 1$. The emission angle increases with the NA (a1 & a2), and decreases with the amount of negative dispersion (b). Conditions: $\lambda = 1.2\mu\text{m}$, $n_\omega = 1.5$.

- figure (4.9.a) illustrates the influence of the focusing conditions on the harmonic signal obtained from a homogeneous non-dispersive medium. The tighter the focus, the larger the angle α is and consequently, the larger β is. Since we consider we are in the far field, the intensity profile created by a Bessel beam β is ring-shaped.

2. figure (4.9.b) illustrates the influence of the dispersion on the angle of emission. In this case, we consider an homogeneous medium and a single focusing condition, but three different values for the dispersion: $\Delta n = 0, -0.1$ and -0.2 . As expected, we see that the more negative dispersion we have, the narrower the emission pattern becomes. Not shown in these normalized intensity distributions is the influence of the negative dispersion on the amount of harmonic signal, which increases with the amount of negative dispersion.

Moreover, if we consider a perfect phase-matching condition along the z -axis, the amplitude of the harmonic Bessel beam can be calculated as:

$$A_{3\omega} \propto \int_0^\infty \rho J_0^3(\rho \sin(\beta)k_\omega) J_0(\rho \sin(\alpha)k_{3\omega}) d\rho \quad (4.10)$$

This integral is non-zero only in the case of negative dispersion where $\beta < \alpha$, which is the same result as with Gaussian beams. However, this equation considers a perfect Bessel beam, which intensity is constant everywhere, and may not be well-adapted to describe focused Bessel beams. The phase-matching conditions are significantly different from the case of Gaussian excitation. Therefore, the structure sensitivity of THG with Bessel beams also is significantly different.

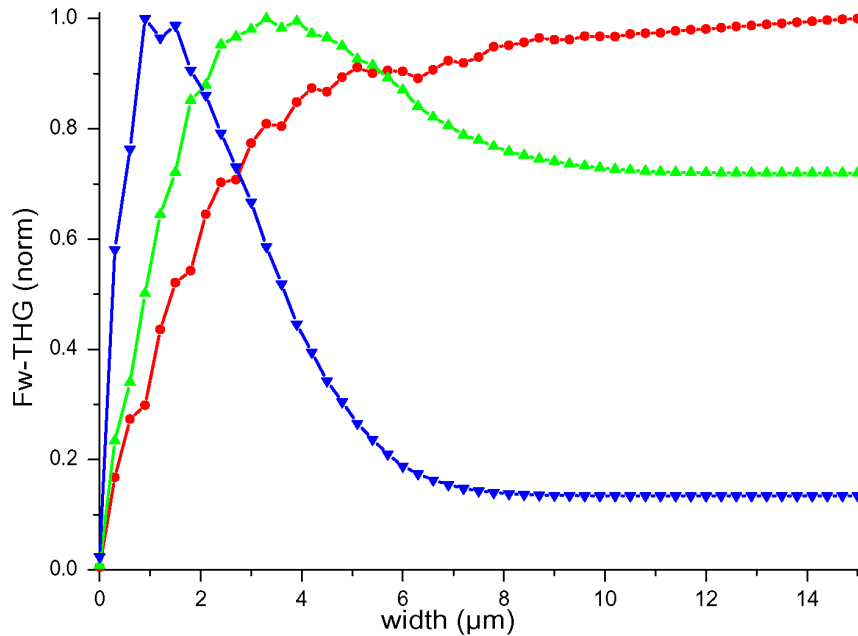


Figure 4.10: THG WITH BESSEL BEAMS AS A FUNCTION OF THE SIZE OF A SLAB

Geometry described in figure (3.3.b) Conditions: Red curve: NA=1.1, Green: NA=1.2, Blue: NA=1.3, $n_\omega = n_{3\omega} = 1.5$.

Figure (4.10) illustrates the THG signal obtained from an xy -oriented slab as a function of its width for three Bessel beams with different numerical apertures, assuming zero dispersion. Consistently with what is predicted in the case of a perfect Bessel beam, we find that some signal can be obtained from a non-dispersive medium, though much less than in the case of negative dispersion. This is consistent with the lateral phase matching conditions that can be written as $k_{3\omega} \sin(\beta)$, as β decreases with the amount of negative dispersion. Moreover, Bessel

beams characterized by a smaller NA appear to be more efficient for producing THG from a homogeneous sample. These results can be interpreted in two different ways:

1. Our calculations may be inaccurate because of the finite size of the simulation domains (reduced focal volume) we consider, as lower numerical apertures imply a longer axial spread of the energy. However, when we increased the size of the domain in both axial and lateral dimensions, we did not find any difference in the shape of the response.
2. If we consider the cubed intensity of the Bessel beam, it seems we can neglect the lateral intensity distribution after the first zero of the Bessel function, so a Bessel beam focused in a homogeneous sample can be compared with a Gaussian beam focused on a narrow axially oriented cylinder, as described in section 3.1.3.1, albeit with a different emission angle. The shape of the size dependence can then be explained not by the increasing amount of signal from a homogeneous sample, but by the reduced amount of signal obtained from a finite slab.

4.4.4 Quasi-Phase-Matching Using Bessel Beams

Since the phase matching conditions can be simply described in Bessel beams thanks to the small variations in both phase and intensity over long distances, Bessel beams are good candidates for quasi-phase matching experiments. For example, quasi-phase-matched second harmonic generation has been experimentally demonstrated [64].

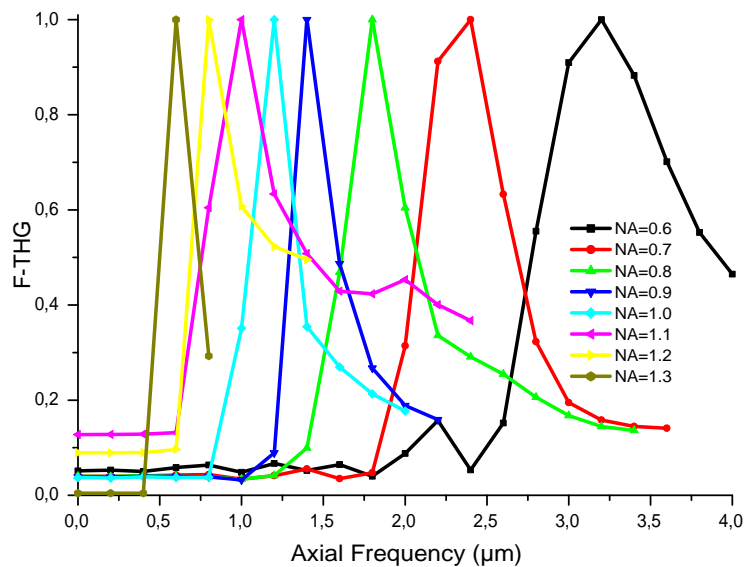


Figure 4.11: QUASI-PHASE-MATCHING OF BESSEL BEAMS
F-THG signal with different focusing conditions and different axial periods.

The case of third harmonic generation in the quasi-phase matching geometry considered in section 3.2 is illustrated in figure (4.11) for several Bessel beams characterized by different numerical apertures. Contrary to the case of QPM THG with Gaussian beams described in section 3.2, we now have a very efficient quasi phase-matching process, because the phase and intensity distribution vary very slowly in the axial direction, and keep the same profile in the lateral direction, which means the phase matching conditions do not depend significantly on the axial position of the sample, and thus the QPM period is the same everywhere and the

increase is larger.

Therefore, a very interesting property of Bessel beams is that they provide a way to probe the axial organization of a sample, since by changing the numerical aperture of the excitation we can change the resonance frequency from $\approx 500nm$ to $\approx 5\mu m$.

4.5 Rapid Wavefront Modulation in 2PEF Microscopy

4.5.1 Introduction

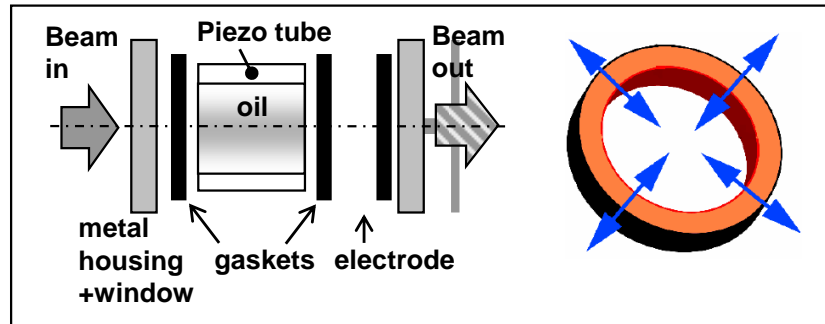


Figure 4.12: SCHEMATIC DESCRIPTION OF THE TAG LENS
See text for more details. Adapted from [65].

This section presents an application of focus engineering in incoherent nonlinear microscopy, and is the result of a collaborative work with the team of Craig Arnold at Princeton University. The wavefront modulator we used is an acousto-optic modulator called TAG⁶ lens developed at Princeton. The TAG lens, described in figure (4.12), consists of a cylindrical piezoelectric shell driven at ultrasonic frequencies (100kHz-2MHz) to generate standing pressure waves in a transparent filling fluid (silicone oil). In turn, the acoustic wave induces a periodic alteration of the refractive index inside the lens with fixed radial nodes [66]. The TAG lens as been shown to allow dynamic beam shaping [67], the production of multi-scale Bessel beams [68, 69], and the focusing of beams with variable focal lengths [70].

The optical index induced by the acoustic field can be expressed as: [66]

$$n(\rho, t) = n_0 + n_a J_0 \left(\frac{\omega \rho}{v} \right) \sin(\omega t) \quad (4.11)$$

where ω is the driving frequency, v is the speed of sound in the medium, n_0 the static index of refraction, and n_a depends on the filling fluid properties. This means the TAG lens can be used to produce Bessel beams. The properties of Bessel beams have been discussed earlier, and their use in increasing the depth of field in incoherent multiphoton microscopy have already been demonstrated elsewhere [23], so the aim of this study was to use the TAG lens as a *rapidly switchable* tool that could provide us with both regular Gaussian beams and Bessel beams in order to do simultaneous interlaced multiphoton imaging with normal and extended depth of field.

The result of this collaboration is presented in the next few pages.

4.5.2 Two-photon Microscopy with Simultaneous Standard & Extended Depth-of-Field Using a Tunable Acoustic Gradient-index Lens

⁶Tunable Acoustic-driven Gradient-index Lens



Figure 4.13: CTRL+C/V

Nicolas Olivier, Alexandre Mermillod-Blondin, Craig B. Arnold, & Emmanuel Beaurepaire
Two-photon microscopy with simultaneous
standard and extended depth of field
using a tunable acoustic gradient-index lens
June 1, 2009 / Vol. 34, No. 11 / OPTICS LETTERS

Two-photon microscopy with simultaneous standard and extended depth of field using a tunable acoustic gradient-index lens

Nicolas Olivier,¹ Alexandre Mermillod-Blondin,² Craig B. Arnold,² and Emmanuel Beurepaire^{1,*}

¹Laboratory for Optics and Biosciences, Ecole Polytechnique, CNRS, INSERM, F-91128 Palaiseau, France

²Department of Mechanical and Aerospace Engineering, Princeton University, Princeton, New Jersey 08544, USA

*Corresponding author: emmanuel.beurepaire@polytechnique.edu

Received March 27, 2009; accepted April 24, 2009;
posted May 7, 2009 (Doc. ID 109299); published May 28, 2009

We describe a simple setup that allows depth of field switching at kilohertz rates in a nonlinear microscope. Beam profile and/or divergence are modulated using a tunable, acoustically driven gradient-index fluid lens. We demonstrate two modulation strategies, one based on fast varifocus scanning during each pixel and the other based on pseudo-Bessel beam excitation. Average beam shape is switched every line during scanning, resulting in the interlaced acquisition of two different images. We apply this approach to the simultaneous standard and $4.5\times$ -extended depth-of-field imaging of developing embryos. © 2009 Optical Society of America

OCIS codes: 180.4315, 140.3300, 230.1040, 110.1080, 180.6900, 170.3880.

Two-photon microscopy [1] is widely used for high-resolution biological imaging, providing micrometer optical sectioning in complex samples. Optical slices are typically recorded by scanning the focused laser beam inside the sample. When needed, a more global representation of the sample can alternatively be obtained by using large depth-of-field optics, such as focused Bessel beams [2,3] produced by axicons [4,5], phase masks [6], or liquid-crystal-based spatial-light modulators [7]. However, these wavefront control strategies are either fixed or too slow to allow for rapid modulation between the two imaging regimes during a scan. Therefore, diffraction-limited and extended-depth images must be acquired sequentially.

We explore here an alternative approach. Using rapidly adjustable acousto-optic fluid lens technology, it is possible to construct a light-efficient imaging method with the ability of depth of field switching at kilohertz rates.

Imaging with shaped beams is performed as follows (see Fig. 1). The output beam from a Ti:sapphire oscillator is sent through a tunable, acoustically driven gradient-index (TAG) fluid lens [8–11], providing phase modulation. The TAG lens consists of a cylindrical piezoelectric shell driven at ultrasonic frequencies (100–800 kHz) to generate standing pressure waves in a transparent filling fluid (silicone oil). In turn, the acoustic wave induces a periodic alteration of the refractive index inside the lens with fixed radial nodes [8,9]. Galvanometric mirrors angularly scan the beam at the pupil of a water-immersion objective, and two-photon-excited fluorescence (2PEF) is epifluoresced using a photon-counting photomultiplier.

To acquire two simultaneous images, we use an interlaced acquisition scheme in which each line is scanned twice, and the modulation amplitude of the acoustic lens is switched between lines during galvanometer flyback. We typically acquire odd lines with

near-zero modulation amplitude (off), and even lines with 10–21 V amplitude sine modulation (on). A stable pattern in the TAG is achieved in a few tens of microseconds, i.e., before the next line starts. The two images are deinterlaced after acquisition.

In a first configuration, we use the TAG lens as a varifocus device (Fig. 2). The TAG lens is positioned at the output of the Ti:sapphire laser where the beam is smallest, so that it experiences the refractive index distribution only near the center of the lens, which can be approximated in cylindrical coordinates by [10]

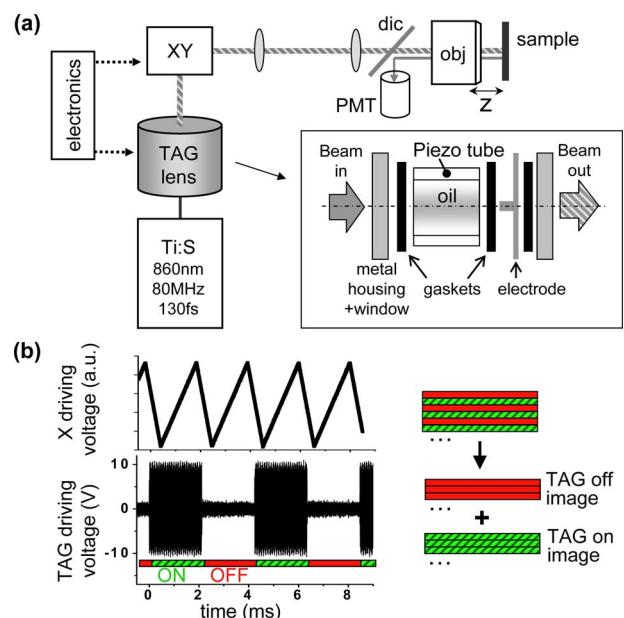


Fig. 1. (Color online) (a) Microscopy with acoustically modulated beams. TAG lens, tunable acoustic gradient-index lens (inset). XY, lateral scanning; dic, dichroic; PMT, photomultiplier; obj, 20×0.95 NA objective with under-filled pupil. (b) Principle of the interlaced acquisition with standard (off) and modulated (on) beams.

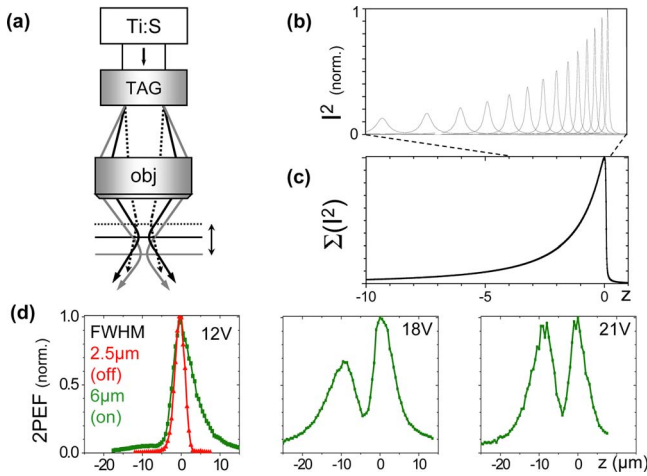


Fig. 2. (Color online) Point-spread functions (PSFs) obtained when using the TAG lens as a fast varifocus device. (a) Principle: beam divergence at the objective pupil is rapidly modulated during one pixel acquisition time. (b), (c) Numerical simulations of the instantaneous (b) and time-averaged (c) on-axis intensity distribution. (d) Experimental axial 2PEF PSFs recorded from 330 nm beads switches from 2.5 μm (lens off) to 6 μm (on) FWHM and exhibits a two-lobe distribution when applying large modulation amplitudes (see text).

$$n(\rho, t) = n_0 + \left(n_a \frac{\omega^2 \rho^2}{4v^2} \right) \sin(\omega t), \quad (1)$$

where ω is the driving frequency, n_0 is the static index of refraction, v is the speed of sound in the acoustic medium, and n_a depends on the medium and the modulation parameters. The lens is located ≈ 1 m before the galvanometric mirrors and is driven at a frequency of 481 kHz. The pixel rate is set to 240 kHz, meaning that each pixel is the sum of ≈ 330 pulses, effectively covering the entire focal range of the lens twice per pixel. Each of these pulses sees the TAG as a fixed lens with optical power ranging from $-\delta_{max}$ to $+\delta_{max}$, resulting in variable beam divergence at the objective pupil. This system can be simply modeled under Gaussian paraxial approximation. Two regimes must be considered. In the first case, the focal length of the acoustic lens is always larger than the distance to the objective. The effective point-spread function (PSF) is then the incoherent superposition of instantaneous PSFs with different axial positions, widths, and intensities, resulting in the broad asymmetric distribution qualitatively predicted in Fig. 2(c) and experimentally illustrated in the first panel of Fig. 2(d), where $\delta_{max} < 2 \text{ m}^{-1}$. (Simulation parameters, $\delta_{max} = 1 \text{ m}^{-1}$; beam waist $w = 1 \text{ mm}$; objective $f = 2 \text{ mm}$.) A second regime occurs if the focal range of the acoustic lens is increased up to where it focuses the beam before the objective, and a second axial lobe builds up. This regime is reached by increasing the modulation amplitude, as illustrated in the remaining panels of Fig. 2(d), where $\delta_{max} > 4 \text{ m}^{-1}$.

The resulting PSF is significantly extended, but it exhibits an axial gap. This issue can be avoided by using the acoustic lens as a pseudo-Bessel beam generator. This is achieved here by driving the TAG lens

at a higher frequency (740 kHz) and by expanding the beam twice so that it fills a larger part of the lens and propagates through a refractive index distribution that can be described as [11]

$$n(\rho, t) = n_0 + n_a J_0 \left(\frac{\omega \rho}{v} \right) \sin(\omega t). \quad (2)$$

As in the previous experiment, the laser and the piezo are not synchronized, meaning that successive pulses experience different modulations. The resulting time-averaged intensity is a multiscale Bessel beam with a transverse profile exhibiting a central peak surrounded by successive rings [11], which may be viewed as intermediate between a Gaussian and a Bessel beam. The position of the TAG lens relative to the microscope is adjusted so that the propagated unshaped beam [off, Fig. 3(a)] and the first major ring [on, Fig. 3(b)] have similar sizes at the objective pupil. When the TAG is on, all the instantaneous PSFs are axially elongated, and their incoherent superposition resembles that of a focused Bessel beam. Figure 3 displays images of 330 nm fluorescent beads in a 3D gel recorded with and without an extended depth of field. Beam shaping results in a 4.5-fold axial increase of the PSF without degrading lateral resolution ($\sim 0.6 \mu\text{m}$ FWHM, not shown), characteristic of Bessel-like excitation. In turn, extended depth of field results in more visible beads.

Finally, we show that this technique can be used for two-photon imaging of biological samples in a

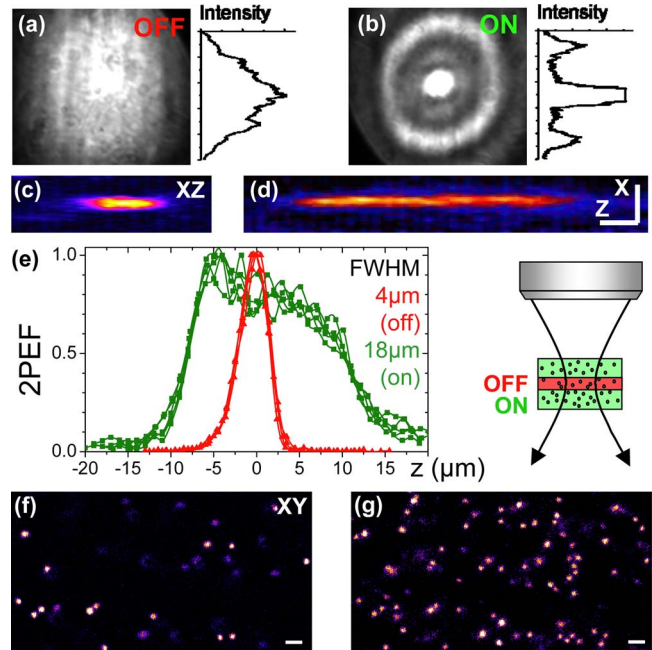


Fig. 3. (Color online) TAG lens used as a pseudo-Bessel beam generator. (a), (b) Average intensity distribution at the back aperture of the objective with the lens off and on. (c), (d) Z-X, 2PEF images of 330 nm fluorescent beads recorded with standard [(c), off] and extended [(d), on] depth of field. (e) z profiles through several bead images. FWHM are $4.0 \pm 0.2 \mu\text{m}$ (off) and $18.3 \pm 0.4 \mu\text{m}$ (on). (f), (g) Beads in a 3D gel imaged with standard and extended depth of field. Scale bars, 3 μm .

straightforward manner. Figures 4(a1) and 4(a2) present simultaneous standard and extended-depth images of a pollen grain recorded in two different planes separated by $12\ \mu\text{m}$. Although the optically sectioned images are very different, the corresponding extended-depth images obtained simultaneously with pseudo-Bessel excitation are similar and provide a more global view of the sample. Figures 4(b1) and 4(b2) (Media 1) illustrate the fast switching capability of the TAG lens, which makes it suitable for imaging dynamic samples. Here, a developing *Drosophila* embryo with green-fluorescent-protein-labeled nuclei is observed continuously in a single plane during gastrulation. We oriented the embryo with the ventral side up (facing the objective) so as to image

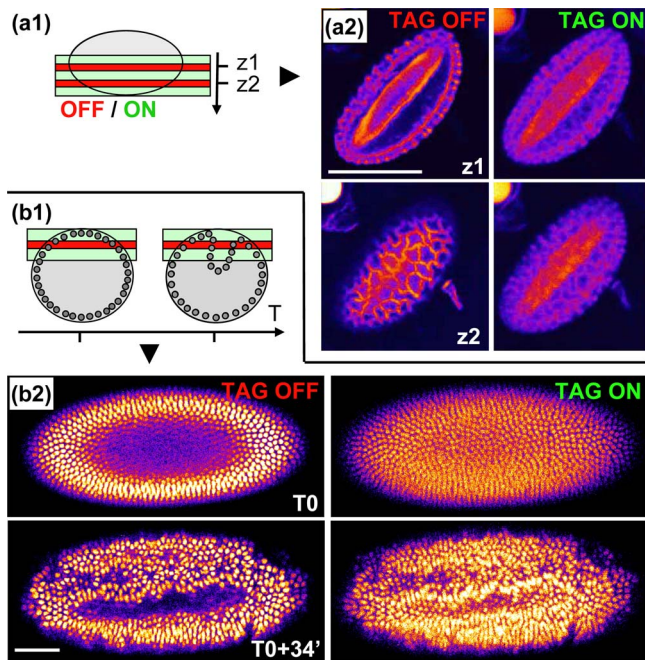


Fig. 4. (Color online) Two-photon imaging of a developing *Drosophila* embryo and of a pollen grain with simultaneous standard and extended depth of field. (a1), (a2) Images of a fixed pollen grain recorded at axial locations separated by $12\ \mu\text{m}$. The standard (off) images provide optical slices, whereas the simultaneously recorded extended-field images (on) provide a more global view of the sample. (b1), (b2) (Media 1) Time-lapse imaging of a developing *Drosophila* embryo with GFP-labeled cell nuclei, during ventral furrow formation. The beam focus was kept just below the outer cells of the ventral side, as illustrated in (b1). The standard movie shows the invaginating ventral cells passing through the focal plane, whereas the simultaneous extended-depth movie provides a global view of lateral cell movements during furrow formation. See Media 1. Scale bars, $50\ \mu\text{m}$.

the formation of the ventral furrow, an early process involving cell invagination toward the middle of the embryo. The imaging plane is positioned just below the outer cells, so that early invaginating cells show up progressively in the standard time-lapse image. The extended-depth image provides a complementary global representation of the tissue that could not be obtained simultaneously using slow or static beam-modulation devices.

In conclusion, we have shown that an acoustically driven fluid lens can provide kilohertz switching rates between standard and extended-depth imaging in two-photon microscopy. This arrangement is simple, inexpensive, and light-efficient (90% transmission over the 750–880 nm range). Furthermore, acoustic lenses can produce more-complex beam shapes, such as multiscale Bessel beams [11], and can be synchronized with the pulse train for increased wavefront control when using kilohertz laser systems. Additional perspectives include imaging with tunable depth-of-field and spatial control of multiphoton processes for imaging and sample-processing applications.

We thank X. Solinas for assistance in electric interfacing, E. McLeod for many discussions, and D. Débarre for comments on the manuscript. This work was partially supported by the Délégation Générale pour l'Armement (DGA), the Agence Nationale de la Recherche (ANR), and the U.S. Air Force Office of Scientific Research (AFOSR).

References

1. W. Denk, J. H. Strickler, and W. W. Webb, *Science* **248**, 73 (1990).
2. J. Durnin, J. J. Miceli, and J. H. Eberly, *Phys. Rev. Lett.* **58**, 1499 (1987).
3. D. McGloin and K. Dholakia, *Contemp. Phys.* **46**, 15 (2005).
4. P. Dufour, M. Piché, Y. De Koninck, and N. McCarthy, *Appl. Opt.* **45**, 9246 (2006).
5. Z. Ding, H. Ren, Y. Zhao, J. S. Nelson, and Z. Chen, *Opt. Lett.* **27**, 243 (2002).
6. E. J. Botcherby, R. Juskaitis, and T. Wilson, *Opt. Commun.* **268**, 253 (2006).
7. J. A. Davis, C. S. Tuvey, O. Lopez-Coronado, J. Campos, M. J. Yzuel, and C. Iemmi, *Opt. Lett.* **32**, 844 (2007).
8. K. A. Higginson, M. A. Costolo, and E. A. Rietman, *Appl. Phys. Lett.* **84**, 843 (2004).
9. E. McLeod and C. B. Arnold, *J. Appl. Phys.* **102**, 033104 (2007).
10. A. Mermillod-Blondin, E. McLeod, and C. B. Arnold, *Opt. Lett.* **33**, 2146 (2008).
11. E. McLeod and C. B. Arnold, *Appl. Opt.* **47**, 3609 (2008).

4.6 Adaptive Optics

In this section we will discuss the correction of aberrations in microscopy, in particular in coherent nonlinear microscopy. The project was implemented with D. Débarre and relied on the methodology she previously developed while in the Booth-Wilson team (Oxford University) for correcting aberrations in 2PEF microscopy [71].

The term *adaptive optics* comes from astronomy [72], where it is defined as a type of aberration correction scheme that can be updated faster than the typical variations of the aberrations, and is different from *active optics* that provide a correction adapted for longer time-scales. In microscopy, the first objective is to correct for static aberrations, but dynamic correction schemes can also be applied, (as we will see in section 4.6.2) and the generic term *aberration correction* is also commonly used.

4.6.1 Introduction

Figure (4.14) illustrates the principles of aberration correction: everything that is between the imaged plane and the detector (eg: the atmosphere in astronomy, the objective and the sample in microscopy) has imperfect optical properties resulting in the presence of aberrations that degrade the image quality. However, by inserting an active element that compensates for the aberrations, the image quality can be restored. Aside from astronomy, adaptive optics has found several applications in ophthalmology [73] (the eye is far from being a perfect optical system)

4.6.2 Aberration Correction in Microscopy

Before active optical elements such as deformable mirrors or spatial light modulators became available⁷, several studies focused on the influence of aberrations in microscopy. The theoretical influence of aberrations modes on the point spread function in confocal microscopy [74–76] and their influence in limiting the imaging depth were investigated [77, 78]. Measurement of sample-induced aberrations has been performed on different types of tissue by Schwertner *et al.* [79, 80].

The first articles demonstrating the correction of aberrations were performed in the case of fluorescence microscopy, for both linear [81] and nonlinear [82–84] excitations, as the maximization of the signal provided an easy optimization strategy (though the demonstration of the effectiveness of this strategy would have to wait for a few years). In both cases, the optimization method relied on the maximization of the fluorescence intensity using different amounts of aberration introduced by a deformable mirror. Aberration corrections in other types of microscopy followed, including CARS [85] and structured illumination microscopy [86].

Correction schemes have been proposed for different types of microscopy: Rueckel *et al.* demonstrated an aberration correction scheme that relied a direct measurement of the aberrations at the focus [87] using coherence-gated wavefront sensing (CGWS) [88], which allows the correction of the aberrations theoretically in one step, and practically in 3-5 iterations. All the other methods rely on the optimization of a criterion, but use different optimization strategies. Several studies relied on stochastic methods such as genetic algorithms [83–85, 89, 90], that rely on a very large number of iterations (several thousands) but can explore a very large optimization space and work even in poorly formulated optimization problems. Another approach

⁷and affordable

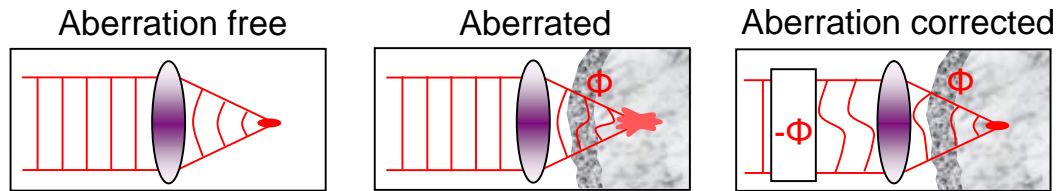


Figure 4.14: PRINCIPLE OF ABERRATION CORRECTION

The aberrations introduced by the propagation through an imperfect optical system can be compensated by the presence of an active element and the image quality can be restored

to the optimization problem is to use model-based methods [71, 81, 86, 91, 92], in which the optimization problem is re-formulated so as to be easier to solve:

1. The dimension of the problem can be reduced by working on aberration modes instead of on the actuators, as the influence of actuators are often not independent (this has also been used in stochastic methods and has provided significantly faster convergence [90])
2. The optimization of one mode can be simplified by choosing the aberration basis and the optimization criterion so as to have a quadratic problem.
3. The optimization of the aberration modes can be made independent, so that all modes can be optimized sequentially.

This reformulation is completely non-trivial. An example is the maximization of the intensity at the focus by using the Strehl ratio as a criterion and the Zernike polynomials as an aberration basis. Débarre *et al.* reformulated several optimization problems [86, 92], whereafter the correction of n aberration modes only requires $(2n + 1)$ measurements. However, in some cases it may be impossible to obtain a perfect re-formulation.

4.6.3 Experimental Setup

Figure (4.15) illustrates a typical setup for aberration correction in nonlinear microscopy. The active element is a deformable mirror (Mirao, Imagine Optics, more details in appendix B.4) with 52 actuators. In order to insure that the induced aberration are mostly uniform within the field of view of the objective, the mirror should be conjugated with the objective lens. Since the two galvanometric mirrors are not perfectly conjugated with the objective, the mirror should be placed either before or after the galvanometric mirrors, depending on the intensity distribution on the mirror: if the intensity is mostly uniform, then the mirror should be placed after the scanning mirrors, while in the case of an underfilled mirror, it is better to place it before.

4.6.4 Reformulation of the Optimizations Problem

We present in this section an application of image-based correction for THG microscopy. As seen in section 4.6.2, the idea is to reformulate a complex optimization problem into a simple one. We will rely on linear algebra as much as possible in order to define a metric and an aberration basis-set that together allow quadratic optimization.

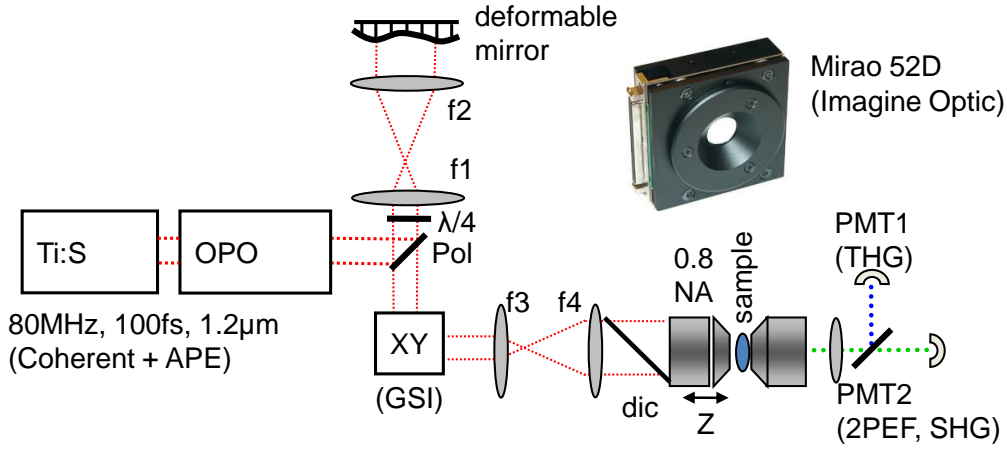


Figure 4.15: EXPERIMENTAL SETUP FOR ABERRATION CORRECTIONS IN NON-LINEAR MICROSCOPY

The excitation wavelength coming from a laser-pumped OPO is reflected by a deformable mirror conjugated with a couple a galvanometric mirrors that are themselves conjugated with the objective lens. (Pol): polarizing beamsplitter cube ($\lambda/4$): Quarter-wave-plate.

4.6.5 Choice of the Metric

Let us assume that we have defined a *quality metric*, calculated from the images, which varies with the aberrations. If we express these as an aberration vector $\mathbf{a} = [a_1 \dots a_n]$ of coefficients on a given basis of aberration-modes, we can write:

$$M(\mathbf{a}) = M(a_1, \dots, a_i, \dots, a_n) \quad (4.12)$$

Ideally, if we choose a suitable metric $M(\mathbf{a})$ should be a quadratic form⁸, so we could define a symmetric matrix A that would verify

$$M(\mathbf{a}) = -\mathbf{a}^T A \mathbf{a} = -\sum_{i,j} a_{ij} a_i a_j \quad (4.13)$$

which should not depend on the imaged sample. This approach has been successfully applied to 2PEF microscopy using the total image intensity as a quality metric [71].

However, because of the complex interplay between the excitation field and the sample geometry in the image formation process in THG microscopy, the problem of choosing a suitable sample-independent metric is difficult to tackle theoretically. We therefore used the following method, described in the following section: first, we defined a set of modes to describe the aberrations, and we subsequently measured on various samples the influence of aberrations on various metric to assess their appropriateness for aberration correction.

4.6.6 Calculation of the Aberration Basis

The aberrations are described by the phase-distribution at the back aperture of the objective. Since this plane is conjugated to the deformable mirror, changing the shape of the mirror produces a phase-only variation of the excitation field in this plane. We can write in the back aperture plane:

⁸or a strictly increasing or decreasing function of a quadratic form

$$E(r) = A(r)e^{i\psi(r)} \quad (4.14)$$

Where $A(r) \in \mathfrak{R}$ is the amplitude and $e^{i\psi(r)}$ is the phase. The deformable mirror used in these experiment is considered to be perfectly linear. It has 52 actuators, so we can write:

$$\psi_X(r) = \sum_{i=1}^{52} x_i \psi_i(r) \quad (4.15)$$

where ψ_i is the phase profile induced by the activation of the actuator i of the mirror and x_i is its displacement amplitude. The phase ψ_X can therefore be expressed as a function of the vector: $\mathbf{X} = [x_1, \dots, x_i, \dots, x_{52}]$. We now have a vector space to describe the aberration induced by the deformable mirror, and using it to calculate the Strehl ratio (S) [93, 94] of the focused aberrated beam, we find:

$$S = 1 - \sum_{X,Y} -X^T \langle X, Y \rangle Y \quad (4.16)$$

where [95]:

$$\langle X, Y \rangle = \frac{\int e^{i\psi_X} e^{i\psi_Y} A(r) dr}{\int A(r) dr} - \frac{\int e^{i\psi_X} A(r) dr \int e^{i\psi_Y} A(r) dr}{(\int A(r) dr)^2} \quad (4.17)$$

is an inner product describing the cross-talk between the different modes with respect to the Strehl ratio. Since S is related to the peak intensity of the excitation beam - a relevant parameter to estimate nonlinear signal generation efficiency - we chose to consider in the following paragraphs the first 11 eigenmodes with respect to this inner product. Since these were derived from mirror modes, they can be accurately reproduced by our mirror, and they correctly describe the low order aberrations that we aim at correcting. This orthogonalization for the Strehl ratio also permits the removal of tip, tilt and defocus from the set of modes that we consider.

4.6.6.1 Intensity

We first tried using the total image intensity as a quality metric, using an image-based orthogonalization of our basis on one sample, and we managed to obtain an optimized image on this sample. However, in order to assess the accuracy of this metric, we compared total image intensity as a function of the amount of aberration in each mode with the total 2PEF intensity recorded simultaneously (which has been shown to reach a maximum in the absence of aberration [71]). For the sample considered in this experiment (lilly pollen grain, see figure 3 of the article), THG signal is maximized for a non-zero amount of aberration, indicating that this metric cannot be used to correct for aberrations.

4.6.6.2 Image Sharpness

We then considered instead the image sharpness as a quality metric, calculated as the sum of the squared pixel values. This choice was motivated by the fact that this measure takes into account the contrast and information content of the images, rather than merely the signal level. We used again as a basis the mirror eigenmodes for the Strehl ratio, cleared of the tip, tilt and defocus that change the position of the focal spot. This means $S(\phi_i, \phi_j) = \delta_{i,j}$ and the phase can be expressed as the vector $\mathbf{a} = [a_1, \dots, a_i, \dots, a_{11}]$. The influence of the modes on the metric were then experimentally estimated on a variety of sample, and we found that we could write:

$$M(\mathbf{a}) = M_0 \exp[-\mathbf{a}^T A \mathbf{a}] \quad (4.18)$$

where A is symmetric positive-definite and exhibits little sample-dependent variations, thereby satisfying the requirements to be used as a quality metric for aberration correction. A is called the *influence matrix*. The knowledge of this matrix is enough to calculate the optimal phase from $(2N+1)$ measurements, as we will see in the next section [96].

4.6.7 Dynamic Aberration Correction for Multiharmonic Microscopy



Figure 4.16: CTRL+C/V

Nicolas Olivier, Delphine Débarre, and Emmanuel Beaurepaire
Dynamic aberration correction
for multiharmonic microscopy
October 15, 2009 / Vol. 34, No. 20 / OPTICS LETTERS

Dynamic aberration correction for multiharmonic microscopy

Nicolas Olivier, Delphine Débarre,* and Emmanuel Beaufrepaire

Laboratory for Optics and Biosciences, Ecole Polytechnique, CNRS, INSERM, F-91128 Palaiseau, France

*Corresponding author: delphine.debarre@polytechnique.edu

Received July 21, 2009; revised September 8, 2009; accepted September 11, 2009;
 posted September 16, 2009 (Doc. ID 114535); published October 8, 2009

We demonstrate image-based aberration correction in a third-harmonic generation (THG) microscope. We describe a robust, mostly sample-independent correction scheme relying on prior measurement of the influence of aberration modes produced by a deformable mirror on the quality of THG images. We find that using image sharpness as an image quality metric, correction of N aberration modes is achieved using $2(2N+1)$ measurements in a variety of samples. We also report aberration correction in combined multiharmonic and two-photon excited fluorescence experiments. Finally, we demonstrate time-dependent adaptive THG imaging in developing embryonic tissue. © 2009 Optical Society of America

OCIS codes: 180.4315, 190.4160, 110.1080, 170.3880, 180.6900.

Nonlinear microscopy is commonly used for biological tissue imaging in a variety of contexts. However, aberrations degrade image quality in thick samples, and aberration correction (AC) strategies are being actively investigated [1,2]. Because direct wavefront sensing *in situ* is nontrivial, image-based modal AC is an attractive possibility [3,4], as shown e.g., for two-photon-excited fluorescence (2PEF) microscopy [5]. The case of image-based AC for coherent nonlinear microscopies such as third-harmonic (TH) generation (THG) [6] or second-harmonic generation (SHG) imaging deserves particular attention, as the harmonic intensity strongly depends on the excitation phase distribution near the focal volume [7,8]. Furthermore, the adaptive observation of living biological samples puts constraints on correction strategies, because the acceptable number of measurements used for the correction is limited by sample evolution. In this Letter we develop a robust, efficient AC strategy for THG microscopy, allowing adaptive THG imaging of dynamic tissue.

In modal AC approaches, the aberrated phase is described by a vector $\mathbf{a}=\{a_i\}$ of projections on a basis set of aberration modes $\{X_i\}$. Here we restricted ourselves to the 11 most influential eigenmodes of our deformable mirror (DM) [Fig. 1(b)], excluding tip, tilt, and defocus, and orthogonalized for the Strehl ratio S [9],

$$\frac{\int \sqrt{I}X_iX_jd\mathbf{r}}{\int \sqrt{I}d\mathbf{r}} - \frac{\int \sqrt{I}X_i d\mathbf{r} \int \sqrt{I}X_j d\mathbf{r}}{\left(\int \sqrt{I}d\mathbf{r}\right)^2} = \delta_{ij}, \quad (1)$$

where I is the excitation intensity at the pupil plane of the objective, δ_{ij} is the Kronecker delta, and the integral is taken over the objective pupil. This choice ensures that low-order aberrations can be properly described, that the correction phase can be accurately produced by the DM, and that for small aberration amplitude, $S \approx 1 - |\mathbf{a}|^2$. Using this representation, AC requires a limited number of measurements if the influence of each aberration mode on image quality,

quantified by a metric M , can be described with a single-peaked function that is mostly independent of the sample structure. Such schemes have proven effective for various incoherent microscopy techniques and permit AC in N modes with only $2N+1$ measurements [3–5].

Owing to the coherent summation of the waves created at different points within the focal volume, the TH signal level results from a complex interplay between sample and field structure [8]; an extended point-spread function can result in a higher signal level [7], and a given amount of aberration may produce sample-dependent intensity variations. Consequently, total image intensity (brightness) is an ill-defined quality metric. Instead, it can be expected that a metric reflecting the information content in the image, such as image sharpness (i.e., the sum of the squared pixel values), would be more robust for the design of a sample-independent AC scheme. Indeed, we observed experimentally in all the tested

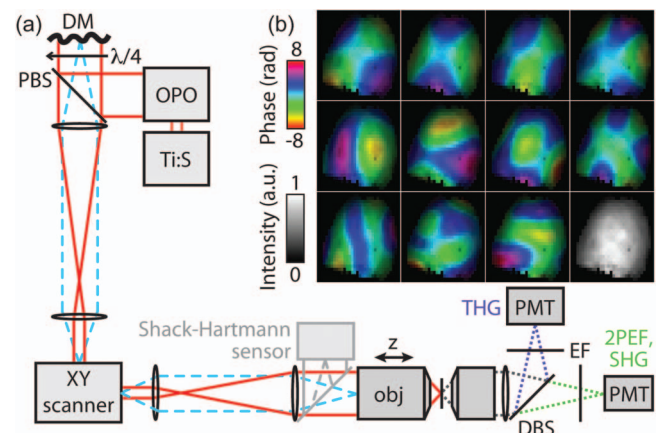


Fig. 1. (a) Experimental setup: $\lambda/4$, quarter wave plate; PBS, polarizing beamsplitter; DBS, dichroic beamsplitter. Solid lines, excitation path; gray, DM characterization path (not used during AC); dotted lines, emission path; dashed lines, conjugated Fourier planes. (b) Modes X_i used for correction, as measured on the SH sensor. The phase is color coded from purple to red (online) with a brightness proportional to excitation intensity. The last image (lower right) shows the intensity profile alone.

samples that, unlike total image intensity, image sharpness could be approximated as

$$M \approx M_0 \exp \left[- \sum_{i,j} \alpha_{ij} a_i a_j \right] = M_0 \exp [- \mathbf{a}^T \cdot \mathbf{A} \cdot \mathbf{a}], \quad (2)$$

where the influence matrix $A = \{\alpha_{ij}\}$ is symmetric positive-definite (i.e., M reaches its maximum value only in the absence of aberration) and exhibits little sample-dependent variation ($< 10\%$). In most situations, image sharpness is thus a suitable metric for AC purpose.

The nondiagonal elements of A , α_{ij} , describe the variation in the correction in one mode i as a function of the amount of aberration in mode j . If the modes have independent influence on M (i.e., $\alpha_{ij} = \delta_{ij}$), the optimal correction can be obtained without prior knowledge of A from a set of $2N+1$ measures of M with different known aberrations introduced with the DM [4]; M_0 with no introduced aberration, and $\{M_{i-}\}$ (respectively, $\{M_{i+}\}$) with $-b_i$ (respectively, $+b_i$) aberration added in mode i , where $b_i \approx 1.5/\sqrt{\alpha_{ii}}$ is chosen to experimentally optimize correction precision. The correction vector $-\mathbf{a}$ is then calculated as

$$-\mathbf{a} = \left\{ \frac{b_i}{2} \frac{\ln M_{i+} - \ln M_{i-}}{2 \ln M_0 - \ln M_{i-} - \ln M_{i+}} \right\}. \quad (3)$$

Alternatively, if there is crosstalk between modes, prior knowledge of A is required and $-\mathbf{a}$ is obtained as

$$-\mathbf{a} = A^{-1} \left\{ \frac{b_i}{2} \frac{\ln M_{i+} - \ln M_{i-}}{2 \ln M_0 - \ln M_{i-} - \ln M_{i+}} \right\}. \quad (4)$$

We implemented this AC scheme on a lab-built microscope [7,10] incorporating a DM and a Shack–Hartmann (SH) sensor (MIRAO-52 and HASO-3, Imagine Optic), and a 20×0.95 NA water-immersion objective with an underfilled pupil (Olympus) [Fig. 1(a)]. Excitation pulses centered at 1180 nm were provided by an optical parametric oscillator (APE).

Results on a coverslip-covered fixed elderberry stem slice are shown in Fig. 2. To obtain an AC scheme that is mostly sample independent, we measured A on various samples [Figs. 2, 3(a), and 3(d)] as detailed in [4], and calculated an average [Fig. 2(c)] used for all subsequent experiments. AC with this matrix increases THG brightness but also the lateral and axial resolution, which could not be obtained by increasing the excitation power. As we used an average A not specific to this sample, the AC process converged only after two iterations, thus requiring a total of 46 exposures. Subsequent iterations did not yield further improvement. Albeit, the residual aberration amplitude being reduced for each AC run, the second run yields significant improvement only for large initial aberration, typically $\mathbf{a}^T \cdot \mathbf{A} \cdot \mathbf{a} \geq 0.3$. Hence for smaller amplitudes, correction does not significantly improve further after more than a single round. In contrast, when assuming a diagonal matrix A , iterative corrections yield a vanishing intensity

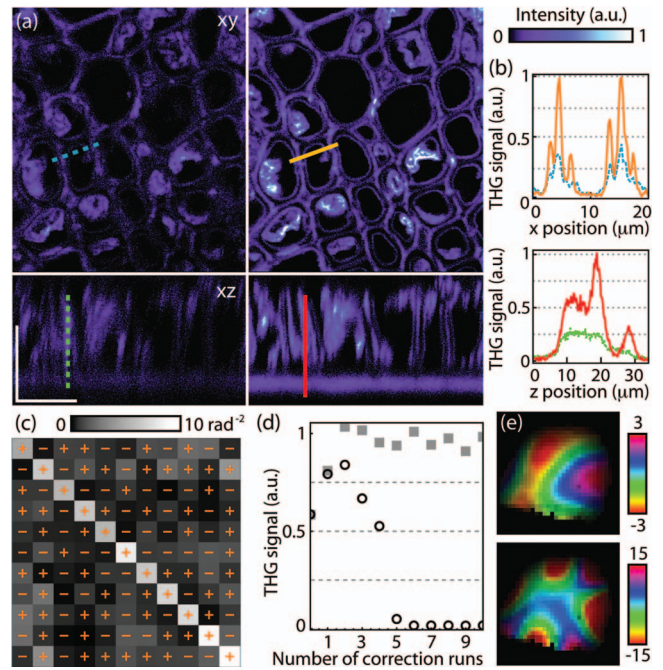


Fig. 2. (a) THG images of an elderberry stem slice (left) before and (right) after AC on the middle plane of the z stack. Scale bars, $20 \mu\text{m}$. (b) Profiles along the lines in (a). (c) Averaged influence matrix A . (d) TH image brightness as a function of the number of AC runs, using A (squares) or assuming independent modes (circles). (e) Corresponding final phases (in radians). The top phase was applied for the corrected image in (a).

and an incorrect AC phase [Figs. 2(d) and 2(e)]. This demonstrates that prior knowledge of A is required for accurate AC.

Although the number of images required for complete correction is large, smaller images can be used to perform correction [5]; we found experimentally that for typical signal levels in these images (as low as 10 photons/pixel), the sampling of images could be greatly reduced provided that the sample structure was still visible. Here in all experiments, the scanning speed and the pixel size were multiplied by 4 so that during AC the imaging time was divided by 16. The increase in sample exposure due to AC was thus limited to $\approx 300\%$ when two rounds of correction were needed and $\approx 150\%$ for one round.

To test the accuracy of this THG sharpness-based scheme, we performed AC on lily pollen grains producing THG and endogenous 2PEF signals. Average 2PEF intensity has been shown theoretically and experimentally to be a suitable metric for sample-independent AC [5]. As expected, after two runs of THG-based AC, the correction phase and signal increases were the same as for 2PEF brightness-based AC [Figs. 3(a) and 3(c)]. Indeed, THG sharpness variations with the amount of aberrations in one mode exhibited a Gaussian shape [see Eq. (2)] with a global maximum at the same position as the 2PEF brightness curve and without other local maxima [Fig. 3(b) shows the case of mode 1]. THG brightness is also plotted for comparison and would yield incorrect AC in this case. It should be noted that the TH signal increase is much greater than that of 2PEF;

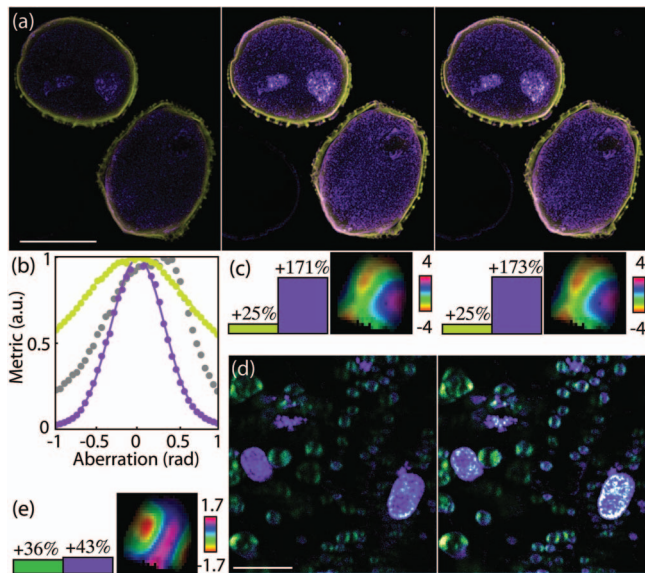


Fig. 3. (a) (**Media 1**, high resolution; **Media 2**, low resolution) Combined 2PEF (online)/THG (interior) images of coverslip-covered lily pollen grains, without AC (left), with THG (center), and 2PEF (right) AC. Scale bar, 50 μm . (b) Metric versus aberration amplitude in mode 1 [see Fig. 1(b)] for THG sharpness (bottom curve), 2PEF brightness (top curve) and THG brightness (middle curve). Lines, Gaussian fits. (c) Applied phase and 2PEF (left block)/THG (right block) signal increase in (a): left, THG AC; right, 2PEF AC. (d) Combined THG (light)/SHG (dark) images of a coverslip-covered lily anther slice, before (left), and after (right) THG AC. (e) Corresponding AC phase and signal increase. Scale bar, 20 μm .

this might be due to the coherent nature of THG, for which field summation is affected by the excitation phase distribution. Interestingly, THG-based AC can be used to optimize complex nonlinear signals, such as SHG from starch granules, as shown in Figs. 3(d) and 3(e). The low signal gain compared with Fig. 3(a) stems from the smaller corrected phase amplitude.

Finally we show that, owing to the limited number of needed measurements, our AC scheme can be used on evolving tissue. One application of THG microscopy is the long-term observation of embryo morphogenesis in small organisms [10]. Here we demonstrate time-resolved aberration-corrected imaging of a developing *Drosophila* embryo at the gastrulation stage. Since correction is updated between each frame, only a small phase needs to be added between successive images so that only one AC run was necessary (except for the first time point, for which two runs were used). Sample illumination was thus multiplied by 2.5 (3.5, including the uncorrected image acquired for comparison) compared to imaging without correction. A development sequence with one corrected frame every minute is shown in Fig. 4 (**Media 3**, high resolution; **Media 4**, low resolution), confirming a significant improvement of both signal and resolution. Note that AC was achieved here using the matrix A previously measured on other samples, demonstrating that our scheme is mostly sample independent. Interestingly, AC amplitudes in different modes vary during development, indicating that at

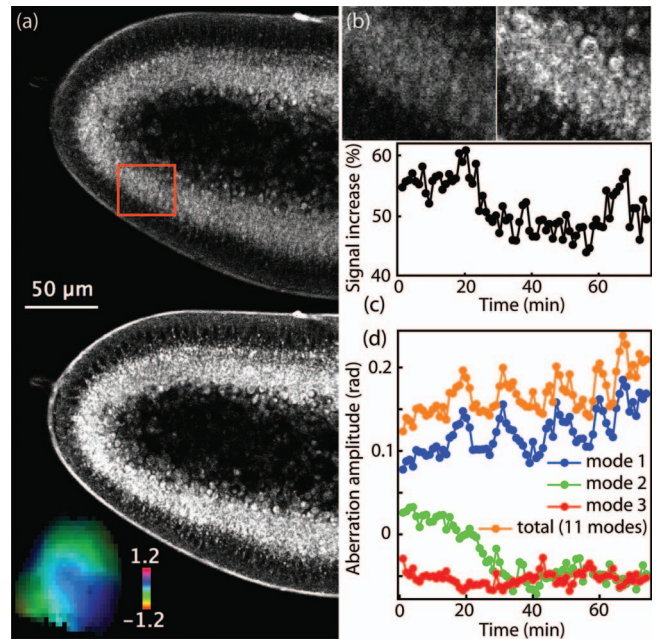


Fig. 4. (a) (**Media 3**, high resolution; **Media 4**, low resolution) *Drosophila* development imaging without (top) and with (bottom) time-resolved THG-AC. Inset, correction phase (in radians). (b) Zoom on the square in (a). (c) Signal increase after AC. (d) AC amplitude in three modes and total amplitude.

least one part of the aberrations arises from the embryo optical properties. As these can be measured over time, this experiment paves the way for their systematic study *in vivo*, which would permit optimization of AC updating frequency.

In conclusion, we proposed an image-based AC scheme suitable for THG-SHG-2PEF microscopy and demonstrated adaptive imaging of a developing embryo. This methodology should generally prove useful in tissue imaging applications.

This work was supported by the Délégation Générale pour l'Armement and by the Agence Nationale de la Recherche (ANR-RIB).

References

1. P. N. Marsh, D. Burns, and J. M. Girkin, *Opt. Express* **11**, 1123 (2003).
2. M. Rueckel, J. Mack-Bucher, and W. Denk, *Proc. Natl. Acad. Sci. USA* **103**, 17137 (2006).
3. M. J. Booth, M. A. A. Neil, R. Juškaitis, and T. Wilson, *Proc. Natl. Acad. Sci. USA* **99**, 5788 (2002).
4. D. Débarre, E. J. Botcherby, M. J. Booth, and T. Wilson, *Opt. Express* **16**, 9290 (2008).
5. D. Débarre, E. J. Botcherby, T. Watanabe, S. Srinivas, M. J. Booth, and T. Wilson, *Opt. Lett.* **16**, 2495 (2009).
6. Y. Barad, H. Eisenberg, M. Horowitz, and Y. Silberberg, *Appl. Phys. Lett.* **70**, 922 (1997).
7. D. Débarre, W. Supatto, and E. Beaurepaire, *Opt. Lett.* **30**, 2134 (2005).
8. N. Olivier and E. Beaurepaire, *Opt. Express* **16**, 14703 (2008).
9. R. Herloski, *J. Opt. Soc. Am. A* **2**, 1027 (1985).
10. D. Débarre, W. Supatto, E. Farge, B. Mouliat, M.-C. Schanne-Klein, and E. Beaurepaire, *Opt. Lett.* **29**, 2881 (2004).

Conclusion

This chapter focused on different aspects of wavefront control in multiphoton microscopy. The first part described numerical simulations of THG with different excitation structures, while the second part describes experimental implementations of wavefront-control in incoherent and coherent nonlinear microscopy.

The main result of the numerical simulation part is to identify potential types of sample structures that would benefit from the implementation of focus-engineering schemes, the shapes that could be used to do size and spatial frequency spectroscopy, and the phase-matching conditions of Bessel beams that could allow extended depth-of-field imaging.

The first experimental applications presented relies on a known theory but a new technical development that allows fast switching, while the second one uses a technology that has already been demonstrated, but in the new context of coherent nonlinear microscopy.



Bibliography

- [1] J. W. GOODMAN. *Introduction to Fourier optics*. McGraw-Hill, New York (1995).
- [2] R. KANT. *Superresolution and increased depth of focus: an inverse problem of vector diffraction*. *Journal of Modern Optics*, 47:905–916 (2000).
- [3] C. MAURER, A. JESACHER, S. FURHAPTER, S. BERNET, AND M. RITSCH-MARTE. *Tailoring of arbitrary optical vector beams*. *New J. Phys.*, 9(3):78 (2007).
- [4] C. LUTZ, T. S. OTIS, V. DESARS, S. CHARPAK, D. A. DIGREGORIO, AND V. EMILIANI. *Holographic photolysis of caged neurotransmitters*. *Nat. Meth.*, 5(9):821–827 (2008).
- [5] I. J. COX, C. J. R. SHEPPARD, AND T. WILSON. *Reappraisal of arrays of concentric annuli as superresolving filters*. *J. Opt. Soc. Am.*, 72(9):1287–1291 (1982).
- [6] T. WILSON AND S. J. HEWLETT. *Superresolution in confocal scanning microscopy*. *Opt. Lett.*, 16(14):1062–1064 (1991).
- [7] M. MARTINEZ-CORRAL, P. ANDRES, J. OJEDA-CASTANEDA, AND G. SAAVEDRA. *Tunable axial superresolution by annular binary filters. application to confocal microscopy*. *Optics Commun.*, 119(5-6):491 – 498 (1995).
- [8] M. MARTINEZ-CORRAL, P. ANDRES, C. J. ZAPATA-RODRIGUEZ, AND M. KOWALCZYK. *Three-dimensional superresolution by annular binary filters*. *Opt. Commun.*, 165(4-6):267 – 278 (1999).
- [9] S. QUABIS, R. DORN, M. EBERLER, O. GLOCKL, AND G. LEUCHS. *Focusing light to a tighter spot*. *Opt. Commun.*, 179(1-6):1 – 7 (2000).
- [10] R. DORN, S. QUABIS, AND G. LEUCHS. *Sharper focus for a radially polarized light beam*. *Phys. Rev. Lett.*, 91(23):233901 (2003).
- [11] A. BOIVIN. *On the theory of diffraction by concentric arrays of ring-shaped apertures*. *J. Opt. Soc. Am.*, 42(1):60–64 (1952).
- [12] W. T. WELFORD. *Use of annular apertures to increase focal depth*. *J. Opt. Soc. Am.*, 50(8):749–752 (1960).
- [13] B. J. THOMPSON. *Diffraction by semitransparent and phase annuli*. *J. Opt. Soc. Am.*, 55(2):145–148 (1965).
- [14] J. OJEDA-CASTANEDA, L. R. BERRIEL-VALDOS, AND E. MONTES. *Spatial filter for increasing the depth of focus*. *Opt. Lett.*, 10(11):520–522 (1985).
- [15] C. J. R. SHEPPARD AND Z. S. HEGEDUS. *Axial behavior of pupil-plane filters*. *J. Opt. Soc. Am. A*, 5(5):643–647 (1988).
- [16] J. ARLT AND M. J. PADGETT. *Generation of a beam with a dark focus surrounded by regions of higher intensity: the optical bottle beam*. *Opt. Lett.*, 25(4):191–193 (2000).
- [17] Y. XIA AND J. YIN. *Generation of a focused hollow beam by an 2π -phase plate and its application in atom or molecule optics*. *J. Opt. Soc. Am. B*, 22(3):529–536 (2005).

-
- [18] S. W. HELL AND J. WICHMANN. *Breaking the diffraction resolution limit by stimulated emission: stimulated-emission-depletion fluorescence microscopy*. Opt. Lett., 19(11):780–782 (1994).
- [19] T. A. KLAR, S. JAKOBS, M. DYBA, A. EGNER, AND S. W. HELL. *Fluorescence microscopy with diffraction resolution barrier broken by stimulated emission*. Proc. Natl. Acad. Sci. USA, 97(15):8206–8210 (2000).
- [20] M. DYBA AND S. W. HELL. *Focal spots of size $\lambda/23$ open up far-field fluorescence microscopy at 33 nm axial resolution*. Phys. Rev. Lett., 88(16):163901 (2002).
- [21] V. WESTPHAL AND S. W. HELL. *Nanoscale resolution in the focal plane of an optical microscope*. Phys. Rev. Lett., 94(14):143903 (2005).
- [22] K. I. WILLIG, R.D JAHN, V. WESTPHAL, S. O. RIZZOLI, AND S. W. HELL. *Sted microscopy reveals that synaptotagmin remains clustered after synaptic vesicle exocytosis*. Nature, 440:935–939 (2006).
- [23] S. W. HELL, P. E. HENNINEN, A. KUUSISTO, M. SCHRADER, AND E. SOINI. *Annular aperture two-photon excitation microscopy*. Optics Commun., 117(1-2):20–24 (1995).
- [24] C. IBÁÑEZ-LÓPEZ, G. SAAVEDRA, G. BOYER, AND M. MARTINEZ-CORRAL. *Quasi-isotropic 3-D resolution in two-photon scanning microscopy*. Opt. Express, 13:6168 (2005).
- [25] J. BEWERSDORF, R. PICK, AND S.W. HELL. *Multifocal multiphoton microscopy*. Opt. Lett., 23(9):655–657 (1998).
- [26] V. ANDRESEN, A. EGNER, AND S.W. HELL. *Time-multiplexed multifocal multiphoton microscope*. Opt. Lett., 26(2):75–77 (2001).
- [27] J. E. JURELLER, H. Y. KIM, AND N. F. SCHERER. *Stochastic scanning multiphoton multifocal microscopy*. Opt. Express, 14(8):3406–3414 (2006).
- [28] E. Y. S. YEW AND C. J. R. SHEPPARD. *Effects of axial field components on second harmonic generation microscopy*. Opt. Express, 14(3):1167–1174 (2006).
- [29] E. Y. S. YEW AND C. J. R. SHEPPARD. *Second harmonic generation polarization microscopy with tightly focused linearly and radially polarized beams*. Optics Commun., 275(2):453–457 (2007).
- [30] K. YOSHIKI, K. RYOSUKE, M. HASHIMOTO, T. ARAKI, AND N. HASHIMOTO. *Second-harmonic-generation microscope using eight-segment polarization-mode converter to observe three-dimensional molecular orientation*. Opt. Lett., 32(12):1680–1682 (2007).
- [31] V. V. KRISHNAMACHARI AND E. O. POTMA. *Focus-engineered coherent anti-stokes raman scattering microscopy: a numerical investigation*. J. Opt. Soc. Am. A, 24(4):1138–1147 (2007).
- [32] V. V. KRISHNAMACHARI AND E. O. POTMA. *Detecting lateral interfaces with focus-engineered coherent anti-stokes raman scattering microscopy*. Journal of Raman Spectroscopy, 39:593–598 (2008).
- [33] V. V. KRISHNAMACHARI AND E. O. POTMA. *Multi-dimensional differential imaging with fe-cars microscopy*. Vibrational Spectroscopy, 50(1):10 – 14 (2009).
-

- [34] M. R. BEVERSLUIS AND S. J. STRANICK. *Enhanced contrast coherent anti-stokes raman scattering microscopy using annular phase masks*. Applied Physics Letters, 93(23):231115 (2008).
- [35] F. LU, W. ZHENG, AND Z. HUANG. *Coherent anti-stokes raman scattering microscopy using tightly focused radially polarized light*. Opt. Lett., 34(12):1870–1872 (2009).
- [36] L. CHENG, S. VEETIL, AND D. Y. KIM. *Differential imaging in coherent anti-stokes raman scattering microscopy ii: a filter-assisted laguerre-gaussian beam detection scheme*. Opt. Express, 15(19):12050–12059 (2007).
- [37] D. DÉBARRE, W. SUPATTO, AND E. BEAUREPAIRE. *Structure sensitivity in third-harmonic generation microscopy*. Opt. Lett., 30(16):2134–2136 (2005).
- [38] D. ORON AND Y. SILBERBERG. *Third-harmonic generation with cylindrical gaussian beams*. J. Opt. Soc. Am. B, 21(11):1964–1968 (2004).
- [39] S. YANG AND Q. ZHAN. *Third-harmonic generation microscopy with tightly focused radial polarization*. J. Optics A, 10(12):125103–+ (2008).
- [40] O. MASIHZADEH, P. SCHLUP, AND R. A. BARTELS. *Control and measurement of spatially inhomogeneous polarization distributions in third-harmonic generation microscopy*. Opt. Lett., 34(7):1090–1092 (2009).
- [41] O. MASIHZADEH, P. SCHLUP, AND R. A. BARTELS. *Enhanced spatial resolution in third-harmonic microscopy through polarization switching*. Opt. Lett., 34(8):1240–1242 (2009).
- [42] T. JABBOUR AND S. KUEBLER. *Vector diffraction analysis of high numerical aperture focused beams modified by two- and three-zone annular multi-phase plates*. Opt. Express, 14(3):1033–1043 (2006).
- [43] C. J. R. SHEPPARD. *The use of lenses with annular aperture in scanning optical microscopy*. Optik, 48:329–334 (1977).
- [44] T. WULLE AND S. HERMINGHAUS. *Nonlinear optics of bessel beams*. Phys. Rev. Lett., 70:1401–1404 (1993).
- [45] J. DURNIN, J. J. MICELI, AND J. H. EBERLY. *Diffraction-free beams*. Phys. Rev. Lett., 58(15):1499–1501 (1987).
- [46] J. DURNIN. *Exact solutions for nondiffracting beams. i. the scalar theory*. J. Opt. Soc. Am. A, 4(4):651–654 (1987).
- [47] J. E. DURNIN, J. J. MICELI, JR., AND J. H. EBERLY. *Comparison of Bessel and Gaussian beams*. Optics Lett., 13:79–80 (1988).
- [48] E. T. WHITAKER. *On the partial differential equations of mathematical physics*. Math. Ann., 57:333 (1903).
- [49] D. MCGLOIN AND K. DHOLAKIA. *Bessel beams: diffraction in a new light*. Contemporary Physics, 46:15–28 (2005).

-
- [50] J. H. MCLEOD. *The axicon: A new type of optical element*. J. Opt. Soc. Am., 44(8):592–592 (1954).
- [51] J. H. MCLEOD. *Axicons and their uses*. J. Opt. Soc. Am., 50(2):166–166 (1960).
- [52] J. ARLT AND K. DHOLAKIA. *Generation of high-order bessel beams by use of an axicon*. Opt. Commun., 177:297–301 (2000).
- [53] A. VASARA, J. TURUNEN, AND A. T. FRIBERG. *Realization of general nondiffracting beams with computer-generated holograms*. J. Opt. Soc. A, 6:1748–1754 (1989).
- [54] J. A. DAVIS, E. CARCOLE, AND D. M. COTTRELL. *Nondiffracting interference patterns generated with programmable spatial light modulators*. Appl. Opt., 35(4):599–602 (1996).
- [55] B. GLUSHKO, B. KRYZHANOVSKY, AND D. SARKISYAN. *Self-phase-matching mechanism for efficient harmonic generation processes in a ring pump beam geometry*. Phys. Rev. Lett., 71(2):243–246 (1993).
- [56] S. P. TEWARI, H. HUANG, AND R. W. BOYD. *Theory of self-phase-matching*. Phys. Rev. A, 51(4):R2707–R2710 (1995).
- [57] S. P. TEWARI, H. HUANG, AND R. W. BOYD. *Theory of third-harmonic generation using bessel beams, and self-phase-matching*. Phys. Rev. A, 54(3):2314–2325 (1996).
- [58] V. E. PEET AND R. V. TSUBIN. *Third-harmonic generation and multiphoton ionization in bessel beams*. Phys. Rev. A, 56(2):1613–1620 (1997).
- [59] V. E. PEET AND S. V. SHCHEMELJOV. *Spectral and spatial characteristics of third-harmonic generation in conical light beams*. Phys. Rev. A, 67(1):013801 (2003).
- [60] C. F. R. CARON AND R. M. POTVLIERGE. *Phase matching and harmonic generation in bessel gauss-beams*. J. Opt. Soc. Am. B, 15(3):1096–1106 (1998).
- [61] C. F. R. CARON AND R. M. POTVLIERGE. *Optimum conical angle of a bessel-gauss beam for low-order harmonic generation in gases*. J. Opt. Soc. Am. B, 16(9):1377–1384 (1999).
- [62] K. SHINOZAKI, X. CHANG-QING, H. SASAKI, AND T. KAMIJOH. *A comparison of optical second-harmonic generation efficiency using Bessel and Gaussian beams in bulk crystals*. Opt. Commun., 133:300–304 (1997).
- [63] J. ARLT, K. DHOLAKIA, L. ALLEN, AND M. J. PADGETT. *Efficiency of second-harmonic generation with Bessel beams*. Phys. Rev. A, 60:2438–2441 (1999).
- [64] A. PISKARSKAS, V. SMILGEVIČIUS, A. STABINIS, V. JARUTIS, V. PAŠIŠKEVIČIUS, S. WANG, J. TELLEFSEN, AND F. LAURELL. *Noncollinear second-harmonic generation in periodically poled ktiopo₄ excited by the bessel beam*. Opt. Lett., 24(15):1053–1055 (1999).
- [65] N. OLIVIER, A. MERMILLOD-BLONDIN, C. B. ARNOLD, AND E. BEAUREPAIRE. *Two-photon microscopy with simultaneous standard and extended depth of field using a tunable acoustic gradient-index lens*. Opt. Lett., 34(11):1684–1686 (2009).
- [66] E. MCLEOD AND C. B. ARNOLD. *Mechanics and refractive power optimization of tunable acoustic gradient lenses*. J. Ap. Phys, 102(3):033104 (2007).
-

- [67] A. MERMILLOD-BLONDIN, E. MCLEOD, AND C.B. ARNOLD. *Dynamic pulsed-beam shaping using a tag lens in the near uv*. Applied Physics A, 93:231–234(4) (2008).
- [68] E. MCLEOD, A. B. HOPKINS, AND C. B. ARNOLD. *Multiscale besel beams generated by a tunable acoustic gradient index of refraction lens*. Opt. Lett., 31(21):3155–3157 (2006).
- [69] E. MCLEOD AND C. B. ARNOLD. *Optical analysis of time-averaged multiscale besel beams generated by a tunable acoustic gradient index of refraction lens*. Appl. Opt., 47(20):3609–3618 (2008).
- [70] A. MERMILLOD-BLONDIN, E. MCLEOD, AND C. B. ARNOLD. *High-speed varifocal imaging with a tunable acoustic gradient index of refraction lens*. Opt. Lett., 33(18):2146–2148 (2008).
- [71] D. DÉBARRE, E. J. BOTCHERBY, T. WATANABE, S. SRINIVAS, M. J. BOOTH, AND T. WILSON. *Image-based adaptive optics for two-photon microscopy*. Opt. Lett., 34(16):2495–2497 (2009).
- [72] R. K. TYSON. *Principles of adaptive optics*. Boston Academic Press, Boston (1998).
- [73] E. J. FERNÁNDEZ, I. IGLESIAS, AND P. ARTAL. *Closed-loop adaptive optics in the human eye*. Opt. Lett., 26(10):746–748 (2001).
- [74] S. HELL, G. REINER, C. CREMER, AND E.H. K. STELZER. *Aberrations in confocal fluorescence microscopy induced by mismatches in refractive index*. J. Microsc., 169:391–405 (1993).
- [75] C. J. R. SHEPPARD, M. GU, K. BRAIN, AND H. ZHOU. *Influence of spherical aberration on axial imaging of confocal reflection microscopy*. Appl. Opt., 33(4):616–624 (1994).
- [76] C. J. R. SHEPPARD AND P. TOROK. *Effects of specimen refractive index on confocal imaging*. J. Microsc., 185:366–374 (1997).
- [77] P. THEER AND W. DENK. *On the fundamental imaging-depth limit in two-photon microscopy*. Proc. SPIE, 5463:45–55 (2004).
- [78] P. THEER AND W. DENK. *On the fundamental imaging-depth limit in two-photon microscopy*. J. Opt. Soc. Am. A, 23(12):3139–3149 (2006).
- [79] M. SCHWERTNER, M. BOOTH, AND T. WILSON. *Characterizing specimen induced aberrations for high na adaptive optical microscopy*. Opt. Express, 12(26):6540–6552 (2004).
- [80] M. SCHWERTNER, M.J. BOOTH, AND T. WILSON. *Specimen-induced distortions in light microscopy*. J. Microscopy, 228:97–102(6) (2007).
- [81] M. J. BOOTH, M. A. A. NEIL, R. JUSKAITIS, AND T. WILSON. *Adaptive aberration correction in a confocal microscope*. Proc. Natl. Acad. Sci. USA, 99(9):5788–5792 (2002).
- [82] M. A. A. NEIL, R. JUSKAITIS, M. J. BOOTH, T. WILSON, T. TANAKA, AND S. KAWATA. *Adaptive aberration correction in a two-photon microscope*. J. Microsc., 200:105–108(4) (2000).
- [83] O. ALBERT, L. SHERMAN, G. MOUROU, T. B. NORRIS, AND G. VDOVIN. *Smart microscope: an adaptive optics learning system for aberration correction in multiphoton confocal microscopy*. Opt. Lett., 25(1):52–54 (2000).

-
- [84] L. SHERMAN, J. Y. YE, O. ALBERT, AND T. B. NORRIS. *Adaptive correction of depth-induced aberrations in multiphoton scanning microscopy using a deformable mirror*. J. Microsc., 206:65–71(7) (2002).
- [85] A. J. WRIGHT, S. P. POLAND, J. M. GIRKIN, C. W. FREUDIGER, C. L. EVANS, AND X. S. XIE. *Adaptive optics for enhanced signal in cars microscopy*. Opt. Express, 15(26):18209–18219 (2007).
- [86] D. DÉBARRE, E. J. BOTCHERBY, M. J. BOOTH, AND T. WILSON. *Adaptive optics for structured illumination microscopy*. Opt. Express, 16(13):9290–9305 (2008).
- [87] M. RUECKEL, J.A. MACK-BUCHER, AND W. DENK. *Adaptive wavefront correction in two-photon microscopy using coherence-gated wavefront sensing*. Proc. Natl. Acad. Sci. USA, 103(46):17137–17142 (2006).
- [88] M. FEIERABEND, M. RÜCKEL, AND W. DENK. *Coherence-gated wave-front sensing in strongly scattering samples*. Opt. Lett., 29:2255–2257 (2004).
- [89] P. MARSH, D. BURNS, AND J. GIRKIN. *Practical implementation of adaptive optics in multiphoton microscopy*. Opt. Express, 11(10):1123–1130 (2003).
- [90] T. A. PLANCHON, W. AMIR, J. J. FIELD, C. G. DURFEE, J. A. SQUIER, P. ROUSSEAU, O. ALBERT, AND G. MOUROU. *Adaptive correction of a tightly focused, high-intensity laser beam by use of a third-harmonic signal generated at an interface*. Opt. Lett., 31(14):2214–2216 (2006).
- [91] M. BOOTH. *Wave front sensor-less adaptive optics: a model-based approach using sphere packings*. Opt. Express, 14(4):1339–1352 (2006).
- [92] D. DÉBARRE, M. J. BOOTH, AND T. WILSON. *Image based adaptive optics through optimization of low spatial frequencies*. Opt. Express, 15(13):8176–8190 (2007).
- [93] K. STREHL. *Aplanatische und fehlerhafte abbildung im fernrohr*. Zeitschrift für Instrumentenkunde, 15 (1895).
- [94] V. N. MAHAJAN. *Zernike annular polynomials for imaging systems with annular pupils*. J. Opt. Soc. Am., 71(1):75–85 (1981).
- [95] R. HERLOSKI. *Strehl ratio for untruncated aberrated gaussian beams*. J. Opt. Soc. Am. A, 2(7):1027–1030 (1985).
- [96] N. OLIVIER, D. DÉBARRE, AND E. BEAUREPAIRE. *Dynamic aberration correction for multiharmonic microscopy*. Opt. Lett., 34(20):3145–3147 (2009).

Acknowledgements V

Ecole Polytechnique used to be located downtown Paris, rue Descartes⁹. This is unfortunately not the case anymore, as it now stands proudly atop the Plateau de Saclay, some 20 kilometers south of Paris. This means that people who live in Paris have to commute for ≈ 2 hours daily, or, in the course of this Thesis, approximately 2 months. This means I had a LOT of time to read books. However, I already quoted my whole iTunes library a few pages back, and lists of authors/books really look overly pretentious in a I-have-better-taste-than-you sort of way¹⁰, which means I will rather thank the people I commuted¹¹ with or who recommended me books to read: Ana, Delphine, Paul, Sylvan, Agathe, Charlotte, Patrick, Guillaume, Edward, Nicolas, Padra, Alexander,...



Figure 4.17: A group of anonymous people. The fact that they look like some of the aforementioned lab people is purely coincidental.

I also want to use this space to thank all the people I went to conferences with (or housed me there), and made them way more enjoyable¹²: Ariane, Emmanuel, Delphine, Sylvan, Marie-Claire, Marc & Brigitte, Caroline, Matthias, Rajesh, Israel, Luciano, Erica, Julien,...

⁹a 10 minutes walk away from my apartment

¹⁰Yes, even to me !

¹¹on bikes, trains, buses or cars

¹²thanks also to everyone who wrote postcards in my stead !

Finally, Thanks to all the people I worked with ¹³ during my summer 'vacations' in Scotland & in California, especially Laure, Arnaud, Celine, Fanny & Jeanne¹⁴.

To everyone I have forgotten, Thank you.

to be continued (?)

¹³and the kids I worked for, for not being too much of a nuisance, I guess.

¹⁴thanks also to everyone who wrote postcards in my stead !

Chapter 5

Biological Applications of Third Harmonic Generation Microscopy

Contents

5.1 Multimodal Multiphoton Imaging of the Human Cornea	164
5.1.1 Introduction	164
5.1.2 Nonlinear Contrasts in the Human Cornea	165
5.1.3 Multiharmonic Imaging of the Corneal Stroma	170
5.1.4 Polarization of the THG Signal	172
5.1.5 Perspectives & Conclusions	174
5.2 Zebrafish	176
5.2.1 Introduction	176
5.2.2 Reconstruction of the Zebrafish Early Development Using Multiharmonic Microscopy	178
Bibliography	188

INTRODUCTION

This chapter describes two different biological applications of coherent nonlinear microscopy that were developed during this thesis.¹ Each study results from multiple collaborations. The first one is on the multimodal multiphoton imaging of the human cornea, while the second one is on the reconstruction of the zebrafish early development using multiharmonic microscopy.²

¹In both cases, it is a work in progress, and this chapter is therefore adapted from the drafts of 3 articles.

²■ This introduction is meant to be read whilst listening to either “Killing the Flies” by The Ocean (Aeolian, 2005) or “Killing all the Flies” by Mogwai (Happy Songs for Happy People, (2003)) in memory of all the drosophila embryos that died during this thesis.

5.1 Multimodal Multiphoton Imaging of the Human Cornea

5.1.1 Introduction

This section presents a biomedical application of nonlinear microscopy to the imaging of the human cornea, with a particular emphasis on the elucidation of the harmonic signals (especially THG), and the evaluation of the potential of combining different nonlinear imaging modalities. This work was done in collaboration between three labs:

- Florent Aptel and Jean-Marc Legeais, ophthalmologists at the *Laboratoire Biotechnologie et Oeil* (Université Paris V), Hôtel-Dieu Hospital, Paris France.
- Karsten Plamann at the *Laboratory for Applied Optics (LOA)* (ENSTA-Polytechnique), Palaiseau France.
- Ariane Deniset-Besseau & Marie-Claire Schanne-Klein at the *Laboratory for Optics & Biosciences (LOB)* (Polytechnique), Palaiseau France.

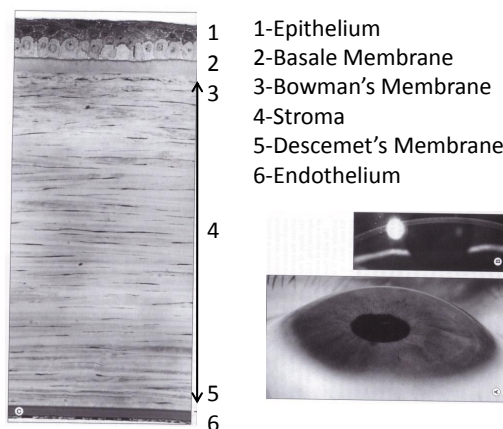


Figure 5.1: ORGANIZATION OF THE CORNEA

Location of the cornea in the eye, and organization of the different layers of the cornea.

Adapted from [1].

³ Non-invasive optical methods that enable in vivo or in situ visualization of tissue components are of particular relevance in ophthalmology because they provide key information about the physiology and diseases of the eye. Optical coherence tomography (OCT) [2] and confocal reflectance microscopy [3] are two commonly used techniques for obtaining in situ ophthalmic images. These two techniques detect scattered light, and provide three-dimensional cell-scale information. However, as their contrast mechanism relies on spatial variations of refractive indices, they may sometimes offer limited contrast and specificity. An alternative method for obtaining virtual biopsies from intact tissue is multiphoton microscopy (MPM) [4]; that can provide structural and biochemical information on unstained samples which are not accessible to other noninvasive methods.

We will present the results in two different sections: an evaluation of the nonlinear contrasts that can be obtained on the different layers of the cornea (defined in figure 5.1) by using combined THG, SHG & 2PEF microscopy in section 5.1.2, and a more precise analysis of the origin of the harmonic signals in the stroma in section 5.1.3 & 5.1.4.

³ ■ Sad Eyed Lady Of The Lowlands, Bob Dylan, Blonde on Blonde (1965)

5.1.2 Nonlinear Contrasts in the Human Cornea

Figure (5.2) illustrates the setup used in this study for the nonlinear imaging of the cornea using three modalities: 2PEF, SHG, and THG. The fresh corneal button is mounted in between two coverslips⁴ (5.2.a), and is either imaged using an excitation wavelength of $\approx 730\text{nm}$ (5.2.b) that allows recording of 2PEF and SHG images (either in transmission or in epidetection), or at $\approx 1200\text{nm}$ (5.2.c) that allows THG and SHG imaging (in transmission).

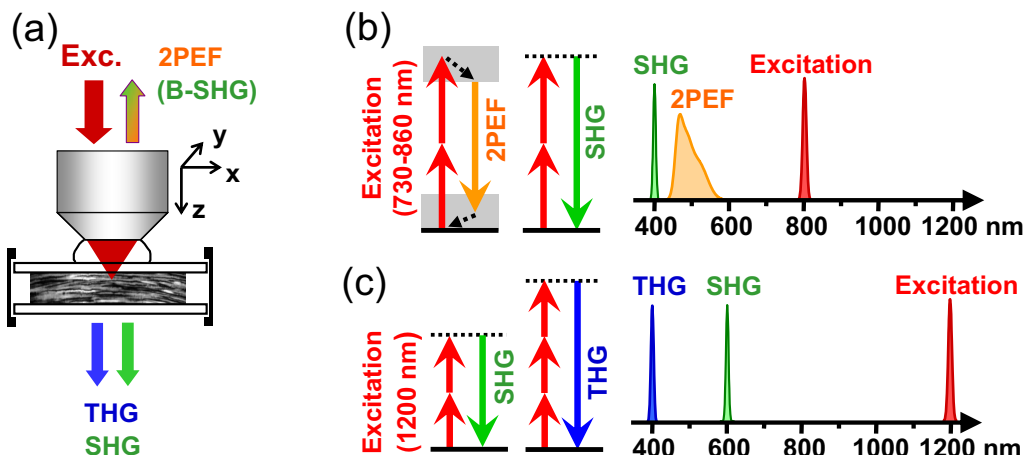


Figure 5.2: SETUP

Principles of multiphoton/multiharmonic imaging. (a) Experimental arrangement and signal directionality. (b) SHG/2PEF with excitation in the 730-860 nm range. (c) THG/SHG with 1200 nm excitation.

2PEF imaging with 700-900nm excitation can detect the distribution of endogenous chromophores such as Nicotinamide Adenine Dinucleotide (phosphate) (NAD(P)H), flavins, retinoids, lipofuscin, elastin, and others [5]. Previous studies have reported the use of 2PEF for visualizing corneal epithelial cells, limbus stem cells, and stromal keratocytes [6–9]. SHG emission occurs at exactly half the excitation wavelength, and has been shown to be a sensitive probe of the structural organization of collagen in tissues [10, 11], and is therefore an effective approach for imaging collagen lamellae in the corneal stroma [8, 11–13].

Third harmonic generation (THG) is an additional contrast mechanism that can be used for imaging unstained samples. THG is obtained from optical inhomogeneities of size comparable to the beam focus. This nonlinear contrast mechanism produces highly contrasted images, and in particular a strong signal is observed at the interface between an aqueous medium (e.g. cell cytoplasm) and a lipidic, mineralized or absorbing organelle a few 100s of nm in size. Besides this basic contrast mechanism, THG can also detect birefringence using appropriate polarization of the excitation beam [14].

In the following paragraphs, we evaluate the combination of THG, SHG and 2PEF microscopy for imaging intact human eye tissue and we unravel some original nonlinear optical properties of the cornea and the trabecular meshwork. We show that these contrast mechanisms provide three-dimensional images with a micrometric resolution of several key tissue components over the full thickness of the anterior eye segment, which should prove of interest in ophthalmologic research.

⁴The sample preparation is describe in appendix B.7

5.1.2.1 Epithelium

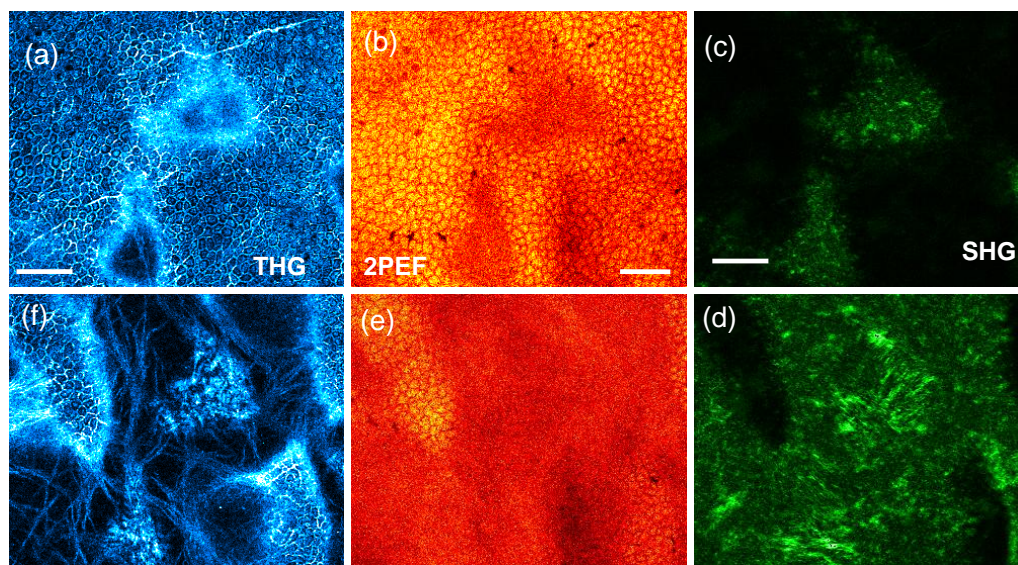


Figure 5.3: EPITHELIUM

THG/SHG/2PEF imaging of corneal epithelium and epithelium-stroma junction. (a-f) large-scale imaging of an unstained cornea. (a) THG, (b) 2PEF, and (c) SHG images of the epithelium recorded $38 \mu\text{m}$ below the surface. (d) THG, (e) 2PEF, and (f) SHG images of the epithelium-stroma junction recorded $43 \mu\text{m}$ below the surface.

Representative multiphoton images of the corneal epithelium are presented in figure (5.3). High NA THG imaging with $1.2 \mu\text{m}$ excitation provides a detailed view of the epithelium architecture, by revealing cells and nuclei boundaries. Nuclear membrane visibility results from optical contrast between nuclei and cytoplasm, creating an interface between two bulk media. Cell-cell junction contrast is of a different nature and can only be explained by the presence of a sizable “slab” of inter-cellular medium. This contrast makes it possible to readily distinguish squamous cells, wing cells, and deeper basal cells based on their size and morphology. Punctuate signals in the cytoplasm probably originate from non-aqueous or dense organelles. Additionally, 2PEF imaging with 730 nm excitation, using $390\text{-}450 \text{ nm}$ bandpass detection reveals fluorescent cytoplasmic organelles emerging over a diffuse background. These signals most likely correspond to NAD(P)H fluorescence. We note that these combined THG/2PEF images provide an immediate diagnosis of epithelium quality.

Multimodal images of the epithelial-stromal junction are shown in figure (5.3). Basal epithelial cells are adjacent to the fluorescent Bowman’s layer beyond which a $20\text{-}30 \mu\text{m}$ thick region appears dark in the THG images. This layer exhibits a relatively uniform or speckle-like SHG signal, consistent with the disruption of lamellar organization of the collagen at the anterior stroma [13]. Also visible in the THG images are the ribbon-like anchoring structures that assemble into fascicles connecting the epithelium to the stroma. Since these structures are visible in the THG images but not in SHG, they likely exhibit a density contrast compared to collagen-I fibrils in the stroma, which may be consistently explained by the presence of other collagen types or extracellular matrix components. Combined SHG/THG imaging of the epithelial-stroma junction could therefore be an effective way to study abnormal adhesion complexes involved in common corneal pathologies. Finally, sub-basal nerve fibers [15] are

readily visible in THG images (figure 5.3.f) and in 2PEF images with a lower contrast [9].⁵

5.1.2.2 Stroma

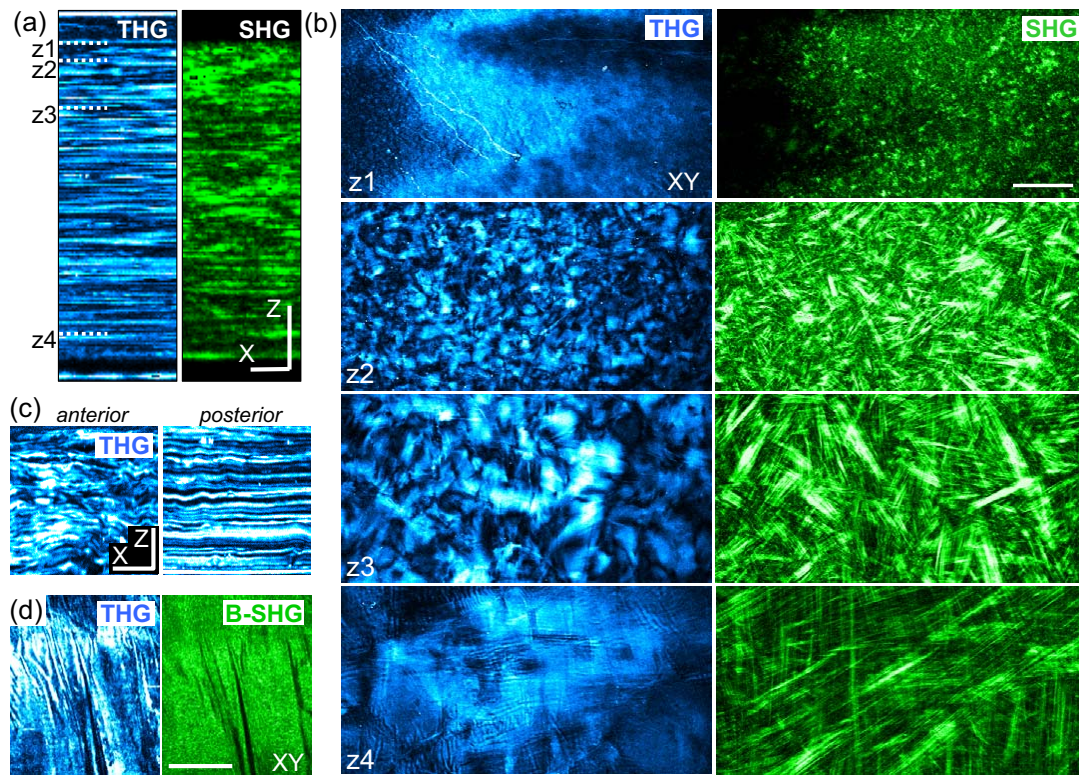


Figure 5.4: STROMA

THG/SHG imaging of stromal organization at different depths. (a) XZ reprojection of a series of THG / F-SHG images recorded with the epithelium (top) facing the objective. NA=0.75, scale bars $20\ \mu\text{m}$ (X) \times $100\ \mu\text{m}$ (Z). (b) XY images recorded at depths indicated in (a). Scale bar $100\ \mu\text{m}$.

In healthy (transparent) human corneas, multimodal images can be recorded over the entire corneal thickness with little loss in resolution. An example of integral SHG/THG imaging is shown in figure (5.4). As discussed in several studies, stromal SHG signals originate from collagen fibrils. Since individual fibrils are not resolved because of their small diameter (35 nm) and dense packing, harmonic emission results from interference processes governed by coherence lengths that are different in the forward and backward directions. Forward-detected SHG images exhibit striated features that likely reflect the orientation and distribution of the fibrils (see figure (5.4).b). Backward-SHG (B-SHG) images result from a shorter coherence length and appear as relatively uniform or speckle-like at all depths.

THG images provide complementary information. As discussed later, stromal THG arise from differences in anisotropy between successive lamellae, so that XZ-projected THG images reveal the stacked organization of the stroma (figure 5.4.c). Combined SHG-THG imaging provides a rich description of the lamellar organization of the intact stroma over its entire thickness. One striking feature of these images is that they reveal the different large-scale

⁵ ■ Tired Eyes, Neil Young, Tonight's the Night (1975)

organizations of collagen lamellae at successive depths, as exemplified in figure (5.4.b.) Tissue-scale heterogeneity is more pronounced in the anterior stromal region, whereas the posterior stroma exhibits a more regular, long-range stacked organization.

5.1.2.3 Visibility of Keratocytes

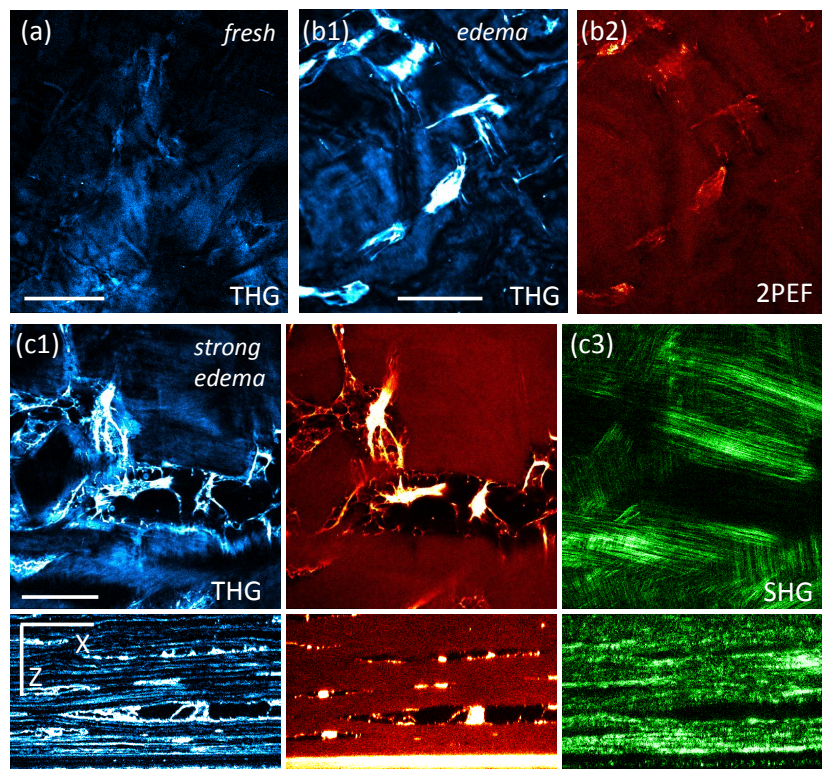


Figure 5.5: VISIBILITY OF KERATOCYTES

THG/2PEF imaging of keratocytes and water accumulation in edematous corneas. (a) Fresh non-edematous cornea. (b1, b2) Same cornea after 24h in 1% dextran solution. Strong THG is observed around keratocytes. (c1-3) THG-2PEF-SHG imaging of a cornea with strong edema. Bottom images are XZ reprojections. Images (a), (b1) and (c1) are presented with similar color scales. Excitation wavelength for 2PEF: 730 nm. Scale bars 50 μm

In healthy fresh corneas, relatively weak THG signals are also obtained from the stromal keratocytes (see figure 5.5.a). The ratio of peak keratocytes THG over peak stromal THG is typically 1.7 ± 0.5 . However, this signal is significantly enhanced in edematous stroma. This is illustrated in figure (5.5.b), showing THG/2PEF images recorded in the same cornea as in figure (5.5.a) after 24h storage in a hypotonic culture medium in order to induce corneal swelling (Hanks medium with 1% dextran supplementation). Cell-to-stroma signal ratio increases to $\approx 4 - 9$, and the keratocytes network and interconnections become readily visible.

This THG signal increase is not consistently correlated with changes in cell fluorescence, as shown in figure (5.5.b) This indicates that the THG signal reflects the local swelling of the tissue around cells at the onset of edema. In strongly edematous corneas however (figure 5.5.c), keratocytes exhibit strong fluorescence reflecting their metabolic activity besides strong THG signal. Under such conditions, THG/SHG/2PEF images indicate that 10-100 μm large vacuoles devoid of fibrillar collagen are present between stromal lamellae, and THG/2PEF imaging reveal

the presence of cells within these regions, forming bridges between the disconnected lamellae. We also observed that THG from keratocytes is enhanced to a lesser extent in corneas that have been kept in a storage medium containing phenol red. In this commonly used protocol, the observed increased THG from cellular structures may be attributed to resonant enhancement through two- or three- photon absorption [16], since phenol red linear absorption peaks at 430 nm and 560 nm.

We point out that although this protocol may be used to enhance keratocytes visibility in THG images, it prevents 2PEF imaging because of increased background fluorescence and of photodamage onset ⁶

5.1.2.4 Endothelium

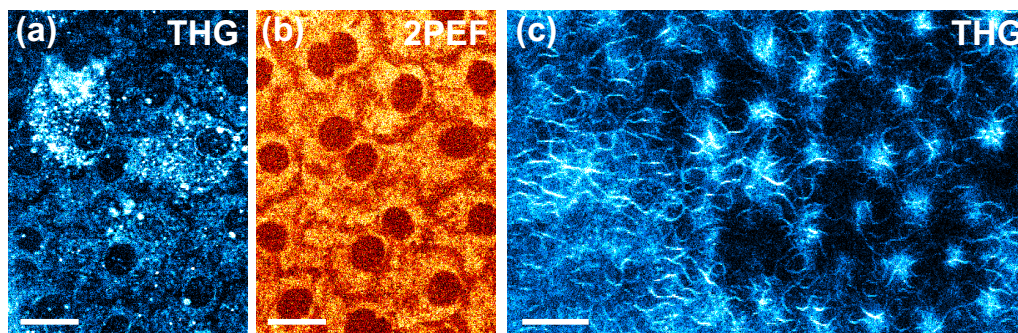


Figure 5.6: ENDOTHELIUM

THG/2PEF imaging of endothelial structures. (a,b) representative THG/2PEF images of endothelial cells. (c) THG images of junction structures located between the endothelium and the Descemet's membrane. Scale bars 20 μm .

Figure (5.6) shows typical THG and 2PEF images of the endothelium (5.6.a & .b), and a THG image of the endothelial-stromal junction (5.6.c). THG is mainly observed from cytoplasmic organelles and, to a lesser extent, from nuclear membranes. Like in the epithelium, fluorescence may be attributed mostly to mitochondria, delineating the cell nucleus and boundary as dark regions. Both image modalities exhibit heterogeneity in cell-to-cell signal level, suggesting that they may be used to assess cellular metabolism. When imaging the endothelium at a larger scale, the detailed morphological information present in THG/2PEF images provides a direct diagnosis of tissue quality with potential relevance in e.g. grafting operations. Finally, THG images acquired 10 μm above the endothelial cells reveal a hexagonal array of fibrous patches (see figure 5.6.c), producing a signal typically 5 ± 2 times dimmer than cell components. These structures likely correspond to Descemet's membrane collagen fibrils that connect the endothelial cells to the stroma.

5.1.2.5 Trabecular meshwork

Representative 2PEF/SHG images of the trabecular meshwork are shown in figure (5.7). They take advantage of the strong endogenous fluorescence of elastin, which is readily detected along with collagen SHG [5, 17]. Figure (5.7) shows a prominent Schwalbe's line composed of fibrillar collagen oriented parallel to the limbus and covered by endothelial-like cells. The anterior edge of the meshwork shows numerous intermingled cord-like structures composed of

⁶ ■ Hurt, Johnny Cash, American IV: The Man Comes Around (2002)

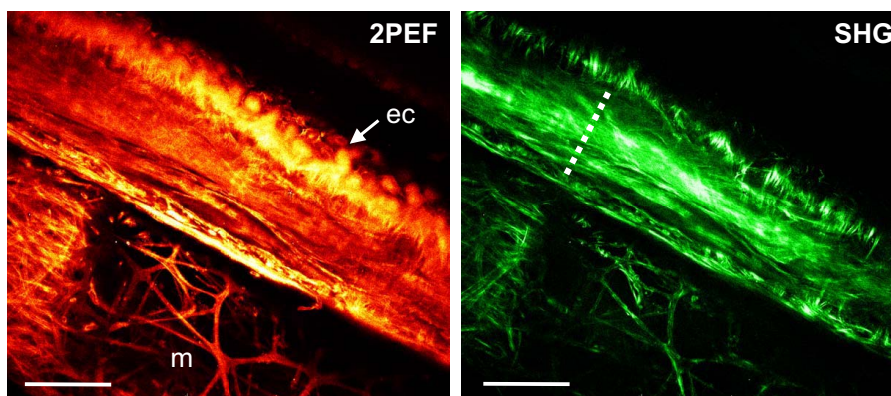


Figure 5.7: TRABECULUM

2PEF/SHG imaging of the trabeculum. Excitation wavelength, 860 nm. Visible structures include endothelial cells (ec), trabecular meshwork (m), and Schwalbe's line (dashed line). Scale bar 100 μm .

elastic fibers and a few collagen fibrils. In the inner corneoscleral meshwork located closest to the anterior chamber, the cord-like trabecular lamellae form a loose three-dimensional network. In the juxtacanalicular meshwork, multiphoton imaging is somehow restricted by the presence of pigmented structures exhibiting low photodamage threshold that may correspond to melanin granules within giant macrophages. We note that THG images also reflect the meshwork structure, without additional specificity.

5.1.3 Multiharmonic Imaging of the Corneal Stroma

This section presents a more detailed analysis of the THG signals in the corneal stroma. We will start from a series of additional observations, and present a simple model that would explain the origin of the nonlinear contrasts.

5.1.3.1 Relative Localization of the THG & SHG Signals

The first observation concerns the relative localization of the SHG and THG signals. Indeed, we found that THG and SHG signals generally exhibit anti-correlated maxima, as illustrated in figure (5.8).⁷

Figure (5.8.a & b) show THG and SHG image of the same region at three successive depths:

- In images (a1) and (b1), we have a low THG signal and high SHG signal with structures that are all oriented in the same direction.
- In images (a2) and (b2), we have a high mostly uniform THG signal and a low SHG signal with structures that are all oriented in two orthogonal direction.
- In images (a3) and (b3), we have a low THG signal again, and high SHG signal with structures that are all oriented in the same direction that is orthogonal to the direction of image (b1).

Figure (5.8.c) compares the THG (c1) and SHG (c2) signals as a function of depth on a larger scale. The intensity as a function of depth is plotted, and the signal appear to be

⁷ ■ One of Us Cannot Be Wrong, Leonard Cohen, Songs of Leonard Cohen (1967)

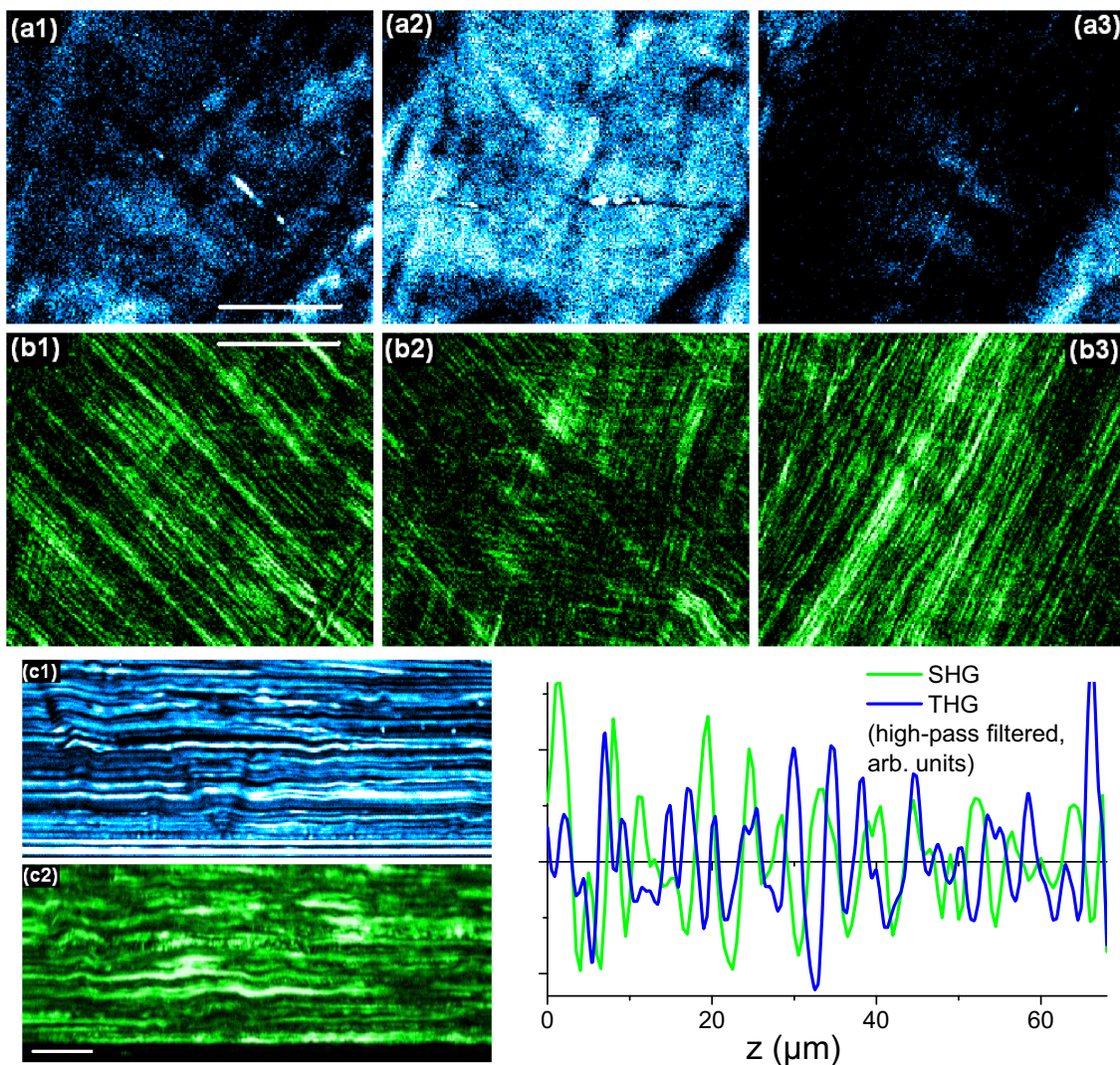


Figure 5.8: THG+SHG ANTI-CORRELATION (a) THG and (b) SHG images at three different depths ($\Delta z = 2\mu\text{m}$) (c1) THG and (c2) SHG xz-reprojections. Conditions: $\lambda = 1.2\mu\text{m}$, $\text{NA}=1.2$. Scale bar = $10\mu\text{m}$.

mostly anti-correlated. We therefore make the following hypotheses concerning the origin of the harmonic signals in the stroma:

1. The SHG signal depends on the organization of the collagen on a macro-molecular level and is maximum in the middle of a layer where the organization is the most crystal-like. The maximum signal signals are therefore correlated with the places where the images show structures that are oriented in the same direction. The oscillations of the SHG signal in one layer is more puzzling, and is probably due to coherence effects that should be further examined.
2. THG is sensitive to the presence of interfaces and inclusions, and is maximum at the interface between layers that have orthogonal orientations. This is consistent with anti-correlated THG/SHG signals.

Since we have organized anisotropic media, more informations on the origin of the contrasts can be obtained by taking into account the influence of the polarization on the harmonic signals, as we will see in the next paragraph.

5.1.3.2 Influence of the Polarization in THG Images

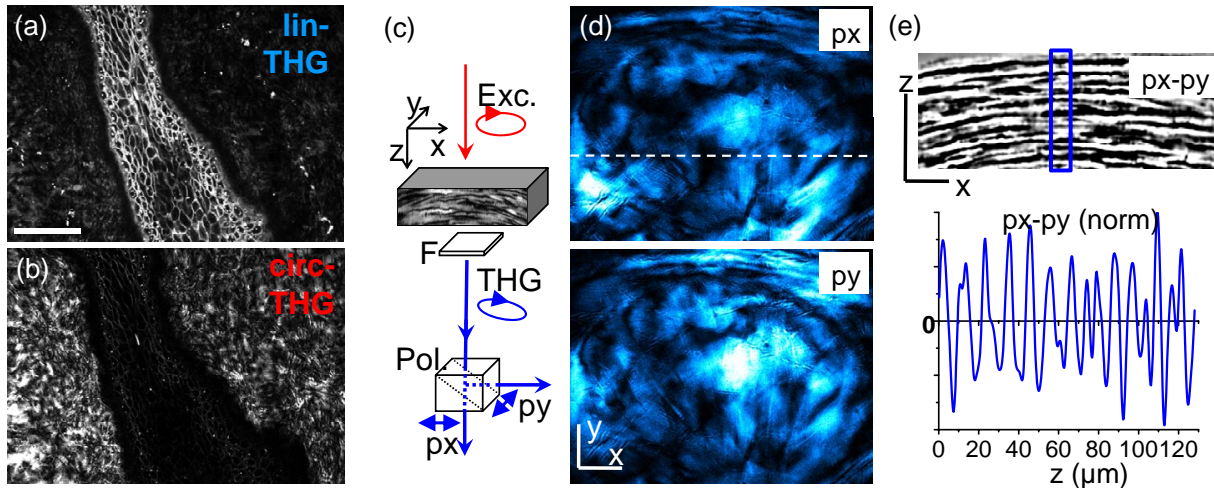


Figure 5.9: INFLUENCE OF THE POLARIZATION IN THG IMAGES

(a) Linearly polarized THG and (b) circularly polarized THG (scale bar= $50\ \mu\text{m}$) (c) Geometry & experimental setup. (d) Polarization-resolved THG image with circularly polarized excitation. (e) xz -reprojection of the $P_x - P_y$ THG image, and low-pass filtered axial profile. Conditions: $\text{NA}=0.8$, $\lambda = 1.2\ \mu\text{m}$.

Figure (5.9) illustrates the influence of the polarization of the excitation in THG microscopy of the cornea. Figure (5.9.a) compares linearly polarized THG image of a folded cornea in which we can see both epithelium cells (in the middle) and the stroma with a circularly polarized THG image of the same place, in which we can only see the stroma since the epithelium is made of isotropic media.

Figures (5.9.c to e) concentrate on the THG signal obtained in the stroma with a circularly polarized excitation and a polarization resolved detection. Figure (5.9.d) compares the x -polarized and y -polarized THG images, and although we see the same structures in both images, the relative contrast between different areas can be very important. This difference is not random, though, as we can see in figure (5.9.e) which shows a xz -reprojection of the difference between the x -polarized and y -polarized THG images on which we can see the layered structure of the corneal stroma appear.

The polarization of the THG signal therefore seems to be a signature of the orientation of the collagen lamellae, and the aim of the next section is to understand this by modeling THG from a stacked anisotropic sample.

5.1.4 Polarization of the THG Signal

⁸ Figure (5.10.a) illustrates the plywood-like structure of the stroma, with successive layers exhibiting a quasi-crystal structure with orthogonal orientations, as resolved by electron microscopy. The crystal structure we will consider is that of a crystal with one main axis along the x -axis with a $C_{\infty v}$ symmetry. The third order nonlinear tensor corresponding to this crystal has been described in equation (3.24). Figure (5.10.b) illustrates the geometry that will be considered in this section, which is similar to the one used in paragraph 3.3.5.3. However, we

⁸ ■ Polar 70, 5ive, Hesperus (2008)

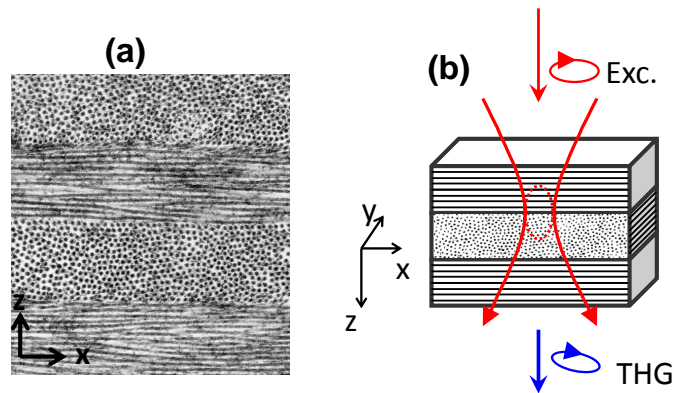


Figure 5.10: STRUCTURE OF THE STROMA.

(a) Electron micrograph, adapted from [1] (b) geometry considered in this section.

recall that in this sample geometry, we found that a circularly polarized excitation beam always produced a circularly polarized third-harmonic emission, independently of the z -position of the interface.

This model does not reflect the alternate THG polarization directions observed experimentally (Figure (5.9.d)). It is therefore sufficient for explaining the origin of the observed THG emission as coming from the interfaces, but it does not account for the complexity of the stromal polarization response. Moreover, typical electron micrographs [1] indicate that lamellae thickness is not constant, and that fibril stacking may present some disorder near interfaces. Therefore the 3rd order hyperpolarizability tensor may not be constant within a lamella, and in some cases the excitation volume may encompass more than two lamellae. It would be a formidable task to analyze all the possible tensor geometries; however we will see that the observed THG polarization sensitivity can be understood by making the simple (and realistic) assumption that stromal lamellae are more organized in their center than near their interfaces, following the distribution given in figure (5.11.c).

Numerical simulations are performed using the approach described in [18], assuming that the nonlinear polarization is expressed as:

$$\begin{aligned}
 \mathbf{P}_+^{(3\omega)} &= \begin{bmatrix} Ex.(\chi_{\parallel}(z).Ex.^2 + \chi_{cr}.Ey^2 + \chi_{cr}.Ez^2) \\ Ey.(\chi_{cr}.Ex.^2 + Ey^2 + \chi_{\perp}.Ez^2) \\ Ez.(\chi_{cr}.Ex.^2 + \chi_{\perp}.Ey^2 + \chi_{\perp}.Ez^2) \end{bmatrix} \\
 \mathbf{P}_-^{(3\omega)} &= \begin{bmatrix} Ex.(\chi_{\perp}.Ex.^2 + \chi_{cr}.Ey^2 + \chi_{\perp}.Ez^2) \\ Ey.(\chi_{cr}.Ex.^2 + \chi_{\parallel}(z).Ey^2 + \chi_{cr}.Ez^2) \\ Ez.(\chi_{\perp}.Ex.^2 + \chi_{cr}.Ey^2 + \chi_{\perp}.Ez^2) \end{bmatrix} \quad (5.1)
 \end{aligned}$$

where the parameters χ_{\parallel} now depends on the axial (z) position within the layer. If we consider a simple modulation, where χ_{\parallel} is maximized at the center of a layer and equal to 1 (=isotropic medium) at the interface (Figure (5.11.c)), we find that the polarization of the THG emission is also a function of z (Figure (5.11.b)). THG polarization exhibits an oscillation behavior between a main ellipticity in one direction and a main ellipticity in the other direction, and is circular at the interface.

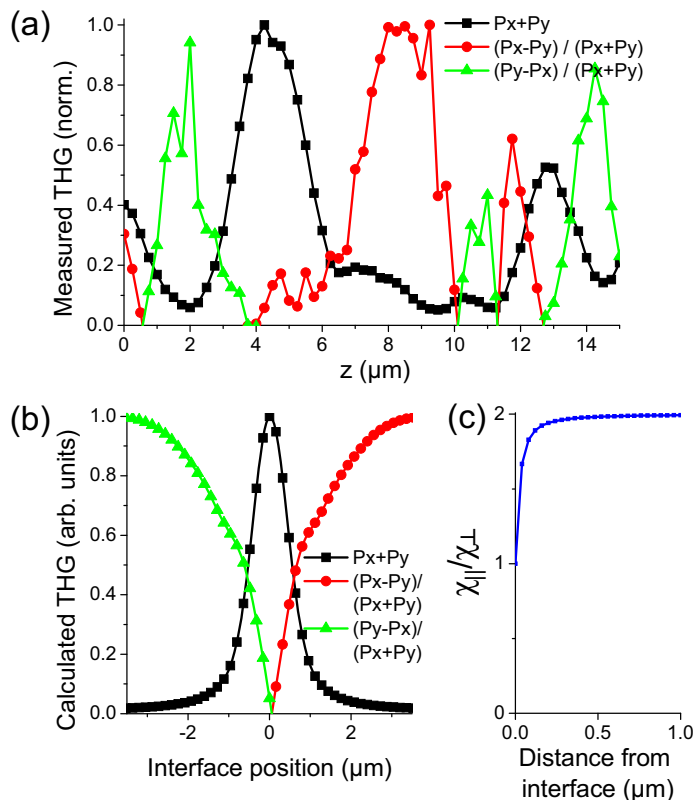


Figure 5.11: POLARIZATION-RESOLVED THG: EXPERIMENT AND SIMULATION.

(a) z -profile of the total and polarization-resolved THG signal across a few stromal lamellae. The total signal maxima ($z = 4$ and 13) and the THG ellipticity maxima are generally anti-correlated, even though the contrast is less clear when the layers are smaller than the axial resolution of the microscope (*e.g.* $z = 11$). (b) Numerical simulation for the case of an interface between two semi-infinite layers with different orientation, assuming that the interface is less structured than the interior of the slabs. (c) Distribution of χ_{\parallel} within a layer assumed for simulation (b). ($NA = 1.2$ $\lambda = 1.18\mu\text{m}$)

5.1.5 Perspectives & Conclusions

⁹As a perspective, the applicability of harmonic/fluorescence imaging for in vivo diagnostic applications would be of great interest. Although the backward-detected harmonic signals are weak (particularly in the case of THG), in vivo epidetection will be enhanced by reflections at intra-ocular interfaces, which should redirect ≈ 4 -10% of the forward-directed emission toward the objective. A recent study on fixed mouse eyes showed that it is indeed possible to use back-reflected photons [19]. This effect will be even more pronounced in opaque corneas, so that epidetection may be a direct indication of edema [20]. Epi-THG can be further enhanced by using large-field optics [21] and shorter pulses, since third-order signals are inversely proportional to the pulse duration squared. Extensive studies will be necessary however to determine which experimental conditions can be safely used in vivo.

In conclusion, our study unravels original nonlinear optical properties of the anterior segment of the human eye with physiological relevance, and elucidates contrast mechanisms involved in

⁹ ■ Conclusion, Apocalyptica, Reflections (2003)

THG microscopy of the cornea. THG/SHG imaging provides a detailed view of stromal micro-architecture. Also of particular relevance are the THG/2PEF signals reflecting the status of the keratocyte network, an essential actor in corneal inflammatory responses and wound healing processes [22]. Finally, in situ imaging of the connective and cellular components of intact trabecular meshwork may provide crucial information about glaucoma physiopathology [23]. The contrast and specificity provided by nonlinear imaging and the ability to image the entire thickness of the anterior segment should generally prove relevant for biomedical research.

Finally, our study demonstrates the superior contrast of nonlinear techniques compared with linear techniques, especially on the corneal stroma where linear techniques cannot reveal the stacking of the collagen lamellae as clearly as THG microscopy does. The study of the nonlinear contrast in other organized structures should therefore be investigated.

5.2 Zebrafish

5.2.1 Introduction

¹⁰This section presents an application of nonlinear microscopy in developmental biology developed during this thesis. Our aim was to provide a complete description of the unstained zebrafish early development using coherent nonlinear microscopy. The zebrafish embryo is an important model organism in developmental biology [24–26] and in genetics [27–30], with an important recent activity concerning the influence of maternal factors [31–33] and micro RNAs [34, 35]. However, the visualization of early mitotic events is not straightforward, for several reasons:

- The fluorescent markers that are commonly used in fluorescence techniques (confocal, 2PEF or SPIM) need to mature and to localize, and are therefore not adapted for the imaging of the early stages.
- The spherical geometry of the embryo is not adapted to the raster scan method used in most scanning techniques.
- The size of the embryo (images have to be performed at depths larger than $400\mu\text{m}$) makes it hard for linear techniques to get high quality images in the whole dividing tissue.

The description of the early zebrafish development has been pioneered by Kane & Kimmel [24, 26, 27], who described a succession of synchronous (until the 32 cell stage) and so called “meta-synchronous” (or “mitotic waves”) division cycles (from the 32 cell stage to the $1k$ -cell stage), followed by an abrupt transition to a patch-like regime following the onset of zygotic expression at the midblastula transition. Our data allows us to reconsider these models.

We will show in the next section that combining nonlinear harmonic signals based on endogenous harmonophores is an adapted method to tackle this problem, and that it allowed us to get the whole cell lineage tree of several unstained embryos up to the midblastula transition at stage $1k$ -cell. This work was done in collaboration between four labs:

- Louise Duloquin & Nadine Peyrieras at the *Institut de Neurobiologie Alfred Fessard* (INAF), Gif, France¹¹.
- Miguel Lorengo-Oroz & Andres Santos at the *Universidad Politécnica de Madrid* (UPM), Madrid, Spain.
- Paul Bourguine & Thierry Savy at the *Centre de Recherche en Epistémologie Appliquée* (CREA), Ecole Polytechnique, Paris, France.
- Israël Veilleux, Xavier Solinas & Delphine Débarre at the *Laboratory for Optics & Biosciences* (LOB), Ecole Polytechnique, Palaiseau, France.

¹⁰■ The River, Bruce Springsteen, The River (1980)

¹¹■ Giant Squid, The Ichthyologist (2009)

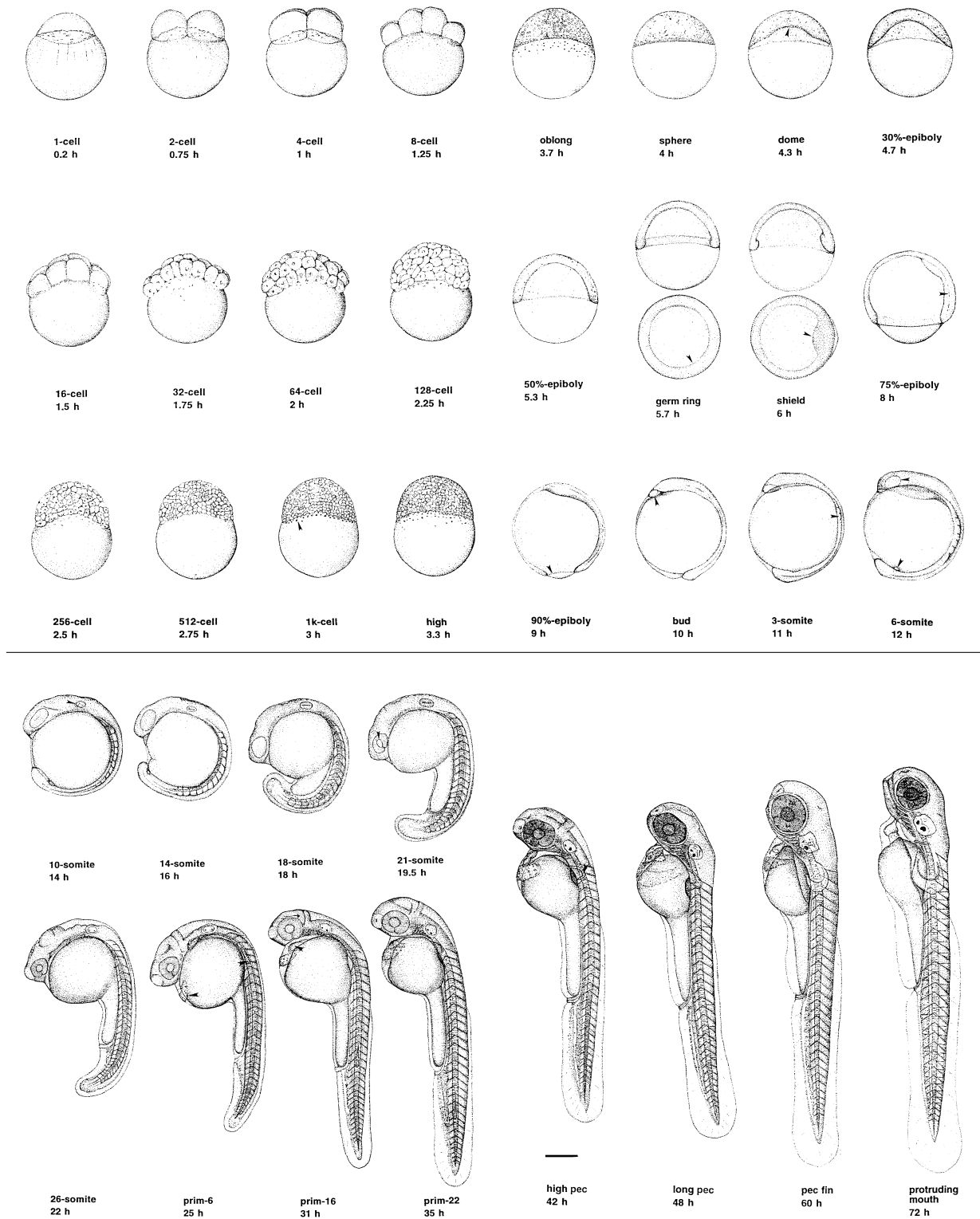


Figure 5.12: DEVELOPMENT OF THE ZEBRAFISH EMBRYO
 This study focuses on the stages 1cell-1kcell. Adapted from [24].

5.2.2 Reconstruction of the Zebrafish Early Development Using Multiharmonic Microscopy

5.2.2.1 Introduction

Vertebrate embryo development involves the spatio-temporal synchronization [36] of large ensembles of morphogenetic processes including collective cell movements, cell divisions [37–43], and resource mobilization [44–48]. In toto imaging and reconstruction of cell fate is a long-standing goal of embryology; however global imaging of morphogenesis in complex vertebrate systems with sub-cellular resolution is technically challenging because the shape and opacity of embryos hamper deep imaging, even in relatively transparent systems such as the zebrafish embryo.

Investigators typically face a compromise between information content in the deepest regions and imaging rate. Parallelized linear microscopy approaches such as digital scanned laser light sheet fluorescence microscopy [49] provide fast imaging (e.g. one 3D image every 90s) but suffer from severe loss of information with depth. Point scanning two-photon microscopy provides deeper imaging but exhibits slower frame rates incompatible with in toto imaging. Furthermore, the usual implementations of these two paradigms do not allow homogeneous illumination in non-plane (e.g. spherical) samples. This involves trading off the visibility of deep structures against the absence of illumination-induced perturbation in superficial regions. Additionally, the observation of embryos at early stages bears the difficulty that fluorescent protein expression is generally weak and unspecific until 3 hours post-fertilization (hpf). Finally, error-free tracking of hundreds of dividing cells requires dedicated analyzing schemes and verification procedures.

5.2.2.2 Microscopy Method

¹²Point-scanning multiphoton microscopy is effective for deep imaging of thick samples [50, 51]. However the usual raster scanning approach is not adapted to non-flat samples, because scattering and aberrations reduce excitation intensity in the deepest regions. This scheme results in inhomogeneous illumination and signal level across the field of view. We implemented conformal scanning for imaging spherical embryos in the following manner: each plane was scanned along a spiral trajectory with variable galvanometer speed, and only a half-sphere was imaged in order to minimize acquisition time.

Figure (5.13) illustrates the image acquisition strategy used in this study:

- (a) Optical sections of a sphere.
- (b) Experimental setup: the de-chorionated embryo is placed in a well filled with embryo medium. Harmonic signals are detected in transmission, while fluorescence is epideTECTED.
- (c) THG/SHG/2PEF emission spectra for an excitation at $\lambda = 1.2\mu m$.
- (d) Comparison between raster scan (top) and conformal scan (bottom) techniques.
- (e) Experimental comparison between a raster (top) and a conformal (bottom) THG image of a zebrafish embryo. Internal structures are clearly more visible in the conformal image. scale bar= $20\mu m$.

¹²■ Queen of the Borrowed Light, Wolves in The Throne Room, Diadem of 12 Stars (2006)

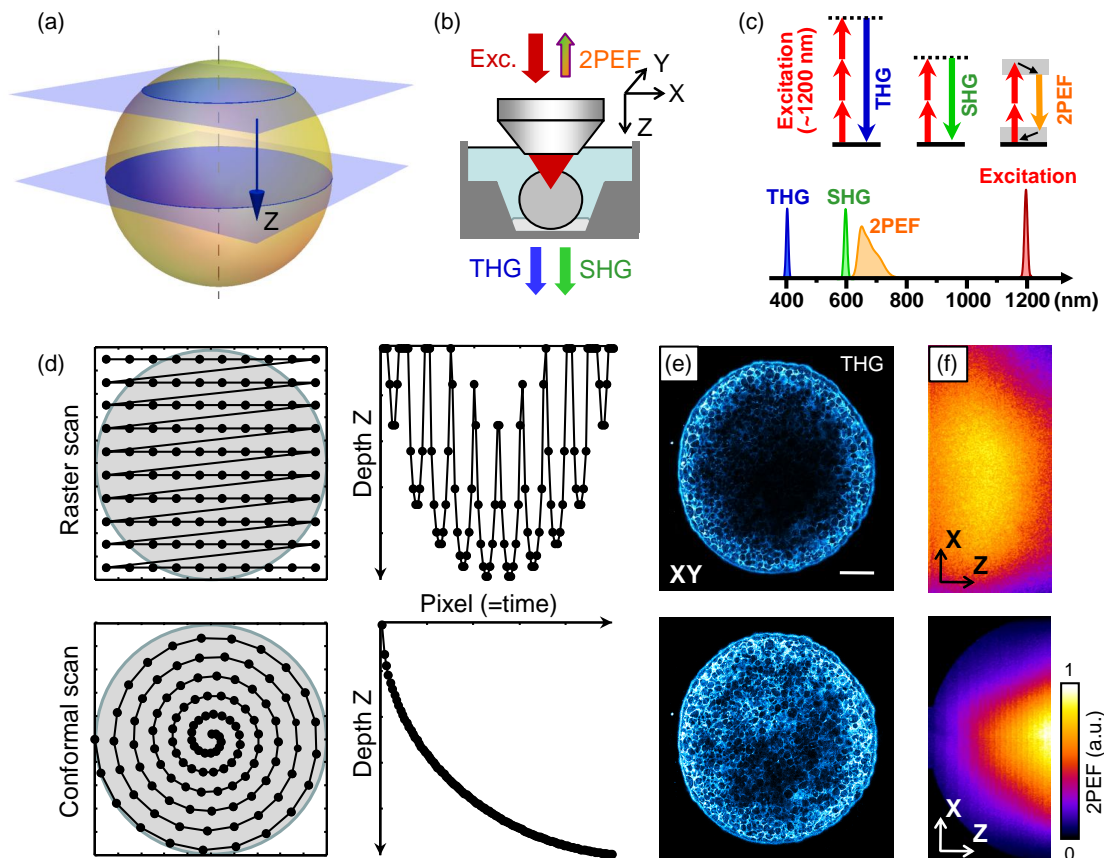


Figure 5.13: GEOMETRY & CONFORMAL SCANNING see text for more details.

- (f) xz -reprojection of 2PEF in a homogeneous solution of fluorophores with either raster scanning (top) or conformal scanning (bottom). Conformal scanning allows collection of more nonlinear signals in positions deep inside the embryo without increasing the power at the surface.

This scheme has several advantages:

1. Acquisition time can be distributed in order to accumulate signal only where necessary.
2. Fast scanning can be used to image the embryo periphery, which minimizes photoperturbation.
3. Depending on the application, "non-interesting" regions can be undersampled or skipped in order to reduce acquisition time.
4. Scanning speed is adjusted continuously, which minimizes acceleration artifacts.

In practice, scanning voltages targeted an Archimedes spiral with a constant radial step and a linear variation of sampling density along the trajectory, while the pixel clock was kept constant. Galvanometer positions were measured along with the optical signals and were used for projecting the SHG/THG images on a square grid. We could then image a $440\mu\text{m}$ -radius half-sphere with $2 \times 2 \times 4\mu\text{m}^3$ voxels and 80s temporal resolution. Most importantly, this scheme enabled us to detect all the SHG signals originating from mitotic spindle formation (see below) including in the deepest regions of the embryo, under illumination conditions preserving normal development.

5.2.2.3 Identification of the Contrasts

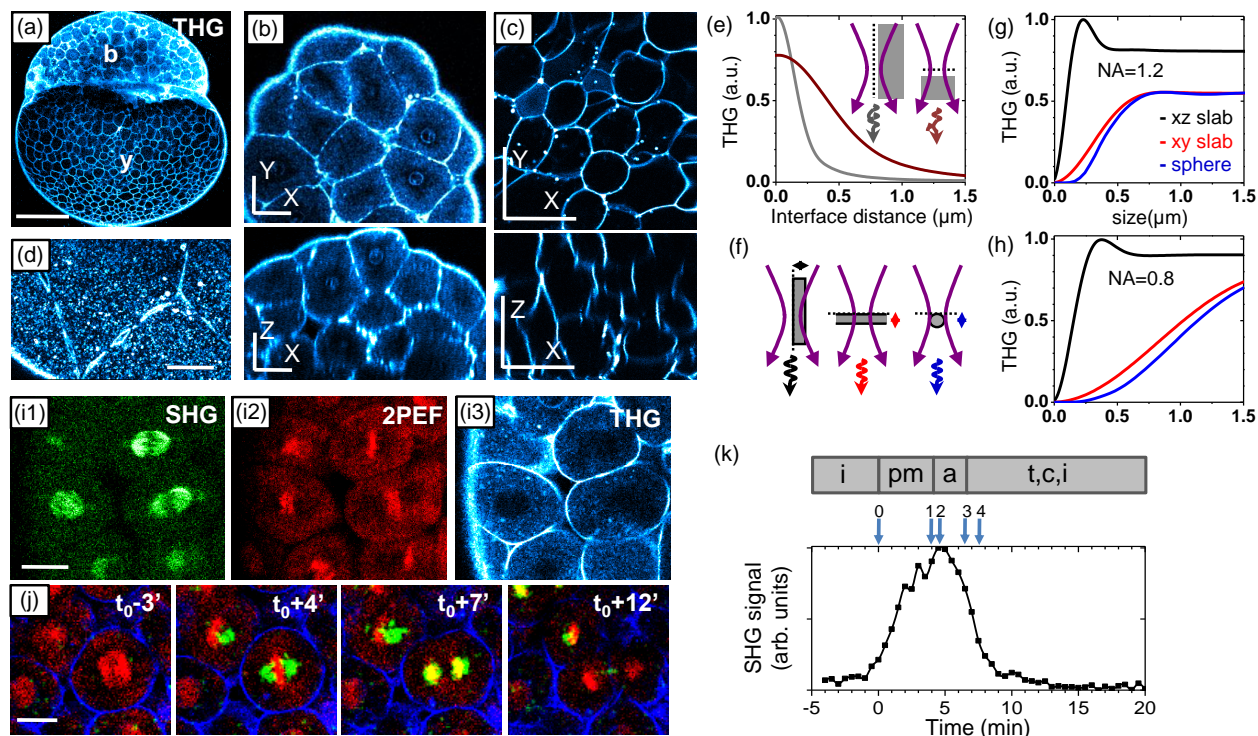


Figure 5.14: HARMONIC GENERATION CONTRASTS IN THE ZEBRAFISH EMBRYO see text for more details.

¹³ Representative THG images of zebrafish embryo during divisions are presented in figure (5.14). Strong signals are observed near the interface of dividing cells at post-cellularization stages. Since no THG can be obtained from a homogeneous medium, this signal reflects the presence of a sizable inter-cellular space, as indicated by numerical simulations (figure (5.14.efgh)). This interpretation is corroborated by high-NA THG images of dividing cells showing locally double interfaces (figure (5.14.d)) and by the observation that membrane visibility diminishes in connective epithelial and differentiated cells. THG therefore highlights dividing and motile cells, and provides a direct visualization of cell morphology with unique contrast in the early embryo. The cellularization process at stage 32 is also readily visible, as well as the formation of filopodia in post-MBT motile cells and the traffic of intracellular lipidic vesicles during divisions.

Combined THG/SHG imaging can be used to detect a number of key events during cell divisions [52]. THG images reveal cell shapes, cellularization dynamics, and nuclear membrane formation/fragmentation, whereas SHG reveals the formation of mitotic spindles. We performed a series of multimodal THG-SHG-2PEF experiments in H2B-mCherry mutants in order to define the timing of THG/SHG signals with respect to chromatin dynamics (figure (5.14.j)) and use that information for subsequent analyses in unstained embryos. We found that the SHG intensity exhibits a nearly-Gaussian temporal behavior permitting to measure division timings and cell cycle duration with 30s precision.

We note that additional intracellular information can be obtained from these signals. The visibility of the spindle midzone in SHG images after cell divisions (figure (5.14.i1)) indicates

¹³ ■ My Dying Bride, Songs of Darkness, Words of Light (2004)

that the midzone is partially polarized. THG provides morphological information that can be used to check the absence of phototoxicity. Finally, high-NA THG imaging reveals nucleus heterogeneity.

THG images also provide a detailed morphologic description of the yolk (figure (5.14.a)). Here, the signal stems from the contrast between yolk globules and the layer of interstitial fluid. These images provide a striking view of yolk dynamics during cleavage stages: restructuration of the large initial channels, transport processes, and deformations (the dynamics of these events can be analyzed using statistical analysis methods [53]) are seen with a contrast not obtained with linear techniques.

THG image formation is relatively complex and the visibility of specific structures depends on their size relative to the focal volume [54]. We chose here moderate NA focusing ($3.5\mu\text{m}$ Z-FWHM) which provided enhanced signal from cell boundaries compared to smaller heterogeneities and was still compatible with cell segmentation.

THG and SHG imaging have contradictory requirements in terms of incident polarization. SHG from mitotic spindles is reduced in the case of an incident linear polarization orthogonal to the spindle axis. Therefore imaging should preferentially be done with circularly polarized light, in order to get similar signal levels from all the spindles - at least the ones that are not orthogonal to the imaging plane. However, THG with circular incident polarization vanishes except in the case of anisotropic media [14], and THG imaging of dividing tissue should be performed using linear polarization. We therefore rapidly rotated the linear incident polarization ($\approx 1500\text{rpm}$) during image acquisition using a motorized half-waveplate in order to optimize both signals.

Overall, conformal scanning, 100MHz photon-counting detection, high excitation intensity tolerable at long wavelength, resolution and polarization control enabled us to image all the mitotic spindles and simultaneous cell morphology with $\approx 80\text{s}$ resolution in unstained embryos.

5.2.2.4 Image Analysis of the Multiharmonic Data

¹⁴Multiharmonic microscopy data required a specific analysis methodology in order to extract the lineage tree from SHG data and associated cell morphological information from THG data. A dedicated image processing pipeline for reconstructing the first 10 cell cycles of zebrafish development (see figure (5.15)) was designed in Madrid by Miguel Luengo-Oroz¹⁵ and Andres Santos.

Figure (5.15) illustrates the image analysis strategy developed for treating the THG and SHG images of the developing zebrafish embryo:

- (a) SHG spot detection. Mitosis detection (in red) over-imposed to x-y projections of SHG signal. Consecutive time points corresponding to 32 mitosis wave.
- (b) THG image segmentation. Cross-sections of 8 cell (a) and 128 cells (b) segmentation.
- (c) Virtual embryo reconstruction from 1 cell to 512 cells. Volume rendering color code corresponds to the clonal descendants of first 8 blastomeres.

¹⁴■ Dream Theater, Images & Words (1992)

¹⁵who wrote the paragraph from which this section is adapted

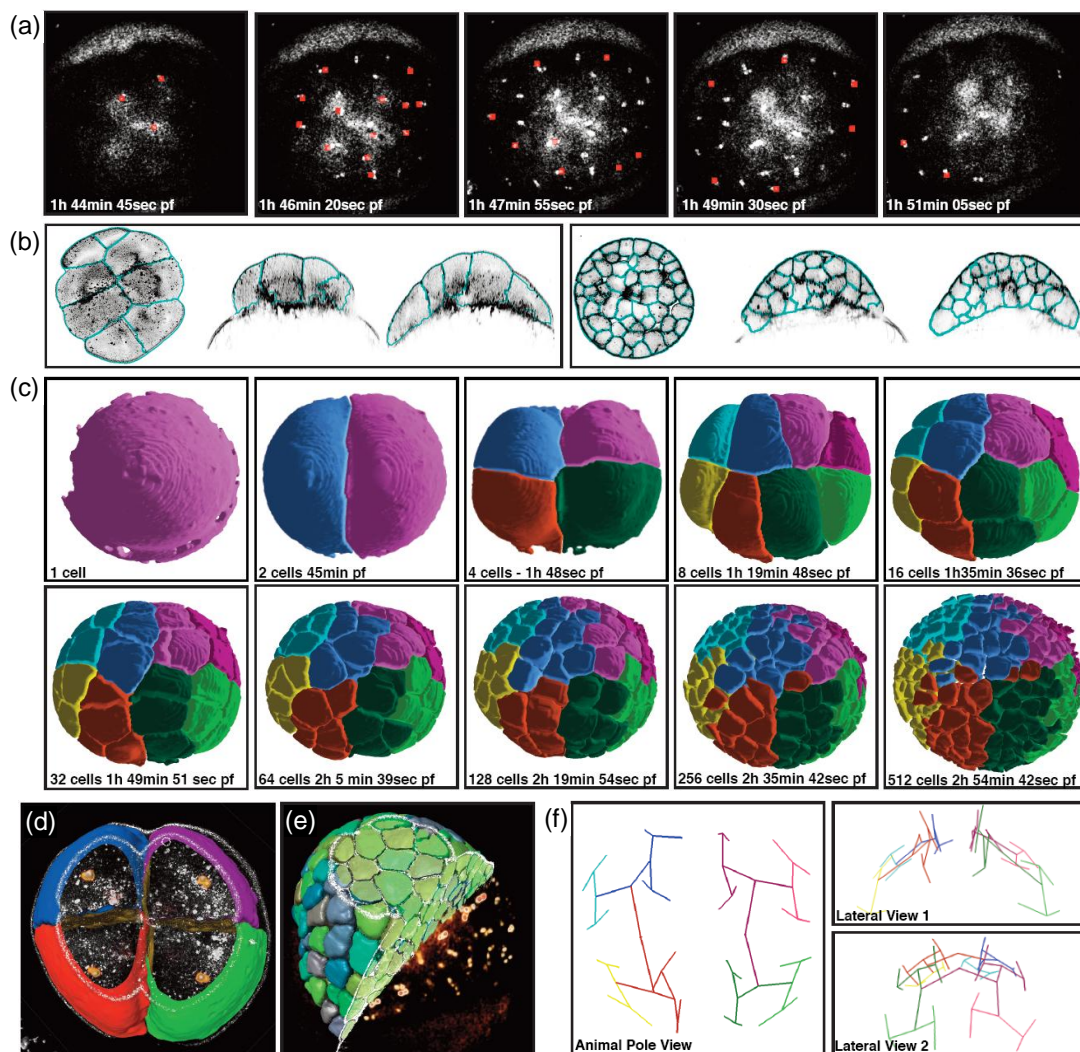


Figure 5.15: IMAGE ANALYSIS STRATEGY

Designed at UPM by Miguel Luengo-Oroz and Andres Santos, see text for more details.

- (d) & (e) Complete reconstruction of 4-cell and 256-cells stage. In white orthoslices of THG signal. In orange, rendering of SHG signal. In colors, surfaces of segmented cells.
- (f) Lineage representation from 2 cells to 32 cells (note the perfect fractal organization and symmetry)

Data from both channels are first filtered to remove experimental noise. Since early divisions occur in cycles, all the SHG 3D stacks corresponding to a given cycle are then binned into one frame. Therefore image sequences typically consisting of one hundred time points are reduced to ten, each corresponding to a division cycle and containing all the cells. In parallel, the segmentation of the outermost layer of the embryo is extracted from THG data by means of mathematical morphology operators. The reduced SHG data and the embryo external surface (THG) are then used together for extracting the lineage tree. The procedure is initialized by finding the two maxima corresponding to the first two mitoses (2-cells stage). A Voronoi partition is generated inside the embryo mask from the positions of the detected nuclei, and provides a first robust approximation of membrane shape. After the mitosis, the daughter cells are identified by finding two symmetric SHG maxima inside the Voronoi region assigned to the

mother cell in the previous cycle. A number of SHG spots (2, 4, 8, etc.) corresponding to the current cell cycle is automatically detected, and the divisions found are manually validated and corrected with the MOVIT exploration interface (developed by CREA & N. Peyrieras). Then, the Voronoi partition is generated from the detected spots inside the embryo mask of the next cell cycle and the procedure of automatic detection and validation/correction is iterated for all the cycles.

This procedure extracts all the cell centers and their lineage. Nevertheless, the temporal coordinates of the divisions are not precisely defined at this stage, as we worked in the reduced time sequence. In order to extract the timing information, SHG intensity maxima along the temporal dimension are estimated for each division using Gaussian fitting of the original data. SHG maxima correspond to a precise time point during the cell cycle and can be used to measure cell cycle duration with sub-minute accuracy. After the temporal coordinate of each mitosis is obtained with this procedure, the lineage tree is expanded to its original time length. Then, the cell nuclei positions are used for seeding a more precise THG membrane segmentation step, based on a viscous watershed segmentation algorithm.

This processing pipeline provides an error-free cell lineage tree with the following information: nuclear position in each time step (detected from mitotic spindles SHG signals), parental relation between cells, cell cycle duration, and cell shape estimated using both the Voronoi approximation and the viscous watershed segmentation. These data are organized in a database that can be visualized interactively with the MOVIT interface. For the work presented here, methods were implemented in Matlab and the whole process for analyzing a dataset typically took 72h of computation time on a Core2duo platform with 8 GB RAM, and 4h of user interaction for manual checking of the detected SHG spots and script launching.

5.2.2.5 Quantitative Analysis of the Mitotic Waves

Figure (5.16) illustrates the analysis performed on the mitotic waves in the zebrafish embryo

- (a) Mitosis distribution per time interval (90s) for the 6 reconstructed embryos.
- (b) Representation of the mitotic wave at the stage 128-256, where the time between the division of a cell and the time of the first division of the wave is color-coded.
- (c) Relation between time and the distance from the starting point of each mitotic wave for all the mitotic events in one of the reconstructed embryo.
- (d) Origin of the mitotic waves at stages 6-10.
- (e) Average cell-cycle duration of each division cycle for the 6 reconstructed embryos, an mean value for the 6 embryos.
- (f) Cell-cycle duration of each division cycle for two categories of cells: cells near the origin of the mitotic wave, and cells near the ending of the wave.

The first four divisions form a remarkably symmetric spatial pattern with orthogonal successive directions. On the temporal side, a progressive asynchrony of the mitoses ($> 90\text{sec}$) could be detected as early as the 8-cells stage given our time resolution. Mitotic waves then get increasingly apparent from 8-cells to 1k-cells stages. At later stages divisions occur in seemingly random patches as seen from partial datasets. Mitotic waves start from the top of the embryo

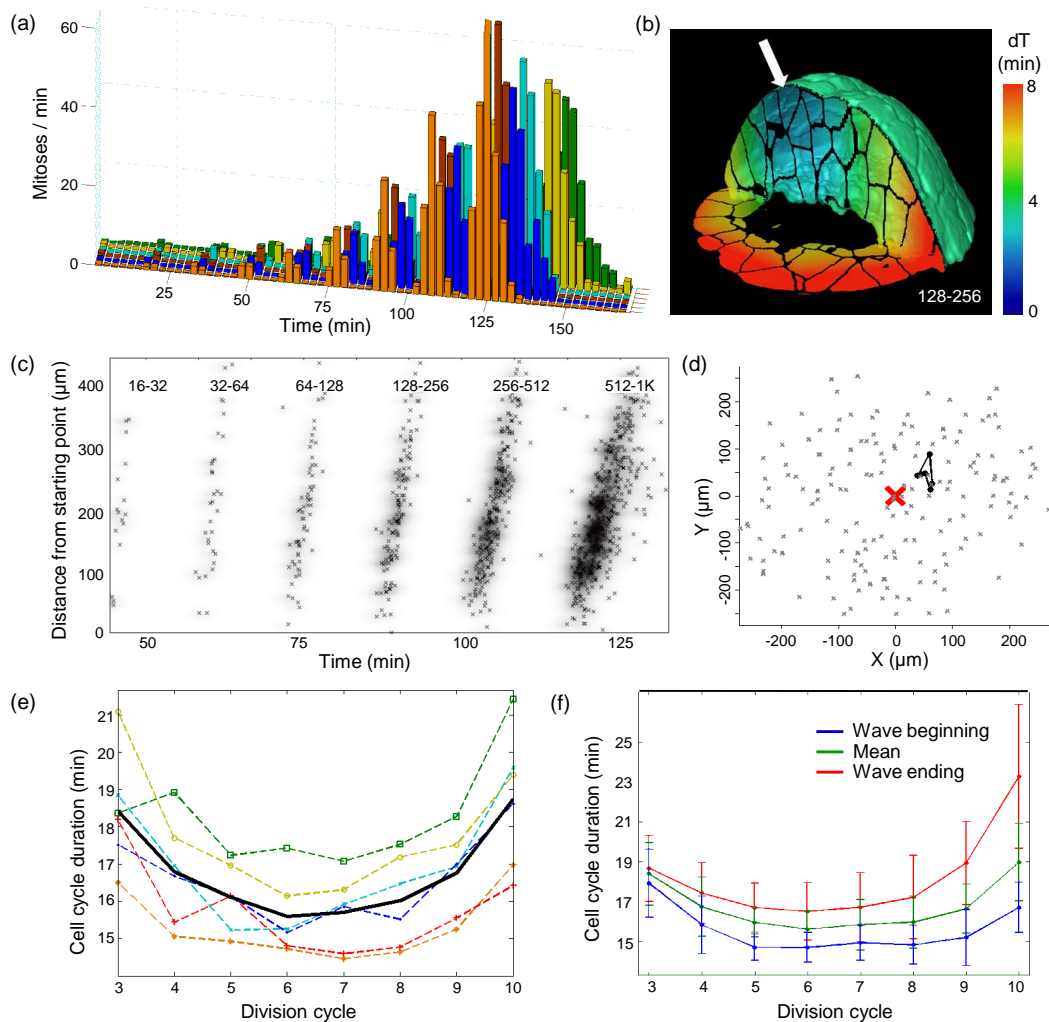


Figure 5.16: QUANTITATIVE ANALYSIS OF THE MITOTIC WAVES
See text for more details.

with a small offset from the animal pole (figure 5.16.d) and propagate across the embryo. We note that the spatial offset is maintained during all the division waves, so that the 3D spherical wave that spans the embryo resembles a peripheral wave when reaching the bottom cells.

The speeds of the successive waves can be estimated by linear fitting and are seen to decrease with division cycles from 125 ± 30 to $11 \pm 7 \mu\text{m}/\text{min}$ (figure 5.16). Our data also reveal that wave speed is proportional to the mean cell surface (assuming a constant tissue volume), and discard hypotheses of wave speed being proportional to mean cell radius or volume.

Analysis of the divisions timing deduced from the SHG signal and the lineage tree reveals that the cell cycle duration exhibits progressive changes with successive mitotic waves. Cycle shortens from $18.5 \pm 1.5 \text{min}$ at the 4-cell stage down to $15.5 \pm 1.0 \text{min}$ at the 32-cell stage, i.e. when cellularization occurs. Cell cycle then lengthens again up to $18.5 \pm 1.5 \text{min}$ at the 512-cell stage. This evolution is the signature of a progressive change in the division regime. Cell cycle before the 32-c stage is likely limited by maternal determinants from the yolk. Cellularization seems to enable the subsequent cycle lengthening, which may be a requirement for zygotic expression and midblastula transition.

5.2.2.6 Cell Lineage Tree

¹⁶An example of the whole cell lineage tree of a zebrafish embryo between the one cell stage and the $1k$ -cell stage is illustrated in figure (5.17).

- (a). Lineage tree from 2 to 512 cells. Each color corresponds to the clonal descendants of first 8 blastomeres.
- (b) Enlarged sight of a subtree corresponding to the red box in (a). Each square corresponds to a cell at one time point. Each time point is 95 seconds.
- (c) Enlarged sight of the red boxed subtree in (b).
- (d) Volume rendering showing the 256 cells stage with the 8 colors. The red squared cell corresponds to the one with the red square in (c)

5.2.2.7 Conclusion

We have demonstrated the potential of multiharmonic microscopy for the study of the zebrafish early development. The combination of two modalities that give us a global information about the shapes of the cells (THG) and a local indicator of cell divisions (SHG) allowed the tracking of all the dividing cells in the developing embryo until the $1k$ -cell stage, and resulted in the construction of the cell lineage tree. This should pave the way to studies on other teleosts or on other stages of the zebrafish development, although both the imaging conditions and the automated image analysis strategies may have to be adapted.

¹⁶■ Lemon Tree, Fool's Garden, Dish of the Day (1995)

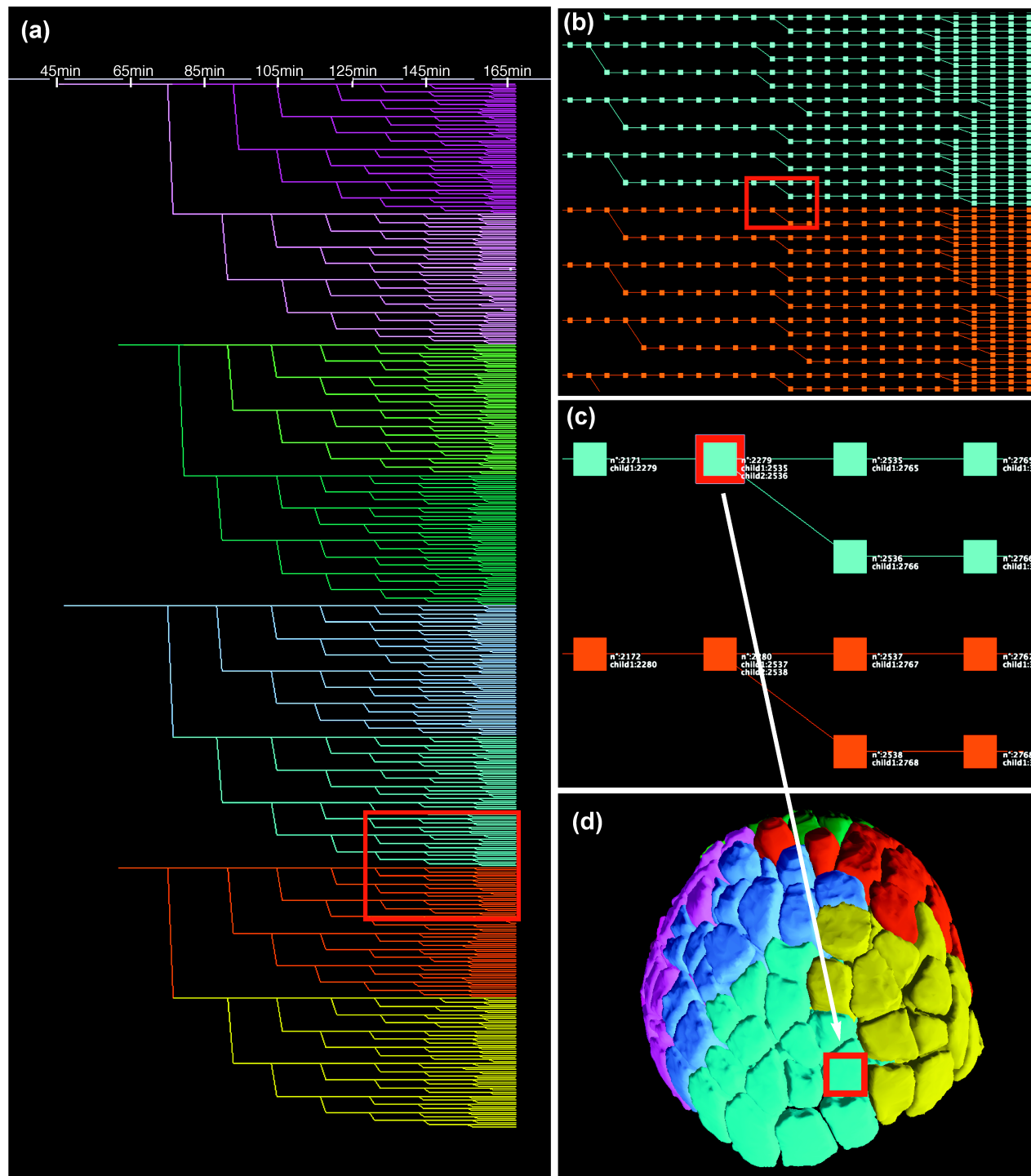


Figure 5.17: CELL LINEAGE TREE

Figure assembled by Louise Duloquin, using the software developed at CREA.

Conclusion

In this chapter, we have shown the current situation of two collaborations on applications of coherent nonlinear microscopy. This part has been realized in parallel with the rest of the work, and there are therefore several “intersections” concerning the contrast mechanisms. The contrasts in the zebrafish images at different numerical apertures for example, or the understanding of the THG signal in the cornea.

The cornea is an interesting sample, since its structure provides both SHG and THG signals that together may provide new insights on the collagen organization in the stroma, while the ability to investigate edema and to characterize the quality of an endothelium prior to a transplant may have clinical applications.

The combination of SHG and THG on the Zebrafish embryo allowed the first reconstruction of the cell lineage tree from the 1-cell stage to the $1k$ -cell stage with spatio-temporal information about division times, localization and cell shape, and may be used to characterize mutants or in other organisms.



Bibliography

- [1] R.T. NISHIDA. *Cornea, 2nd Edition*. Elsevier Mosby (2005).
- [2] W. DREXLER AND J. G. FUJIMOTO. *State-of-the-art retinal optical coherence tomography*. Prog. Retin. Eye Res., 27(1):45–88 (2008).
- [3] I. JALBERT, F. STAPLETON, E. PAPAS, D.F. SWEENEY, AND M. CORONEO. *In vivo confocal microscopy of the human cornea*. Br. J. Ophthalmol., 87:225–36 (2003).
- [4] W.R. ZIPFEL, R.M. WILLIAMS, AND W.W. WEBB. *Nonlinear magic: multiphoton microscopy in the biosciences*. Nat. Biotechnol., 21(11):1369–1377 (2003).
- [5] W.R. ZIPFEL, R.M. WILLIAMS, R. CHRISTIE, A.Y. NIKITIN, B.T. HYMAN, AND W.W. WEBB. *Live tissue intrinsic emission microscopy using multiphoton-excited native fluorescence and second-harmonic generation*. Proc. Natl. Acad. Sci. USA, 100(12):7075–7080 (2003).
- [6] D. W. PISTON, B. R. MASTERS, AND WEBB W. W. *Three-dimensionally resolved nad(p)h cellular metabolic redox imaging of the in situ cornea with two-photon excitation laser scanning microscopy*. J. Microsc., 178(2):20–26 (1995).
- [7] J. G. LYUBOVITSKY, J. A. SPENCER, T. B. KRASIEVA, B. ANDERSEN, AND B. J. TROMBERG. *Imaging corneal pathology in a transgenic mouse model using nonlinear microscopy*. J. Biomed. Opt., 11(1):014013 (2006).
- [8] S.-W. TENG, H.-Y. TAN, J.-L. PENG, H.-H. LIN, K.H. KIM, W. LO, Y. SUN, W.-C. LIN, S.-J. LIN, S.-H. JEE, P.T.C. SO, AND C.-Y. DONG. *Multiphoton autofluorescence and second-harmonic generation imaging of the ex vivo porcine eye*. Invest. Ophthalmol. Vis. Sci., 47(3):5251–5259 (2006).
- [9] H.F. WANG, Y. FU, P. ZICKMUND, R.Y. SHI, AND J.-X. CHENG. *Coherent anti-stokes raman scattering imaging of axonal myelin in live spinal tissues*. Biophys. J., 89(1):581–591 (2006).
- [10] R.M. WILLIAMS, W.R. ZIPFEL, AND W.W. WEBB. *Interpreting second-harmonic generation images of collagen i fibrils*. Biophys. J., 88:1377–1386 (2005).
- [11] M. HAN, G. GIESE, AND J. F. BILLE. *Second harmonic generation imaging of collagen fibrils in cornea and sclera*. Opt. Express, 13(15):5791–5797 (2005).
- [12] A. T. YEH, N. NASSIF, A. ZOUMI, AND B.J. TROMBERG. *Selective corneal imaging using combined second-harmonic generation and two-photon excited fluorescence*. Opt. Lett., 27(23):2082–2084 (2002).
- [13] N. MORISHIGE, A. J. WAHLERT, M.C. KENNEY, D.J. BROWN, K. KAWAMOTO, T. CHIKAMA, T. NISHIDA, AND J.V. JESTER. *Second-harmonic imaging microscopy of normal human and keratoconus cornea*. Invest. Opht. Vis. Sci., 48(3):1087–94 (2007).
- [14] D. ORON, E TAL, AND Y. SILBERBERG. *Depth-resolved multiphoton polarization microscopy by third-harmonic generation microscopy*. Opt. Lett., 28(23):2315–2317 (2003).

-
- [15] D. V. PATEL AND C. N. J. MCGHEE. *Mapping of the Normal Human Corneal Sub-Basal Nerve Plexus by In Vivo Laser Scanning Confocal Microscopy*. Invest. Ophthalmol. Vis. Sci., 46(12):4485–4488 (2005).
- [16] C.-H. YU, S.-P. TAI, C.-T. KUNG, W.-J. LEE, Y.-F. CHAN, H.-L. LIU, J.-Y. LYU, AND C.-K. SUN. *Molecular third-harmonic-generation microscopy through resonance enhancement with absorbing dyes*. Opt. Lett., 33(4):387–9 (2008).
- [17] T. BOULESTEIX, A. M. PENA, N. PAGES, G. GODEAU, M. P. SAUVIAT, E. BEAUREPAIRE, AND M.-C. SCHANNE-KLEIN. *Micrometer scale ex vivo multiphoton imaging of unstained arterial wall structure*. Cytometry A, 69A:20–26 (2006).
- [18] N. OLIVIER AND E. BEAUREPAIRE. *Third-harmonic generation microscopy with focus-engineered beams: a numerical study*. Opt. Express, 16(19):14703–14715 (2008).
- [19] S.-Y. CHEN, H.-C. Y. I-JONG WANG, AND C.-K. SUN. *Infrared-based third and second harmonic generation imaging of cornea*. J. Biomed. Opt., 14(4):1–7 (2009).
- [20] V. NUZZO, K. PLAMANN, M. SAVOLDELLI, M. MERANO, D. DONATE, O. ALBERT, P. F. GARDEAZÁBAL RODRIGUEZ, G. MOUROU, AND J.-M. LEGEAIS. *In situ monitoring of second-harmonic generation in human corneas to compensate for femtosecond laser pulse attenuation in keratoplasty*. J. Biomed. Opt., 12(6):064032 (2007).
- [21] D. DÉBARRE, N. OLIVIER, AND E. BEAUREPAIRE. *Signal epidetection in third-harmonic generation microscopy of turbid media*. Opt. Express, 15(14):8913–8924 (2007).
- [22] M. C. HELENA, F. BAERVELDT, W. J. KIM, AND S. E. WILSON. *Keratocyte apoptosis after corneal surgery*. Invest. Ophthalmol. Vis. Sci., 39(2):276–283 (1998).
- [23] J. C. TAN, D.M. PETERS, AND P.L. KAUFMAN. *Recent developments in understanding the pathophysiology of elevated intraocular pressure*. Curr. Opin. Ophthalmol., 17(2):168–74 (2006).
- [24] C. B. KIMMEL, W. W. BALLARD, S. R. KIMMEL, B. ULLMANN, AND T. F. SCHILLING. *Stages of embryonic development of the zebrafish*. Dev. Dyn., 203(3):253–310 (1995).
- [25] EDWARD C. ROOSEN-RUNGE. *On the early development –bipolar differentiation and cleavage–of the zebrafish, BRACHYDANIO RERIO*. Biol. Bull., 75(1):119–133 (1938).
- [26] DA KANE. *Cell cycles and Development in the embryonic zebrafish*. Meth. Cell Biol., 59:11+ (1999).
- [27] D. A. KANE, H. M. MAISCHEIN, M. BRAND, F. J. M. VAN EEDEN, M. FURUTANI-SEIKI, M. GRANATO, P. HAFFTER, M. HAMMERSCHMIDT, C. P. HEISENBERG, Y. J. JIANG, R. N. KELSH, M. C. MULLINS, J. ODENTHAL, R. M. WARGA, AND C. NUSSLEIN-VOLHARD. *The zebrafish early arrest mutants*. Development, 123(Sp. Iss. SI):57–66 (1996).
- [28] M. P. S. DEKENS, F. J. PELEGRI, H. M. MAISCHEIN, AND C. NUSSLEIN-VOLHARD. *The maternal-effect gene futile cycle is essential for pronuclear congression and mitotic spindle assembly in the zebrafish zygote*. Development, 130(17):3907–3916 (2003).
-

- [29] S MATHAVAN, SGP LEE, A MAK, LD MILLER, KRK MURTHY, KR GOVINDARAJAN, Y TONG, YL WU, SH LAM, H YANG, YJ RUAN, V KORZH, ZY GONG, ET LIU, AND T LUFKIN. *Transcriptome analysis of zebrafish embryogenesis using microarrays*. PLOS Genetics, 1(2):260–276 (2005).
- [30] S. O’BOYLE, R. T. BREE, S. MCLOUGHLIN, M. GREALY, AND L. BYRNES. *Identification of zygotic genes expressed at the midblastula transition in zebrafish*. Biochem. & Biophys. Res. Comm., 358(2):462–468 (2007).
- [31] F. PELEGRI. *Maternal factors in zebrafish Development*. Dev. Dyn., 228(3):535–554 (2003).
- [32] D. S. WAGNER, R DOSCH, K. A. MINTZER, A. P. WIEMELT, AND M. C. MULLINS. *Maternal control of Development at the midblastula transition and beyond: Mutants from the zebrafish II*. Dev. Cell, 6(6):781–790 (2004).
- [33] B. M. FARLEY AND S. P. RYDER. *Regulation of maternal mRNAs in early Development*. Crit. Rev. in Biochem. and Mol. Bio., 43(2):135–162 (2008).
- [34] E. WIENHOLDS, W. P. KLOOSTERMAN, E. MISKA, E. ALVAREZ-SAAVEDRA, E. BEREZIKOV, E. DE BRUIJN, H. R. HORVITZ, S. KAUPPINEN, AND R. H. A. PLASTERK. *Microrna expression in zebrafish embryonic development*. Science, 309:310–311 (2005).
- [35] M. FERG, R. SANGES, J. GEHRIG, J. KISS, M. BAUER, A. LOVAS, M. SZABO, L. YANG, U. STRAEHLE, M. J. PANKRATZ, F. OLASZ, E. STUPKA, AND F. MUELLER. *The TATA-binding protein regulates maternal mRNA degradation and differential zygotic transcription in zebrafish*. EMBO Journal, 26(17):3945–3956 (2007).
- [36] M. H JOHNSON AND M. L. DAY. *Egg timers: how is Developmental time measured in the early vertebrate embryo?* Bioessays, 22(1):57–63 (2000).
- [37] E ZAMIR, Z KAM, AND A YARDEN. *Transcription-dependent induction of G(1) phase during the zebra fish midblastula transition*. Mol. and Cell. Bio., 17(2):529–536 (1997).
- [38] O. C. M. SIBON, V. A. STEVENSON, AND W. E. THEURKAUF. *DNA-replication checkpoint control at the Drosophila midblastula transition*. Nature, 388(6637):93–97 (1997).
- [39] R. IKEGAMI, A. K. RIVERA-BENNETTS, D. L. BROOKER, AND T. D. YAGER. *Effect of inhibitors of DNA replication on early zebrafish embryos: evidence for coordinate activation of multiple intrinsic cell-cycle checkpoints at the mid-blastula transition*. Zygote, 5(2):153–175 (1997).
- [40] R. IKEGAMI, P. HUNTER, AND T. D YAGER. *Developmental activation of the capability to undergo checkpoint-induced apoptosis in the early zebrafish embryo*. Dev. Biol., 209(2):409–433 (1999).
- [41] M. CONCHA AND R. ADAMS. *Oriented cell divisions and cellular morphogenesis in the zebrafish gastrula and neurula: a time-lapse analysis*. Development, 125:983–994 (1998).
- [42] J. L. SHEPARD, H. M. STERN, K. L. PFAFF, AND J. F. AMATRUDA. *Analysis of the cell cycle in zebrafish embryos*. Meth. Cell Biol., 76:109–125 (2004).

-
- [43] D. E. D. NOGARE, P. T. PAUERSTEIN, AND M. E. LANE. *G2 acquisition by transcription-independent mechanism at the zebrafish midblastula transition*. Dev. Biol., 326(1):131–142 (2009).
- [44] A YARDEN AND B GEIGER. *Zebrafish cyclin E regulation during early embryogenesis*. Dev. Dyn., 206(1):1–11 (1996).
- [45] C YOON, K KAWAKAMI, AND N HOPKINS. *Zebrafish vasa homologue RNA is localized to the cleavage planes of 2- and 4-cell-stage embryos and is expressed in the primordial germ cells*. Development, 124(16):3157–3165 (1997).
- [46] S. E. WEBB AND A. L. MILLER. *Calcium signalling during zebrafish embryonic Development*. Bioessays, 22(2):113–123 (2000).
- [47] Q. Y. LIU, Z. L. WU, W. J. LY, Y. C. YAN, AND Y. P. LI. *Developmental expression of Cyclin H and Cdk7 in zebrafish: the essential role of Cyclin H during early embryo Development*. Cell Research, 17(2):163–173 (2007).
- [48] E. D. BRABAZON, R. T. BREE, M. W. CARTON, M GREALY, AND L BYRNES. *Cyclin-dependent kinase 8 is expressed both maternally and zygotically during zebrafish embryo Development*. BBA - Gene Struct. & Expr., 1576(1-2):203–208 (2002).
- [49] P. J. KELLER, A. D. SCHMIDT, J. WITTBRODT, AND E. H. K. STELZER. *Reconstruction of Zebrafish Early Embryonic Development by Scanned Light Sheet Microscopy*. Science, 322(5904):1065–1069 (2008).
- [50] H. HELMCHEN AND W. DENK. *Deep tissue two-photon microscopy*. Nat. Methods, 2(12):932–940 (2005).
- [51] D. KOBAT, M. E. DURST, N. NISHIMURA, A. W. WONG, C. B. SCHAFFER, AND C. XU. *Deep tissue multiphoton microscopy using longer wavelength excitation*. Opt. Express, 17(16):13354–13364 (2009).
- [52] C.-K. SUN, S.-W. CHU, S.-Y. CHEN, T.-H. TSAI, T.-M. LIU, C.-Y. LIN, AND H.-J. TSAI. *Higher harmonic generation microscopy for dev. biol.* J. Struct. Biol., 147:19–30 (2004).
- [53] A. GERME. *Thèse de doctorat*. Université Paris VI, Paris (2010: Bonne chance et bon courage !).
- [54] D. DÉBARRE, W. SUPATTO, AND E. BEAUREPAIRE. *Structure sensitivity in third-harmonic generation microscopy*. Opt. Lett., 30(16):2134–2136 (2005).

Conclusion & Perspectives

¹⁷In the first part of this thesis (chapter 1 & 2) we introduced the nonlinear microscopy through its main properties and applications. We gave a special attention to coherent nonlinear microscopy techniques, especially THG microscopy. We also introduced a model for calculating the signal resulting from the interaction between different field and sample structures that could be used for several different nonlinear modalities, and we used simple analytical models to describe some of the properties of nonlinear microscopy.

This model can be improved upon in several ways; for example the calculation of the focal field for arbitrary field distributions at the back aperture of the objective can be optimized compared to the simple quadrature algorithms used, or some of the sub-programs could be written in a more efficient language.

The second part of this thesis (chapter 3 and the first part of chapter 4) used the model introduced in chapter 2 to investigate signal creation and contrast mechanisms in the case of THG microscopy. We chose to concentrate on THG for this study because THG is comparatively more sensitive to the phase of the focal field than SHG and CARS, and less sensitive to sample structure than SHG. It is therefore a good model to understand psf engineering in coherent nonlinear microscopy. We started by considering the signals obtained from simple geometries that can represent different parts of biological samples in typical imaging conditions, and evaluate the influence of the focusing conditions. Structured samples are considered, and potential uses of non-Gaussian excitations are investigated. Although some experiments are used to illustrate some of the calculations, this is essentially a theoretical study on the contrast mechanisms.

The third part of this thesis (second part of chapter 4) deals with experimental implementations of wavefront control, with two different tools: an acousto-optic modulator (TAG lens) used to provide Bessel-like excitations for extended depth of field in 2PEF microscopy, and a deformable mirror used to correct the specimen-induced aberrations in THG microscopy.

There are several perspectives that can easily be envisioned to complement these parts. First, the ideas explored in the numerical calculations will have to be tested by incorporating a spatial light modulator (SLM) in the microscope. One perspective will also be to expand them to other nonlinearities than THG. For example, SHG from organized structures will be particularly sensitive to the polarization properties of engineered beams. It will also be interesting to compare signals from the same sample obtained with different modalities; for example THG and CARS both depend on the $\chi^{(3)}$ of the sample and have different phase-matching conditions. Regarding aberration correction, the scheme could be further optimized by taking into account the spatial and temporal evolution of the aberration.

The final part of this thesis (chapter 5) deals with biomedical applications of nonlinear microscopy. This manuscript does not accurately represent the relative importance of this part

¹⁷■ Epilogue, Opeth, My Arms, Your Hearse (1998)

Chapter 5. Biological Applications of Third Harmonic Generation Microscopy

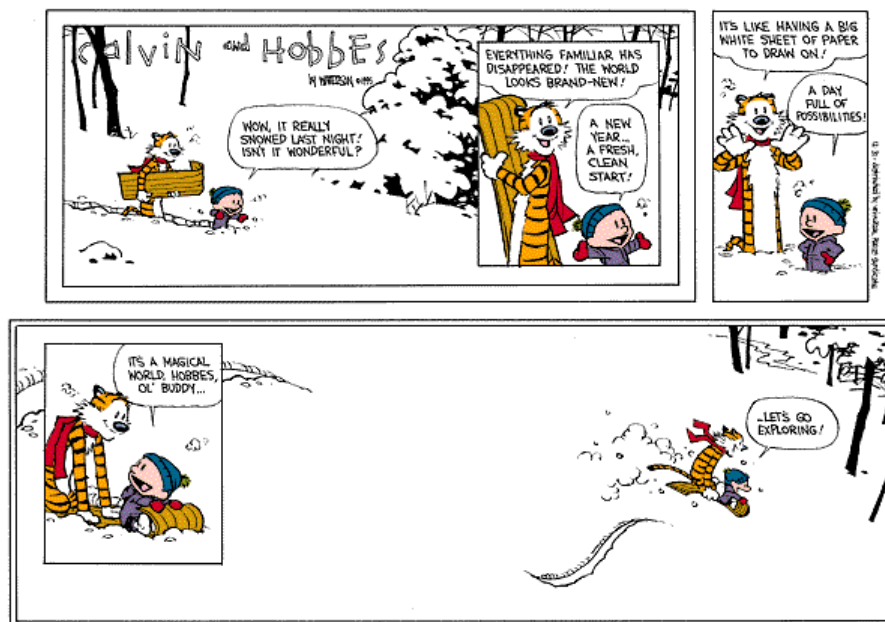
compared to the study of the contrast mechanisms, because most of these applications are still in progress. This part illustrates the importance of the collaborations during this thesis, since the two applications presented involve respectively three and four different laboratories. Nonlinear imaging of the cornea is very interesting for both physicists - since it is an organized structure that presents different levels of organization and provides different contrasts for all the nonlinear modalities - and physicians - since the nonlinear images provide a better visualization of several important structures (stacking of the stroma, keratocyte activity in edema) than linear techniques¹⁸.

The reconstruction of a digital zebrafish embryo from the 1-cell stage to the 1*k*-cell stage encompasses so many different technical aspects, a number of which performed outside the lab, that it would be too long here to describe all the aspects of this project extensively. We therefore tried to present the main results, with a bias towards the microscopy techniques.

There are many perspectives that can be envisioned concerning these applications. The work performed on the wild-type zebrafish could be extended to mutant embryos, or to another related fish to enable comparative analysis. The ex-vivo work on the cornea may pave the way to in-vivo applications once both photo-toxic effects and quantity of backscattered signals in a whole eye have been studied.

An natural idea when considering chapters 4 & 5 would be to combine focus engineering techniques with the coherent imaging of the cornea, which should allow the probing of several levels of organization in the stroma. Another match between chapters 4 & 5 would be to combine adaptive optics with the imaging of the zebrafish development, which could increase the image quality at large depths and late stages of development.

The end.[16]



¹⁸and it also makes really nice images

Appendix A

Nonlinear Optics

Contents

A.1	Nonlinear Wave Equation	195
A.2	The Gaussian Beam	198
A.3	The Bessel Beam	199
A.4	Phase-Matching Plane Waves	200
A.5	Harmonic Generation with Focused Gaussian Beams	202
A.6	Harmonic Generation with Focused Bessel Beams	205
A.7	Comparison Between THG & NR-CARS	208

In this appendix, we tried to present some of the most used analytical models that are used in nonlinear optics, and to discuss their use in nonlinear microscopy by taking into account different hypotheses they entail. It is adapted from several reference books [1–5].

A.1 Nonlinear Wave Equation

We start from Maxwell’s equations:

$$\nabla \cdot \mathbf{D}(\mathbf{r}, t) = \rho(\mathbf{r}, t) \tag{A.1}$$

$$\nabla \cdot \mathbf{B}(\mathbf{r}, t) = 0 \tag{A.2}$$

$$\nabla \times \mathbf{E}(\mathbf{r}, t) = -\frac{\partial \mathbf{B}(\mathbf{r}, t)}{\partial t} \tag{A.3}$$

$$\nabla \times \mathbf{H}(\mathbf{r}, t) = \frac{1}{c^2} \frac{\partial \mathbf{D}(\mathbf{r}, t)}{\partial t} + \mathbf{j}(\mathbf{r}, t) \tag{A.4}$$

with:

$$\mathbf{D}(\mathbf{r}, t) = \epsilon_0 \mathbf{E}(\mathbf{r}, t) + \mathbf{P}(\mathbf{r}, t) \tag{A.5}$$

$$\mathbf{H}(\mathbf{r}, t) = \frac{1}{\mu_0} \mathbf{B}(\mathbf{r}, t) - \mathbf{M}(\mathbf{r}, t) \tag{A.6}$$

where $\mathbf{P}(\mathbf{r}, t)$ and $\mathbf{M}(\mathbf{r}, t)$ are the polarization and the magnetization, and depend on $\mathbf{E}(\mathbf{r}, t)$ and $\mathbf{H}(\mathbf{r}, t)$

Combining equations A3 and A4 yields:

$$\begin{aligned}\nabla \times \nabla \times \mathbf{E}(\mathbf{r}, t) + \frac{1}{c^2} \frac{\partial^2 \mathbf{E}(\mathbf{r}, t)}{\partial t^2} &= -\mu_0 \frac{\partial}{\partial t} \left(\mathbf{j}(\mathbf{r}, t) + \frac{\partial \mathbf{P}(\mathbf{r}, t)}{\partial t} + \nabla \times \mathbf{M}(\mathbf{r}, t) \right) \\ \nabla \times \nabla \times \mathbf{H}(\mathbf{r}, t) + \frac{1}{c^2} \frac{\partial^2 \mathbf{H}(\mathbf{r}, t)}{\partial t^2} &= \nabla \times \frac{\partial \mathbf{P}(\mathbf{r}, t)}{\partial t} + \nabla \times \mathbf{j}(\mathbf{r}, t) + \mu_0 \frac{\partial \mathbf{M}(\mathbf{r}, t)}{\partial t}\end{aligned}\quad (\text{A.7})$$

A.1.1 Linear Isotropic Medium

We consider a homogeneous, isotropic, linear and sourceless medium. This means:

$$\mathbf{D} = \epsilon_0 \epsilon \mathbf{E} \quad (\text{A.8})$$

$$\mathbf{B} = \mu_0 \mu \mathbf{H} \quad (\text{A.9})$$

And the wave equation becomes:

$$\nabla \times \nabla \times \mathbf{E}(\mathbf{r}, t) + \frac{1}{c^2} \frac{\partial^2 \mathbf{E}(\mathbf{r}, t)}{\partial t^2} = -\mu_0 \epsilon_0 \chi_e \frac{\partial^2 \mathbf{E}(\mathbf{r}, t)}{\partial t^2} \quad (\text{A.10})$$

If we introduce the optical index: $n^2 = (1 + \mu_0 \epsilon_0 \chi_e)$:

$$\nabla \times \nabla \times \mathbf{E}(\mathbf{r}, t) = -\frac{n^2}{c^2} \frac{\partial^2 \mathbf{E}(\mathbf{r}, t)}{\partial t^2} \quad (\text{A.11})$$

and use the identity;

$$\nabla \times \nabla \times = \nabla \cdot \nabla - \Delta \quad (\text{A.12})$$

we get:

$$\Delta \mathbf{E}(\mathbf{r}, t) = \frac{n^2}{c^2} \frac{\partial^2 \mathbf{E}(\mathbf{r}, t)}{\partial t^2} \quad (\text{A.13})$$

A.1.2 Monochromatic Fields

We consider a monochromatic field at the frequency ω :

$$\mathbf{E}(\mathbf{r}, t) = \mathbf{E}(\mathbf{r}) \cdot e^{i\omega t} \quad (\text{A.14})$$

and we get:

$$\Delta \mathbf{E}(\mathbf{r}) + k^2 \mathbf{E}(\mathbf{r}) = 0 \quad (\text{A.15})$$

with $k = n\omega/c$.

A.1.3 Paraxial Approximation

The paraxial approximation implies that we consider a light beam that propagates in a particular direction, that is defined as the **optical axis** and is written z . In this hypothesis, the beam never deviates from this axis by more than very small angles.

$$\mathbf{E}(\mathbf{r}) = \mathbf{A}(\mathbf{r})e^{ikz} \quad (\text{A.16})$$

We can write, for the wave-vector:

$$k_z \gg k_x, k_y \Rightarrow k_z \approx k - \frac{k_x^2 + k_y^2}{2k} \quad (\text{A.17})$$

A.1.4 Slowly Varying Amplitude Approximation

The Slowly Varying Amplitude Approximation is the assumption that the envelope of a forward-traveling beam varies slowly in time and space compared to the wavelength, and can written as:

$$\left| \frac{d^2 A}{dz^2} \right| \ll \left| k \frac{dA}{dz} \right| \quad (\text{A.18})$$

Under these hypothesis, we can now rewrite the wave equation as:

$$(2ik \frac{\partial}{\partial z} + \frac{\partial^2}{\partial x^2} + \frac{\partial^2}{\partial y^2})E(x, y, z) = 0 \quad (\text{A.19})$$

A.1.5 Nonlinear Wave-Equation

We do not consider a linear medium anymore. P can now be expressed as a Taylor expansion:

$$\begin{aligned} \mathbf{P} &= \mathbf{P}_0 + \epsilon_0 \chi^{(1)} \cdot \mathbf{E}(\omega) + \frac{\epsilon_0}{2} \chi^{(2)} \cdot \mathbf{E}(\omega) \cdot \mathbf{E}(\omega) + \frac{\epsilon_0}{4} \chi^{(3)} \cdot \mathbf{E}(\omega) \cdot \mathbf{E}(\omega) \cdot \mathbf{E}(\omega) \\ &+ \dots + \mathbf{P}^{(n)}(n\omega) \end{aligned} \quad (\text{A.20})$$

with :

$$\mathbf{P}^{(n)}(n\omega) = \frac{1}{2^{n-1}} \epsilon_0 \chi^{(n)} \cdot \mathbf{E}(\omega)^n \quad (\text{A.21})$$

$\chi^{(n)}$ is called the n -th order hyperpolarizability and is intrinsically a tensor of order $(n+1)$. This shows that a field with frequency ω can induce a polarization with frequency $n\omega$, which can then create a field with frequency $n\omega$. We can then replace P by its expression in eq (A.7), and we get:

$$\Delta \mathbf{E} - \frac{1}{c^2} \frac{\delta^2 \mathbf{E}}{\delta t^2} = \frac{1}{\epsilon_0 c^2} \frac{\delta^2 (\chi^{(1)} \cdot \mathbf{E}(\omega) + \mathbf{P}_{NL})}{\delta t^2} \quad (\text{A.22})$$

$$\Delta \mathbf{E}(\omega) + \frac{n^2(\omega)\omega^2}{c^2} \mathbf{E}(\omega) = -\frac{\omega^2}{\epsilon_0 c^2} \mathbf{P}_{NL}(\omega) \quad (\text{A.23})$$

Which is called the *Non-Linear Helmholtz Equation*. It has to be written for every frequency involved in the process, so for second harmonic generation we have:

$$\Delta \mathbf{E}(\omega) + \frac{n^2(\omega)\omega^2}{c^2} \mathbf{E}(\omega) = -\frac{\omega^2}{\epsilon_0 c^2} \chi^{(2)}(\omega; 2\omega; -\omega) \mathbf{E}(2\omega) \mathbf{E}^*(\omega) \quad (\text{A.24})$$

$$\Delta \mathbf{E}(2\omega) + \frac{n^2(2\omega)(2\omega)^2}{c^2} \mathbf{E}(2\omega) = -\frac{(2\omega)^2}{\epsilon_0 c^2} \chi^{(2)}(2\omega; \omega; \omega) \mathbf{E}^2(\omega) \quad (\text{A.25})$$

In multiphoton microscopy, because the conversion process is so inefficient, we usually accept the hypothesis that we have a non-depleted pump, which means we consider $E(\omega)$ to be constant, and thus only consider one equation. For example, in the case of third harmonic generation, we have the following equation:

$$\Delta \mathbf{E}(3\omega) + \frac{n^2(3\omega)(3\omega)^2}{c^2} \mathbf{E}(3\omega) = -\frac{(3\omega)^2}{\epsilon_0 c^2} \chi^{(3)}(3\omega; \omega; \omega; \omega) \mathbf{E}^3(\omega) \quad (\text{A.26})$$

A.2 The Gaussian Beam

Gaussian beams are a solution to the paraxial monochromatic wave equation that quite accurately describe the electric field produced by a laser. They have been extensively studied, and often provide analytical solutions.

$$(\nabla_T + 2ik \frac{\partial}{\partial z}) E(\mathbf{r}, z) = 0 \quad (\text{A.27})$$

If we consider a Gaussian profile $E(x, y, 0) = E_0 e^{-\frac{x^2+y^2}{w_0^2}}$ as an initial conditions, the solution to this equation is called a Gaussian beam, and can be written as:

$$E(x, y, z) = \frac{E_0 e^{-ikz}}{(1 + 2iz/kw_0^2)} e^{-\frac{(x^2+y^2)}{w_0^2} \frac{1}{(1+2iz/kw_0^2)}} \quad (\text{A.28})$$

where w_0 is the beam waist.

If we introduce the following abbreviations:

$$b = \frac{kw_0^2}{2}: \text{Rayleigh range} \quad (\text{A.29})$$

$$w(z) = w_0 \sqrt{1 + z^2/b^2}: \text{Beam radius} \quad (\text{A.30})$$

$$R(z) = z + \frac{b^2}{z}: \text{Wavefront radius} \quad (\text{A.31})$$

$$\eta(z) = \arctan(z/b): \text{Gouy phase-shift} \quad (\text{A.32})$$

we can write:

$$E(x, y, z) = E_0 \frac{w_0}{w(z)} e^{-\frac{(x^2+y^2)}{w(z)^2}} e^{i(kz - \eta(z) + k(x^2+y^2)/(2R(z)))} \quad (\text{A.33})$$

The intensity can be written as

$$I(x, y, z) = E_0^2 \frac{w_0^2}{w(z)^2} e^{-\frac{2(x^2+y^2)}{w(z)^2}} \quad (\text{A.34})$$

The first representation has the advantage of depending directly on the beam waist, but the second representation is better for separating amplitude and phase.

A.3 The Bessel Beam

The Bessel beam also is a solution of the paraxial wave equation [6] that can be written:

$$E(\rho, z) = E_0 e^{-ik_\omega \cos(\alpha)z} J_0(k_\omega \sin(\alpha)\rho) \quad (\text{A.35})$$

The Bessel beam is non-diffractive, as the intensity distribution does not depend on the position along the z -axis. It depends on only one parameter: the α angle.

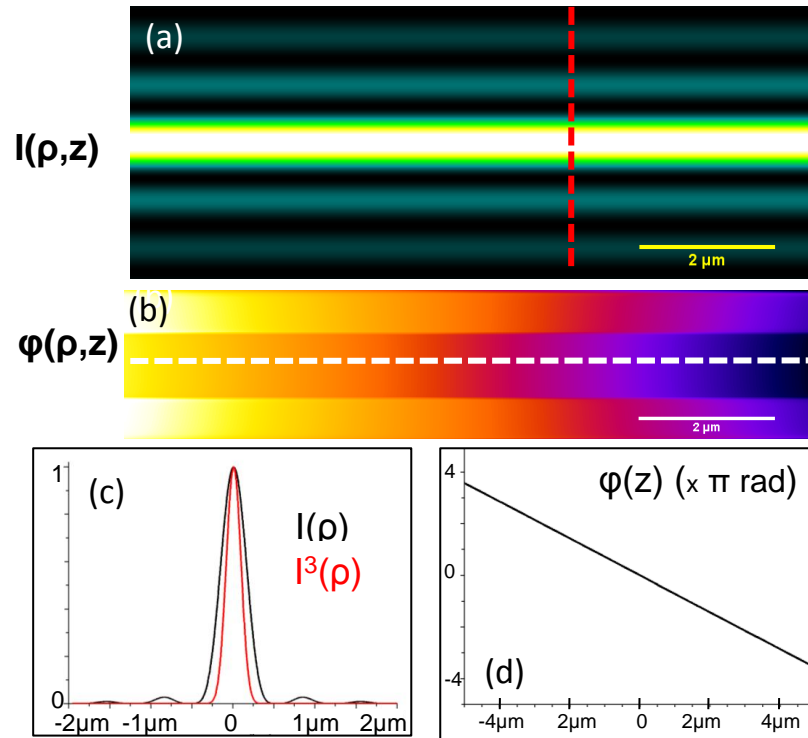


Figure A.1: INTENSITY AND PHASE DISTRIBUTION OF THE BESSEL BEAM

(a) Intensity and (b) phase of the Bessel beam described by equation A.35 with $\alpha = \pi/3$. (c) and (d): phase and intensity profile taken along the dotted line drawn in (a) & (b).

The phase and intensity distribution of the Bessel beam are described in figure (A.1). Both the non-diffractive nature of the beam and the lateral Bessel intensity distribution are apparent.

A.3.1 The Bessel-Gauss Beam

The Bessel-Gauss beam also is a solution of the paraxial wave equation [7].

$$E(\rho, z) = \frac{E_0}{\sqrt{1 + i(2z/b)}} J_0 \left(\frac{k_\omega \sin \alpha \rho}{1 + i(2z/b)} \right) \exp \left[-\frac{k(\rho^2 + z^2 \sin^2 \alpha)}{b(1 + (2z/b)^2)} \right] \\ \times \exp \left[i \left(k_\omega \cos \alpha z - \arctan(2z/b) + (2z/b) \frac{k(\rho^2 + z^2 \sin^2 \alpha)}{b(1 + (2z/b)^2)} \right) \right] \quad (\text{A.36})$$

In the limit $a \rightarrow 0$ equation (A.36) yields the usual Gaussian beam, while in the limit $b \rightarrow \infty$ it yields a Bessel beam¹.

A.4 Phase-Matching Plane Waves

In this section, we consider plane waves at both the fundamental and the harmonic frequency. This means we only phase aspect of the Harmonic generation process.

$$E_\omega(z, t) = A_1 e^{i(k_\omega z - \omega t)} \quad (\text{A.37})$$

$$E_{n\omega}(z, t) = A_n(z) e^{i(k_{n\omega} z - n\omega t)} \quad (\text{A.38})$$

with $k_\omega = \frac{n_\omega \omega}{c}$

A.4.1 Second Harmonic Generation

We first consider the case of second harmonic generation. The 1D nonlinear wave-equation can be written as:

$$2ik \frac{\partial}{\partial z} E_{2\omega}(z) = CA_1^2 e^{2i(k_\omega z)} \quad (\text{A.39})$$

$$\Downarrow \\ \frac{\partial}{\partial z} A_2(z) = CA_1^2 e^{i(\Delta k z)} \quad (\text{A.40})$$

where $\Delta k = k(2\omega) - 2k(\omega)$

This equation can be easily integrated, and the harmonic field can be written as:

$$E(2\omega, z = l) = -CA_1^2 \int_0^l e^{i\Delta k z} dz \quad (\text{A.41})$$

$$= -\frac{i\omega \chi^{(2)}}{n_{2\omega} c} A_1^2 l \text{sinc} \Delta k l / 2 \quad (\text{A.42})$$

In the case of perfect phase-matching ($\Delta k = 0$), the SHG intensity increases quadratically, but if there is some phase-mismatch, we observe a dampened oscillation (*sinc* function) with a characteristic pseudo-period of $p_\phi = \pi/\Delta k$: as soon as the interaction length is larger than this period, the signal starts to decrease.

¹The true connoisseur of long analytical calculations will enjoy having a look at the phase-matching conditions in third harmonic generation of Bessel-Gauss beams derived in reference [8, 9]

This length is referred to as the **coherence length** (noted l_c) of this particular nonlinear interaction.

$$l_c^{F-SHG} = \frac{\pi}{|k(2\omega) - 2k(\omega)|} \quad (\text{A.43})$$

A.4.2 n^{th} Harmonic Generation

This same calculations can be easily performed in the case of n^{th} harmonic generation:

$$2ik \frac{\partial E_{n\omega}}{\partial z} = C_n E_1^n \quad (\text{A.44})$$

$$\Downarrow$$

$$\frac{dA_n(z)}{dz} = C_n A_1^n e^{i(\Delta k z)} \quad (\text{A.45})$$

where $\Delta k = k(n\omega) - nk(\omega)$, and we get:

$$E(n\omega, z = l) = C_n A_1^n \text{sinc} \Delta k l / 2 \quad (\text{A.46})$$

and the coherence length for this process is:

$$l_c^{F-NHG} = \frac{\pi}{|k(n\omega) - nk(\omega)|} = \frac{\lambda}{2n|n_{n\omega} - n_\omega|} \quad (\text{A.47})$$

A.4.3 Backward Emission

The case of backward emission is described by the exact same equation, except that we have:

$$E_\omega(z, t) = A_1 e^{i(k_\omega z - \omega t)} \quad (\text{A.48})$$

$$E_{2\omega}(z, t) = A_2(z) e^{i(-k_{2\omega} z - 2\omega t)} \quad (\text{A.49})$$

We can the perform the same calculations as in the forward case, except with $\Delta k_{b\omega} = k(n\omega) + nk(\omega)$. This means that for backward n^{th} harmonic generation, the coherence length is defined as:

$$l_c^{B-NHG} = \frac{\pi}{|k(n\omega) + nk(\omega)|} \approx \frac{\lambda}{4.n.n_\omega} \quad (\text{A.50})$$

Thus, the coherence length depends almost linearly on the order of the nonlinear process.

A.4.4 Lateral Emission

We now consider an emission at an angle θ from the optical axis. The phase matching conditions are now vectorial, and we have:

$$\Delta k_z(\theta) = n(k_\omega) - k_{n\omega} \cos(\theta) \quad (\text{A.51})$$

$$\Delta k_x(\theta) = k_{n\omega} \sin(\theta) \quad (\text{A.52})$$

The only way to satisfy both conditions is to have $n \cdot k_\omega = k_{n\omega}$ and $\theta = 0$. However, if we consider an interface of inhomogeneities along the x axis, the phase-matching condition in that direction is not constraining anymore, and we can get out of axis emission.

A.5 Harmonic Generation with Focused Gaussian Beams

This section discusses the model used in Boyd's *Nonlinear Optics* [1]. We start from the nonlinear wave equation for a n^{th} harmonic generation process in the paraxial approximation:

$$\nabla_T^2 A_n + 2ik_{n\omega} \frac{\partial A_n}{\partial z} = -C_n \cdot A_1^n \cdot e^{i\Delta k} \quad (\text{A.53})$$

We then make the hypothesis that both excitation and harmonic beam can be described by Gaussian beams with the same confocal parameter, which can be written as:

$$A_n(r, z) = \frac{B_n}{1 + 2iz/b_n} e^{-r^2/w_n^2(1+2iz/b_n)} \quad (\text{A.54})$$

with:

$$\begin{aligned} w_n^2 &= w_0^2/n \\ b_n &= k_{n\omega} w_n^2 \end{aligned} \quad (\text{A.55})$$

and we introduce:

$$\Delta k = \frac{2\pi\Delta n}{\lambda} \quad (\text{A.56})$$

Since some energy will be transferred from the fundamental wavelength to the harmonic wavelength, we add a z dependence of the harmonic signal (neglecting the variations at the fundamental wavelength).

$$A_k(r, z) = \frac{B_k(z)}{1 + 2iz/b_k} e^{-r^2/w_k^2(1+2iz/b_k)} \quad (\text{A.57})$$

$$= B_k(z) \cdot G_k(r, z) \quad (\text{A.58})$$

If we introduce this expression into the nonlinear wave equation, we get:

$$\begin{aligned} C_n G_1(r, z)^n &= (\nabla_r^2 + 2ik_{n\omega} \frac{\partial}{\partial z})(B_n(z) \cdot G_n(r, z)) \\ &= B_n(z) \nabla_r^2(G_n(r, z)) + 2ik_{n\omega} B_n(z) \frac{\partial}{\partial z}(G_n(r, z)) + G_n(r, z) \frac{\partial B_n(z)}{\partial z} \\ &= G_n(r, z) \frac{\partial}{\partial z}(B_n(z)) \end{aligned} \quad (\text{A.59})$$

since $G_k(r, z)$ is solution to the paraxial wave equation, and thus $(\nabla_r^2 + 2ik_{n\omega})(G_n(r, z)) = 0$. Moreover, since:

$$\frac{G_1(r, z)^n}{G_n(r, z)} = \frac{e^{i\delta kz}}{(1 + 2iz/b)^{(n-1)}} \quad (\text{A.60})$$

This equation can easily be integrated, and we find:

$$B_n(z) = B_0 \int_{z_0}^z \frac{e^{i\Delta k \zeta} d\zeta}{(1 + 2i\zeta/b_1)^{(n-1)}} \quad (\text{A.61})$$

$$= B_0 J_n(\Delta k, z_0, z) \quad (\text{A.62})$$

The properties of this so-called J integral are discussed in the next section.

A.5.1 The J Integral

The J integral can be written as:

$$J_n(\Delta k, z_0, z) = \int_{z_0}^z \frac{e^{i\Delta k \zeta} d\zeta}{(1 + 2i\zeta/b)^{(n-1)}} \quad (\text{A.63})$$

This equation usually has no analytical solution except in the case of an infinite homogeneous medium, so we will calculate it numerically for 2 geometries: interfaces & slabs of varying sizes.

A.5.1.1 Homogeneous Medium

Let us consider the case of a homogeneous sample : $z_0 = -\infty$, $z = +\infty$.

$$J_{homogeneous}^{(n)}(\Delta k) = \int_{-\infty}^{+\infty} \frac{e^{i\Delta k \zeta} d\zeta}{(1 + 2i\zeta/b)^{(n-1)}} \quad (\text{A.64})$$

For $n \geq 3$, we have:

$$J_H^{(n)}(\Delta k > 0) = \frac{b}{2} \frac{2\pi}{(n-2)} \left(\frac{b\Delta k}{2} \right)^{(n-2)} e^{-b\Delta k/2} \quad (\text{A.65})$$

$$J_H^{(n)}(\Delta k \leq 0) = 0 \quad (\text{A.66})$$

in the case of SHG, this model does not work very well, and additional parameters have to be taken into account [10].

A.5.1.2 At Interfaces

We consider here that $z_0 = 0$

Second Harmonic Generation The J integral in this case can be written as:

$$J_I^{(2)}(\Delta k, z) = \int_0^z \frac{e^{i\Delta k \zeta} d\zeta}{(1 + 2i\zeta/b)} \quad (\text{A.67})$$

Figure (A.2) illustrates the amount of Second Harmonic signal as a function of the linear index mismatch Δn and the width of the interface. We can see that the maximum amount of signal is obtained when Δn is small.

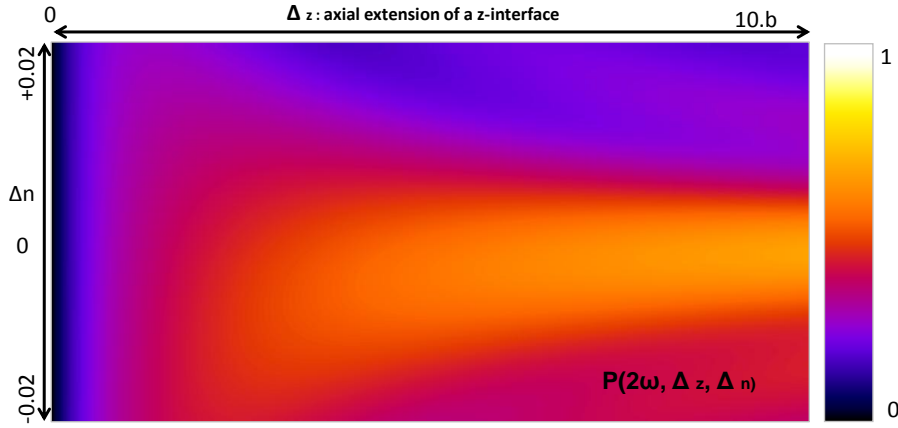


Figure A.2: SHG FROM INTERFACES AS A FUNCTION OF Δn AND z
 Conditions: $b=2\mu m$, $n = 1.35$, $-0.05 < \Delta n < 0.05$, $0 < z < 20\mu m$

Third Harmonic Generation: The J integral in this case can be written as:

$$J_I^{(3)}(\Delta k) = \int_0^z \frac{e^{i\Delta k \zeta} d\zeta}{(1 + 2i\zeta/b)^2} \quad (\text{A.68})$$

Figure (A.3) illustrates the amount of Third Harmonic signal as a function of the linear index mismatch Δn and the width of the interface. We can see that the maximum amount of signal is obtained when Δn is negative, which makes sense since it counters the phase-mismatch introduced by the Gouy phase-shift.

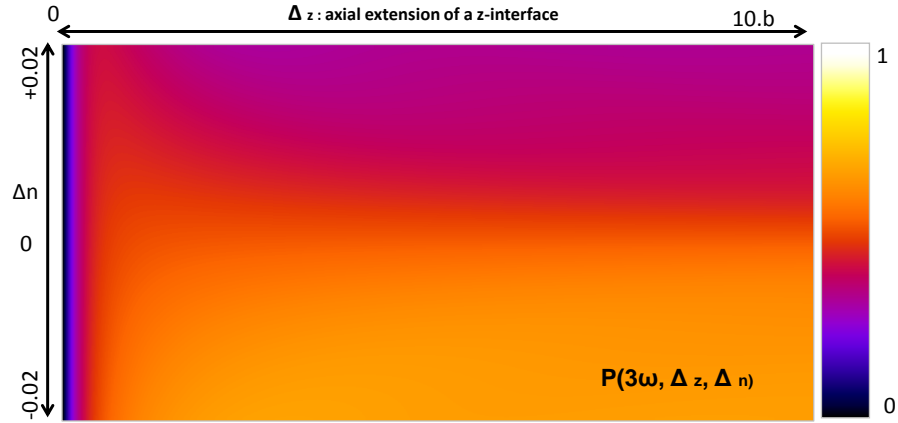


Figure A.3: THG FROM INTERFACES AS A FUNCTION OF Δn AND Δz
 Conditions: $b=2\mu m$, $n = 1.35$, $-0.05 < \Delta n < 0.05$, $0 < z < 20\mu m$

A.5.1.3 On Slabs

The geometry considered in this section is that of a centered slab of infinite transverse extend, and of axial width $2z$ centered in $z = 0$.

Second Harmonic Generation: The J integral in this case can be written as:

$$J_{slab}^{(2)}(\Delta k, \Delta z) = \int_{-z}^{+z} \frac{e^{i\Delta k \zeta} d\zeta}{(1 + 2i\zeta/b)} \quad (\text{A.69})$$

Figure (A.4) illustrates the amount of Second Harmonic signal as a function of the linear index mismatch Δn and the width of the interface. We can see that the maximum amount of signal is obtained when Δn is small.

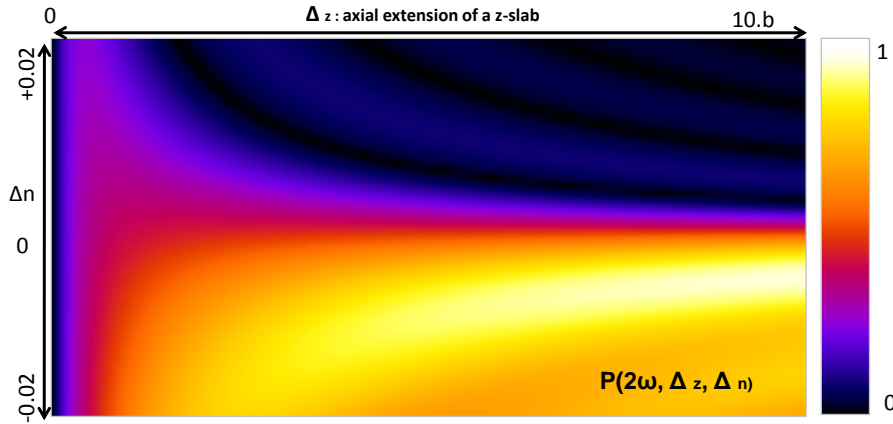


Figure A.4: SHG FROM SLABS AS A FUNCTION OF Δn AND Δz
 Conditions: $b=2\mu m$, $n = 1.35$, $-0.05 < \Delta n < 0.05$, $0 < \Delta z < 20\mu m$

Third Harmonic Generation: The J integral in this case can be written as:

$$J_I^{(3)}(\Delta n, \Delta z) = \int_{-z}^{+z} \frac{e^{i\frac{2\pi\Delta n}{\lambda}\zeta} d\zeta}{(1 + 2i\zeta/b)^2} \quad (\text{A.70})$$

Figure (A.5) illustrates the amount of Third Harmonic signal as a function of the linear index mismatch Δn and the width of the slab. We can see that the maximum amount of signal is obtained when Δn is negative, which makes sense since it counters the phase-mismatch introduced by the Gouy phase-shift.

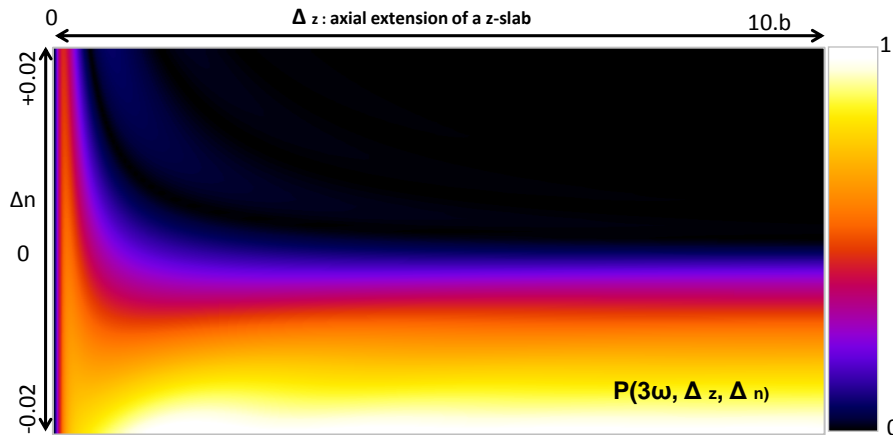


Figure A.5: THG FROM SLABS AS A FUNCTION OF Δn AND Δz
 Conditions: $b=2\mu m$, $n = 1.35$, $-0.05 < \Delta n < 0.05$, $0 < \Delta z < 20\mu m$.

A.6 Harmonic Generation with Focused Bessel Beams

In this section, we follow the treatment of Tewari *et al* [11, 12], and consider the interaction between two Bessel beams.

$$E_1(\rho, z, \omega) = E_0 e^{-ik_\omega \cos \alpha z} J_0(k_\omega \sin(\alpha)\rho) \quad (\text{A.71})$$

$$E_n(\rho, z, 3\omega) = A_n(z) e^{-ik_{n\omega} \cos \beta z} J_0(k_{n\omega} \sin(\beta)\rho) \quad (\text{A.72})$$

We remind the paraxial wave equation as:

$$\nabla_T^2 E_n + 2ik_{n\omega} \frac{\partial E_n}{\partial z} = C_n E_n^n \quad (\text{A.73})$$

Introducing equation A.72 into the wave equation yields:

$$2ik_{3\omega} \cos \beta J_0(k_{3\omega} \sin \beta \rho) \frac{dA_n(z)}{dz} = C_n J_0(k_\omega \sin \alpha \rho)^3 e^{iz(k_{3\omega} \cos \beta - 3k_\omega \cos \alpha)} \quad (\text{A.74})$$

Multiplying both sides by $k_{3\omega} \rho \sin \beta J_0(k_{3\omega} \sin \beta \rho)$ yields:

$$2ik_{3\omega}^2 \cos \beta \sin \beta \frac{dA_n(z)}{dz} (\rho J_0^2(k_{3\omega} \sin \beta \rho)) = C_n e^{iz(k_{3\omega} \cos \beta - 3k_\omega \cos \alpha)} k_{3\omega} \sin \beta \times (\rho J_0(k_\omega \sin \alpha \rho)^3 J_0(k_{3\omega} \sin \beta \rho)) \quad (\text{A.75})$$

We can now integrate both sides of the equation over $0 < \rho < \infty$, and use the identity:

$$\int_0^\infty \rho J_0^2(k_{3\omega} \sin \beta \rho) d\rho = \frac{1}{2k_{3\omega} \sin \beta} \quad (\text{A.76})$$

we get:

$$I_{lat}(\alpha, \beta) = \int_0^\infty \rho J_0(k_{3\omega} \sin(\beta)\rho) J_0(k_\omega \sin(\alpha)\rho)^3 d\rho \quad (\text{A.77})$$

Figure (A.6) illustrates the value of the I_{lat} integral for various linear index mismatch assuming perfect axial phase matching. We can see that if we have negative dispersion, We get some signal from a homogeneous medium, while in the case of positive dispersion, the intensity of the harmonic Bessel beam goes to zero. However, we can see that the model is not adapted, as the nonlinear effect is not confined (though it was expected in the axial direction) and the signal varies significantly as the integration is performed for larger and larger radii even when they are much larger than our resolution.

Equation A.75 can finally be written:

$$ik_{3\omega} \cos \beta \frac{dA_n(z)}{dz} = C_n e^{iz(k_{3\omega} \cos \beta - 3k_\omega \cos \alpha)} k_{3\omega} \sin \beta I_{lat}(\alpha, \beta) \quad (\text{A.78})$$

$$\Downarrow$$

$$\frac{dA_n(z)}{dz} = C_n \tan \beta e^{iz(k_{3\omega} \cos \beta - 3k_\omega \cos \alpha)} I_{lat}(\alpha, \beta) \quad (\text{A.79})$$

We introduce $\Psi(\alpha, \beta) = (k_{3\omega} \cos \beta - 3k_\omega \cos \alpha)$, and integrate between 0 and z :

$$A_n(z) = C_n \tan \beta I_{lat}(\alpha, \beta) \int_0^z e^{iz\Psi(\alpha, \beta)} dz \quad (\text{A.80})$$

$$= C_n \tan \beta I_{lat}(\alpha, \beta) z \frac{\sin(z\Psi(\alpha, \beta))}{\Psi(\alpha, \beta)} \quad (\text{A.81})$$

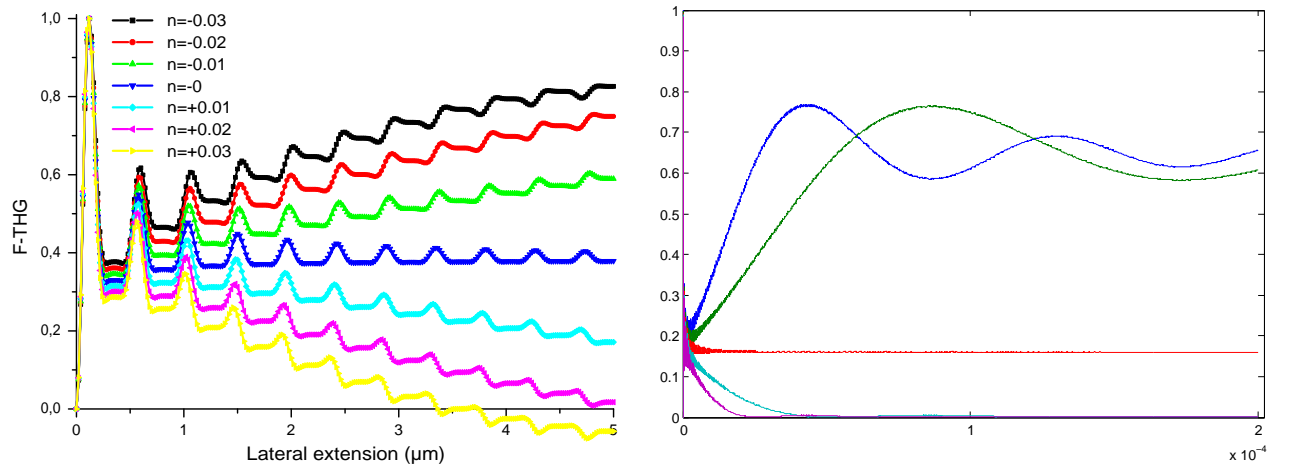


Figure A.6: I_{lat} AND I_{lat}^2 AS A FUNCTION OF Δn :
 Oscillations of the amplitude of the harmonic field as the function of the lateral extension of the domain. (Left) on a μm scale, and (Right) over $200\mu\text{m}$. Conditions: $\alpha = \pi/3$, $\lambda = 1.2\mu\text{m}$, $n_\omega = 1.5$, $n_{3\omega} = 1.5 + \Delta n$

A.7 Comparison Between THG & NR-CARS

In this section, we compare phase-matching conditions in THG and non-resonant CARS microscopy. In order to simplify the discussion, we will not consider a regular CARS process, but a degenerate version involving only one wavelength corresponding to the self phase modulation. We remind the nonlinear susceptibilities of THG and CARS for an isotropic medium [1]:

$$P_i^{(3\omega)} = \sum_{jkl} \chi_{ijkl}^{(3)} E_j(\omega) E_k(\omega) E_l(\omega) \quad (\text{A.82})$$

with:

$$\chi_{ijkl}^{(3)} = \chi_0 \cdot (\delta_{ij} \cdot \delta_{kl} + \delta_{ik} \cdot \delta_{jl} + \delta_{il} \cdot \delta_{jk}) \quad (\text{A.83})$$

and:

$$P_i^{(CARS)}(2\omega - \omega = \omega) = \sum_{j,k,l} \chi_{ijkl}^{(3)} E_j(\omega) E_k^*(\omega) E_l(\omega) \quad (\text{A.84})$$

with :

$$\chi_{ijkl}^{(3)} = \chi_1 \cdot (\delta_{ij} \cdot \delta_{kl} + \delta_{ik} \cdot \delta_{jl}) + \chi_2 \cdot (\delta_{il} \cdot \delta_{jk}) \quad (\text{A.85})$$

Since we will consider a Gaussian excitation, we will use the scalar approximation, and the two nonlinear polarizations can be written as [13, 14]:

$$P^{(CARS)}(2\omega - \omega = \omega) = \chi_1 I_x(\omega) E_x(\omega) \quad (\text{A.86})$$

$$P^{(THG)}(3\omega) = \chi_1 E_x^3(\omega) \quad (\text{A.87})$$

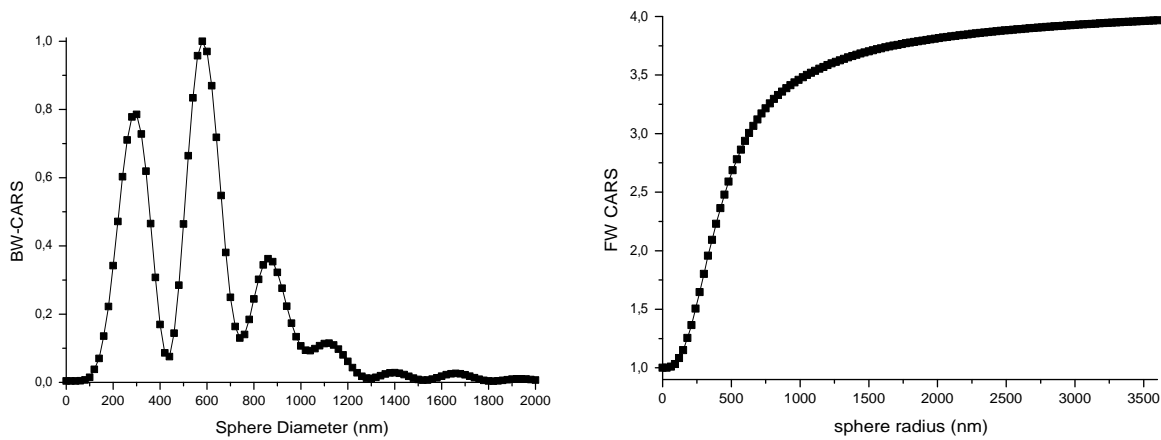


Figure A.7: B-CARS & F-CARS

Comparison between B-CARS and F-CARS from a centered sphere of nonlinear susceptibility $\chi^{(3)} = 2$ surrounded by a medium with $\chi^{(3)} = 1$ (Right) Numerical simulation, Conditions: $NA = 1.2$, $n_\omega = n_{3\omega} = 1.5$

What can be noticed immediately from equation (A.87) is that although the amplitude of both polarizations are equal, their phases are completely different, with the phase of the THG

polarization equal to three times that of the CARS polarization. The main consequence of this is illustrated in figure (A.7): There is some forward emitted signal from a homogeneous sample in CARS microscopy, and the signal is proportional to the square of the nonlinear susceptibility. The forward CARS coherence length can be approximated as:

$$l_{fw} = \frac{\pi}{\Delta k} = \frac{\pi}{(k_\omega + k_G) - k_\omega} = \frac{\pi}{k_g} \quad (\text{A.88})$$

and was estimated in [13, 14] as: $l_{fw} \approx 2.1\lambda$ in the conditions we used. This coherence length being longer than the optical confinement, the destructive interferences that occur once this size has been reached are negligible and the signal stays constant.

The backward CARS signal is quite similar to backward THG (fig 3.5), with a large phase mismatch that implies the presence of damped oscillations. This backward coherence length can be calculated the same way as the THG coherence length defined in equation (3.12):

$$l_{bw} = \frac{\pi}{k_{\omega - (-k_\omega)}} = \frac{\lambda}{4n_\omega} \quad (\text{A.89})$$

Since we consider a sphere and not a slab, the maximum signal is obtained for a slightly larger diameter than predicted, for the same reason as in the case of B-THG described in section 3.1.2.2.

An interesting perspective would be to combine NR-CARS microscopy with 3rd order sum frequency generation. The phase matching conditions would be the same as the ones we just described, but both nonlinear wavelengths could be detected, and could provide sub-resolution size and orientation information about the sample.

Appendix B

Experimental Setup

Contents

B.1	Description of the Setup	212
B.2	Characteristics of the Laser & OPO	213
B.3	Microscope Setup with Adaptive Optics	214
B.4	Characteristics of the Deformable Mirror	215
B.5	Setup Using the TAG lens	216
B.6	Characteristics of the Microscope Objectives	217
B.7	Cornea Preparation	218
	Bibliography	219

B.1 Description of the Setup

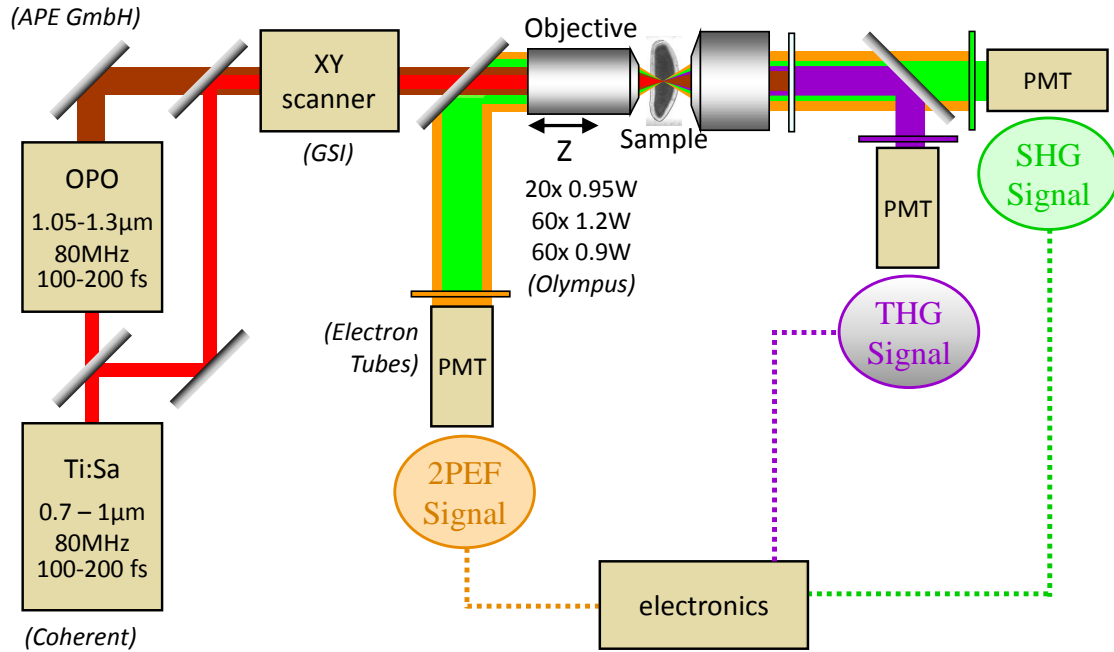


Figure B.1: EXPERIMENTAL SETUP:

The output power from a titanium:sapphire (Ti:Sa) oscillator (Chameleon Ultra II, Coherent (USA), described in more details in the next section) is modulated using a half-wave plate (HWP) and a polarizer (POL) [not shown]. The polarized beams are either sent into an optical parametric oscillator (OPO, APE (Germany), described in the next section), or directly into the scanning microscope. Mechanical shutters are used to select the OPO or the Ti:S beam [not shown]. The excitation beam is scanned with galvanometric mirrors (GSI, USA), and expanded to fill the back aperture of a water-immersion objective (Obj, described in appendix B.6). The nonlinear signals are detected by photon-counting photomultiplier modules (PMT, ET Enterprises (UK)), and 100MHz counting electronics (X. Solinas, LOB). Scanning and acquisition are synchronized using Labview software and a multichannel I/O board (NI, USA). 2PEF is typically epi-detected through the same objective and selected using a dichroic mirror and filters. THG and SHG light are typically detected in the transmitted direction through a condenser and selected using a dichroic beam splitter and band-pass filters.

B.2 Characteristics of the Laser & OPO

B.2.1 Chameleon Ultra II

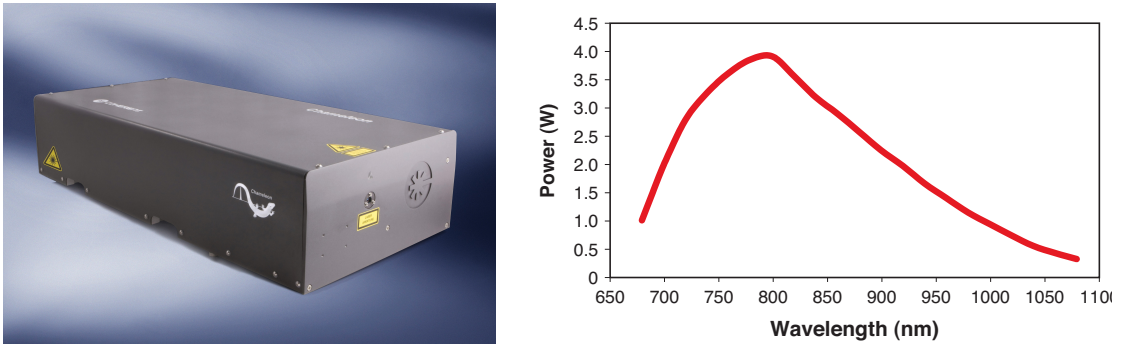


Figure B.2: CHARACTERISTICS OF THE CHAMELEON ULTRA II LASER. (Left) Photograph of the laser. (Right) Output power as a function of the center wavelength.

The laser used on the THG microscope is a Chameleon Ultra II Ti:Sapphire oscillator (Coherent, USA). It is a turn key computer-controlled laser that provides pulses of $\approx 100fs$ at a repetition rate of $80MHz$ and is tunable between $660nm$ and $1080nm$. The output power as a function of the central wavelength is illustrated in figure (B.2).

B.2.2 OPO

The synchronously pumped OPO (APE GmbH, Berlin) uses a KTP crystal to generate longer wavelengths through optical parametric generation. In typical imaging experiments, it is pumped at the wavelength of $820nm$ and an average power of $3.3W$ and has an output wavelength at $\lambda \approx 1180nm$ with a pulse duration of $\approx 200fs$ (that can be compressed down to $80fs$ at the focus using a prism-based compressor), and an output power of $1W$.

B.3 Microscope Setup with Adaptive Optics

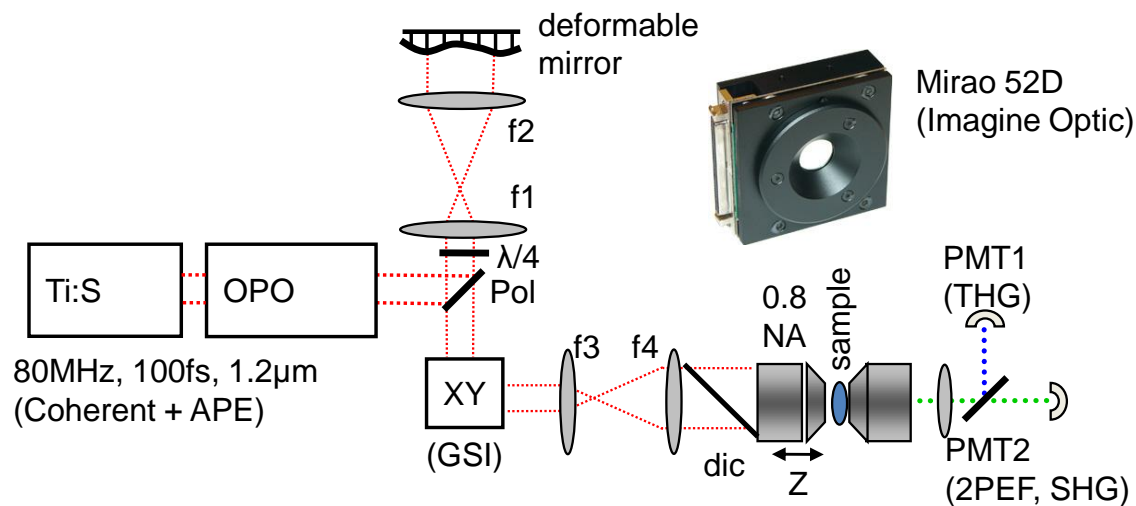


Figure B.3: EXPERIMENTAL SETUP FOR ABERRATION CORRECTIONS IN NON-LINEAR MICROSCOPY

(Pol): polarizing beamsplitter cube ($\lambda/4$): Quarter-wave-plate.

The excitation wavelength coming from a laser-pumped OPO is reflected by a deformable mirror conjugated with a pair of galvanometric mirrors that are themselves conjugated with the objective lens. The characteristics of the deformable mirror used are described in the next section.

B.4 Characteristics of the Deformable Mirror

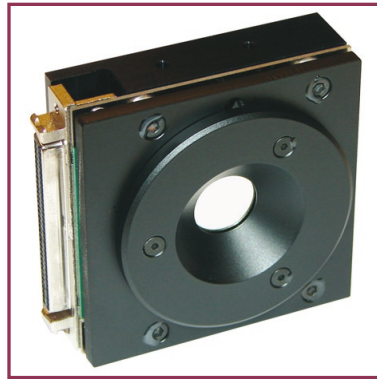


Figure B.4: MIRA0

The deformable mirror used on the nonlinear microscope is an electromagnetic deformable mirror (shown in figure B.4) with 52 actuators (MIRA0, Imagine Optic, Orsay). The technical specifications of this mirror are given in figure (B.5).

Main specifications	
Number of actuators	52
Maximum generated wavefront (PV)	50 μm (tilt)
Surface quality (RMS active flat)	0.01 μm
Wavefront quality (RMS active flat)	0.02 μm
Integrated tip/tilt correction	Yes
Spatial frequency correction	Zernike orders up to 6
Effective diameter	15 mm
Linearity	> 95%
Hysteresis	< 2%
Actuator input voltage	$\pm 1\text{V}$ max in each of the 52 channels Sum of absolute voltages < 25 V
Coatings	Protected silver
Power consumption	50 W max.
Dimensions / weight (DM unit only)	64 x 64 x 23 mm / 490 g
Connectivity	USB 2

Figure B.5: SPECIFICATIONS OF MIRA0

B.5 Setup Using the TAG lens

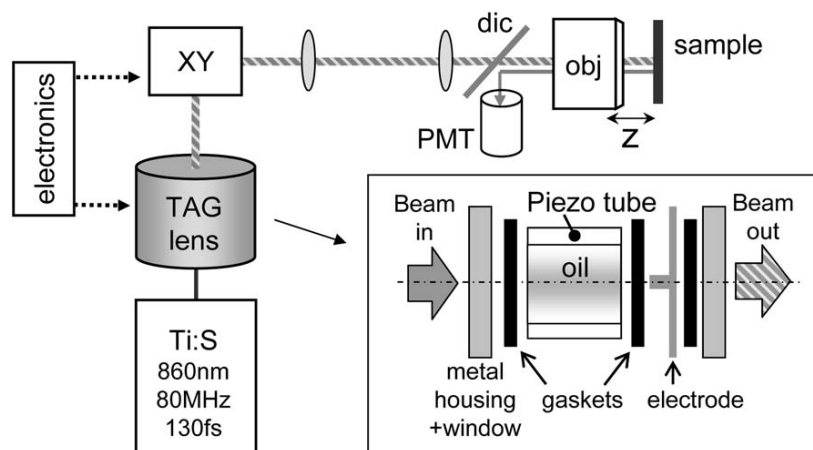


Figure B.6: EXPERIMENTAL SETUP WHEN USING THE TAG LENS

The excitation coming from the Ti:SA laser goes through the TAG lens and propagates until the galvanometric mirrors that are conjugated with the objective lens. The TAG is not imaged on the galvanometric mirrors, but instead propagates for a long distance to reach them which means we have an amplitude-modulated beam.

B.5.1 Limitation & Perspectives

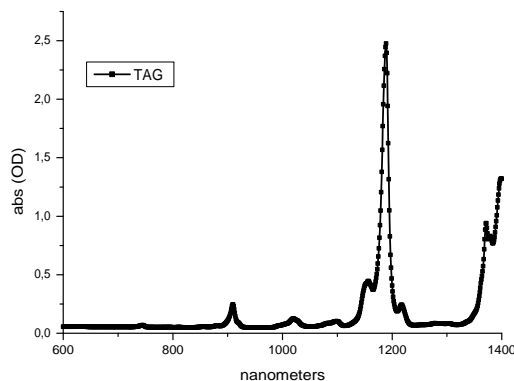


Figure B.7: ABSORPTION SPECTRUM OF THE TAG LENS

Figure (B.7) illustrates the main limitation of the current implementation of the TAG lens for THG microscopy: the filling fluid exhibits a strong absorption peak at the wavelength typically used in our THG imaging experiments ($\lambda = 1180\text{nm}$). It means that only 2PEF (750 – 950nm) is practical using this particular filling fluid. Future studies will determine which alternative liquid can be used at the typical THG wavelength.

B.6 Characteristics of the Microscope Objectives

Table B.1 describes the main properties of the objectives used on the THG Microscope.

	NA	d (mm)	w_{th} (μm)	w_{exp} (μm)	FOV (μm)
Olympus, 60x, W	0.9	2	2.2	2.0	330
Olympus, 20x, W	0.55 – 0.95	2.2	–	2.5 – 6	1000
Olympus, 60x, W	1.2	0.3	1.1	1.3	330

Table B.1: DIFFERENT OBJECTIVES USED FOR THG MICROSCOPY.

The axial resolution is measured as the full-width half maximum of a THG axial profile on a water/glass interface, and is given for an excitation wavelength of $\lambda = 1180\text{nm}$. The Numerical Aperture given for the 20x objective corresponds to effective apertures used in typical experiments as the back aperture of the objective is very large and often under-covered. The theoretical resolution is calculated with equation 1.4. Adapted from [15].

B.7 Cornea Preparation

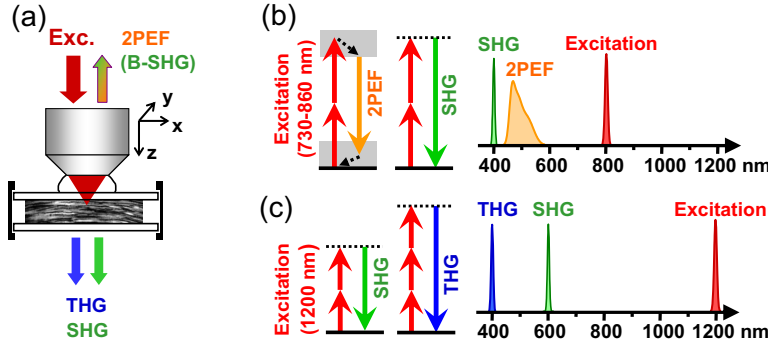


Figure B.8: SETUP

Principles of multiphoton/multiharmonic imaging. (a) Experimental arrangement and signal directionality. (b) SHG/2PEF with excitation in the 730-860 nm range. (c) THG/SHG with 1200 nm excitation.

The study was conducted according to the tenets of the Declaration of Helsinki and the French legislation for scientific use of human corneas, and was approved by the French Society of Ophthalmology Ethics Committee. We analyzed fresh human corneal buttons obtained from patients that underwent penetrating keratoplasty. Immediately after their removal, the whole trephined corneal buttons were placed in Hanks medium (Sigma-Aldrich, St. Louis, MO) supplemented with 5% Dextran T500 (Sigma-Aldrich) to avoid edema. Corneal buttons were maintained between two 150 μ m -thick glass coverslips to flatten the corneal surface and imaged from the epithelium side or the endothelium side, depending of the experiment. When estimating epidetected SHG and THG signals, the bottom glass lamella was covered with black tape to minimize light reflection at the glass-liquid interface.

Trabeculum was imaged in human corneas obtained from the Banque Française des Yeux (French Eye Bank) of Paris that were unsuitable for transplantation mostly because of low endothelial cell density. Corneoscleral discs were stored using the organ culture technique in CorneaMax medium (Eurobio, Courtaboeuf, France). They were maintained in a custom-made acrylic glass dish filled with Hanks solution supplemented with Dextran, and imaged from the endothelium side with underlying coverslip.

Bibliography

- [1] R.W. BOYD. *Nonlinear optics, 2nd edition*. Academic Press (2003).
- [2] Y. R. SHEN. *The Principles of Nonlinear Optics*. Wiley, New-York (1984).
- [3] L. NOVOTNY AND B. HECHT. *Principles of Nano-Optics*. Cambridge Univ Press (2006).
- [4] A. YARIV. *Quantum Electronics*. Willey, New York (1975).
- [5] J. W. GOODMAN. *Introduction to Fourier optics*. McGraw-Hill, New York (1995).
- [6] E. T. WHITAKER. *On the partial differential equations of mathematical physics*. Math. Ann., 57:333 (1903).
- [7] F. GORI, G. GUATTARI, AND C. PADOVANI. *Bessel-Gauss beams*. Optics Communications, 64:491–495 (1987).
- [8] C. F. R. CARON AND R. M. POTVLIEGE. *Phase matching and harmonic generation in bessel gauss-beams*. J. Opt. Soc. Am. B, 15(3):1096–1106 (1998).
- [9] C. F. R. CARON AND R. M. POTVLIEGE. *Optimum conical angle of a bessel-gauss beam for low-order harmonic generation in gases*. J. Opt. Soc. Am. B, 16(9):1377–1384 (1999).
- [10] D. A. KLEINMAN, A. ASHKIN, AND G. D. BOYD. *Second-harmonic generation of light by focused laser beams*. Phys. Rev., 145(1):338–379 (1966).
- [11] S. P. TEWARI, H. HUANG, AND R. W. BOYD. *Theory of self-phase-matching*. Phys. Rev. A, 51(4):R2707–R2710 (1995).
- [12] S. P. TEWARI, H. HUANG, AND R. W. BOYD. *Theory of third-harmonic generation using bessel beams, and self-phase-matching*. Phys. Rev. A, 54(3):2314–2325 (1996).
- [13] J.-X. CHENG AND X.S. XIE. *Green’s function formulation for third harmonic generation microscopy*. J. Opt. Soc. Am. B, 19(7):1604–1610 (2002).
- [14] J.-X. CHENG AND X.S. XIE. *Coherent anti-stokes raman scattering microscopy: instrumentation, theory, and applications*. J. Phys. Chem. B, 108:827–840 (2004).
- [15] D. DÉBARRE. *Thèse de doctorat*. Ecole Polytechnique, Palaiseau (2006).
- [16] NICOLAS.. *Congratulations, you have read the whole thing !. As a reward, you earned a cookie (or a coffee) for next time you meet me ! (password is footnote number 3, chapter 5)*. Cheers, N. (2010).

Mécanismes de contraste et contrôle du front-d'onde en microscopie non-linéaire cohérente

Ce travail de thèse présente une étude théorique et expérimentale de la microscopie non-linéaire cohérente pour l'étude de systèmes biologiques.

Dans un premier temps, nous avons étudié l'origine des signaux et les mécanismes de contrastes en microscopie non-linéaire cohérente. En particulier, nous avons analysé l'influence de la microstructure de l'échantillon sur le signal de troisième harmonique rayonné. Nous illustrons cette discussion par une étude sur les contrastes endogènes de la cornée humaine.

Dans un second temps, nous nous sommes intéressés à diverses méthodes de contrôle de front d'onde afin de moduler le contraste des images. Nous avons effectué par une étude théorique du signal obtenus à l'aide de modes d'excitation spatiale non-Gaussiens, puis avons implémenté deux systèmes de modulation du front d'onde : un modulateur acousto-optique permettant d'obtenir une profondeur de champ étendue en microscopie par fluorescence excitée à deux photons, et un miroir déformable permettant d'effectuer une correction dynamique des aberrations en microscope par génération de troisième harmonique.

Enfin, nous nous sommes intéressés à l'application de la microscopie non-linéaire cohérente pour l'observation du développement précoce d'organismes modèles en embryologie: la drosophile et le poisson zèbre.

Mots Clés : Microscopie, THG, Mise en forme spatiale, Optique adaptative, Biologie du développement.

Contrast Mechanisms & Wavefront Control in Coherent Nonlinear Microscopy

This thesis deals with theoretical and experimental aspects of coherent nonlinear microscopy.

We first study the physical origin of the signals and the contrast mechanism in coherent non-linear microscopy. In particular, we analyzed the influence of the microstructure of the sample on the intensity of third harmonic signal. We illustrate this discussion by a study on the nonlinear endogenous contrasts of the human cornea.

We then considered different implementations of wave-front control methods in order to modulate the contrast of the images. We carried out a theoretical study of the third harmonic signal obtained using higher order Hermit-Gaussian modes, then implemented two systems of wave front modulation:

- an acousto-optic modulator (TAG Lens) that allowed us to obtain an extended depth of field in Two-Photon Excited Fluorescence microscopy without compromising the lateral resolution.
- a deformable that allowed us to dynamically compensate for the aberrations induced by an evolving sample in THG microscopy.

Lastly, we considered application of coherent non-linear microscopy for the observation of the early development of model organisms in embryology: the *Drosophila* and the Zebrafish.

Keywords : Microscopy, THG, SHG, Wavefront control, Adaptive Optics, Developmental Biology.